ISTANBUL TECHNICAL UNIVERSITY ★ GRADUATE SCHOOL

DETERMINATION OF PATTERN, TIMING AND MECHANISM OF THE ACTIVE TECTONIC DEFORMATION IN THE WESTERN FLANK OF THE CENTRAL TAURIDES

Ph.D. THESIS

Tunahan AYKUT

Department of Solid Earth Sciences

Geodynamic Programme

SEPTEMBER 2024

ISTANBUL TECHNICAL UNIVERSITY ★ GRADUATE SCHOOL

DETERMINATION OF PATTERN, TIMING AND MECHANISM OF THE ACTIVE TECTONIC DEFORMATION IN THE WESTERN FLANK OF THE CENTRAL TAURIDES

Ph.D. THESIS

Tunahan AYKUT
(602202004)

Department of Solid Earth Sciences

Geodynamic Programme

Thesis Advisor: Prof. Dr. Cengiz YILDIRIM

SEPTEMBER 2024

ISTANBUL TEKNİK ÜNİVERSİTESİ ★ LİSANSÜSTÜ EĞİTİM ENSTİTÜSÜ

ORTA TOROSLARIN BATI KANADINDA AKTİF TEKTONİK DEFORMASYONUN DESENİNİN, ZAMANLAMASININ VE MEKANİZMASININ BELİRLENMESİ

DOKTORA TEZİ

Tunahan AYKUT
(602202004)

Katı Yer Bilimleri Anabilim Dalı

Jeodinamik Programı

Tez Danışmanı: Prof. Dr. Cengiz YILDIRIM

EYLÜL 2024

Tunahan AYKUT, a Ph.D. student of ITU Graduate School student ID 602202004 successfully defended the thesis/dissertation entitled "DETERMINATION OF PATTERN, TIMING AND MECHANISM OF THE ACTIVE TECTONIC DEFORMATION IN THE WESTERN FLANK OF THE CENTRAL TAURIDES", which he prepared after fulfilling the requirements specified in the associated legislations, before the jury whose signatures are below.

Thesis Advisor :	**Prof. Dr. Cengiz YILDIRIM** İstanbul Technical University	.....
Jury Members :	**Prof. Dr. Tahsin Attila ÇİNER** Istanbul Technical University	.....
	Prof. Dr. Tolga GÖRÜM Istanbul Technical University	.....
	Prof. Dr. Hüseyin TUROĞLU Istanbul University	.....
	Doç. Dr. Cihan BAYRAKDAR Istanbul University	.....

Date of Submission : 06 July 2024

Date of Defense : 02 September 2024

To the memory of my beloved mother,

FOREWORD

This dissertation is the culmination of a four-year journey during which I have been privileged to be a part of the Eurasia Institute of Earth Sciences at Istanbul Technical University. This period has profoundly shaped my development as a researcher, allowing me to collaborate with eminent scientists and gain invaluable experience.

First and foremost, I would like to express my deepest gratitude to my family for their unwavering support throughout this journey. Their encouragement has been a constant source of strength.

I owe a special debt of gratitude to my supervisor, Prof. Dr. Cengiz YILDIRIM, who has been a mentor and an inspiration to me. His guidance and support have been instrumental in navigating the challenges of this research, and his mentorship has been pivotal in the successful completion of this dissertation. I am also deeply grateful to Assoc. Prof. Dr. Tonguç Uysal for his significant support, which has been invaluable during this period.

My heartfelt thanks go to Prof. Dr. Uwe RİNG for his assistance with fieldworks and his advice on structural geological work. I also extend my gratitude to the team at the Radiogenic Isotope Facility at The University of Queensland, especially Prof. Dr. Jian-xin ZHAO and Dr. Nicole LEONARD, for their support in U-Th and U-Pb carbonate geochronology work. Additionally, I am thankful to Dr. Gang XİA for his considerable help in the sample preparation laboratory and to Gökhan YILDIRIM for his assistance with microstructural analyses.

I would also like to acknowledge the steering committee members, Prof. Dr. Hüseyin TUROĞLU and Prof. Dr. Attila ÇİNER, for their valuable advice, reviews, and for meticulously guiding this research over the past four years. This dissertation would not have been possible without the collective support and contributions of these remarkable individuals, to whom I am sincerely grateful.

Finally, I would also like to extend my gratitude to the Scientific and Technological Research Council of Türkiye and the Scientific Research Projects Department of Istanbul Technical University for their essential funding support for this study. This study was funded by the Scientific and Technological Research Council of Türkiye (TUBITAK) within the “2232 International Fellowship for Outstanding Researchers Program” (Grant No: 118C275). This study also was supported by the Scientific and Technological Research Council of Türkiye’s “2214-A International Research Fellowship Programme for PhD Students” (Grant No: 1059B142200520) and the Scientific Research Projects Department of Istanbul Technical University (Project No: TDKB-2024-45553).

July-2024 Tunahan AYKUT

TABLE OF CONTENTS

Page

ABBREVIATIONS

AT : Aksu Thrust
BZSZ : Bitlis-Zagros Suture Zone
CAP : Central Anatolian Plateau
CS : Cyprus Slab
CSZ : Cyprus Subduction Zone
CT : Central Taurides
CY : Cyprus
DEM : Digital Elevation Model
DSFZ : Dead Sea Fault Zone
EACZ : East Anatolian Contractional Province
EAFZ : East Anatolian Fault Zone
EC : Eskiköy Canyon
ES : Eratosthenes Seamount
GPS : Global Postioning System
HPS : High Paleo-Surface
IAEZSZ : Izmir-Ankara-Erzincan Suture Zone
IDW : Inverse Distance Weighting Interpolation
KDE : Kernel Density Estimate Curve
KF : Kırıkkavak Fault
ksn : The steepness index
LA-ICP-MS : Laser Ablation Inductively Coupled Plasma Mass Spectrometer
MC-ICP-MS : Multi-Collector Inductively Coupled Plasma Mass Spectrometer
MSWD : Mean Squared Weighted Deviates
NAFZ : North Anatolian Fault Zone
PDP : Probability Density Plot Curve
PF : Paphos Transform Fault
RRIM : Red Relief Image Map
WAEP : West Anatolian Extensional Province
CYA : Cyprus Arc
HA : Hellenic Arc

SYMBOLS

U	**:** Uranium
Th	**:** Thorium
Pb	**:** Lead
mm	**:** Milimeter
km	**:** kilometer
m	**:** meter
cm	**:** centimeter
mg	**:** milligram
ml	**:** milliliter
µm	**:** micrometer
Ma	**:** mega annum
ka	**:** kilo annum
(R)	**:** Stress Ratio
CO_2	**:** Carbon Dioxide
°C	**:** Degree Celsius
Mj	**:** Megajoule
HNO_3	**:** Nitric Acid
H_2O_2	**:** Hydrogen Peroxide
HF	**:** Hydrofluoric Acid
Ca	**:** Calcium
Sr	**:** Strontium
cps	**:** cycle(s) per second
ThO	**:** Thorium monoxide
Hz	**:** Hertz
J	**:** Joule
s	**:** Second
AD	**:** Angular Deviation
ppm	**:** Part Per Million
ppb	**:** Part Per Billion

LIST OF TABLES

Page

LIST OF FIGURES

Page

DETERMINATION OF PATTERN, TIMING AND MECHANISM OF THE ACTIVE TECTONIC DEFORMATION IN THE WESTERN FLANK OF THE CENTRAL TAURIDES

SUMMARY

The Central Taurides is located in the southern margin of the Central Anatolian Plateau and corresponds to the upper crust of the subduction between African and Anatolian plates, with a high relief of up to 2 km. This mountainous region has distinctive geomorphological features and presents a unique setting to investigate the mechanism of orogenic plateau margin development related to subduction and topographic evolution around the Eastern Mediterranean. Here, we combine new kinematic data from exposed fault planes, tectonic landforms from high-resolution digital elevation models, microstructural analysis and U-Th and U-Pb geochronology on syn-tectonic calcites to elucidate the pattern, mechanism and timing of active tectonic deformation in the western Central Taurides, above the Cyprus Subduction Zone.

Our geomorphic analyses reveal a post-orogenic transient actively deforming topography. The geomorphic markers constrain long-term surface uplift pattern with a mean cumulative surface uplift of 1,710 ± 50 m and shows an increasing trend from west to east, from 1,600 ± 50 to 1,800 ± 50 m. Our results suggest a dome-like uplift pattern in the west-east direction across the southern margin that reaches up to maximum cumulative uplift values in the quadrangle of Alanya-Başyayla-Ermenek-Gazipaşa. Our kinematic measurements on the exposed fault planes reveal the presence of normal, strike-slip, and thrust/reverse faults, indicating a multiphase history of brittle deformation. Microstructural studies on syn-tectonic calcites show brittle deformation features such as microcracks, brecciation, and calcite twinlets, providing evidence of tectonic control over calcite precipitation. U-Th ages of fault-related calcites show continuous normal faulting from the Middle/Late Pleistocene to the Holocene due to NE-SW horizontal extension, with a conspicuous clustering at circa 450 ka, indicating a connection/coupling between deep-seated and surface processes. It suggests that extensional deformation and rapid surface uplift may occur concurrently, creating relief-bounding normal fault zones and high-relief dynamic landscapes on a short timescale in the overriding plates.

The U-Pb carbonate geochronology of syn-tectonic calcite samples indicates three distinct phases of faulting from the Late Cretaceous to the Quaternary. Thrust/reverse faulting events, which represents the first faulting phase, were observed in the Late Cretaceous. The second faulting phase, strike-slip faulting, occurred from the Early Eocene to the Early Miocene with a clear cluster in the Oligocene. Normal faulting was the last faulting phase and is prevalent from the Early Miocene to the Quaternary. The Late Cretaceous thrust/reverse faulting could be associated with the collision of different tectonic blocks in Anatolia. The Oligocene strike-slip shearing in the region

was probably driven by the convergence and collision of tectonic plates in Eastern Anatolia and the resulting block rotations in Southern Türkiye. The onset of normal faulting in the Early Miocene indicates a shift towards extensional tectonics during the Oligocene-Miocene transition, which continuous until the present day. The last faulting phase has been possibly driven by the coupling geodynamic processes such as slab retreat, slab deformation and mantle upwelling associated with convergence along the Cyprus Subduction Zone. Our findings have significant implications for understanding the morphotectonic evolution and post-orogenic deformation in the plateau margins and geodynamic evolution of the Eastern Mediterranean.

ORTA TOROSLARIN BATI KANADINDA AKTİF TEKTONİK DEFORMASYONUN DESENİNİN, ZAMANLAMASININ VE MEKANİZMASININ BELİRLENMESİ

ÖZET

Orta Toroslar, Türkiye Jeomorfolojisi'nde en büyük fizyografik unsurlardan biridir. Son yıllarda Orta ve Doğu Torosların yükselim mekanizması, hızı ve deseni ilgili çalışmalar yayınlanmış ancak Orta Torosların Antalya ile Gazipaşa arasında kalan "Batı Kanat" olarak tarif ettiğimiz bölgesinde yapılan neotektonik çalışmalar oldukça sınırlı kalmıştır. Saha yüksek bir rölyefe ve oldukça belirgin çizgiselliklere sahip olmasına rağmen sahanın maruz kaldığı neotektonik deformasyon ile ilgili bilgilerimiz oldukça sınırlıdır. Örneğin çok yakın bir zaman önce yayınlanan Türkiye Diri Fay Haritası'na baktığımızda burada herhangi bir diri fay görülmemektedir ancak bölgesel jeoloji haritalarına baktığımızda sahada oldukça fazla fayın haritalandığı görülmektedir. Torosların bu bölümünde özellikle Neojen ve Kuvatener yaşlı birimlerin çok az olması ve sahada karstik süreçlerin etkili olması gibi nedenler; sahadaki neotektonik deformasyonun deseni, mekanizması ve fayların aktivitesi ile ilgili olarak geleneksel yöntemlerle çıkarımlar yapılmasını zorlaştırmaktadır. Bununla beraber son yıllarda hızla gelişen, akarsuların tektonik deformasyona karşı muhtemel tepkilerini dikkate alarak deformasyon desenini çıkartabilen morfometrik analizler ile faylar boyunca meydana gelen tektonik deformasyonun zamanlamasını mutlak bir şekilde belirleyebilen U-Th ve U-Pb karbonat jeokronolojisi oldukça başarılı bir şekilde kullanılmaktadır. Özellikle çalışma alanımız gibi genç çökellerin mevcut olmadığı ve fayların Kuvaterner öncesi kayaçları kestiği ortamlarda bu yöntem çok başarılıdır.

Orta Toroslar, Orta Anadolu Platosu'nun güney kenarında yer almakta olup, Afrika ve Anadolu plakaları arasındaki dalma-batma zonunun üst kabuğuna karşılık gelir ve 2 km'ye kadar yüksek bir rölyefe sahiptir. Bu dağlık bölge, belirgin jeomorfolojik özelliklere sahip olup, Doğu Akdeniz çevresindeki dalma-batma ile ilişkili jeodinamik süreçlerin yüzeydeki izlerini, ve orojenik plato kenarlarının topoğrafik evrimini araştırmak için eşsiz bir ortam sunar. Bu çalışma ile birlikte Orta Torosların batı kanadında faylanmanın tarihi ve tektonik deformasyonun zamanlamasının ortaya konması, bu verilerin yapısal ve morfometrik veriler ile birlikte yorumlanması ile bölgesel (Doğu Akdeniz) jeodinamik ve kabuksal süreçlerin daha iyi anlaşılması için literatüre önemli bir katkı konması hedeflenmektedir. Bu amaçla bu tez çalışmasında, fay yüzlekleri boyunca yapılan kinematik ölçümler ve paleo-stress analizleri, yüksek çözünürlüklü dijital yükseklik modellerinden elde edilen morfo-tektonik analizler, ve syn-tektonik kalsitler üzerinde yapılan mikro yapısal analizler ile U-Th ve U-Pb jeokronolojisi sonuçları sunulmaktadır.

Jeomorfik analiz sonuçlarımıza göre, uzun dönemli yüzey yükselim değeri ortalama 1,710 ± 50 m'dir ve bu değer çalışma sahası boyunca batıdan doğuya doğru 1,600 ± 50 m'den 1,800 ± 50 m'ye kadar yükselmektedir. Düşük rölyefli tünemiş aşınım yüzeylerinin mekansal dağılış özellikleri, akarsu sarplık indeksi değerleri, akarsu vadileri boyunca tektonik-kökenli eğim kırıklıkları ve rölyef değerleri Orta Anadolu

Platosu'nun güney kenarı boyunca batı-doğu yönünde dom benzeri bir yükselme deseni göstermektedir. Bu yükselme Alanya-Başyayla-Ermenek-Gazipaşa dörtgeninde maksimum kümülatif değerlere ulaşmaktadır. Fay yüzeylerindeki kinematik ölçümlerimiz, normal, doğrultu atımlı ve ters fayların varlığını ortaya koymakta, böylece birden çok faz geçmişine sahip bir faylanma tarihine işaret etmektedir. Bu bağlamda paleo-stress analizleri, bu faylanma olaylarıyla ilişkili gerilim rejimlerini aydınlatmakta olup, normal faylarda NE-SW çekme geriliminin baskın olduğunu gösterir. Doğrultu atımlı faylar NE-SW çekme/NW-SE sıkışma ve NW-SE çekme/NE-SW sıkışma gerilimlerinin bir kombinasyonunu göstermektedir. Bindirme/ters faylar ise NE-SW sıkışma gerilimi yansıtmaktadır.

Syn-tektonik kalsitler üzerindeki mikroyapısal çalışmalar, mikro çatlaklar, breşleşme ve kalsit fiberleri gibi kırılgan deformasyon özelliklerinn altını çizmekte, kalsit minerallerinin tektonik deformasyonla ilişkili çökeldiğini doğrulamaktadır. Fayla ilişkili kalsitlerin U-Th yaşları, Orta/Geç Pleistosen'den günümüze kadar süren aktif tektonik deformasyonun KD-GB doğrultulu genişleme rejimi ve normal faylanmayla ilişkili olduğuna işaret etmektedir. U-Th yaşları yaklaşık 450 bin yıl öncesinde dikkat çekici bir kümelenme göstermektedir. Bu kümelenme, bölgedeki çok hızlı (son 450 bin yılda 1.5 km) yüzey yükseliminin başlama dönemiyle çakışmakta, bu da son 450 bin yıl boyunca, Kıbrıs Dalma-Batma Zonu'nun üst kabuğundaki hızlı yükselme ve normal faylanmanın yaşıt olduğunu göstermektedir. Bu çıkarım bölgedeki Kuvaterner deformasyonunun manto süreçleri ile ilişkisine işaret etmektedir. Bölgedeki mevcut jeofizik, jeodinamik, jeomorfolojik ve biyostratigrafik veriler de düşünüldüğünde, levha dili deformasyonu ve astenosferik yükselmenin, Orta Toroslar'da gözlemlenen hızlı yükselmeyi ve aktif faylanmayı kontrol eden temel itici güç olduğu düşünülmektedir. Bu çalışmanın sonuçları, dalma-batma zonlarının üst kabuğunda genişlemeli deformasyon ve hızlı yüzey yükselmesinin eşzamanlı olarak kısa zaman süreleri içerisinde (<500 ka) gerçekleşebileceğini ve rölyef sınırlayan normal fay zonlarının ve yüksek rölyefli dinamik topoğrafyaların oluşabileceğinin altını çizmektedir.

Syn-tektonik kalsit örneklerinin U-Pb karbonat jeokronolojisi, Geç Kretase'den Kuvaterner'e kadar üç farklı faylanma fazının varlığına işaret etmektedir. İlk faylanma fazını temsil eden ters faylanma olayları Geç Kretase'de gözlemlenmiştir. İkinci faylanma fazı olan doğrultu atımlı faylanma, Erken Eosen'den Erken Miyosen'e kadar olup, Oligosen'de belirgin bir kümelenme göstermektedir. Normal faylanma, son faylanma fazı olup, Erken Miyosen'den Kuvaterner'e kadar yaygındır. Geç Kretase'deki ters faylanma fazı, Anadolu'daki farklı tektonik blokların çarpışmasıyla ilişkilendirilebilir. Oligosen'de şiddetlenen doğrultu atımlı faylanma fazı, muhtemelen Doğu Anadolu'daki tektonik plakaların birbirine yakınlaşması, çarpışması ve bunun sonucu Güney Türkiye'deki blokların dönme hareketleri ile ilgilidir. Erken Miyosen'de normal faylanmanın başlaması, Oligosen-Miyosen geçişi sırasında genişlemeli tektonik rejime doğru bir geçişe işaret etmekte olup, bu rejim günümüze kadar devam etmektedir. Son faylanma fazı, muhtemelen Kıbrıs Dalma-Batma Zonu boyunca kıta dili gerilemesi, kıta dili deformasyonu ve manto yükselmesi gibi jeodinamik süreçler tarafından yönlendirilmiştir.

Bu tez çalışmasının sonuçları, Orta Torosların batı kanadı boyunca aktif tektonik deformasyonun deseni, mekanizması ve zamanlaması konusunda önemli bulgular sunmaktadır. Bu bulgular, orojenik plato kenarlarındaki morfotektonik evrimin, orojenez sonrası deformasyonun ve Doğu Akdeniz'in jeodinamik gelişiminin daha iyi anlaşılması için önemli katkılar koymaktadır. Aynı zamanda Güney Anadolu'daki

bölgesel tektonik dinamiklerin daha iyi anlaşılmasına katkıda bulunmakta ve Doğu Akdeniz'deki jeodinamik modellerin iyileştirilmesine yardımcı olmaktadır. Ayrıca, bu çalışmanın sonuçları, konverjant levha sınırlarının jeolojik evrimini anlama konusunda U-Th ve U-Pb karbonat jeokronolojisinin önemini vurgulamaktadır. Yöntemlerimiz ve sonuçlarımız, manto kaynaklı üst kabuk deformasyonu ve aktif levha sınırları üzerindeki sismik tehlike potansiyeli konusunda yapılacak ileri çalışmalar için büyük potansiyele sahiptir.

1. INTRODUCTION

Central Anatolia in the Eastern Mediterranean exhibits a high elevated-low relief landscape known as the Central Anatolian Plateau (CAP) (Figure 1). CAP has evolved into a prominent landscape in the junction of the complex geodynamic mechanisms, which was governed by the convergence between African and Eurasian plates and following collision between Anatolian and Arabian Plates in the Early-Middle Miocene (Şengör & Yılmaz, 1981; Okay et al., 2010). This orogenic plateau is located in the transition zone between Western Anatolian Extensional and Eastern Anatolian Contractional Neotectonic Provinces (Şengör et al., 1985) with an average of 1,000 m elevation and bounded by Pontides and Taurides in its northern and southern margins, respectively. Margins of the CAP have higher topographic relief than the plateau interior, implying the different modes of active deformation. While the active deformation and surface uplift in the northern margin of the CAP has been interpreted as a result of restraining bend and strain accumulation related to the North Anatolian Fault Zone (Yıldırım et al., 2011), numerous studies proposed mantle-related processes like slab tearing, slab breakoff and asthenospheric upwelling (Biryol et al., 2011; Cosentino et al., 2012; Facenna et al., 2006; Schildgen et al., 2012a, 2012b, 2014), and lower crustal thermal deformation as a consequence of fore-arc sedimentation (Fernández-Blanco et al., 2020) to explain the surface uplift along the central part of the southern margin of the CAP.

The southern margin of the CAP rises in the upper plate north of the Cyprus Subduction Zone where the African Plate subducts beneath the Anatolian Plate

(Figure 1.1). The convergence between the African, Arabian and Eurasian Plates has dominated the geological evolution of the Eastern Mediterranean throughout the Mesozoic and Cenozoic (Jolivet and Faccenna, 2000; Vidal et al., 2000; Schattner, 2010). The subduction of the African Plate under Anatolia is accommodated along two active plate boundaries: The Hellenic and Cyprus trenches. These included the north dipping Cyprus and ENE-dipping Antalya slabs, which are currently separated by an upper mantle slab gap (Biryol et al., 2011; Mutlu and Karabulut, 2011; Portner et al., 2018). Segmentation of these slabs, and associated mantle flow, may have contributed to <8 Ma uplift of the Central Anatolian Plateau (Schildgen et al., 2014). Further west, the relationship between slab retreat, southward migration of the magmatic arc and lithospheric extension (e.g. normal faulting) in the Aegean Sea (i.e. Hellenic Arc) transect is well-constrained (McKenzie, 1972; Ring et al., 2010; England et al., 2016). However, this relationship, particularly across the Cyprus Subduction Zone, has remained equivocal due to the lack of isotopic age data (Wdowinski et al., 2006; Biryol et al., 2011; Cosentino et al., 2012; Howell et al., 2017; Öğretmen et al., 2018; Portner et al., 2018; Güvercin et al., 2021).

Study area presents a high relief up to a 2 km topography, which is one of the biggest physiographic features in Türkiye's geomorphology. This mountainous region has distinctive geological and geomorphological features and presents a unique setting to investigate mechanisms for orogenic plateau development, subduction-related active deformation pattern, and topographic evolution in the Eastern Mediterranean. Although there are several studies that discuss the mechanism, rate and pattern of the active deformation in the eastern Central Taurides (Schildgen et. al., 2012a, 2012b, 2014; Sarıkaya et. al., 2015; Yıldırım et. al., 2016; Öğretmen et. al., 2018; Racano et. al., 2020, 2021), neotectonic studies are scarce in the western part of the mountain belt (between Antalya-Gazipaşa). The upper crust of the Cyprus Subduction Zone between Seydişehir and Gazipaşa presents a series of NW-SE striking fault zones (Şenel, 2002) that have prominent topographical expressions

across the highly erosional and karstified orogenic plateau margin. Despite the active convergence and significant effects of mantle-rooted and crustal processes across the region (Faccenna et al., 2006; Biryol et al., 2011; Schildgen et al., 2014; Racano et al., 2021; Aykut et al., 2023), the Quaternary faulting history and seismic hazard potential remain unknown. The erosional character of the landscape and a dearth of fault related stratigraphic and sedimentological markers along the overriding plate delimit deciphering the timing of the brittle deformation.

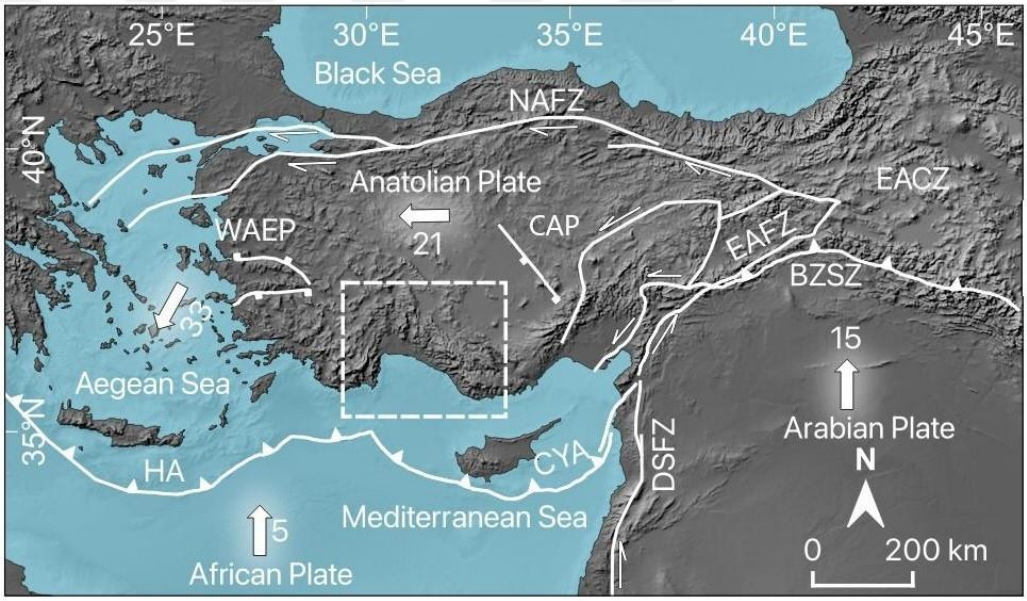

Figure 1.1: Simplified active tectonic map of the Eastern Mediterranean and Anatolia. The white box indicates the study area. White arrows denote the movement directions relative to Eurasia. GPS velocities (mm/yr) are from Reilinger et al., (2006). WAEP: Western Anatolian Extensional Province, EACZ: Eastern Anatolian Contractional Province, BZSZ: Bitlis-Zagros Suture Zone, NAFZ: North Anatolian Fault Zone, EAFZ: East Anatolian Fault Zone, DSFZ: Dead Sea Fault Zone, CYA: Cyrpus Arc, HA: Hellenic Arc, CAP: Central Anatolian Plateau.

Previous studies focused on mainly deep-seated processes with a limited contribution to the upper crustal deformation explaining the landscape evolution. Deep-seated processes can only define the relief, whereas the upper crustal deformation defines the texture (e.g., ruggedness) of topography. The landscape evolution models neglecting this interaction might be inadequate for understanding plateau margin developments, especially in regions with a high fault density. In this thesis study, we aim to provide new findings from the western flank, where robust field data is inadequate. We analyze tectonic landforms from high-resolution digital elevation models to elucidate the pattern of neotectonic deformation. We evaluate the deformation pattern based on the spatial distribution of geomorphic markers such as relict low relief upland surfaces, drainage reorganizations, hanging valleys, disrupted karst basins and deep bedrock incision from drainage divides to shoreline. We also investigate relief bounding faults from the Mediterranean coast to the Central Anatolian Plateau interior across the overriding Anatolian Plate (southern part) (Figure 1.1). We collect kinematic field data from the major relief-bounding fault zones with clear slicken fibres/striations to decipher the sense of motion between fault blocks. We use paleo-stress analysis to determine the extension and shortening directions, to unravel the mechanism of brittle deformation. We utilize U-series (U-Th) geochronology of syn-tectonic calcites, and we present first radiometric U-Th age data of Quaternary brittle deformation across the orogenic plateau margin to understand the spatio-temporal brittle deformation patterns above this complex subduction zone in the Eastern Mediterranean region. We also present U-Pb geochronology data from different generations of fault-related syn-tectonic calcites to decipher the long-term evolution of the faulting. We further utilize microstructural studies on sampled fault-related calcites to record micro-scale footprints of faulting-related deformation. In summary, we analyze geomorphic markers, provide geochronological constraints on poly-phase faulting history, examine the kinematic and microstructural features of the brittle structures, and discuss their origins considering the conceptual models and geodynamic drivers. Elucidating the pattern, timing and the mechanism of the tectonic deformation in the western Central Taurides fills a major gap in the literature and provides a better understanding of the deformation history throughout the paleotectonic and neotectonic periods in the Eastern

Mediterranean, revealing the feedbacks between crustal brittle deformation, plate convergence and deep-seated processes.

1.1 Literature Review

The study area is western flank of the southern margin, Central Taurides, of the Central Anatolian Plateau. It is a NW-SE trending deformation zone with a high topography. The study area is delimited by north-south directed and west vergent Aksu Thrust in the west, Alanya Metamorphic Complex in the east, The Mediterranean Sea in the south and Beyşehir-Suğla Basins (CAP) in the north (Figure 2.1). The study area is situated above the Cyprus Subduction Zone where the Anatolian Plate overrides the African Plate. These tectonic plates converge at rates of ~5-15 mm/yr (Reilinger et al., 2006). The subduction zone extends eastwards from the Hellenic Arc south of Crete, crosses the south of Cyprus with an arcuate shape and transitions into left-lateral strike-slip deformation when merging with the Arabian Plate (Figure 1.1). It covers a wide area with partitioned deformation zones rather than a uniform sharp plate boundary.

The dynamic geodynamic history of the region has caused a complex subduction-collision system including deep marine basins (e.g., Antalya, Levant, Adana, Latakia, Cilicia Basins), bathymetric highs (e.g., Florence Rise, Anaximander Mountains, Eratosthenes Seamount) and fault zones (e.g., Pliny and Strabo Faults, Paphos Transform Fault) (Figure 1.1). To the west, the boundary between the Hellenic and Cyprus trenches is controlled by the NE-SW striking Pliny and Strabo shear zones (Huguen et al., 2001). South of the Antalya Basin, the surface projection of the subduction zone turns in a NW-SE direction (Howell et al., 2017; Güvercin et al., 2021). Here, the Pliny and Strabo shear zones merge with a bathymetric high called the Florence Rise (Figure 1.1). This rise consists of strongly deformed and elevated oceanic sediments that bury the subduction interface under a thick sedimentary cover (>10 km). Structural studies and earthquake focal mechanisms (Wdowinski et al., 2006; Imprescia et al., 2012; Howell et al., 2017; Güvercin et al., 2021) provide evidence of ongoing convergence along the Florence Rise. Further to the east, the subduction can be traced along the south of Cyprus, where the Eratosthenes Seamount has formed the collision zone in the latest Pliocene (Robertson, 1998; Schattner, 2010; Ring and Pantazides, 2019). Tomographic imaging suggests that there is no slab from eastern

Cyprus to the Levant mainland (Faccenna et al., 2006; Biryol et al., 2011; Portner et al., 2018). The absence of a slab was related to the lateral migration of the slab break-off (11-8 Ma ago), which propagated from the Bitlis Suture Zone (Keskin, 2003; Şengör et al., 2003) towards eastern Cyprus (Faccenna et al., 2006; Schildgen et al., 2014). The eastern protraction of the Cyprian Arc is more transpressional with a left-lateral component, characterised by wrench tectonics based on kinematic, seismic and bathymetric evidence (McClusky et al. 2000; Vidal et al., 2000; Wdowinski et al., 2006; Kinnaird and Robertson, 2013). The arrival of the Eratosthenes Seamount is thought to have locked the central segment of the Cyprus subduction zone (Robertson, 1998; Schattner, 2010; Kinnaird and Robertson, 2013). As a consequence, the dextral Paphos Transform Fault (PT) formed and segmented the subducting slab into the Western Cyprus Slab (or Antalya Slab) and the Eastern Cyprus Slab which merges into the transpressional, slab-free plate boundary in the east (Biryol et al., 2011; Portner et al., 2018; Güvercin et al., 2021) (Figure 1.1).

The stress fields, rheology and the deformation mechanism of the downgoing African Plate, the overriding Anatolian Plate and subduction interface along the Cyprus Arc has long been debated (Wdowinski et al., 2006; Schildgen et al., 2012b; Howell et al., 2017; Güvercin et al., 2021; Aykut et al., 2023). Because of limited seismic activity, the subduction interface is supposed to be deforming aseismically with low elastic-strain accumulation (Vernant et al., 2014; Howell et al., 2017). Reverse and strike-slip earthquake focal mechanisms from depths >40 km provide evidence for contractional and deep brittle deformation (Howell et al., 2017; Güvercin et al., 2021).

The chain of events that has controlled the internal structure and initial deformation of the CAP southern margin have started with the rifting of the Gondwana continent and the opening of the Neothetys Ocean in the Permo-Triassic (Şengör and Yılmaz, 1981; Moix et al., 2008). Evolution of the Mesozoic Neotethys Ocean, which was separated into different ocean segments bounded by several microcontinents, mainly shaped the lithological and tectonic framework of the region. Paleotectonic deformation of the Central Taurides has been governed by convergence of the continental fragments that led to contraction, crustal thickening, collision and the emplacement of the crustal and oceanic nappe fragments onto the Geyikdağı and Aladağ autochthonous units (Özgül, 1976)

between Triassic-Eocene (Şengör and Yılmaz, 1981; Okay and Tüysüz, 1999; Andrew and Robertson, 2002). Starting of the neotectonic period after the collision of the Arabian Plate and Anatolian Plate in the Early-Middle Miocene along the Bitlis-Zagros Suture Zone (Şengör and Yılmaz, 1981; Bozkurt, 2001; Şengör et al., 2003; Okay et al., 2010), controlled the further deformation of Southern Türkiye and created a structurally complex, intensely deformed post-orogenic high-relief mountain belt. The study area has been affected by different stress regimes throughout Neogene and Quaternary times (Glover and Robertson, 1998a, 1998b; Poisson et. al., 2003, 2011; Üner et. al., 2015). Southwest movement and emplacement of Lycian Nappes onto the Western Taurides has caused another compressional deformation phase lasting until the Langhian in the westernmost part of CT (Akay and Uysal, 1988; Flecker et. al., 1998). Recently, a NW-SE extensional period was defined by Üner et. al., (2015), lasting from Langhian to Messinian. Western escape and counterclockwise rotation of the Anatolian microplate triggered a compressional "Aksu Phase" and deformed the Late Tortonian-Early Pliocene formations, forming the N-NW trending 100 km long Aksu Thrust Zone (Poisson et. al., 2003, 2011; Glover and Robertson, 1998a; Çiner et. al., 2008). The last deformational phase is the multi-directional extensional regime that occurred between the Latest Pliocene and Recent (Glover and Robertson, 1998a; Schildgen et al., 2012b; Üner et. al., 2015, Howell et al., 2017). Earthquake data demonstrate active seismicity and the focal mechanism solutions support the upper crustal extension characterizing shallow normal faulting events (<11 km depth) between Alanya-Seydişehir (Figure 2.1).

The Kırkkavak Fault is a major fault that bound the Köprüçay and Manavgat basins in the western flank (Figure 2.1). Kırkkavak Fault caused the asymmetric subsidence of the Köprüçay Sedimentary Basin in the Middle Miocene with the normal faulting (Çiner et. al., 2008). In the Tortonian, some parts of the Kırkkavak Fault exhibited inversion to a reverse fault as a consequence of Aksu Phase (Karabıyıkoğlu et. al., 2000; Çiner et. al., 2008). After this compressional phase, the faulting mechanism evolved into a strike-slip, then to normal faulting in the Quaternary (Glover and Robertson, 1998a). Farther east between Seydişehir-Manavgat, the active tectonic deformation history is poorly known. The direction of the main lineaments is generally NW-SE and N-S (Figure 2.1). Some of these lineaments coincide with the paleotectonic overthrust zones which have formed as

a result of the Africa-Eurasia plate convergence (Akay and Uysal, 1988; McPhee et. al., 2018). These lineaments were interpreted as the reactivated normal faults as a result of the extensional neotectonic regime (Monod et. al., 2006; Doğan et. al., 2017). Çiner et. al., (2008) mentioned a series of normal faults which cut the Miocene formations of Manavgat Sedimentary Basin and stated that the Late Miocene Compressional Aksu Phase barely affected the Manavgat Basin.

Schildgen et. al., (2012b) argued that these normal faults are formed after the thermally driven uplift of the upper crust as a consequence of asthenospheric upwelling. Asthenospheric upwelling driven by slab deformation also has been proposed to explain rapid surface uplift (at rates of 3.21-3.42 mm/yr over the last 450 ka) of the Central Taurides (Schildgen et al., 2012a, 2012b, 2014; Cosentino et al., 2012; Öğretmen et al., 2018; Racano et al., 2020, 2021; Aykut et al., 2023). Slow seismic velocities under Southern Anatolia have been interpreted to reflect a slab tear that caused upwelling of asthenosphere causing surface uplift (Faccenna et al., 2006; Biryol et al., 2011; Mutlu & Karabulut, 2011; Portner et al., 2018). Biostratigraphic evidence suggests 2 km of surface uplift since 8 Ma (Cosentino et al., 2012; Schildgen et. al. 2012a, 2014). Recent studies revealed that 1.5 km of this surface uplift happened in the last 450 ka (Öğretmen et al., 2018), which is in agreement with accelerating surface uplift over the last 1.6 Ma (Schildgen et al., 2014). Morpho-tectonic markers such as Quaternary tectono-karst depressions, deep bedrock river incision (exceeding 1500 m), characteristic wind gaps, exposed fault planes, prevalent low-relief perched upland surfaces (above 2000 m), uplifted wave-cut notches, marine terraces and major slope-break knickzones further quantified the uplift history (Kelletat and Kayan, 1983; Monod et al., 2006; Schildgen et al., 2012a, 2012b; Cosentino et al., 2016; Racano et al., 2020, 2021; Liberatore et al., 2022; Aykut et al., 2023). Uplifted wave-cut notches, beachrocks and algae fossils yielded 0.5-1.3 m cumulative uplift at rates of 0.9-2 mm/yr throughout the Holocene (Kelletat and Kayan, 1983; Cosentino et al., 2016; Liberatore et al., 2022). Landscape evolution models yielded 1.1-6.3 mm/yr rock uplift rates in the Late Quaternary (Racano et al., 2020, 2021).

The study area contains rocks from the Precambrian to the Quaternary (Özgül, 1976; Akay and Uysal, 1988; Schmid et. al, 2020). Basement units consist of The Mesozoic autochthonous carbonate limestones which are deposited at the depths of the Neotethys

Ocean (Şengör and Yılmaz, 1981; Schmid et., al, 2020). Özgül, (1976) named this unit as Geyikdağı Autochthonous Unit. This basement is overthrust by allochthonous Beyşehir-Hoyran, Antalya and Alanya Nappes which consist of Paleozoic-Mesozoic ophiolitic melanges, metamorphic rocks, limestones and Eocene carbonates-clastics (Özgül, 1976). In the southern part, the Miocene Antalya Basins' (Aksu, Manavgat and Köprüçay Sedimentary Basins) units unconformably overlie the basement units of Geyikdağı Platform Carbonates, Alanya and Antalya nappes. In the general context, the Antalya Miocene basin consists of Miocene marine to non-marine clastic sediments, Miocene reefal limestones and Pliocene to Recent clastic terrestrials and travertines (Karabıyıkoğlu et. al., 2000, Çiner et. al., 2008).

There is a high and steep topography overlains this geology. The maximum elevations tend to increase from western to the eastern parts of the flank, from 2400-2500 meters to 2800-2900 meters (Figure 2.1). There are well-preserved paleo valleys that perched into a wide paleo surface at 2000 meter elevations (Monod et. al., 2006). The common presence of limestone is represented by the Karst landscape with widespread Karst landforms such as tectono-karst poljes, fluvial-karst depressions, ponors and dolines (Doğan et. al., 2017). The general trend of the tectono-karst poljes are comparable with the NW-SE trend of the flank. These relic landscapes and poljes are traversely dissected with by seven major river basins from west to east: Aksu, Köprüçay, Manavgat, Karpuzçay, Ulugüney, Kargı and Dim, respectively. River network generally flows from north-northeast to south-southwest, towards the Mediterranean Sea (Figure 2.1).

1.2 Hypothesis

Recent studies have investigated the mechanism, rate, and pattern of uplift across the Central and Eastern Taurides (Schildgen et al., 2012a, 2012b, 2014; Sarıkaya et al., 2015; Yıldırım et al., 2016; Öğretmen et al., 2018; Racano et al., 2021). However, despite the notable relief and distinct tectonic features of the western Central Taurides between Antalya and Alanya, neotectonic activities in this region remain poorly understood. Notably, the Active Fault Map of Türkiye (Emre et al., 2013) reports no active faults in this area, yet geological maps (Şenel, 2002) indicate the presence of numerous faults, categorized as undefined faults. The formation mechanisms of these faults are also

controversial, with hypotheses ranging from mantle upwelling through slab gaps to slab retreat of the Eastern Cyprus Slab (Schildgen et al., 2012b; Howell et al., 2017; Koçyiğit & Özacar, 2003; Flecker et al., 2005; Glover & Robertson, 1998b; Kelling et al., 2005; Koç et al., 2016; Üner et al., 2015). Moreover, the temporal relationship between deep-seated processes (e.g., slab deformation, asthenospheric upwelling), crustal block motions (e.g., Anatolian Plate rotation), and upper crustal brittle deformation (e.g., faulting) remains unclear due to the absence of isotopic age data. The scarcity of Neogene and Quaternary units and the dominance of karstic processes in this region pose challenges for traditional geological methods aimed at deciphering the pattern, mechanisms, and timing of neotectonic deformation. Recent advances in morphometric analyses, which can delineate deformation patterns by investigating potential responses of rivers to tectonic deformation (Keller and Pinter, 2002; Clark et al., 2006; Wobus et al., 2006; Kirby and Whipple, 2012; Yıldırım and Tüysüz, 2017), and the successful utilization of U-Th and U-Pb carbonate geochronology in determining the absolute timing of brittle deformation across fault zones (Uysal et al., 2007, 2009, 2019; Nuriel et al., 2011, 2012; Karabacak et al., 2021), have been noteworthy, particularly in regions where young sediments are absent due to intense karstification and erosion. Our preliminary fieldwork has revealed the suitability of using U-Th and U-Pb series on numerous fault planes in the area. Consequently, it will be possible to establish the geochronology of fault activities that is hard to achieve due to intense karstification and erosion. Therefore, this thesis aims to utilize MATLAB and GIS-based morphometric analyses to examine the main river basins originating from the western flank of the Central Taurides (Aksu, Köprüçay, Manavgat, Karpuzçay, Ulugüney, Kargı, Oba, and Dim rivers) and flowing towards the Mediterranean Sea. The tectonic landforms and geomorphic indicators will be analyzed and mapped (low-relief relict upland surfaces at high elevations, slope breaks in river longitudinal profiles, etc.), and the pattern of active tectonic deformation in the western Central Taurides will be investigated. To determine the mechanism of active brittle deformation, kinematic measurements will be conducted on suitable fault planes to collect fault-slip data, and paleo-stress analysis will be implemented. For deciphering the timing of active deformation, syn-tectonic calcites will be sampled on fault planes, and will be dated using U-Th and U-Pb (Uranium-Thorium and Uranium-Lead) geochronology. By

analyzing tectonic landforms, geomorphic indicators, fault kinematics, and syn-tectonic calcites; this study intends to elucidate the pattern, mechanism and timing of active tectonic deformation in the western Central Taurides.

2. MATERIALS AND METHODS

2.1 Main Data Sources and Creation of Digital Database

To understand the pattern and the spatial distribution of the active deformation, first, we utilized high-resolution Digital Elevation Models (DEM) including 12.5 m resolution ALOS (The Advanced Land Observing Satellite) Palsar and 30 m resolution SRTM (Shuttle Radar Topography Mission) for morphometric analysis. The synthetic stream network using high-resolution DEM data is produced by following the procedure of determining flow directions and flow accumulations. Red Relief Image Maps (RRIM) is generated (Chiba et. al., 2008) to identify and map tectonic landforms. We used "The TopoToolbox" (Schwanghart and Scherler, 2014) and "The Topographic Analysis Kit" (Forte and Whipple, 2019) for river longitudinal profile and steepness analysis, swath profile and knickpoint extraction, utilizing MATLAB software. The "Spatial Analysis" and "3D Analysis" tools of ESRI's ArcGIS 10.7 software also were implemented for topographical relief, hydrology and RRIM analysis. We also used 1/500.000 scale geological maps published by the General Directorate of Mineral Research and Exploration of Türkiye (MTA) in 2002.

2.2 Tectono-Geomorphological Mapping and Morphometric Analysis

Geomorphological mapping and morpho-tectonic analysis are very important as they greatly contribute to the understanding of spatial distribution and pattern of the active deformation. We implemented morphometric analysis such as extraction of topographical profiles, relief analysis, river longitudinal analysis, knickpoint extraction-classification and determination of steepness values of river segments.

2.2.1 Topographical swath profiles

Topographical swath profiles can be used to infer the general character of topography throughout the desired area. They show the distribution of maximum, mean and minimum elevations across a given rectangular zone. While the minimum elevations denote the valley floors, maximum elevations correspond to the peaks and ridges, hence they display the variation of the topographical relief along the given stripes. We extracted five swath profiles. Four of the swath profiles are 30 km wide, 100-120 km long and orthogonal to and one of the swath profiles is 30 km wide and 180 km long, parallel to the regional psychographic trend (Figure 2.1).

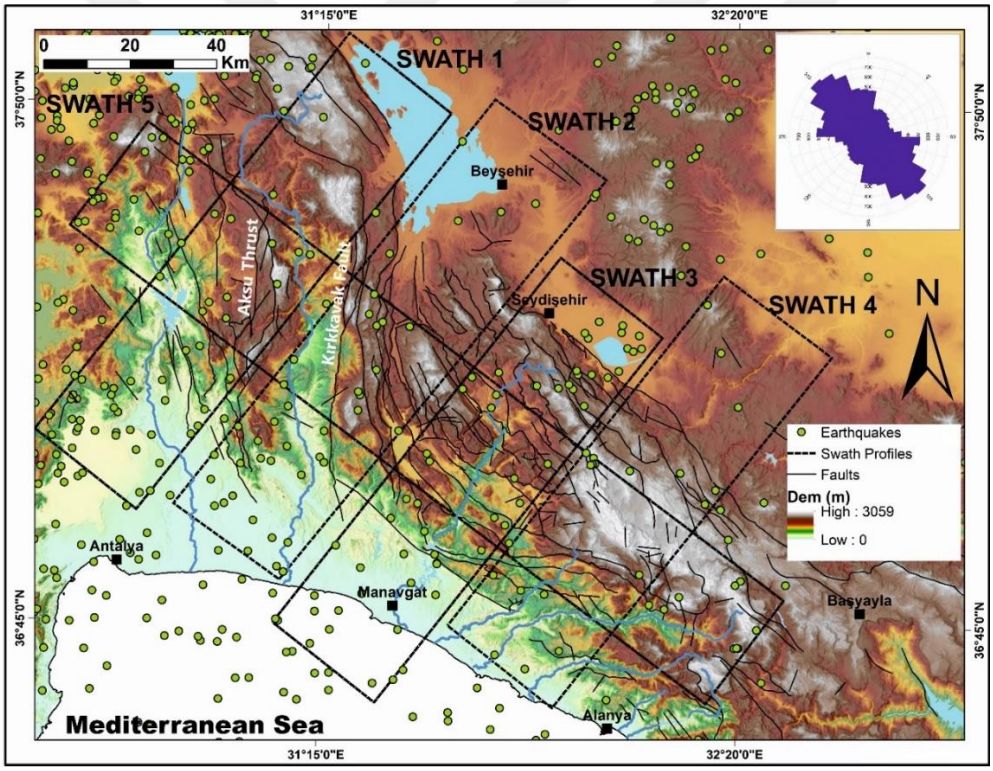

Figure 2.1: The digital elevation model that shows the main topographical features of the study area. Black lines are the main faults and lineaments from the regional geological maps (Şenel, 2002). Black boxes with dashed lines are footprints of topographic swath profiles. Rose diagram of the faults lineament presented as an inlet. Green points represent the earthquakes (Mw 3≤) between 0 and 30 km depths (The data is from "Boğaziçi University-Kandilli Observatory and Earthquake Research Institute," http://www.koeri.boun.edu.tr/sismo/zeqdb/indexeng.asp, and "Disaster and Emergency Management of Türkiye (AFAD)," https:// deprem.afad.gov.tr/event-catalog).

2.2.2 Knickpoint extraction and channel steepness analysis

River longitudinal profiles provide valuable information as they record the interaction between the tectonic and surface processes. Rivers tend to reach a concave-up graded profile in steady tectonic and climatic conditions. Irregularities in the graded profiles and the formation of knickpoints denote deviations from the equilibrium conditions (Kirby and Whipple, 2001, 2012; Keller and Pinter, 2002; Tucker and Whipple, 2002; Wobus et. al., 2006; Demoulin et. al., 2012, 2017; Lague, 2014; Gallen and Wegmann, 2017). Changing of the equilibrium conditions and formation of knickpoints may result as a consequence of climate changes, fluctuations in sediment load, rock uplift, transient profile evolution, lithological variations and displacements related to active tectonic structures (Hack, 1957; Howard et. al., 1994; Kirby et. al., 2003; Larue, 2008, 2011; Gallen, 2018). The steepness index (also referred as normalized steepness index) is the slope of a channel that is normalized to its drainage contribution area. The steepness index (ksn) provides a strong tool for comparing slopes of river channel segments, detecting the deviations in graded river longitudinal profiles and determining deformation patterns (Kirby et al., 2003; Perron and Royden, 2013; Yıldırım and Tüysüz, 2017; Wang et. al., 2019). Stream gradient decreases downstream as a power-law function of contributing drainage area (Hack, 1973; Flint, 1974; Wang et. al., 2019). This relationship can be expressed as:

$$S = k_s A^{-\theta} \tag{2.1}$$

where S= channel gradient, A= upstream drainage area, ks=channel steepness index and θ=channel concavity index.

In erosional landscapes, identifying knickpoints plays an important role in the interpretation of active tectonic deformation as well (Keller and Pinter, 2002; Kirby and Whipple, 2012; Pavano et. al., 2016). As a response to tectonic perturbations, lithological variations, increasing stream flow rates, increasing sediment flux and landslides; new boundaries forms known as the knickpoints, between the downstream region that is adjusting to the new energy state and the upstream reach where the former state is maintained (Kirby and Whipple, 2012; Chen et. al., 2015; Jaiswara et. al., 2019). Knickpoints are generally classified as “vertical-step knickpoints” and “slope-break

knickpoints", according to the morphology of the channel segments in the slope-area plots. While the formation of vertical-step knickpoints has mostly been related to local heterogeneities in the stream channel (like lithological variations), slope-break knickpoints have been linked to spatiotemporally persistent tectonic forcing (Haviv et. al., 2010; Gailleton et. al., 2019; Boulton, 2020).

We calculated best-fit steepness index values and analyzed the longitudinal profiles of all trunk bedrock streams in our study area to detect the deviations from the concave-up graded channel profiles. We extracted the knickpoints for the trunk streams using the function "knickpointfinder" of "TopoToolbox" (Schwanghart and Scherler, 2014) utilizing MATLAB software. We prepared slope-area plots of trunk streams in log-log space to investigate the knickpoint morphology (Figure 3.3, 3.4). In addition, we carried out Inverse Distance Weighting (IDW) Interpolation using the calculated ksn values of all orders of stream channels throughout our study area (Figure 3.6). We used $\theta_{ref} = 0.45$ for steepness index analysis as this value has been accepted and used as the best representative concavity value. This value also varies little across different landscapes and provides a basis for comparing steepness index values across different geomorphological settings (Snyder et. al., 2000; Kirby and Whipple, 2012).

2.2.3 Topographical relief analysis and surface uplift estimates

The ruggedness and high relief of topography are footprints of high stream incision and surface uplift in tectonically active areas. Contrarily, low relief topography demonstrates a relatively quiet tectonic state, steady-state equilibrium conditions and flattened topography by external processes. Therefore, investigating the spatial characterization of the relief across a landscape can provide information about the active deformation pattern (Wobus et. al., 2006; Kirby and Whipple, 2012). Low relief perched upland surfaces are slightly undulated remnants of a pre-existing landscape (Stearns, 1967; Clark et. al., 2006; Whipple et. al., 2017). The coexistence of these relic surfaces with the geomorphic units like steep gorges reflects a transient topography that is trying to adjust the changing surface elevation (Clark et. al., 2006). Reconstruction of the pre-existing landscape provides a datum for determining the spatial distribution and pattern of the surface uplift. If there are perched relic landscapes where the erosion rates are relatively low, the

difference in elevation between the current river at the outlet and the projected relict part of the river at the outlet points out the amount of surface uplift since starting of the deformation (Clark et. al., 2006; Kirby and Whipple, 2012; Prince and Spotila, 2013; Yıldırım and Tüysüz, 2017). All these morphometric analyses will be evaluated for deciphering the active deformation pattern across the western flank of CT.

We carried out local topographic relief analysis for the western flank of the southern margin for elucidating the pattern of surface uplift. We subtracted minimum elevations from maximum elevations and averaged it over a given 2 km sampling window which demonstrates the valley to ridge relief pattern and created a local relief map for our study area. We used ArcGIS softwares' focal statistics and raster calculator tools. We projected paleo-longitudinal profiles for five trunk rivers (Manavgat, Köprüçay, Karpuzçay, Ulugüney and Dim) where there are relict upland surfaces upstream that are bounded by the highest elevated knickpoints. We projected the relict channel gradients downstream along their longitudinal profiles and we estimated the total amount and pattern of the surface uplift along the western flank. In the process of determining paleo-longitudinal channel profiles, we calculated and used best-fit ksn and concavity of channel segments from Equation (2.1).

2.3 Kinematic Analysis and Fault-Related Calcite Sampling

The kinematic measurements provide valuable data for understanding the mechanism of brittle deformation and the sense of motion between fault blocks. Analysis of the fault-slip data enables us to establish principal strain axes along the major fault zones (Petit, 1987; Allmendinger et al., 1989; Delvaux and Sperner, 2003; Karabacak et al., 2021). Through structural analyses we will be able to determine positions and stress ratio (R) of the principal stress axes ($\sigma1$, $\sigma2$, $\sigma3$; compression, intermediate, extension) of the stress tensor along the major fault zones. Outputs of the structural analysis will enable us to establish the states of principal stresses and local tension and compression directions, hence the mechanism of the brittle deformation in the western CT.

To better understand the brittle deformation, we conducted kinematic measurements on fault planes that create topographic lineaments and broad deformation zones between

Gazipaşa-Seydişehir (from coast to plateau), where there is a lack of robust kinematic field data. We measured the strike, dip angle, dip direction and rake features of the fault planes at twenty locations (Table 3.1). We obtained kinematic data from slickenlines and slicken fibres, which demonstrate the sense of motion between fault blocks. We used Win-Tensor software (Delvaux and Sperner, 2003) to plot fault-slip data and determine extension and shortening directions. We plotted paleo-stress fields and principal stress directions (Table 3.2). Because the displacements on the small-scale minor faults are small, we infer that no significant rotations occurred, hence the strain and stress axes are subparallel to each other. We infer that maximum compressive stress and least compressive stress are parallel to shortening and extension directions respectively. Details of paleo-stress analysis are given in Table 3.2.

From twenty key areas, a total of eighty-two fault related calcites (sixty-six striated calcites-slickenfibres, fourteen carbonate coatings and two breccia cements) have been sampled (Table 2.1). Sampled fault-related carbonates were very characteristic and promising for acquiring accurate and precise U-Pb and U-Th ages. We used a drill machine, angle grinder machine, hammer and chisel. We cut and reserved the calcite samples within the sample bags. Considering the probability of low-insufficient Uranium and Thorium amounts within the calcite samples for dating studies, we also collected backup samples from each location.

Table 2.1: Sampled amounts and types of fault-related calcites.

Locations	**Sample Amounts and Types**
Location 1	1 Striated Calcites/Slicken Fibres, 1 Calcite Coatings
Location 2	4 Striated Calcites/Slicken Fibres
Location 3	4 Striated Calcites/Slicken Fibres, 1 Breccia Cement
Location 4	5 Striated Calcites/Slicken Fibres, 1 Calcite Coatings
Location 5	5 Striated Calcites/Slicken Fibres
Location 6	6 Striated Calcites/Slicken Fibres
Location 7	2 Striated Calcites/Slicken Fibres
Location 8	6 Striated Calcites/Slicken Fibres, 2 Calcite Coatings
Location 9	7 Striated Calcites/Slicken Fibres

Table 2.1 (continued): Sampled amounts and types of fault-related calcites.

Location 10	4 Striated Calcites/Slicken Fibres, 3 Calcite Coatings
Location 11	2 Striated Calcites/Slicken Fibres, 1 Calcite Coatings
Location 12	3 Striated Calcites/Slicken Fibres, 1 Calcite Coatings
Location 13	3 Striated Calcites/Slicken Fibres, 1 Breccia Cement
Location 14	3 Striated Calcites/Slicken Fibres, 1 Calcite Coatings
Location 15	3 Striated Calcites/Slicken Fibres, 1 Calcite Coatings
Location 16	2 Striated Calcites/Slicken Fibres
Location 17	1 Striated Calcites/Slicken Fibres, 1 Calcite Coatings
Location 18	2 Striated Calcites/Slicken Fibres
Location 19	1 Striated Calcites/Slicken Fibres
Location 20	2 Striated Calcites/Slicken Fibres, 2 Calcite Coatings
Total = 20 Locations	**66 Striated Calcites/Slicken Fibres, 14 Calcite Coatings, 2 Breccia Cement.**

2.4 U-Th and U-Pb Carbonate Geochronology

During the seismic activity periods, CO_2 degassing events and pressure solution cause carbonate precipitation within the weakness zones such as fault planes (Uysal et al., 2007, 2009; Oren et al., 2020; Karabacak et al., 2021). These carbonates can form during syn-tectonic (calcite fibers, striated calcites, calcite cement), co-seismic (calcite gouge) and inter-seismic (carbonate coatings) periods (Nuriel et al., 2012). Syn-tectonic carbonate precipitates can be used to date the faulting events and are of great importance in paleoseismic and neotectonic studies (Nuriel et al., 2011, 2012; Roberts and Walker, 2016; Uysal et al., 2019; Karabacak et al., 2021).

During the crystallization process, calcite exhibits behavior in acquiring radioactive isotopes such as ^{238}U and ^{235}U into its crystal lattice. The age of calcite and thus the timing of deformation can be determined by measuring the amounts of radioactive and radiogenic isotopes within syn-tectonic calcites using mass spectrometers (Nuriel et al., 2011; Roberts and Walker, 2016; Roberts et al., 2020). The U-Th and U-Pb geochronology utilize the radioactive decay chains which consist of ^{238}U-^{206}Pb, ^{235}U-^{207}Pb, and ^{232}Th-

^{208}Pb chains. The decay half-life of ^{238}U to ^{206}Pb is 4.5 billion years, ^{235}U to ^{207}Pb is 704 million years, and ^{232}Th to ^{208}Pb is 13.9 billion years (Jaffey et al., 1971; Cheng et al., 2000; Dickin, 2005). If we consider a system's age as "t," the following three equations can be written for each radioactive decay scheme (Dickin, 2005):

$$\left(\frac{^{206}Pb}{^{204}Pb}\right)_P = \left(\frac{^{206}Pb}{^{204}Pb}\right)_I + \frac{^{238}U}{^{204}Pb}\left(e^{\lambda 238 t - 1}\right) \quad (2.2)$$

$$\left(\frac{^{207}Pb}{^{204}Pb}\right)_P = \left(\frac{^{207}Pb}{^{204}Pb}\right)_I + \frac{^{235}U}{^{204}Pb}\left(e^{\lambda 235 t - 1}\right) \quad (2.3)$$

$$\left(\frac{^{208}Pb}{^{204}Pb}\right)_P = \left(\frac{^{208}Pb}{^{204}Pb}\right)_I + \frac{^{232}Th}{^{204}Pb}\left(e^{\lambda 232 t - 1}\right) \quad (2.4)$$

In these equations, "P" represents the currently measured quantity of a nuclide, "I" represents the initial quantity of that nuclide, and "λ" defines the decay constants for ^{238}U, ^{235}U, and ^{232}Th. The decay constants for ^{238}U, ^{235}U, and ^{232}Th to ^{206}Pb, ^{207}Pb, and ^{208}Pb are calculated as 1.55125 x 10-10, 9.8485 x 10-10, and 0.49475 x 10-10, respectively (Jaffey et al., 1971; Cheng et al., 2000; Dickin, 2005). Additionally, to determine whether the system remains closed and to ensure the reliability of the calculated age data, each measured isotope is divided by the non-radiogenic ^{204}Pb isotope of Lead. Thus, using the decay constants of radioactive isotopes to radiogenic isotopes and the currently measured quantities from mass spectrometers, the variable "t" in the equations, in other words, the age of a geological material or event, can be calculated.

Through the U-Pb geochronology, age determinations can be made with an upper limit of up to 4.5 billion years. However, for relatively young calcites, the decay events occurring in the ^{238}U-^{230}Th range of the ^{238}U-^{206}Pb decay chain are used for dating. This method is generally referred to as the Uranium-Series (U-Th) Dating Method. The half-life of ^{234}U, formed by the decay of ^{238}U, is approximately 250,000 years, and the half-life of ^{230}Th, resulting from the decay of ^{234}U, is approximately 75,000 years. These relatively short-lived radioactive isotopes make it possible to date relatively young calcites. Through this method, dating can be performed up to an upper limit of 500,000-600.000 years (Dickin,

2005; Zhao et al., 2009). This dating method can be expressed with the following equation (Edwards et al., 1987; Zhao et al., 2009; Zhao and Collins, 2011).

$$1-\left(\frac{^{230}Th}{^{238}U}\right) = (e^{-\lambda_{230}T}) - \left[\left(\frac{^{234}U}{^{238}U}\right) - 1\right] \text{x} \left(\frac{\lambda_{230}}{\lambda_{230} - \lambda_{234}}\right)(1 - e^{(\lambda_{234} - \lambda_{230})T}) \quad (2.5)$$

In this equation, "T" represents the age of the sample, and (^{230}Th/^{238}U) and (^{234}U/^{238}U) represent the measured activity ratios. λ^{230} and λ^{234}, on the other hand, respectively define the decay constants of ^{230}Th and ^{234}U. In this decay series, a "disequilibrium" occurs between ^{238}U-^{234}U-^{230}Th. This happens when Uranium becomes differentiated from Thorium during a geological event. As a result of this process, a carbonate sample that precipitates usually contains trace amounts of Uranium, typically ranging from 0.01 to 100 ppm, while Thorium starts to accumulate in the carbonate through the decay of initial Uranium. This leads to a radioactive decay series from ^{238}U to ^{230}Th. In such a radioactive "disequilibrium" situation, the re-establishment of secular equilibrium between the isotopes occurs in a time seven times the half-life of ^{230}Th (500,000-600.000 years) (Dickin, 2005; Zhao and Collins, 2011). This period also defines the upper limit of U-Th geochronology.

In U-Pb and U-Th carbonate geochronology studies, Laser Ablation Inductively Coupled Plasma Mass Spectrometer (LA-ICP-MS) and Multi-Collector Inductively Coupled Plasma Mass Spectrometer (MC-ICP-MS) systems are generally preferred for isotope measurements (Uysal et al., 2007, 2009; Nuriel et al., 2011, 2019; Goodfellow et al., 2017; Ring and Gerdes, 2016; Hansman et al., 2018; Oren et al., 2020; Weinberger et al., 2020; Karabacak et al., 2020, 2021). In recent years, the integrated use of mass spectrometers, especially with Inductively Coupled Plasma (ICP), has significantly reduced the workload of pre-analysis work and chemical purification processes before obtaining age data. ICP essentially includes a radio-frequency generator that stimulates the flow of ionized argon gas. This generator raises the temperature in the plasma to 5000 °C, efficiently ionizing the elements. The measurement of these ionized isotopes is then read in mass spectrometers to produce age data. In recent years, ICP-MS has reached the sensitivity to measure one part per trillion with the developments in the field. With the integration of MC (Multi-Collector) and LA (Laser-Ablation) systems into ICP-MS, U-Pb and U-Th carbonate geochronology have become an economical, fast, and highly efficient method

for solving geological problems. Thorium's high ionization potential (6.97 eV) makes it suitable for measurement in MC-ICP-MS systems containing Faraday cups (Dickin, 2005; Roberts et al., 2020). Another reason for the preference of these systems in U-Pb and U-Th carbonate geochronology is the complex textural properties of carbonates. Carbonates generally have heterogeneous textural and structural features, which can lead to variations in U-Pb and U-Th data, resulting in reduced data resolution and sensitivity. LA-ICP-MS and MC-ICP-MS systems, with their high-resolution analytical capabilities, especially in tectonic studies, overcome this disadvantage and allow for rapid and economical age determination from syn-tectonic carbonates (Uysal et al., 2007, 2009; Nuriel et al., 2011, 2019; Hansman et al., 2018; Roberts et al., 2020).

2.4.1 Laboratory Procedures

Sample preparation for U-Pb and U-Th carbonate geochronology

The sample preparation procedures have started with samples being crushed, washed and cleaned with Milli-Q Water (Figure 2.2, 2.3, 2.4). Samples then have been sonicated with an ultrasound machine, and got ready for further analysis.

Figure 2.2: Examples of sampled and pre-crushed calcite samples for geochronological analysis. **a,b)** Location 1; **c,d,e,f,g,h,j)** Location 4.

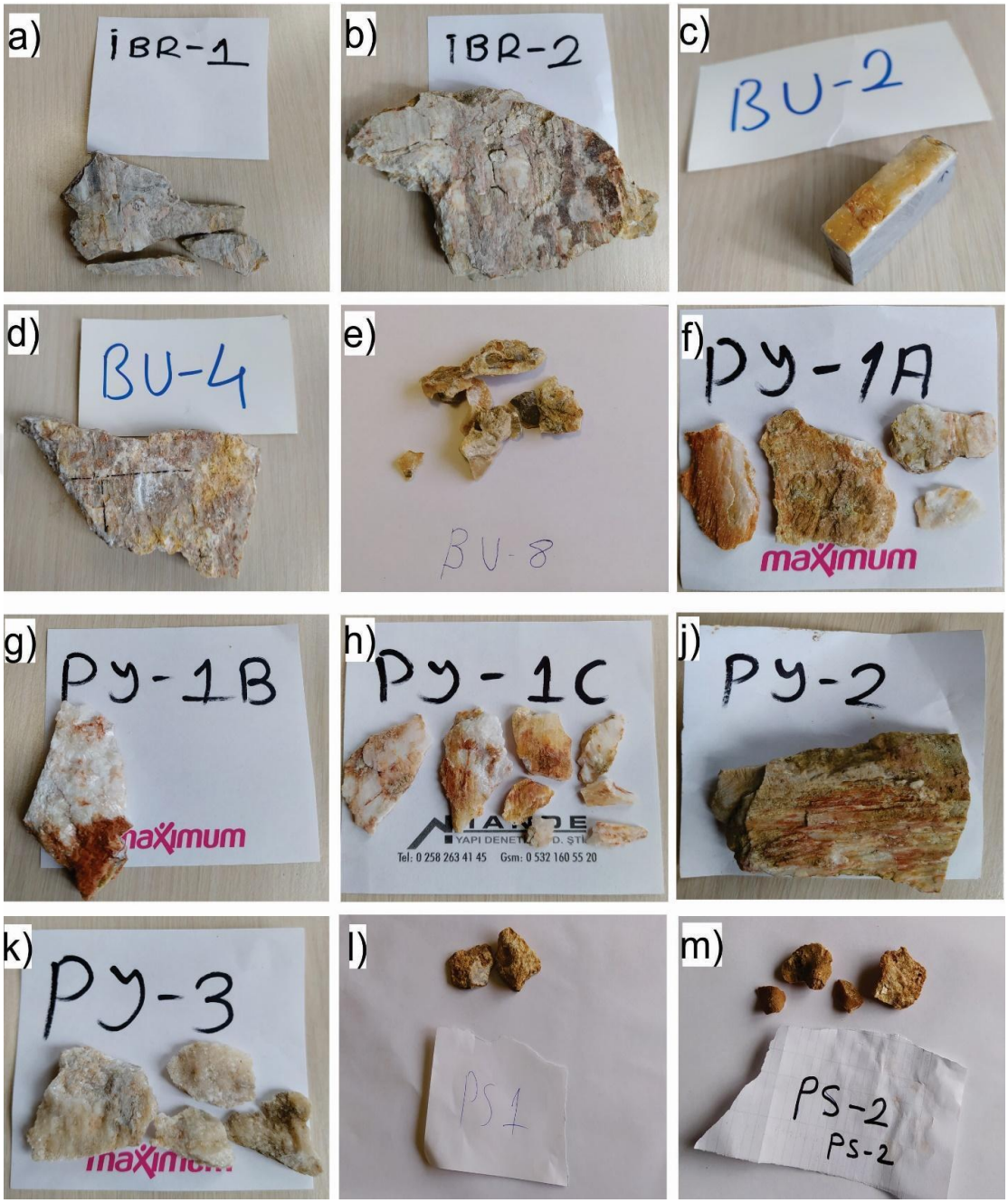

Figure 2.3: Examples of sampled and pre-prepared calcite samples for geochronological analysis. **a,b)** Location 7; **c,d,e)** Location 8; **f,g,h,j,k)** Location 9; **l,m)** Location 10.

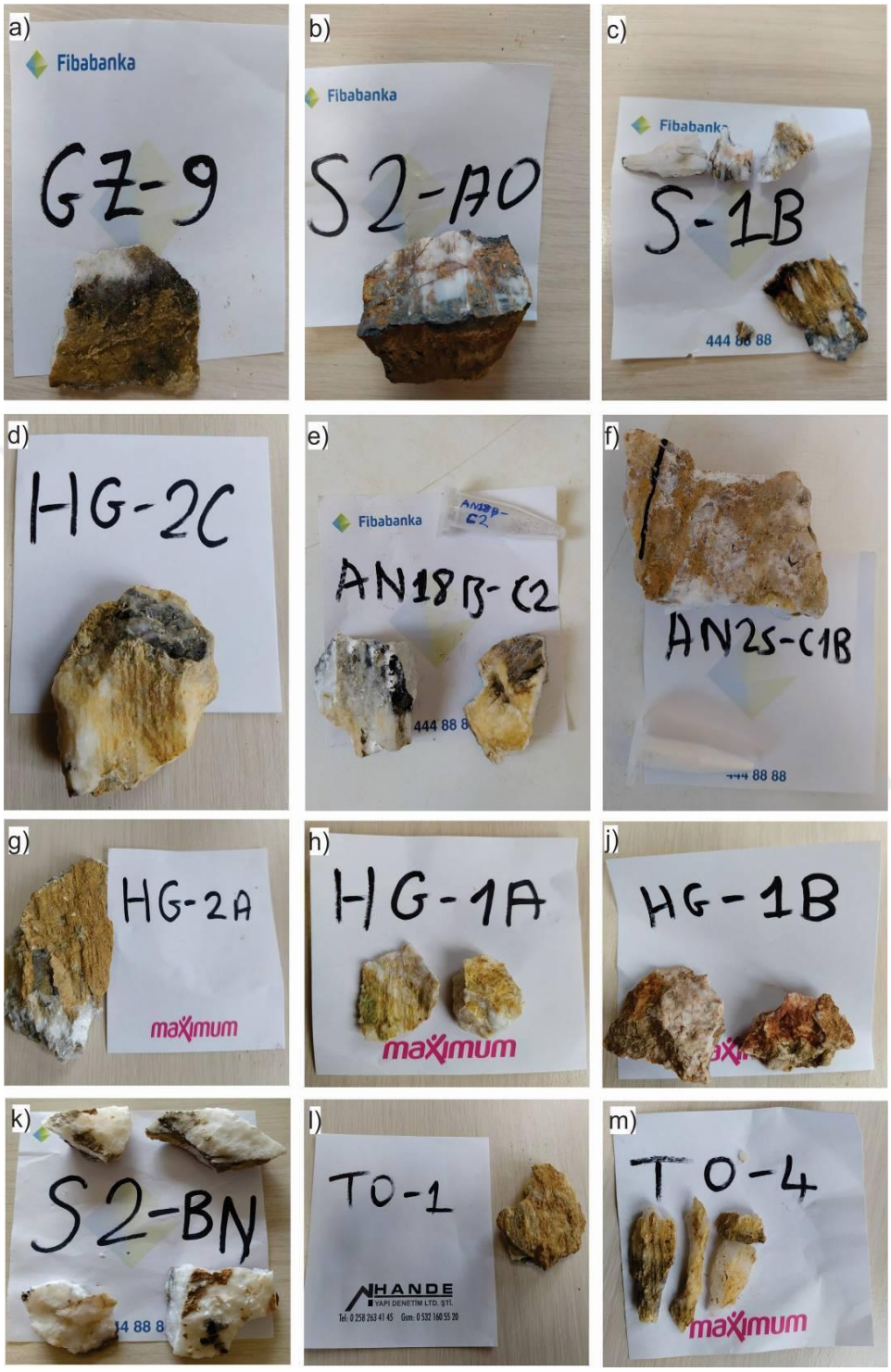

Figure 2.4: Examples of sampled and pre-prepared calcite samples for geochronological analysis. **a)** Location 1; **b,c,k);** Location 2; **d,g)** Location 12; **e)** Location 5; **f)**: Location 6; **h,j)** Location 11; **l)** Location 13; **m)** Location 14.

Cutting, epoxy mounting and polishing for U-Pb dating

The calcite samples were first crushed by a jaw crusher and then cut into smaller pieces with a slab saw (Figure 2.5). The small calcite samples were then placed into the 2.5 cm diameter rings and mounted with epoxy resin (Figure 2.6). After the epoxy resin application, mounts have been polished by the "Pro Grinder and Polishing Machine" (Figure 2.6). A total of twenty-one mounts have been prepared for the U-Pb dating.

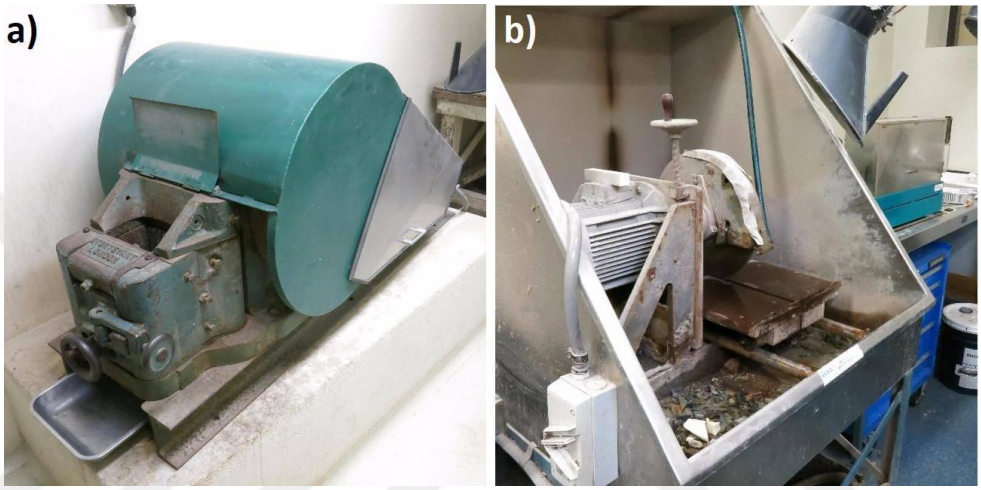

Figure 2.5: a) Jaw crusher, **b)** Slab saw**.**

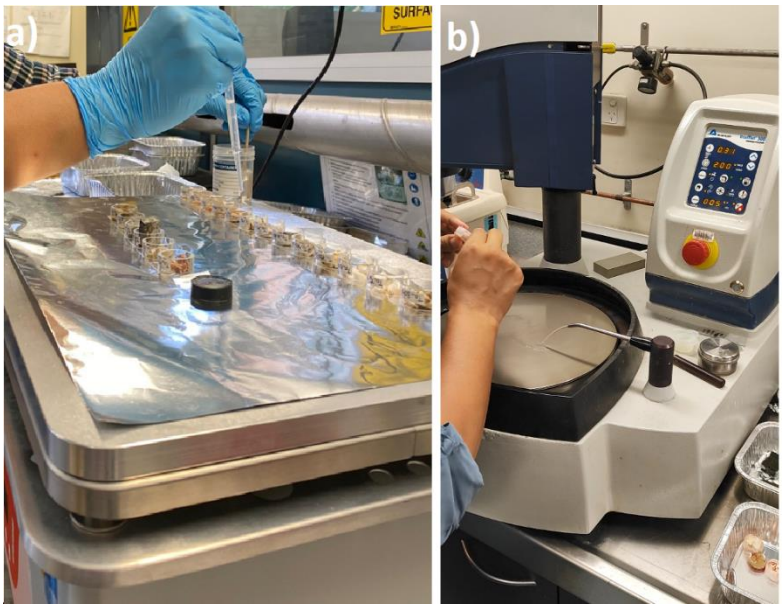

Figure 2.6: a) Mounting calcites in epoxy resin. **b)** Mount Polishing with the "Pro Grinder and Polishing" Machine.

Powdering and chipping for U-Th dating

After cleaning up the samples, a hand crusher (Figure 2.7) was used to crush the specimens. The purest sections were handpicked by a tweezer and were put into a clean laboratory tube. For the samples that have purer conditions; a hand drill (Figure 2.9) was used and carbonate powders (between 150-200 mg per sample) were produced for every sample. Then the agate mortar has been used to make the powders' grain sizes finer (Figure 2.8). Finally, the produced powders were weighed by a precision scale and were put into separate tubes (Figure 2.10). A total of twenty-eight samples have been prepared for U-Th dating.

Figure 2.7: Hand Crusher that has been used to crush calcite specimens for U-Th Dating.

Figure 2.8: a) The crushed calcite sample. **b)** Agate mortar for powdering calcite samples.

Figure 2.9: A hand drill has been used to powder carbonate samples for U-Th age analyses.

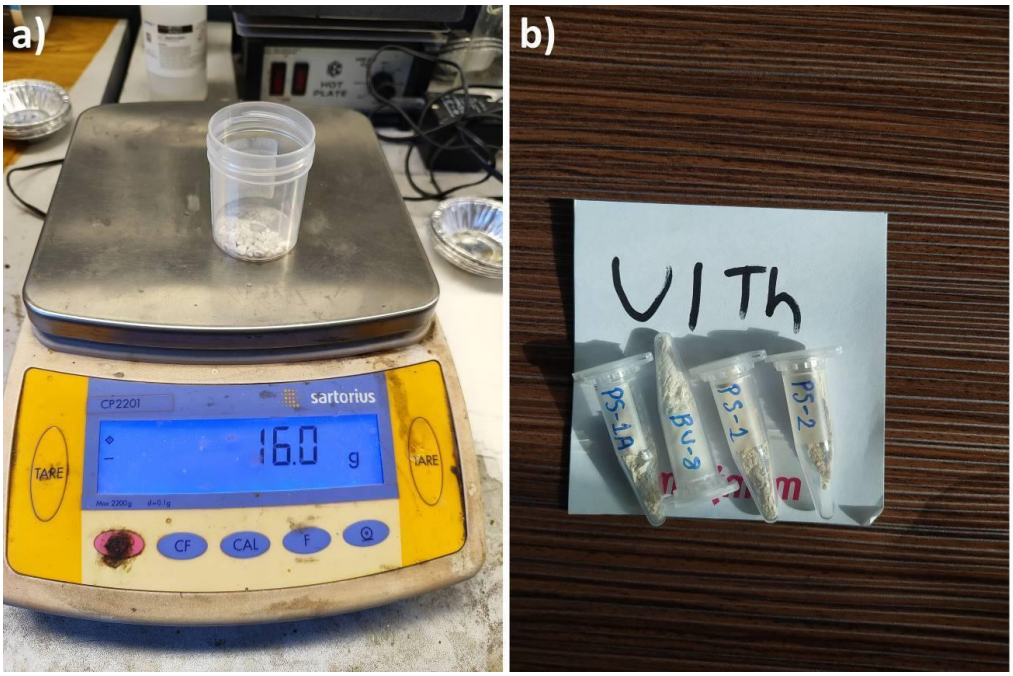

Figure 2.10: a) Weighing of the chipped samples on a precision scale. **b)** Powdered calcite samples in microplastic test tubes.

Isotopic evaluation and screening analysis for U-Pb dating

To determine the zones with high Uranium-Thorium amounts, screening analysis has been carried out in the University of Queensland-Radiogenic Isotope Facility. First, the prepared epoxy mounts were cleaned again with the Mili-Q Water System, were sonicated for 90 minutes, and further decontaminated with the Nitrogen gas. After cleaning the samples, epoxy mounts have been put into the laser ablation box (Figure 2.11, 2.12), fixed by individual springs. After inserting the mount box into the machine, the GeoStar software was operated to control the ablation process. The most suitable ablation spots (homogeneous zones without any matrix material) were handpicked using the built-in microscope, and approximately 120 spots were determined for every calcite mount (Figures 2.13, 2.14, 2.15). These spots were ablated via the ASI RESOlution system (Figure 2.16). The laser system uses an ArF 193 (nm) gas excimer laser, controlled with GeoStar software. 120 spots were ablated with laser ablation with 120 µm spot size, 10 Hz repeat rate and 8.2 Mj energy for each spot. Consequently, high Uranium zones were delineated for every calcite mount for further ablation and U-Pb dating (Figures 2.17, 2.18, 2.19).

Figure 2.11: a,b). The Laser ablation mount box.

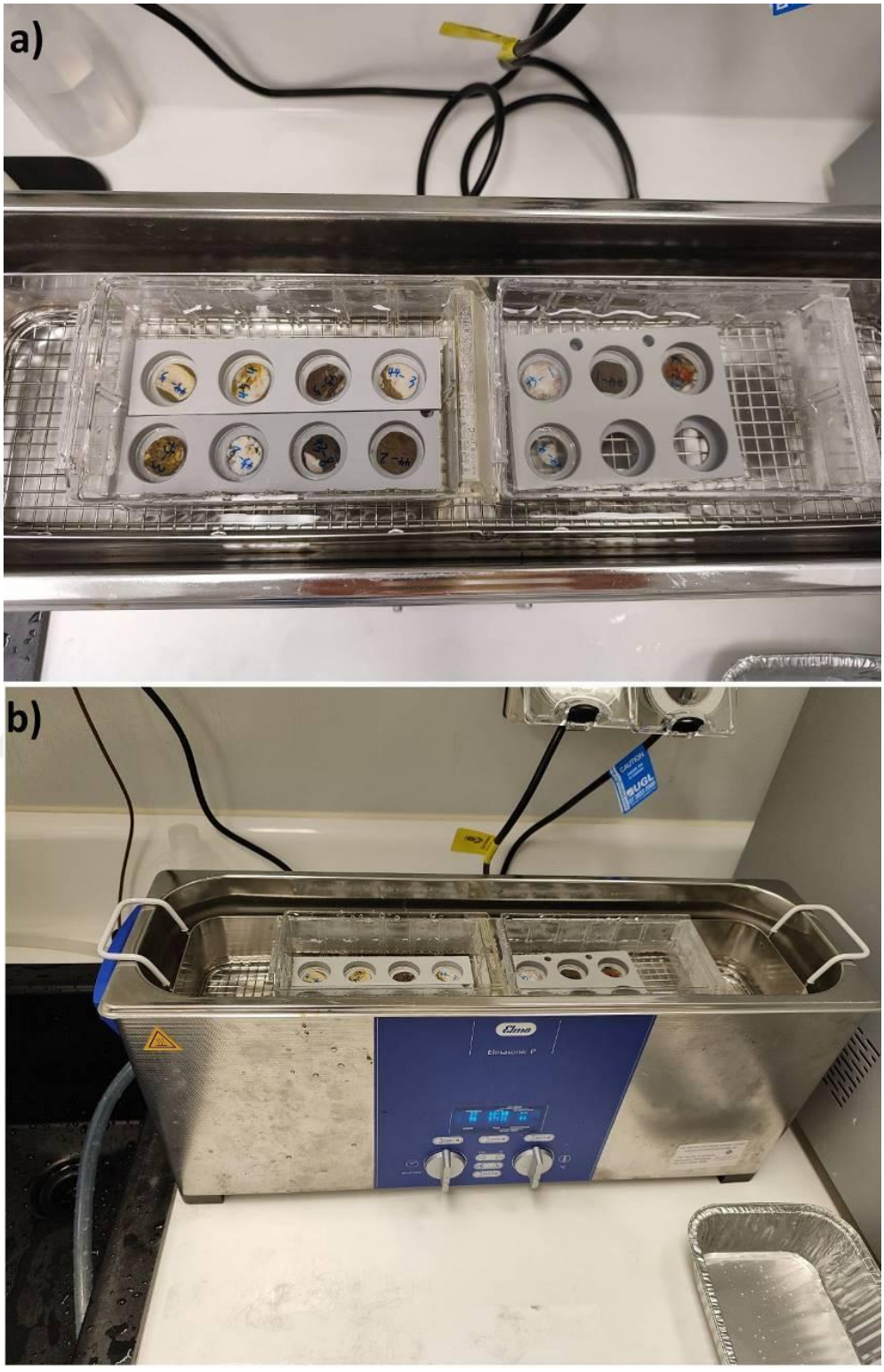

Figure 2.12: a), b). The sonication of the mounts with an ultrasound machine.

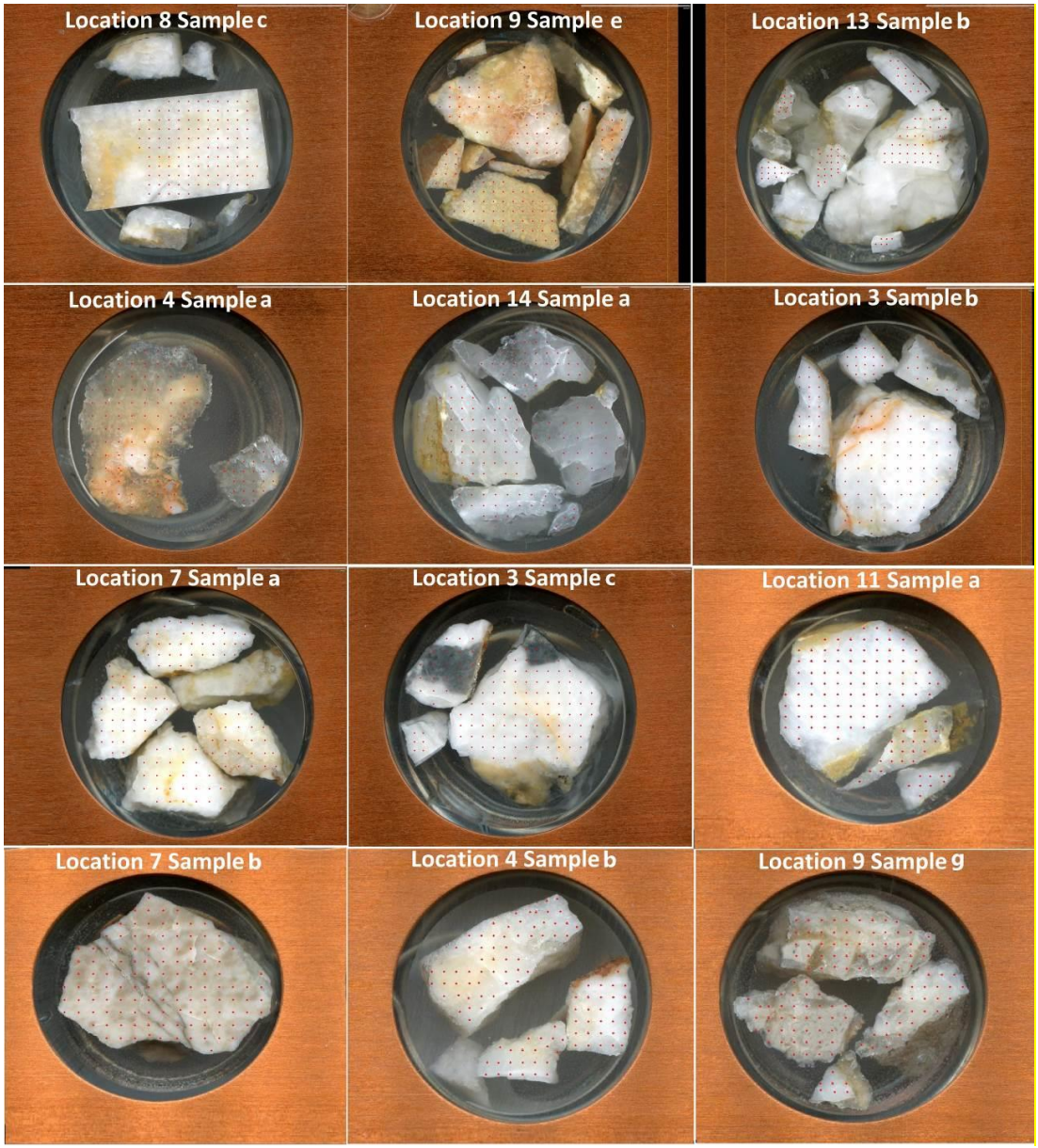

Figure 2.13: Spot locations prior to ablation for elemental screening analyses. Please note that the little red dots show the locations which will be ablated by the laser.

Figure 2.14:. Spot locations prior to ablation for elemental screening analyses. Please note that the little red-blue dots show the locations which will be ablated by the laser.

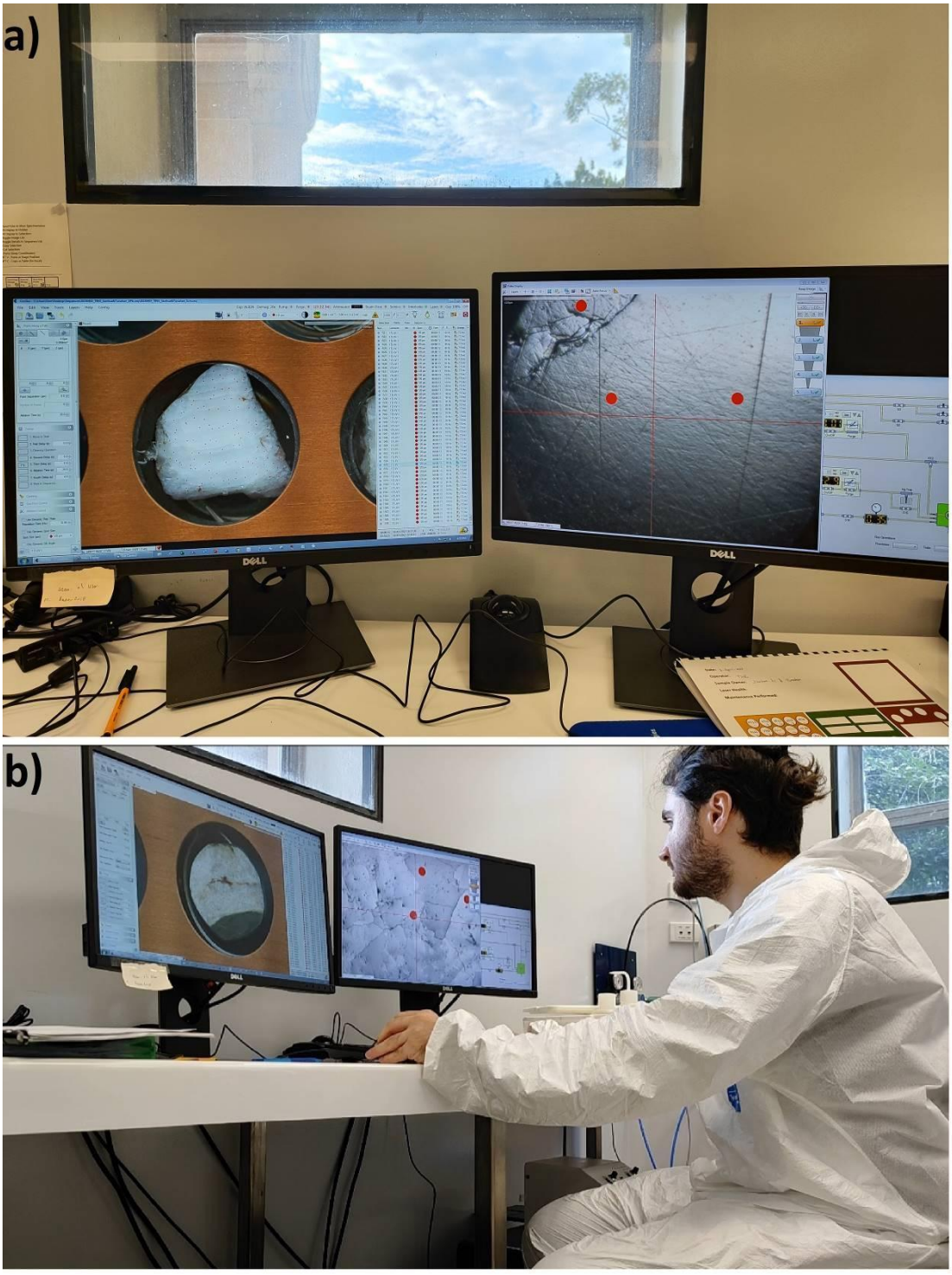

Figure 2.15: a), b) Assigning ablation spots (approximately 120 spots for each mount) using GeoStar software to examine the radioactive-radiogenic properties of the samples.

Figure 2.16: The integrated LA-ICP-MS equipment; “thermo Fisher iCAP RQ” (left) and “quadrupole inductively coupled plasma mass spectrometer (Q-ICP-MS)” (right), which was used for the screening analysis.

Figure 2.17: Delineated high Uranium zones which will be further ablated to calculate the U-Pb ages of the samples.

Figure 2.18: Delineated higher Uranium zones through screening analysis which will be further ablated to calculate the U-Pb ages of the samples.

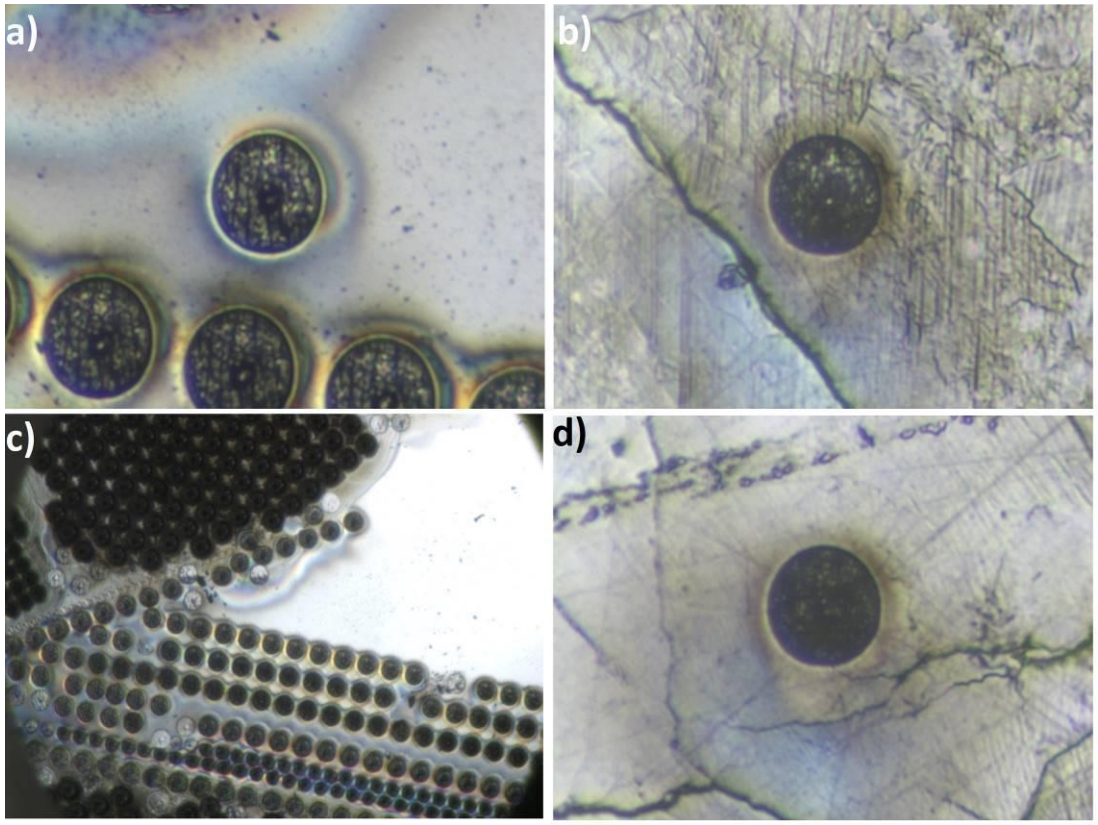

Figure 2.19: Micrograph examples of ablated spots from the screening analysis. Please note that the spot size is 120 µm.

Analytic procedures of U-Th mc-icp-ms and U-Pb la-icp-ms dating

U-series dating was carried out using a Nu Plasma multi-collector inductively-coupled plasma mass spectrometer (MC-ICP-MS) in the Radiogenic Isotope Facility (RIF) at the School of the Environment, The University of Queensland (UQ) following chemical treatment procedures and MC-ICP-MS analytical protocols described elsewhere (Zhao et al. 2009; Clark et al. 2012, 2014). Powdered or chipped sub-samples weighing 3–170 mg were spiked with a mixed ^{229}Th-^{233}U tracer and then completely dissolved in concentrated HNO_3 (Figure 2.20). After digestion, each sample was treated with H_2O_2 to decompose trace amounts of organic matters (if any) and to facilitate complete sample-tracer homogenization. U and Th were separated using conventional anion-exchange column chemistry using Bio-Rad AG 1-X8 resin. After stripping off the matrix from the column using double-distilled 7N HNO_3 as eluent, 3 ml of a 2% HNO_3 solution mixed with trace amount of HF was used to elute both U and Th into a 3.5-ml pre-cleaned test tube, ready for MC-ICP-MS analyses, without the need for further drying down and re-mixing. After

column chemistry, the U-Th mixed solution was injected into the MC-ICP-MS through a DSN-100 desolation nebuliser system with an uptake rate of around 0.1 ml per minute. U-Th isotopic ratio measurement was performed on the MC-ICP-MS using a detector configuration to allow simultaneous measurements of both U and Th isotopes (Figure 2.21) (Zhou et al. 2011; Clark et al. 2014). The $^{230}Th/^{238}U$ and $^{234}U/^{238}U$ activity ratios of the samples were calculated using the decay constants given in Cheng et al., (2000). The non-radiogenic ^{230}Th was corrected using an assumed bulk-Earth atomic $^{230}Th/^{232}Th$ ratio of $4.4\pm2.2\times10^{-6}$. U-series ages were calculated using the Isoplot/Ex 3.75 Program (Ludwig, 2012).

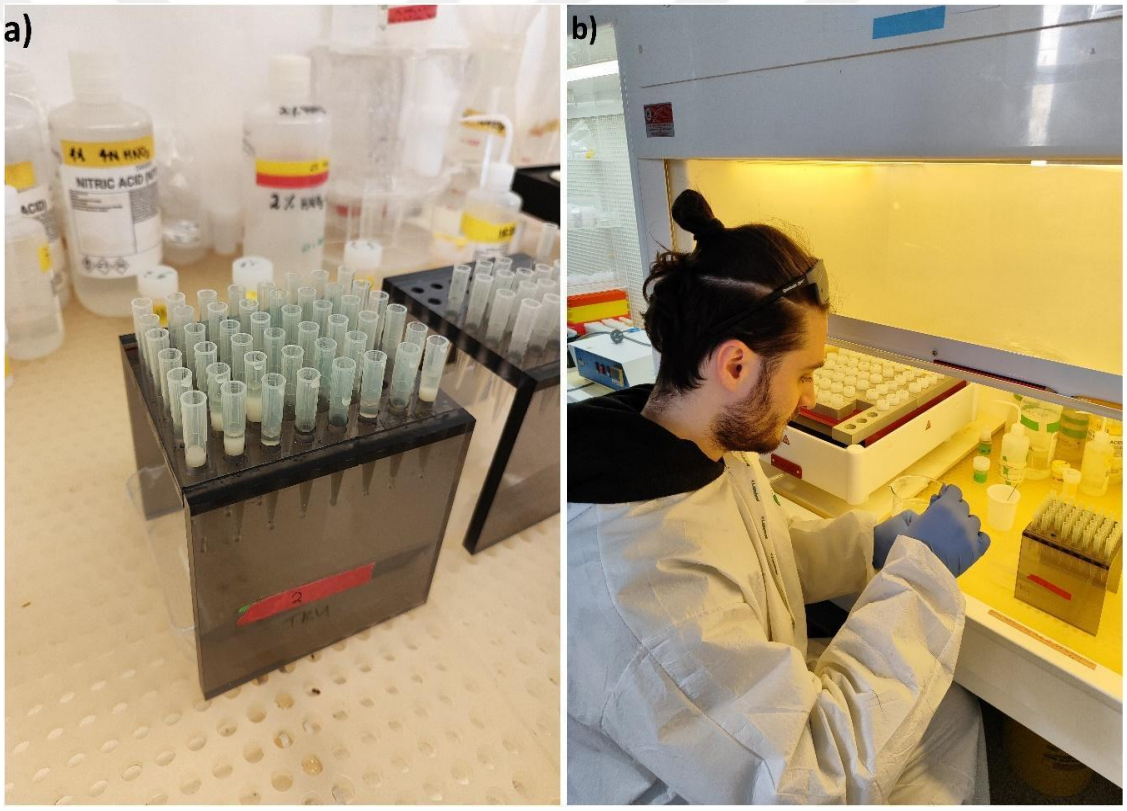

Figure 2.20: a), b). Spiking the samples with a mixed ^{229}Th-^{233}U tracer.

Figure 2.21: Nu-Plasma Multi-Collector Inductively Coupled Plasma Mass Spectrometer which was used for U-Th dating.

Laser ablation-inductively coupled plasma-mass spectrometry (LA-ICP-MS) *in situ* U-Pb dating of calcites were conducted in the Radiogenic Isotope Facility (RIF) at the University of Queensland, using an ASI RESOlution SE 193 nm UV ArF-Excimer laser ablation system coupled to a Thermo iCap-RQ quadrupole ICP-MS. Calcite samples were made into standard 2.5 cm diameter mounts with epoxy resin and polished to a one-micron finish for laser ablation. Prior to U–Pb dating, the carbonate minerals were cleaned and rapidly screened with a ~3 second ablation, targeting ^{206}Pb, ^{207}Pb, ^{208}Pb, ^{232}Th and ^{238}U isotopes. The aim of this screening was to first remove any surficial contamination and to characterize the distribution and variation of U concentrations and U/Pb ratios on microscopic scales. Spots with low U concentration or low U/Pb ratios were removed from full measurement mainly due to too low U content and / or high levels of common Pb to be useful for geochronology. Sometimes, ^{43}Ca and ^{88}Sr isotopes were also measured in high-resolution mode during screening, mainly for the purpose of determining the

mineral composition of individual spots (calcite, dolomite or otherwise) and Sr concentrations (in case Sr isotope analysis by solution or laser-ablation MC-ICPMS might be needed).

For *in situ* U-Pb dating of the calcite mounts, only areas with high U levels and high $^{238}U/^{206}Pb$ ratios were selected, using the Iolite-calculated U, $^{238}U/^{206}Pb$ and $^{207}Pb/^{206}Pb$ data. Extra spots were also placed around areas identified with the best potential for geochronology (i.e. high U and $^{238}U/^{206}Pb$ ratio). Instrument conditions were optimised using a raster line on NIST 612 glass standard, aiming for a working sensitivity of ~800,000cps ^{238}U, ThO/Th < 2% and $^{206}Pb/^{238}U$ >0.2 (typically in the range of 0.22-0.24). When performing LA-ICPMS U-Pb dating on the samples, the laser beam was set to 120 μm diameter spot size, 10 Hz repetition rate and fluence at 2.5 – 3.0 J cm^{-2}. The measurement cycle comprised a cleaning sequence of 30 shots (to remove surface contamination, but not to spots already pre ablated during screening), a pre-ablation background of 15 s, an ablation period of 20 s and a washout time of 10 s. The duty cycle for U-Pb dating included only ^{206}Pb, ^{207}Pb, ^{208}Pb, ^{232}Th, and ^{238}U. The samples were measured together with NIST 614 glass standard and several matrix-matched laboratory working calcite standards, such as AHX-1D (high-U), PTKD-2 (low-U) and WC-1 (high-U). Repeated measurements of the NIST 614 glass standard bracketing the unknown samples and calcite standards were used to correct for $^{207}Pb/^{206}Pb$ fractionation and for instrument-related drift in the $^{206}Pb/^{238}U$ ratios. In-house calcite standard (AHX-1D) repeatedly calibrated to an age of 238.2 ± 1.5 Ma was used for bias correction of the measured $^{238}U/^{206}Pb$ ratios. During analysis of different sessions of our samples, both WC-1 calcite standard independently dated to 254.4 ± 6.4 Ma (Roberts et al., 2017) and our in-house low-U standard PTKD-2 independently dated to 153.7 ± 1.7 Ma was also dated together with our samples as the control standard to ensure reproducibility. WC-1 gave age results within 3% of the reference value among different sessions, whereas PTKD-2 yielded ages usually within 2% of 153.7 Ma. Data reduction was undertaken with the software Iolite v3.71 which runs within the Igor Pro environment (Paton et al., 2011). We adopted the built-in "U-Pb Geochronology" data reduction schemes (DRS) within the Iolite package of Paton et al. (2011) for U-Pb isotope ratio, apparent U-Pb age and U-Th-Pb concentration calculations. Afterwards, the data were regressed on Tera-Wasserburg

concordia plots using Isoplot 3.75 software of Ludwig (2012) to determine each sample's U-Pb age. The calibrated $^{238}U/^{206}Pb$ ratios versus the total $^{207}Pb/^{206}Pb$ ratios are plotted as 2 sigma error ellipses on the Tera-Wasserburg concordia (i.e. total Pb/U isochron) plots. The ages of all dated calcites are determined from lower intercepts on the Tera-Wasserburg concordia plots.

2.5 Microstructural Analysis

Microstructural characteristics of fault-related calcite crystals provide important information on the relationships between the crystal growth and faulting (Uysal et al., 2007, 2009; Nuriel et al., 2011, 2012, 2019; Weinberger et al., 2020). In order to investigate microstructural structures and textures, fault-related calcite crystals have been examined by optical and scanning electron microscope (SEM) analysis on thin sections. SEM analyses were carried out at the Nuclear Science Institute of the Ankara University utilizing ZEISS EVO 40 (500 V- 30 kV). Petrographic microscope analysis was performed using James Swift (England) MP3500A polarizing microscope at the Department of Geological Engineering-Hacettepe University (Figure 2.22). Thin sections have been prepared at the General Directorate of Mineral Research and Exploration of Türkiye (MTA).

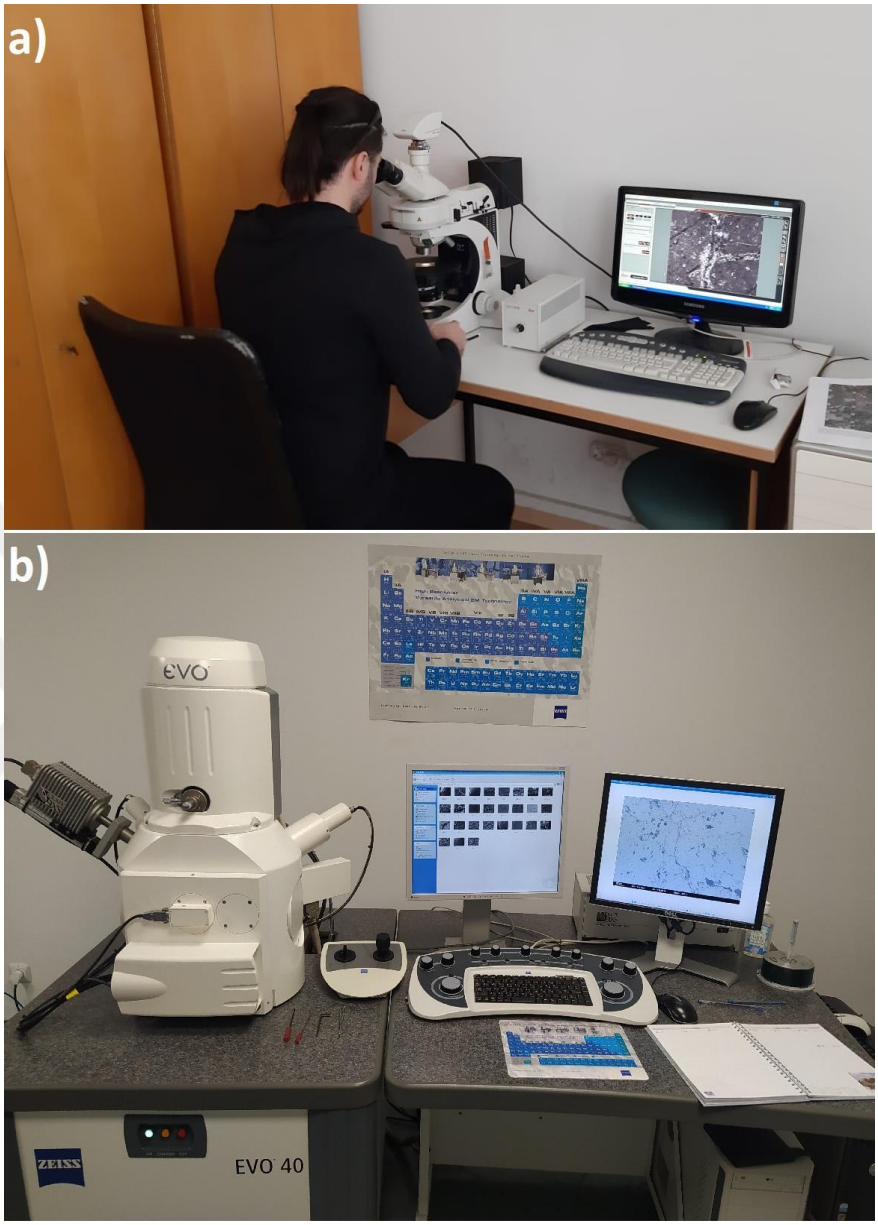

Figure 2.22: a) Optical microscope examinations on thin sections through the James Swift (England) MP3500A polarizing microscope. **b)** ZEISS EVO 40 (500 V- 30 kV) which was used for the scanning electron microscope analysis.

3. RESULTS

3.1 Tectono-geomorphological Mapping and Morphometric Analysis

3.1.1 Topographical swath profiles

Swath profiles orthogonal to the CT (Swath profiles 1-4) denote the controlling effect of the major fault zones over topography. Relief contrasts are widespread in every profile, especially in the transition zones between the mountainous part of the CT and the bounding basins in the northern and southern parts. In the southern part, the topography is relatively smooth, the incision is lower and tectonic control diminishes toward the Mediterranean Sea. Toward mountainous northern parts, elevations tend to increase, and the topographical scarps are well defined. Relief and incision are also higher, rugged topography is very clear, and major knickzones are widespread in between the Antalya Basin and the interior of the CAP. The boundary between Beyşehir-Suğla depression and CT is controlled by undefined faults, and the transition is very sharp. In each profile, there are major knickzones located at approximately 1000 m and 2000 m elevations. These knickzones are mainly controlled by faults. All profiles display recognizable elevated relatively flat surfaces on top of the mountains, between 1500-2000 m elevation zone. Depressions with flat floors correspond to the tectono-karst poljes around Akseki and İbradı (Figure 3.1).

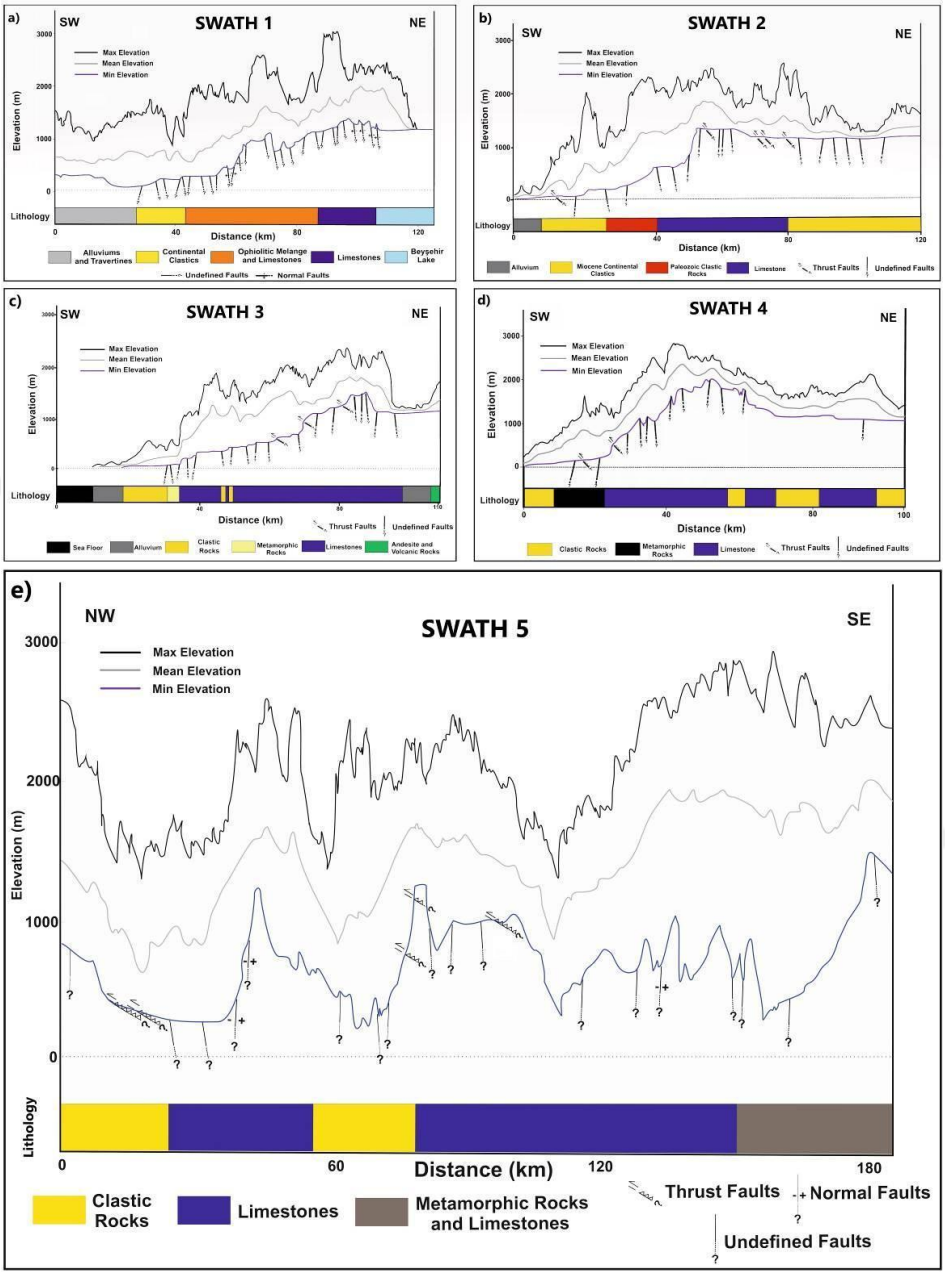

Figure 3.1: (a-d) Topographical swath profiles orthogonal to the CT**. (e)** Topographical swath profile parallel to the CT. Swath profile footprints are given in Figure 2. The color bars under the profiles are lithological classes, legends are given in each profile.

The swath profile that is parallel to the CT and orthogonal to the main drainage systems (Figure 3.1-e) displays a very rugged morphology across a 180 km zone, with the mountain peaks reaching up to the 3000 m elevation in the eastern part. Deeply incised valleys are situated in between steep scarps. These scarps are controlled by NW-SE and

N-S, striking mostly undefined faults. Swath profile 5 reveals that the elevations tend to increase from west to east along the western flank of the southern margin (Figure 3.1-e).

3.1.2 Delineation of stream network and bedrock river basins

We implemented the "Spatial Analysis" and "3D Analysis" tools of ESRI's ArcGIS 10.7 software for hydrology analysis. Next, using high-resolution DEM data the synthetic stream network was produced by following the procedure of determining flow directions and flow accumulations. We delineated eight major river basins from west to east: Aksu, Köprüçay, Manavgat, Karpuzçay, Ulugüney, Kargı, Oba and Dim, respectively. The river network generally flows from north-northeast to south-southwest, towards the Mediterranean Sea (Figure 3.2).

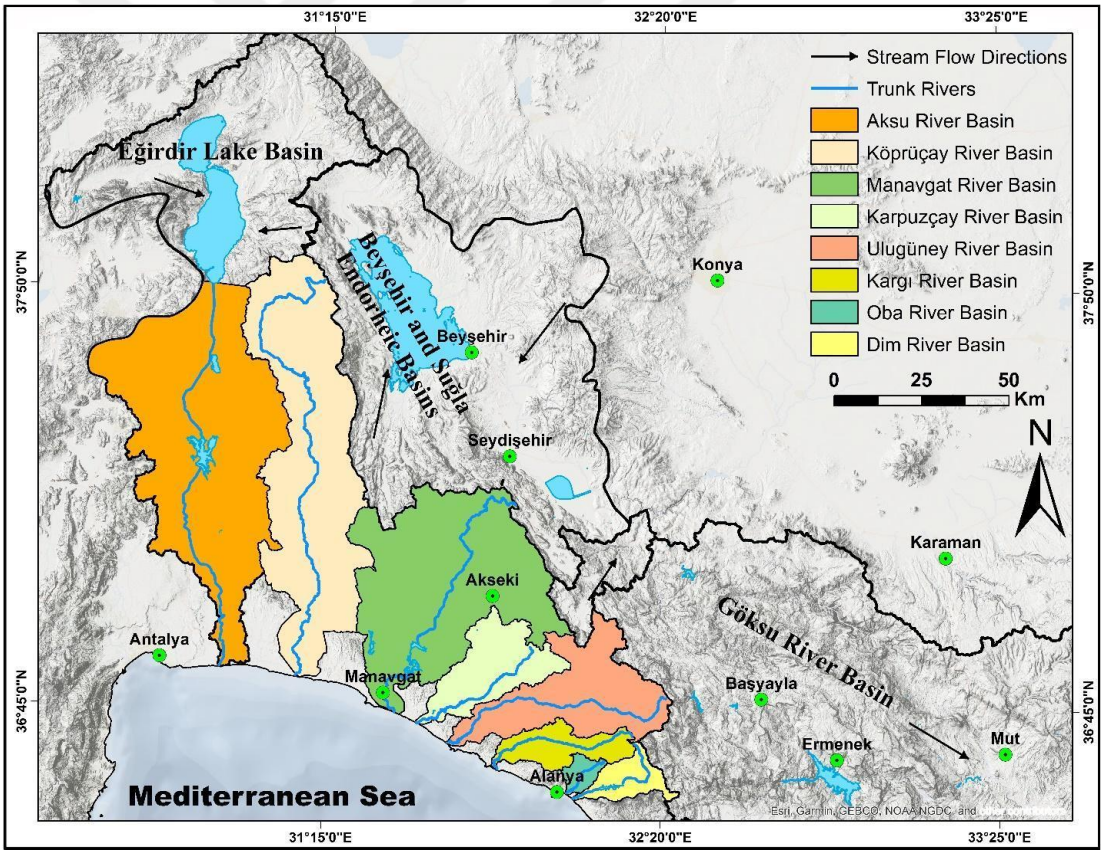

Figure 3.2: The studied drainage basins across the western Central Taurides.

3.1.3 Knickpoint extraction and channel steepness analysis

The longitudinal profiles of the bedrock rivers flowing across the western flank of the Central Taurides exhibit deviations from the graded profile. Slope-area plots and ksn

values show steepened channel segments especially in the downstream parts of the major knickzones (Figure 3.3), and slope-break knickpoints are widespread along the flank. Vertical-step knickpoints mainly coincide with the lithological contacts, and some of them are marked by faults and lithological boundaries together. The relatively minor knickpoints are not distinguishable in the slope-area plots, because of the scattering of the data across an intensely karstified erosional landscape. Therefore, we further investigated and utilized geological maps and our field observations to classify the knickpoints. We identified the lithological and tectonic knickpoints according to their spatial relation to the lithological and tectonic boundaries (Figure 3.3, 3.5, 3.6). Some of the knickpoints coincide with neither lithological contacts nor tectonic boundaries. These knickpoints are attributed to waves of headward erosion processes.

Aksu river drains the westernmost part of the study area. The longitudinal profile of the Aksu river demonstrates deviations from the graded smooth profile and contains knickpoints with different origins. The faults' strikes that affect the Aksu basin are north-south, parallel to the general trend of the basin and the flowing direction of the trunk channel. Tectonic knickpoints are located upstream, where the trunk stream flows over the segments of the Aksu thrust zone (Figure 3.3). The main knickzones are in between 150-300 m and 500-1000 m elevations. The relatively minor knickpoints are related to small lithological variations and headward erosion processes. The slope-area diagram demonstrates a number of vertical-step knickpoints especially in the downstream part of the trunk stream, with channel steepness values reaching up to the 320 ksn value (Figure 3.3, 3.4). The maximum relief reaches 700 meters near the tectonic knickpoints and 500 meters near the main lithologic knickzones (Figure 3.3).

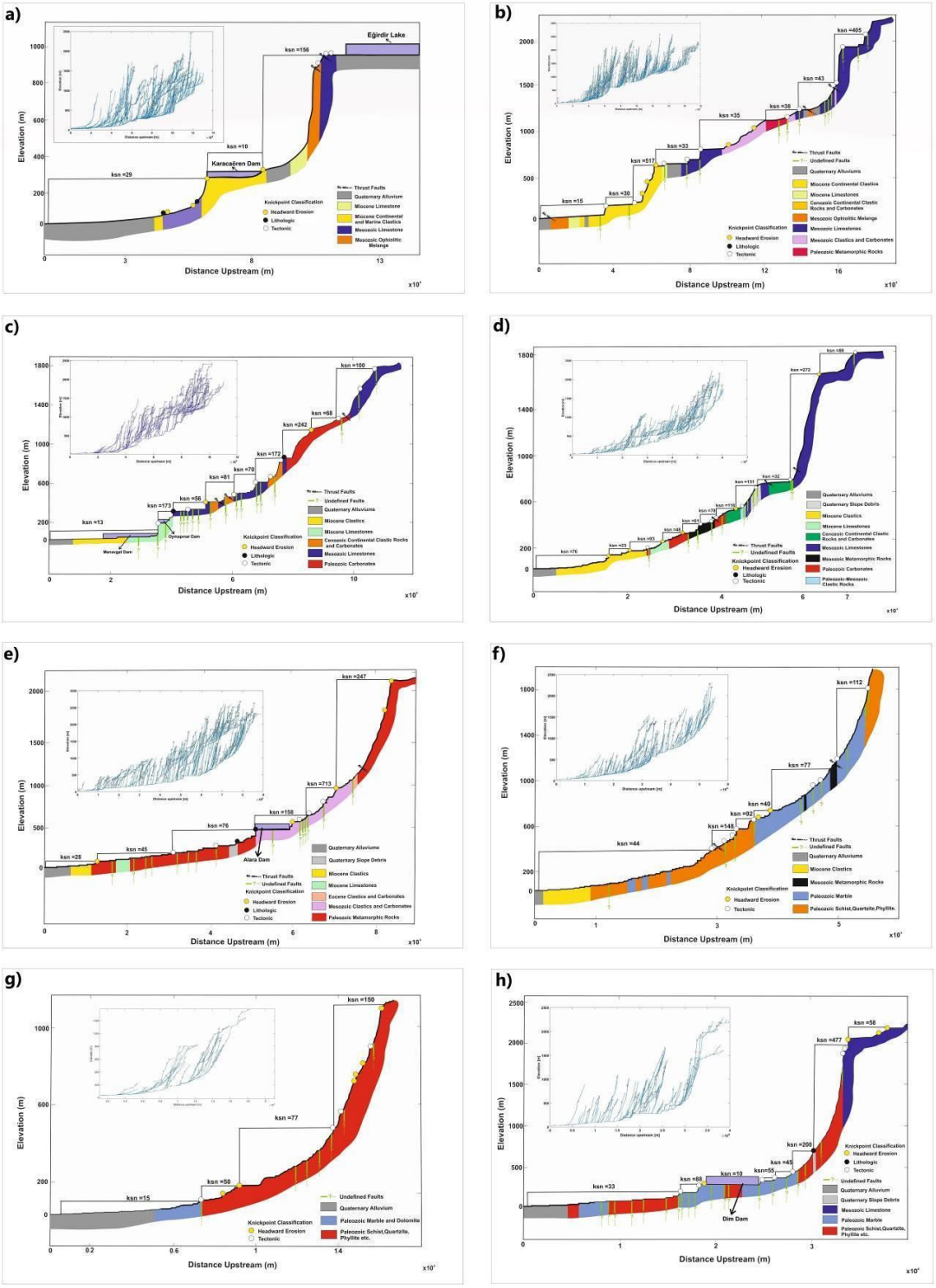

Figure 3.3: Longitudinal topographic and geologic profiles, knickpoint classification and ksn values of the channel segments along the trunk rivers. The legend of the geological features and knickpoints are given within the figures. All knickpoints and longitudinal profiles within river basins presented as inlets. **a)** Aksu River, **b)** Köprüçay River, **c)** Manavgat River, **d)** Karpuzçay River, **e)** Ulugüney River**, f)** Kargı River**, g)** Oba River, **h)** Dim River. Please note that horizontal and vertical scales are different for each profile.

In the east of the Aksu river, the Köprüçay river basin has a very elongated shape, flowing from north to south approximately for 180 km (Figure 3.2). The irregularities and convex channel parts are very widespread in the longitudinal profile. Both vertical-step and slope-break knickpoints are clear in the slope-area plot (Figure 3.3, 3.4). The main knickzone that coincides with the tectonic lineaments is located in between 1500-1800 m elevations at the upper reach of the Köprüçay river (Figure 3.3). Another important knickzone is located in between 200-600 m elevations and exhibits a series of vertical step knickpoints. The maximum ksn values reach up to 517 around the major knickzones and ksn values show fluctuations from upstream to downstream. There are numerous minor knickpoints that originated from the small lithological contacts and relatively small segments of undefined faults (Figure 3.3, 3.5, 3.6).

Farther east, the Manavgat river basin is located between the settlements of Manavgat and Seydişehir (Figure 3.2). The longitudinal profile of the Manavgat river displays a staircase morphology. The trunk channel traverses many undefined fault zones and has been affected by undefined fault segments in its' middle reach. The slope area plot demonstrates a major slope-break knickpoint near the major undefined fault zone around the Oymapınar settlement (Figure 3.4). This knickzone also coincides with the contact of the Manavgat Sedimentary Basin and Central Taurus Mountains, between 250-500 m elevations (Figure 3.3). Ksn values of the channels reach up to 307 in this zone. Another major knickzone is located between 800-1200 m elevations, presented with a convex channel segment that is steeper from the upstream part (Figure 3.3). Ksn values reach up to 242 across this zone, while the upstream best-fit channel steepness values change between 68-132 (Figure 3.3). Another major tectonic knickzone is located in the uppermost reach of the Manavgat river. This knickzone is controlled by a series of undefined faults between 1400-1800 elevations and separates a low-relief relict upland surface that has low ksn values from the steeper ksn channel segment towards downstream (Figure 3.3). Vertical step knickpoints are located in the downstream part of the river, between 50-200-meter elevation level, where the Manavgat and Oymapınar Dams are located.

Karpuzçay river flows in the NE-SW direction, across a 80 km zone and sourcing from the top of the Central Taurides. Staircase morphology of the longitudinal profile is prevalent especially in the lowermost reaches, caused by the series of minor knickpoints.

A major knickzone is observable between 400-600 m elevations that separate a fragment of a low relief upland surface and a steeper channel segment downstream. The biggest knickzone is located between 800-1800 m elevations. Ksn values reach up to 272 along this zone. There is another fragment of low relief upland surface upstream of the highest elevated knickpoint. The low relief relict upland surface fragments are characterized with the lowest ksn values (20-35) in the upper stream of the Karpuzçay stream. The major knickzones are controlled by the tectonic boundaries (Figure 3.3). Slope-area graph of the Karpuzçay trunk exhibits a series of vertical step knickpoints in the lower reaches similar to the other bedrock trunk streams. The major knickzones are marked by the slope-break knickpoints with the channel steepness values peaks from 30-40 to 200-272 values toward the downstream (Figure 3.4).

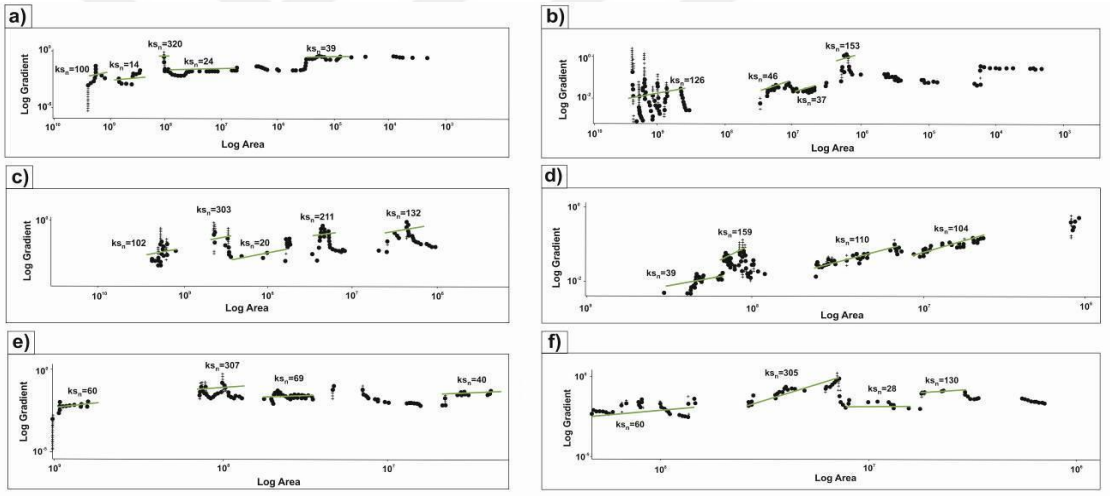

Figure 3.4: Slope-area plots of the best representative trunk streams in log-log space. Green lines are regression lines of the best-fit ksn values of the channel segments. **a)** Aksu River, **b)** Köprüçay River, **c)** Manavgat River, **d)** Kargı River, **e)** Ulugüney River**, f)** Dim River.

The longitudinal profile of the Ulugüney River displays relatively minor knickpoints in the downstream, related to lithological variations and small fault segments. The vertical-step knickpoints are concentrated in the downstream portion of the river profile. The tectonic control is starting to increase from the 500-meter elevation level towards upstream, and the tectonic forcing on channels is underlined by the major slope-break knickzones and very steep channel segments (Figure 3.3). Between 500-1000-meter elevation level, best-fit ksn values rise up to 713 (Figure 3.3). This major knickzone is also clearly seen in the slope-area plot, as the slope of the channel rises from 69 ksn value

to 307 ksn value towards downstream (Figure 3.3). Between 1000-2000 m elevations, there is another major knickzone which has 247 best-fit ksn values. A low relief upland surface with the low ksn value located over this knickzone, implying an actively deforming topography.

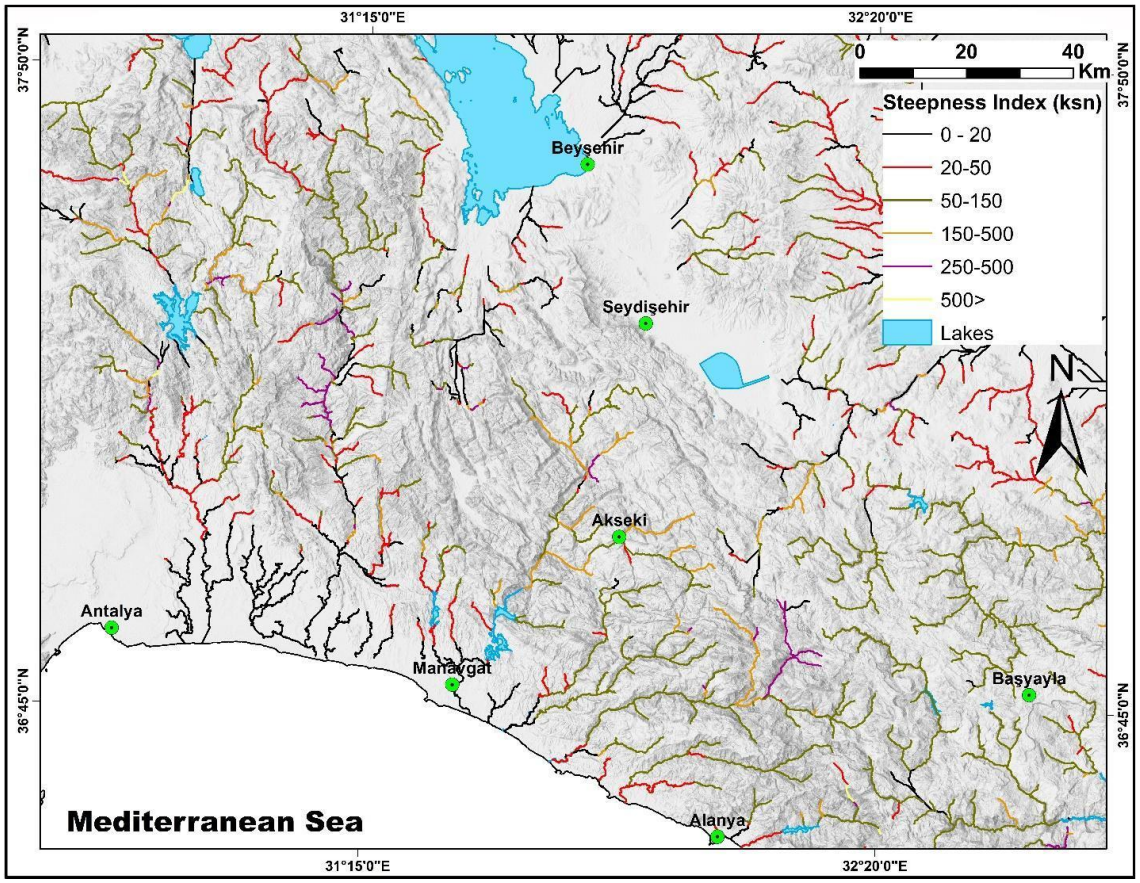

Figure 3.5: The best-fit ksn values of the main stream channels.

The Kargıçay, Oba and Dim rivers flow through the NE-SW direction and drain a part of the Central Tauride Mountains, Alanya Metamorphic Complex and the Manavgat Sedimentary Basin. The lower reach of the Kargıçay river has low ksn values with the relatively graded smooth profile, up until the 400-meter elevation level (Figure 3.3, 3.5). Between 400-1800 meter elevations, there are tectonically controlled slope-break knickzones across the longitudinal profile. As can be seen clearly in the slope-area plot, the best-fit ksn value of the channel is increasing continuously toward the downstream reaches; first from 104 to 110, then to 159 ksn value (Figure 3.3, 3.4). The Dim river is located in the easternmost part of the study area and it is a relatively small stream that is flowing across an approximately 40 km zone (Figure 3.1, 3.3). A very distinct broad

knickzone is located between 500-2000 m elevations. This knickzone is strongly controlled by undefined faults. The elevation of the trunk stream increases 1500 m in a very short distance. The steepness of the channel reaches up to 477 ksn value along this deformation zone. The downstream increment of the stream channel slope and the typical slope-break character of the knickzone are very evident in the slope-area plot (Figure 3.4). A fragment of low relief upland surface located in the upper portion of this knickzone demonstrates that the incision amount along the Dim river is very high. Along the Dim trunk river, the ksn values are gradually decreasing after the 500 m elevation level, toward the Mediterranean Sea.

3.1.4 Topographical relief analysis and surface uplift estimates

The relief or the erosion depth is 1689 m between the valley bottoms and ridge tops across the flank. Low relief areas are mostly distributed along the Antalya and Beyşehir-Suğla basins, approximately between 0-1000 m elevations. The high relief areas are clustered at the middle part, and the southeastern part of the flank, and they correspond to the upthrown blocks of the Aksu, Kırkkavak and the major fault zones. The high relief areas mainly underlie relatively resistant lithological units like Mesozoic limestones and Paleozoic metamorphic rocks. The local topographical relief gradually increases from the western to the eastern parts, from the Aksu River Basin to the Dim River Basin across the flank.

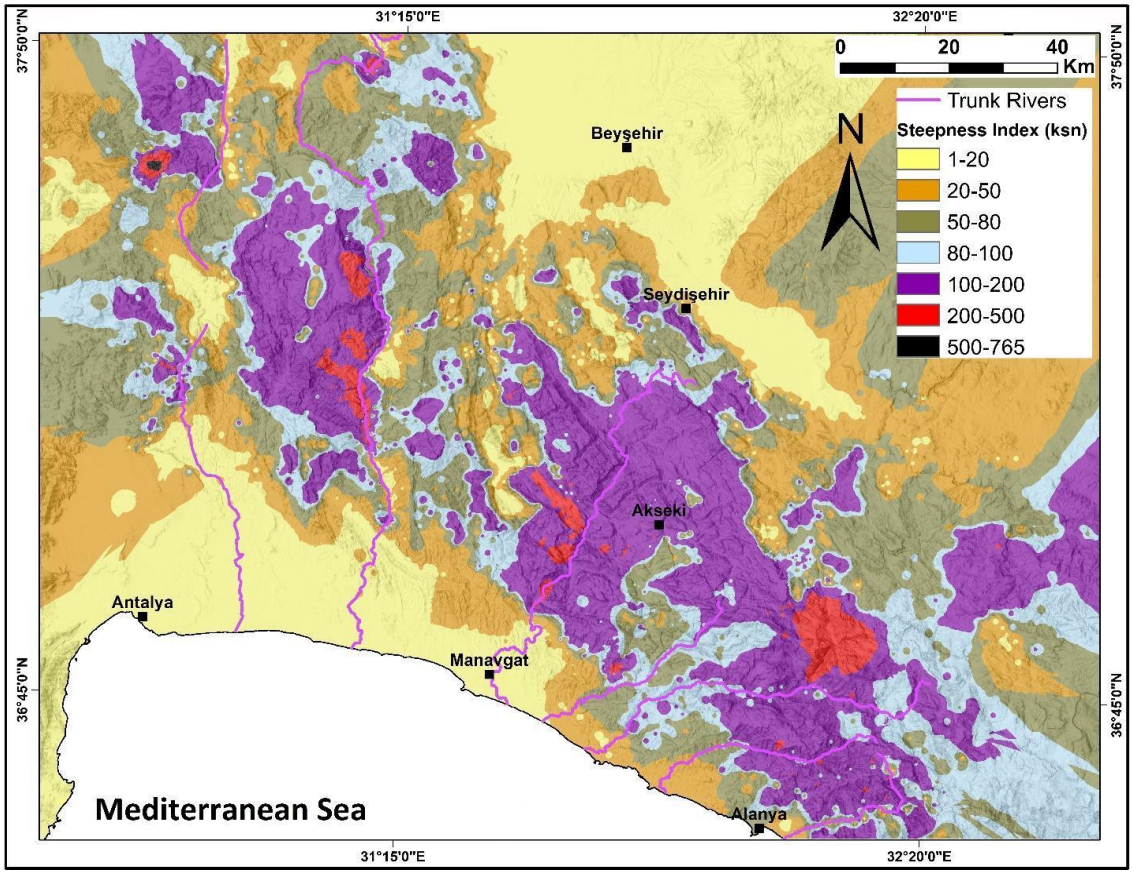

Figure 3.6: The distribution of the ksn values produced by the Inverse Distance Weighting (IDW) Interpolation.

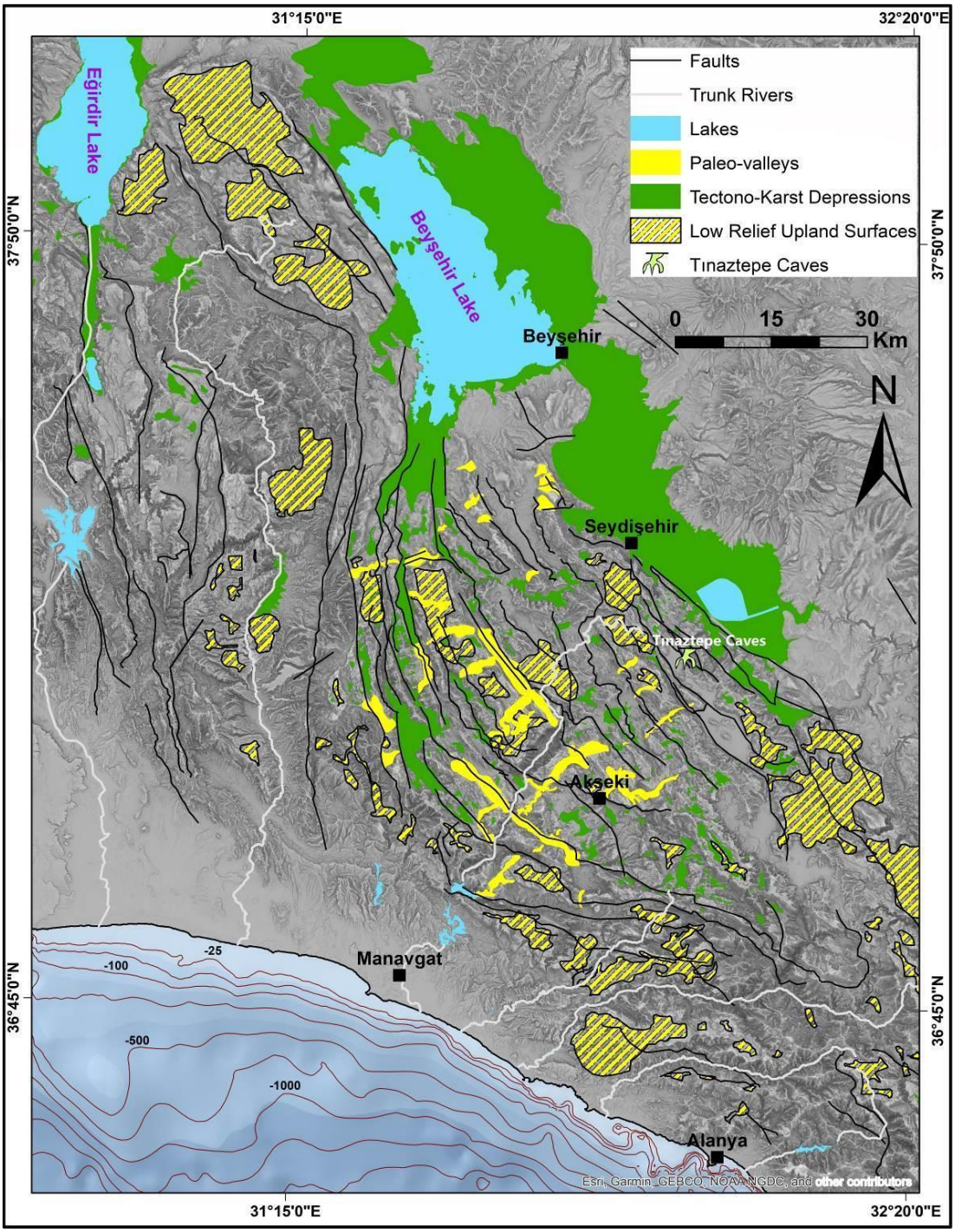

Figure 3.7: Spatial distribution of the low relief upland surfaces, paleo-valleys and tectono-karst depressions. Paleo-valleys are from Monod et. al., (2006). Bathymetry data is from GEBCO (The General Bathymetric Chart of the Oceans) (https://www.gebco.net).

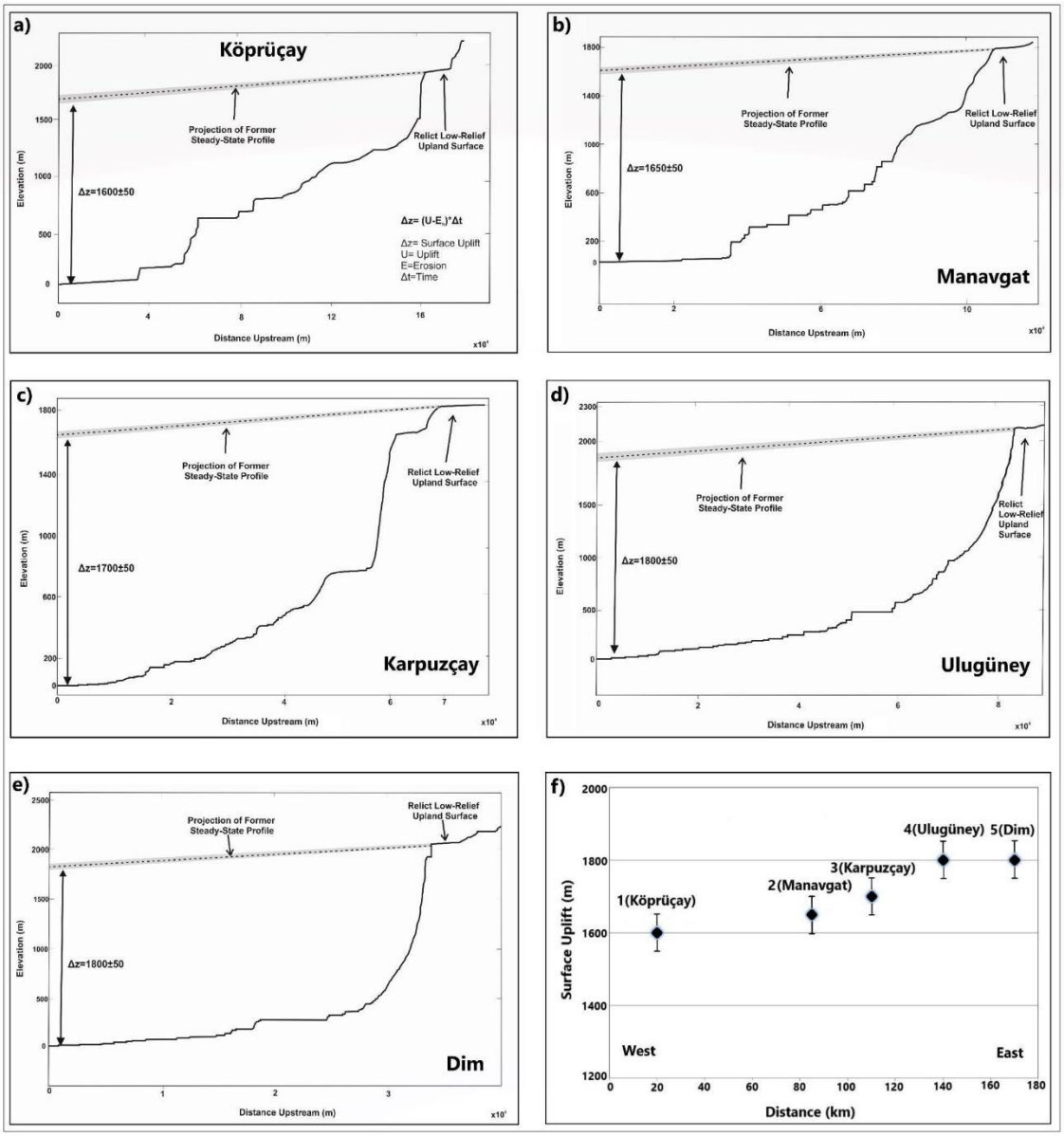

Figure 3.8: (a-e) Current and projected relic longitudinal profiles of the bedrock rivers that are sourcing from the relict low relief upland surfaces. Concepts and the equation (given in (a)) for calculating surface uplift is from Kirby and Whipple, (2012). **a)** Köprüçay river, **b)** Manavgat river, **c)** Karpuzçay river, **d)** Ulugüney river, **e)** Dim river. **(f)** Scatter plot of the surface uplift pattern; from the western part, Köprüçay River basin to the eastern part, Dim River basin.

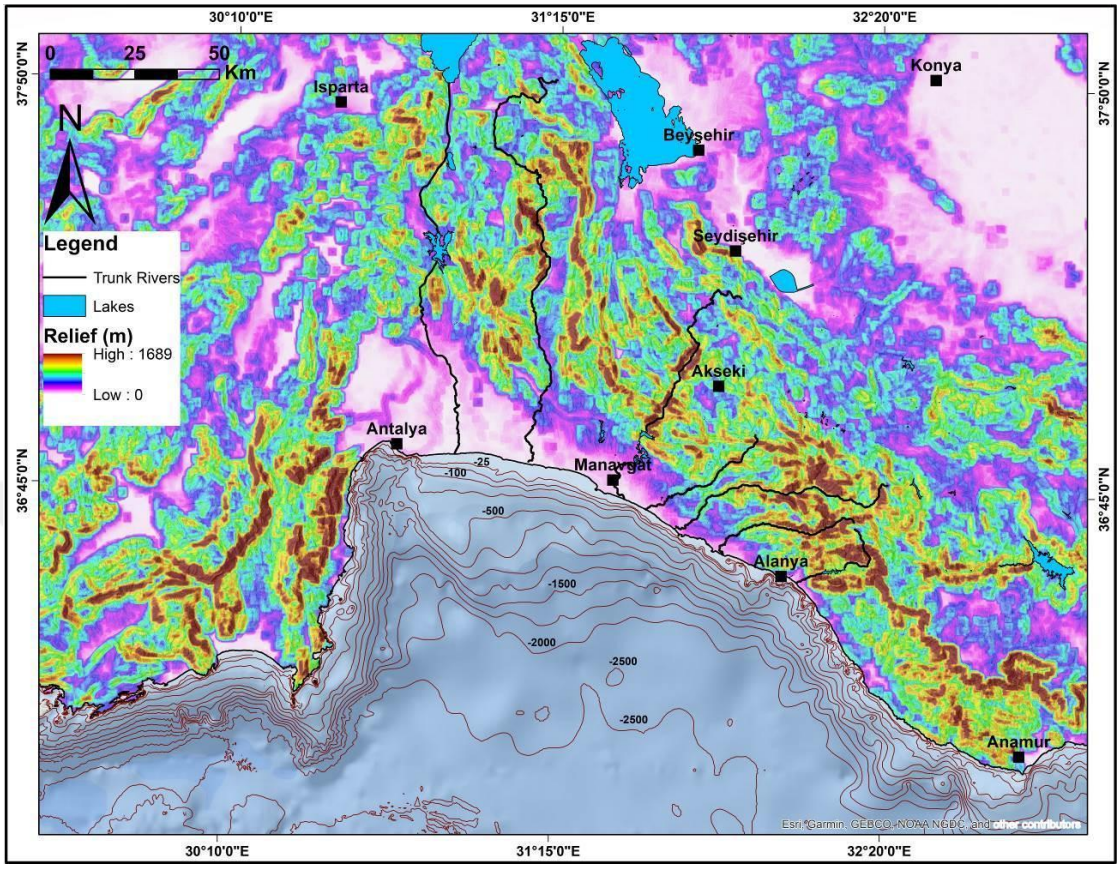

Figure 3.9: The general topographic relief across the western flank of the CT.

The low relief upland surfaces are scattered but continuous across western CT. The relic upland surfaces are usually found as bounded by normal faults and further fragmented by the extensional active tectonics. These surfaces are distributed roughly between 400-2600 meters and clustered around 2000-meter elevations mostly in the mountainous part of western CT. The elevations of these surfaces are higher in the eastern part of the study area. The elevation of the slope-break knickpoints that bound the upland surfaces also increases from 1700-1800 meters in the west to 2000-2100 meters in the east (Figure3.7, 3.8, 3.9).

Using the spatial extent and the modern elevation of the low relief upland surfaces, we estimated the long-term vertical deformation and amount and the pattern of the surface uplift throughout the flank. We selected five bedrock streams (Köprüçay, Manavgat, Karpuzçay, Ulugüney and Dim Rivers) that are sourcing from perched low relief surfaces. We calculated surface uplift as 1600 ± 50 m from Köprüçay River, 1650 ± 50 m from Manavgat River, 1700 ± 50 m from Karpuzçay River and 1800 ± 50 m from Ulugüney

and Dim rivers. The mean surface uplift is 1710 ± 50 m and the surface uplift tends to increase from west to east, from 1600 ± 50 m to 1800 ± 50 m (Figure 3.8, 3.9).

3.2 Fault-slip Data and Paleo-stress Analysis

Most of the fault planes have clear slickenlines, slicken fibres and polished surfaces. Results provided positions and stress ratio (R) of the principal stress axes (σ1, σ2, σ3; compression, intermediate, extension) of the stress tensor (Table 3.1, 3.2). We graphically plotted kinematic measurements and evaluated the states of principal stresses, local extension and compression directions. We mostly observed vertical striations characterizing pure normal and oblique movements along the major fault zones. Analysis of fault-slip data shows that most of the faults display dip-slip motion and normal faulting. "R" values exhibit pure NE-SW extension at locations 2,3a,4,6,7a,8a,9,14,15,16,18,19,20 (Table 3.2). At locations 1,5,7b,8b,10,11,12,13,17, the kinematic analysis present sinistral/dextral strike-slip motion along an NW-SE, NW-SE and E-W striking secondary fault zones. These fault zones yielded NE-SW trending extension/NW-SE trending compression and NW-SE trending extension/NE-SW trending compression. These faults are parallel to the present extension direction and join with the NW-SE trending primary normal fault zones with low angles. At location 3b, we also detected reverse faulting which yields NE-SW compression (Figure 3.10-3.28).

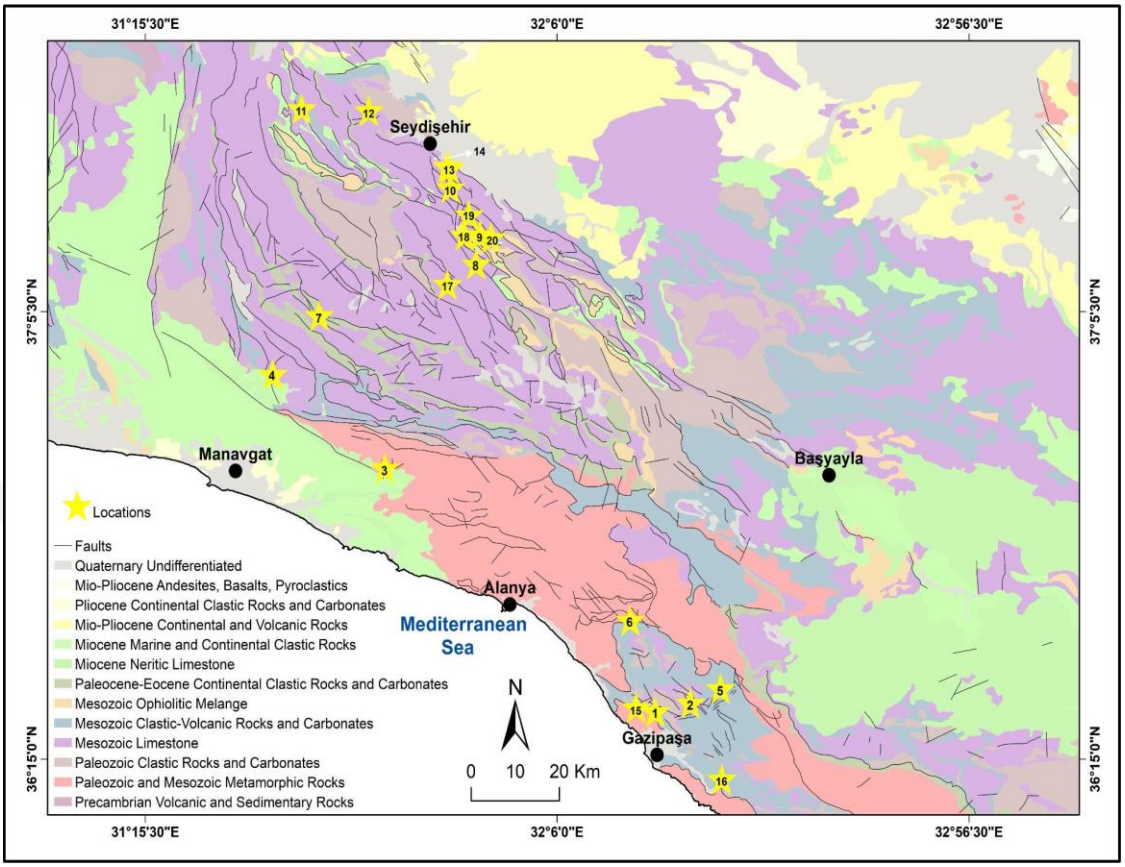

Figure 3.10: Locations of the kinematic analysis and sampled calcites together with lithological formations and faults derived from Şenel, (2002). Measurement locations are shown on the map by yellow stars, location numbers are given within each star.

Table 3.1: Kinematic measurements along the fault planes. Please note that there are different sets of faults in locations 3, 7, and 8. Locations are given in Figure 3.10.

Locations	Strike(°)	Dip Angle (°)	Rake(°)	Coordinates (UTM) (x)	Coordinates (UTM) (y)
Location 1	003 001 005 003 005	66 65 70 66 65	+005 +010 +015 +020 +010	435056	4019289
Location 2	290 110 141 160 140 160 140	81 65 54 65 55 65 55	-130 -135 -090 -130 -090 -125 -090	445681	4025667

Table 3.1 (continued): Kinematic measurements along the fault planes. Please note that there are different sets of faults in locations 3, 7, and 8. Locations are given in Figure 3.10.

Location 3	**Normal Faults**	----------	----------		
		----------	----------		
	158	48	-089		
	151	55	-105		
	192	55	-140		
	180	85	-050		
	250	75	-125		
	260	83	-120	389529	4074463
	165	86	-030		
	166	90	-030		
	Reverse Faults	----------	----------		
		----------	----------		
	170	65	+095		
	160	68	+105		
	165	50	+090		
	160	60	+105		
	160	60	+105		
Location 4	115	45	-090		
	120	45	-090		
	130	45	-090		
	125	45	-090		
	125	45	-090		
	110	45	-090		
	123	45	-090		
	131	46	-090	368369	4092966
	125	45	-090		
	125	45	-090		
	124	46	-090		
	125	45	-090		
	125	45	-090		
Location 5	240	85	+010		
	240	85	+020		
	240	85	+015	434057	4043863
	240	80	+020		
	240	80	+010		
	240	80	+010		
Location 6	195	64	-080		
	195	64	-080		
	195	65	-090		
	195	64	-105	446081	4026488
	200	64	-105		
	200	65	-090		
	190	60	-085		
	195	60	-085		

Table 3.1 (continued): Kinematic measurements along the fault planes. Please note that there are different sets of faults in locations 3, 7, and 8. Locations are given in Figure 3.10.

Location 7	**Normal Faults**	----------	----------		
		280	75	-110		
		285	85	-090		
		305	59	-100		
		305	60	-105		
		300	65	-100		
		305	60	-100		
		295	55	-090	376823	4105059
	Strike-slip Faults	----------	----------		
		275	85	-179		
		265	90	-179		
		265	90	-179		
		275	85	-179		
		275	85	-179		
		265	90	-179		
Location 8	**Normal Faults**	----------	----------		
		010	75	-085		
		013	75	-080		
		015	80	-080		
		020	82	-080		
		005	70	-090		
	Strike-slip Faults	----------	----------	405442	4114959
		023	90	-168		
		023	90	-165		
		030	90	-150		
		030	90	-150		
		025	90	-150		
		023	90	-165		
Location 9	143	41	-088		
	145	40	-090		
	140	40	-085		
	139	41	-090		
	150	42	-090		
	150	42	-090		
	145	40	-089	405671	4121833
	142	45	-090		
	140	40	-090		
	140	40	-090		
	140	40	-090		
	140	40	-090		

Table 3.1 (continued): Kinematic measurements along the fault planes. Please note that there are different sets of faults in locations 3, 7, and 8. Locations are given in Figure 3.10.

Location 10	131	90	-001		
	130	90	-002		
	175	85	-015		
	151	72	-034		
	150	85	-010	400184	4136129
	151	83	-012		
	135	80	-010		
	150	88	-010		
	140	85	-001		
Location 11	125	70	-010		
	105	75	050		
	125	70	030		
	039	10	080	374290	4148281
	040	85	050		
	010	85	015		
	010	85	015		
	010	85	015		
Location 12	005	88	+015		
	001	83	+001		
	065	75	+130	386918	4146314
	060	75	+130		
	110	86	+040		
	085	85	+030		
Location 13	035	77	+030	400123	4136648
	045	70	+050		
	035	78	+035		
	035	78	+060		
	040	86	+005		
	018	67	+007		
	015	67	+030		
Location 14	160	65	-110		
	175	64	-110		
	162	64	-110		
	170	80	-100		
	170	70	-100		
	145	72	-120		
	160	68	-100	399995	4136798
	160	68	-105		
	165	70	-110		
	165	70	-110		
	165	81	+001		
	166	80	+001		

Table 3.1 (continued): Kinematic measurements along the fault planes. Please note that there are different sets of faults in locations 3, 7, and 8. Locations are given in Figure 3.10.

Location 15	295	71	-085		
	290	79	-095		
	290	75	-088		
	300	65	-080		
	320	50	-085		
	315	75	-120	434435	4019811
	295	80	-120		
	295	60	-060		
	275	40	-060		
	335	74	-140		
	305	40	-120		
	310	61	-100		
Location 16	120	75	-090		
	125	70	-080		
	120	70	-090	450534	4009984
	125	75	-090		
	115	75	-088		
	115	70	-080		
Location 17	100	70	-179		
	100	70	-179		
	120	77	-179	399938	4111082
	120	77	-175		
	120	77	-175		
Location 18	285	70	-100		
	285	70	-160		
	285	70	-100		
	325	77	-130		
	325	80	-055		
	320	73	-140		
	280	70	-105		
	325	75	-105	400616	4131770
	285	70	-095		
	280	75	-095		
	320	75	-140		
	320	75	-140		
Location 19	124	53	-090		
	130	50	-085		
	125	51	-088	404281	4123863
	130	53	-090		
	125	55	-083		
	125	51	-088		
Location 20	155	65	-085		
	129	51	-070		
	130	40	-085		
	130	41	-095	407372	4121081
	125	40	-110		
	115	83	-120		
	120	40	-095		

Table 3.2: Summary of paleo-stress analysis and regional stress state. **D° and P°:** Trends and plunges of stress axes in degrees; **R:** Ratio of stress magnitude differences. **AD:** Angular Deviation. The location numbers (1-20) are given in Figure 3.10.

Location	Coordinates (UTM)	Principal Stress Axes (D^0/P^0)			R	AD	Sense of Motion
		σ1	σ2	σ3			
1	435056(X),4019289(Y)	29/323	60/133	04/231	0,50	1,9	Pure Strike-Slip
2	445681(X),4025667(Y)	77/360	11/152	06/243	0,67	25,2	Pure Extension
3a	389529(X),4074463(Y)	58/109	27/325	16/227	0,14	38,1	Extension with strike-slip component
3b	389529(X),4074463(Y)	20/249	07/156	69/047	0.50	9,4	Pure Compression
4	368369(X),4092966(Y)	86/213	00/123	04/033	0,50	6,2	Pure Extension
5	434057(X),4043863(Y)	05/013	74/267	15/105	0,50	3,8	Pure Strike-Slip
6	446081(X),4026488(Y)	71/106	00/015	19/285	0,49	7,5	Pure Extension
7a	376823(X),4105059(Y)	66/184	11/301	21/035	0,48	11,1	Pure Extension
7b	376823(X),4105059(Y)	02/135	87/343	01/225	0,50	4,4	Pure Strike-Slip
8a	405442(X),4114959(Y)	58/292	07/191	31/097	0,51	5,0	Pure Extension
8b	405442(X),4114959(Y)	16/253	68/026	18/158	0,51	7,0	Pure Strike-Slip
9	405671(X),4121833(Y)	86/225	00/321	04/051	0,50	2,7	Pure Extension
10	400184(X),4136129(Y)	11/102	79/304	04/192	0,50	11,6	Pure Strike-Slip
11	374290(X),4148281(Y)	12/297	75/158	10/029	0,50	41,5	Pure Strike-Slip
12	386918(X),4146314(Y)	06/290	82/148	05/020	0,50	38,8	Pure Strike-Slip
13	400123(X),4136648(Y)	09/159	55/056	33/254	0,47	15,2	Pure Strike-Slip
14	399995(X),4136798)Y)	62/034	19/164	20/261	0,54	15,8	Pure Extension
15	434435(X),4019811(Y)	66/204	05/305	23/037	0,35	23,8	Extension with strike-slip component
16	450534(X),4009984(Y)	62/036	04/299	27/207	0,50	5,1	Pure Extension
17	399938(X),4111082(Y)	13/293	76/141	06/025	0,50	19,3	Pure Strike-Slip
18	400616(X),4131770(Y)	55/189	18/308	28/048	0,40	25,7	Pure Extension
19	404281(X),4123863(Y)	82/051	02/305	07/215	0,50	3,2	Pure Extension
20	407372(X),4121081(Y)	87/066	01/310	02/220	0,50	11,9	Pure Extension

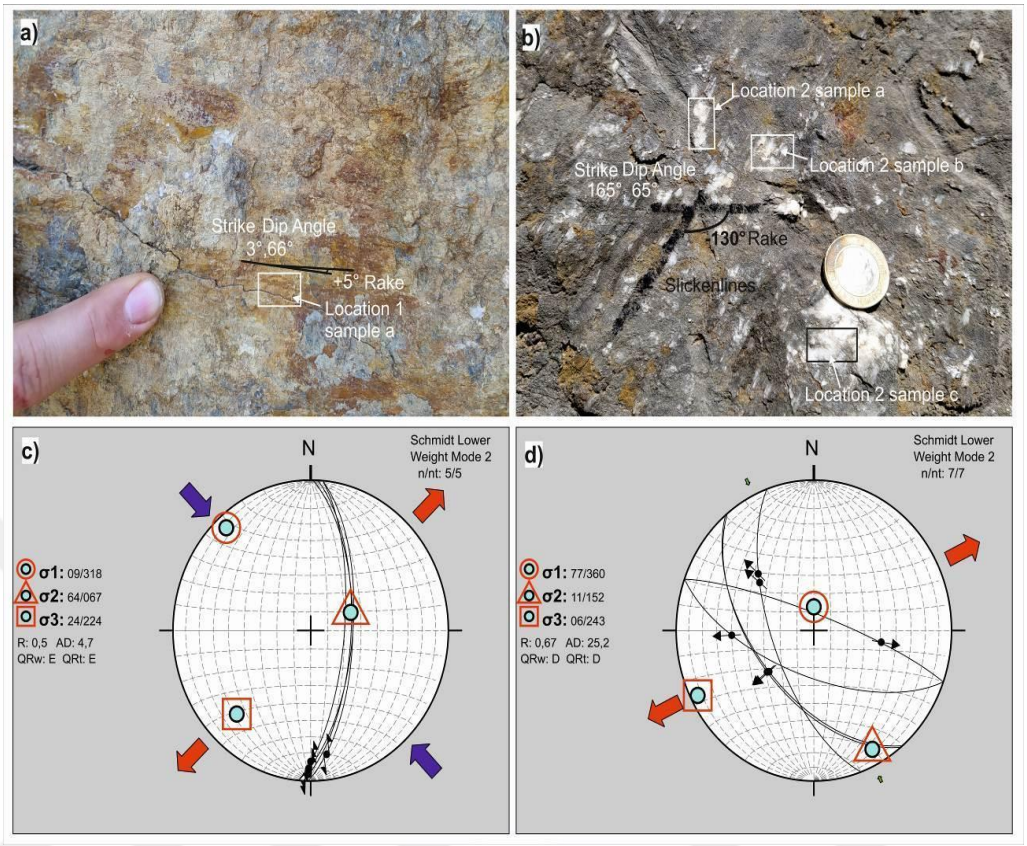

Figure 3.11: a) Sinistral strike-slip movement at Location 1. **b)** Sampled striated calcites at Location 2. Note that the slightly oblique downward movement of the hanging block denotes normal faulting. Strike, dip angle and rake values are given in the photos. Sampled calcite locations are given within boxes**. c-d)** Results of kinematic analysis at location 1 (c) and location 2 (d).

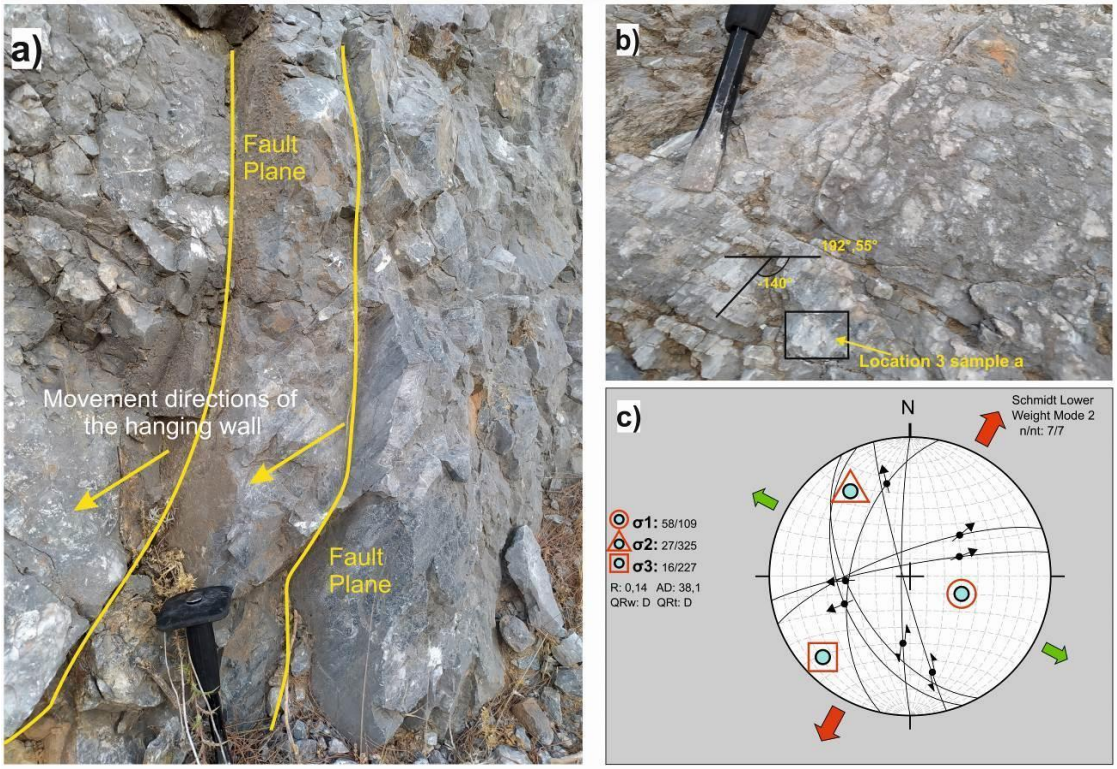

Figure 3.12: a) General view of series of normal fault planes at Location 3. **b)** Sampled calcite fibers on the fault scarp. **c)** Results of fault-slip analysis.

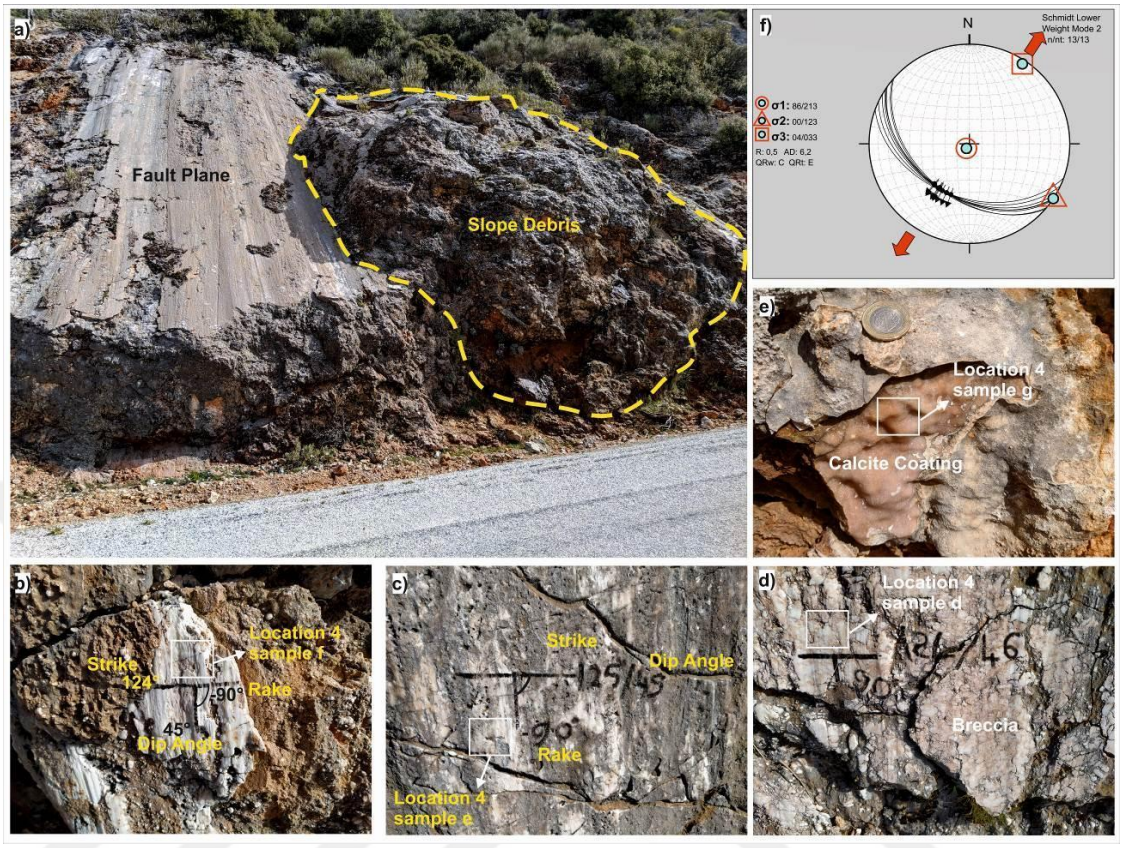

Figure 3.13: a) A big normal fault scarp at Location 4 with very characteristic cataclastic features. Note that a mass of slope debris amalgamated onto the fault plane. **b)** Slope debris was cut by the fault's activity. **c-d)** Very characteristic slickenlines, calcite fibers and fault breccia. **e)** Sampled calcite coating on the fault plane. **f)** Kinematic analysis results.

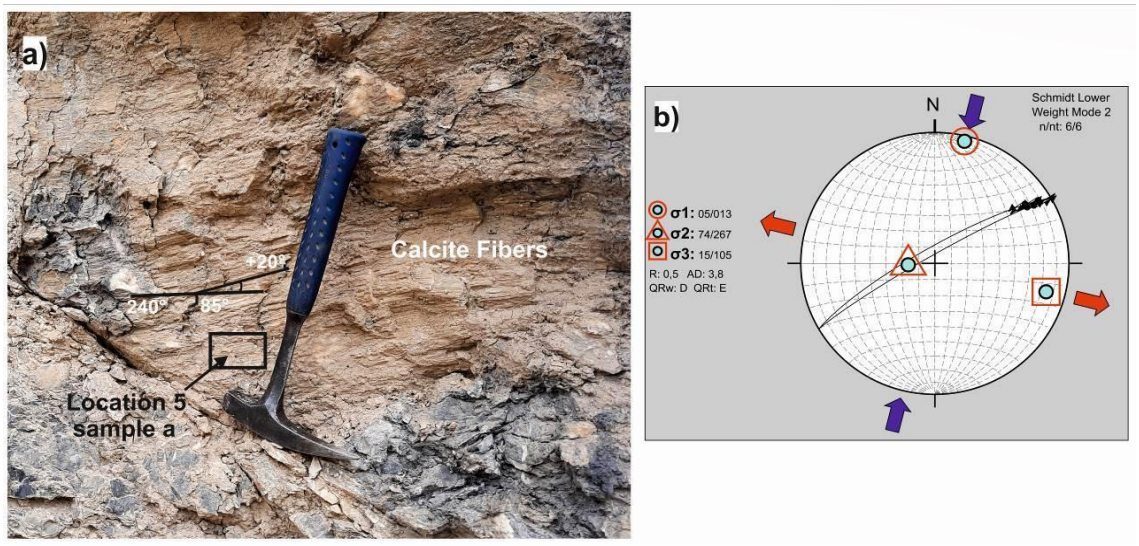

Figure 3.14: a) An example of a fault plane showing sinistral strike-slip movement at Location 5. **b)** The results of kinematic analysis.

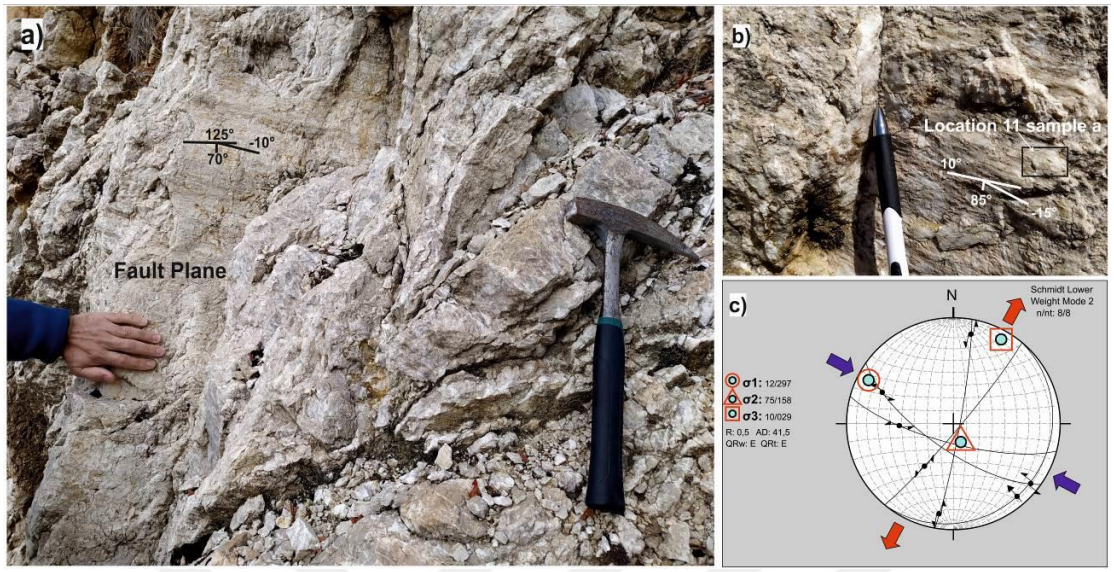

Figure 3.15: a) Sinistral secondary wrench zone at Location 11. **b)** Sampled calcite fiber with horizontal striae. **c)** The results of kinematic analysis.

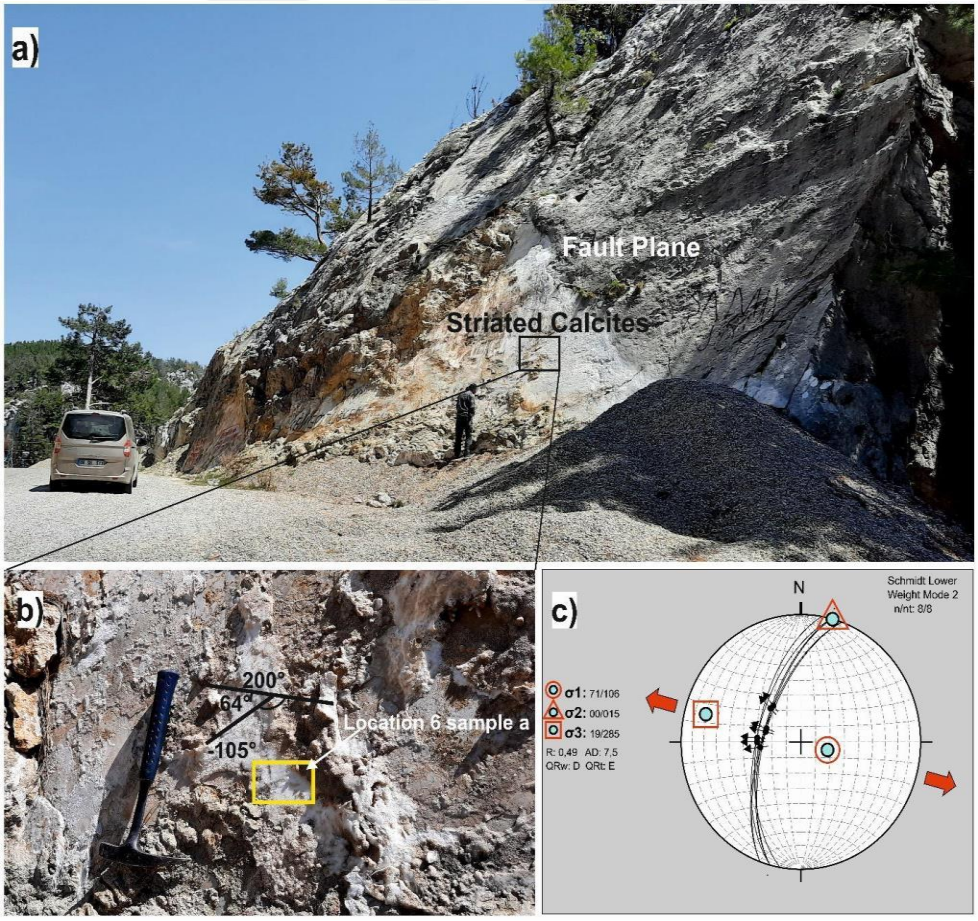

Figure 3.16: a) View of normal fault planes at Location 6. **b)** Sampled syn-tectonic striated calcites. **c)** The results of kinematic analysis.

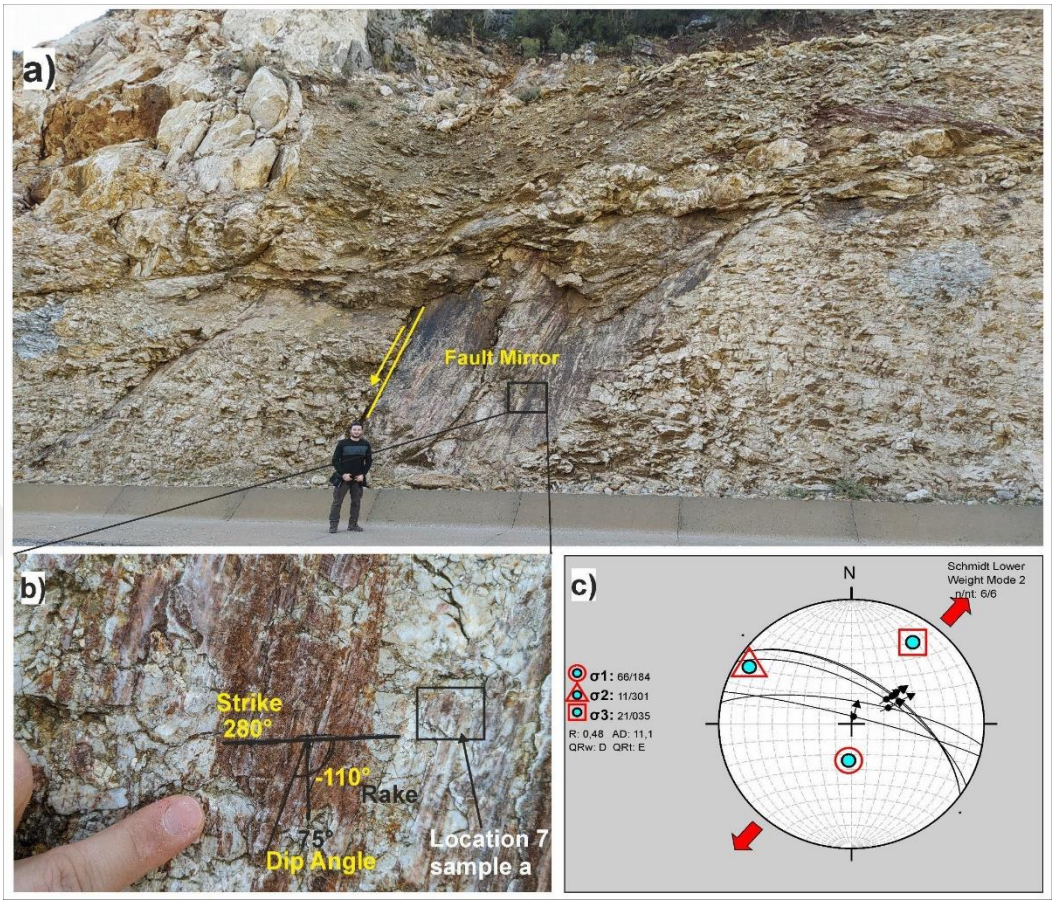

Figure 3.17: a) View of normal faults at Location 7. **b)** The fault plane with kinematic features. **c)** The results of kinematic analysis.

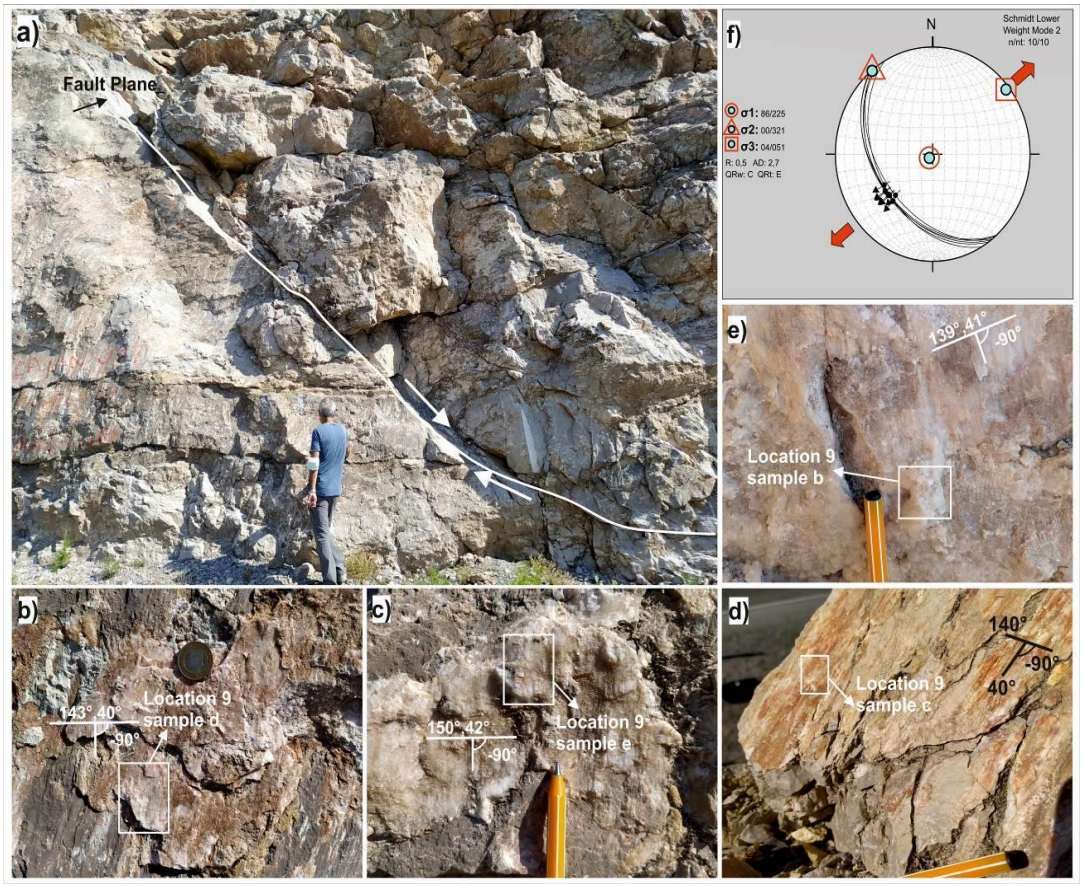

Figure 3.18: a) General view of Location 9. **b-c-d-e)** Fault planes and sampled calcite fibers for U-Th and U-Pb dating. **f)** The results of kinematic analysis.

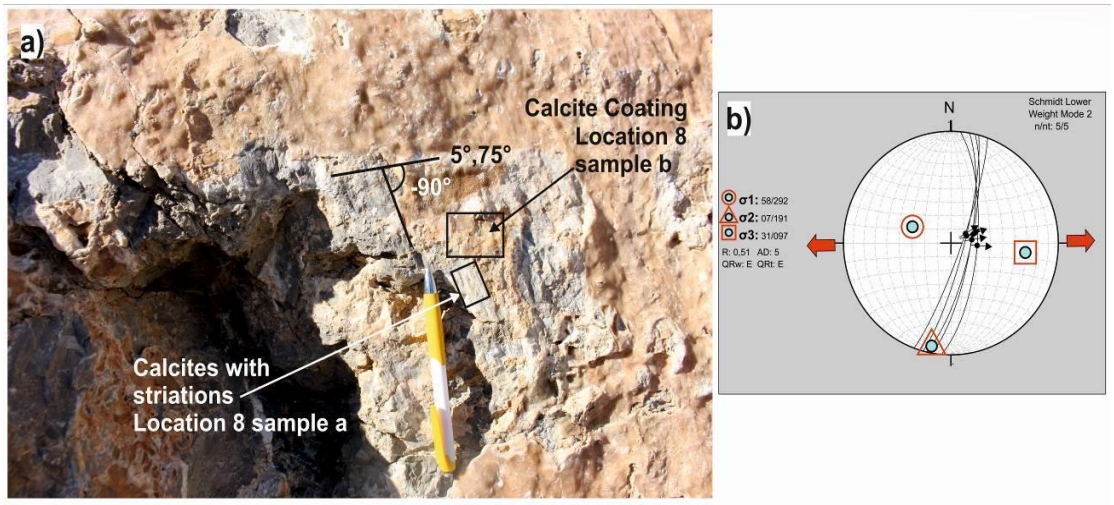

Figure 3.19: a) Striated calcites and calcite coatings presenting the youngest brittle deformation at Location 8. **b)** The results of kinematic analysis.

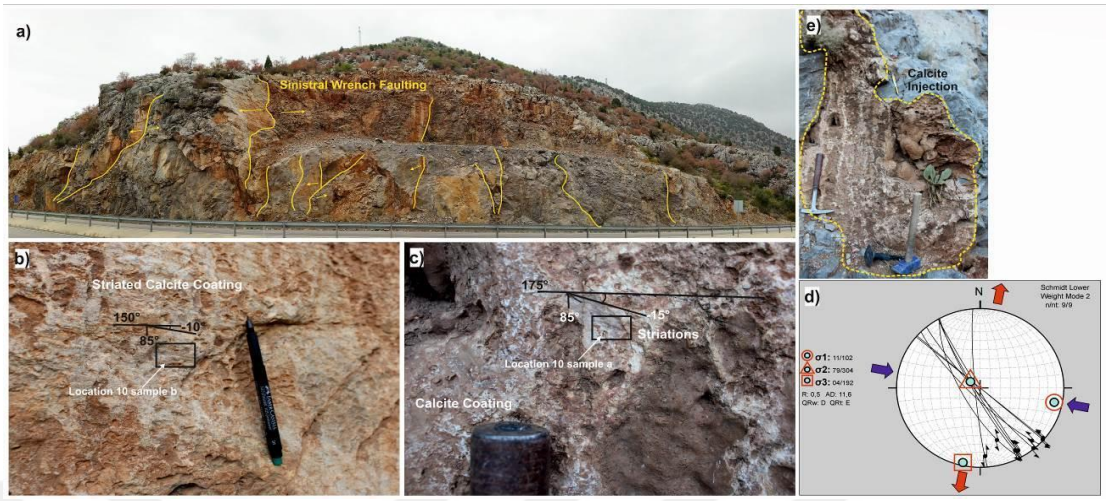

Figure 3.20: a) A shear zone consists of parallel sinistral strike-slip fault planes at Location 10. **b-c)** Calcite precipitates with horizontal striae. **d)** The results of kinematic analysis. **e)** Calcite injections and travertines along the fault planes.

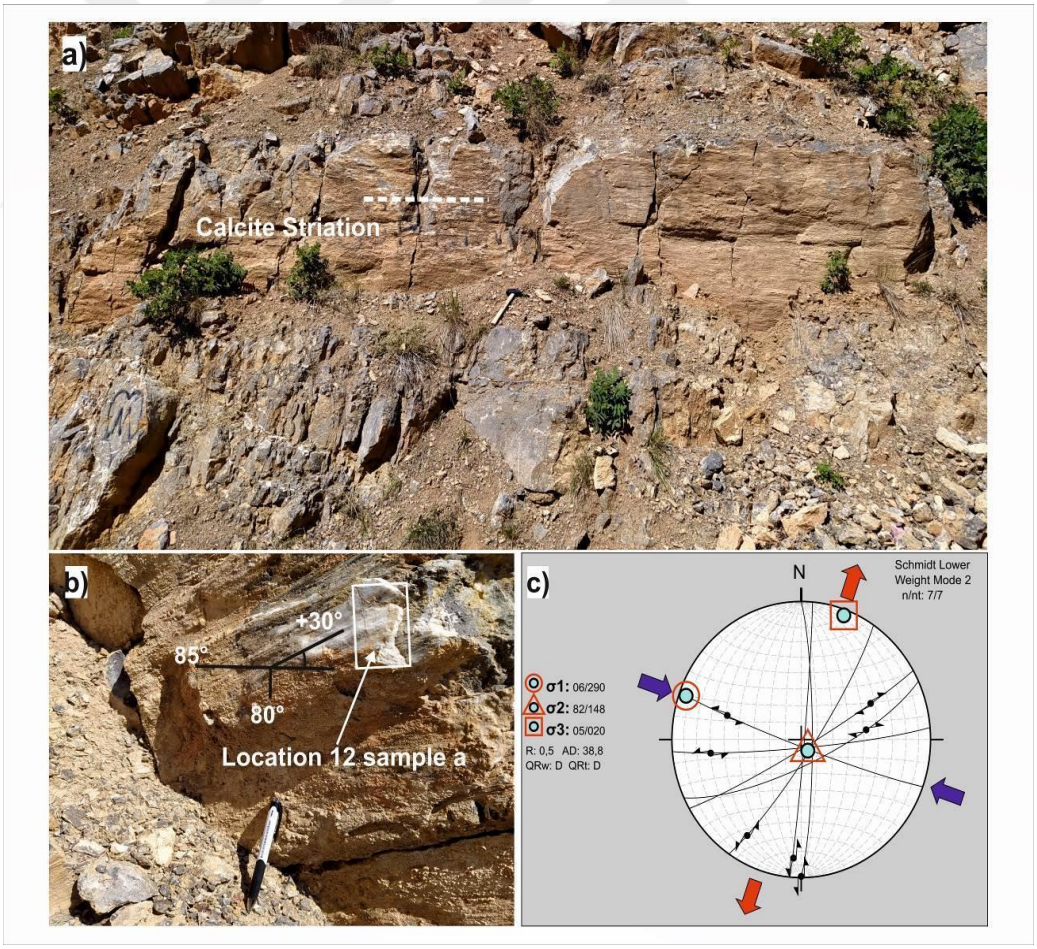

Figure 3.21: a) General view of strike-slip deformation zones at Location 12. **b)** Sampled calcite on the fault plane. **c)** The results of kinematic analysis.

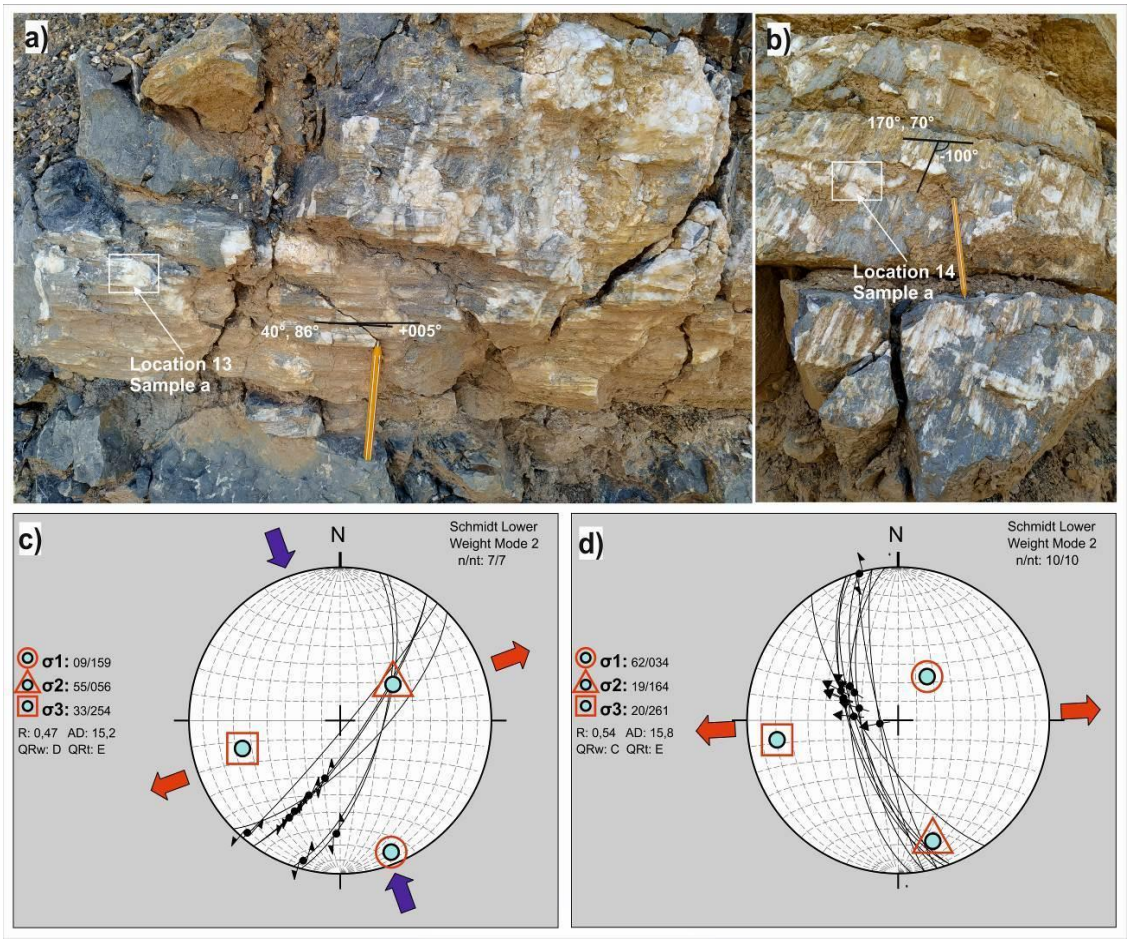

Figure 3.22: a) Left lateral movement and calcite fibers at Location 13. b.) Striated calcite fibers showing normal faulting at Location 14. **c)** The results of kinematic analysis at Location 13. **d)** The results of kinematic analysis at Location 14.

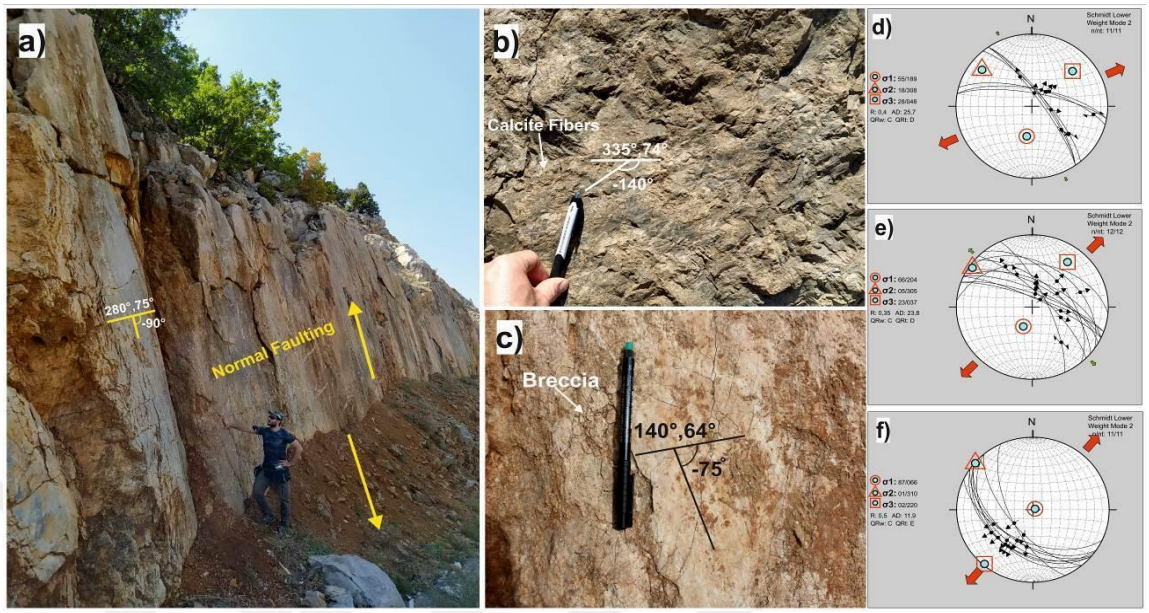

Figure 3.23: a) Dip-slip normal fault scarp and kinematic features at Location 18. **b)** Calcite fibers showing slightly oblique normal faulting at Location 15. **c.)** Kinematic measurements and fault striations at Location 20**. d-e-f)** The results of kinematic analysis at locations 18(d), 20(e) and 15(f) respectively.

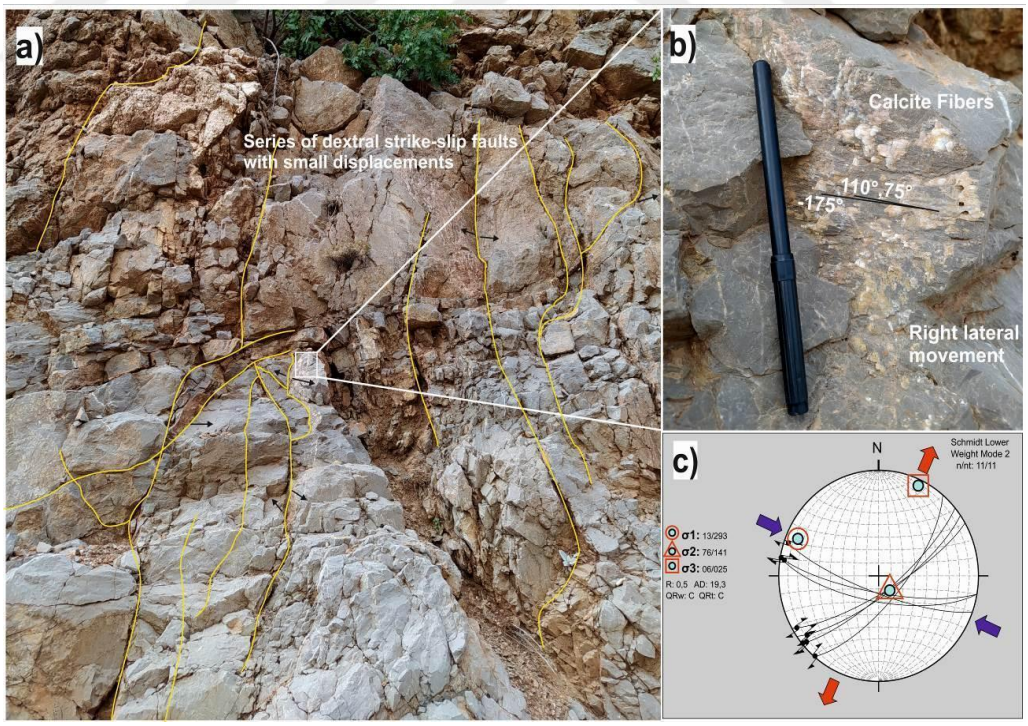

Figure 3.24: a) Secondary shear zone with series of dextral strike-slip movements at Location 17. **b)** Close-up view of calcite fibers on the fault plane showing the sense of motion between fault blocks. **d)** The results of kinematic analysis.

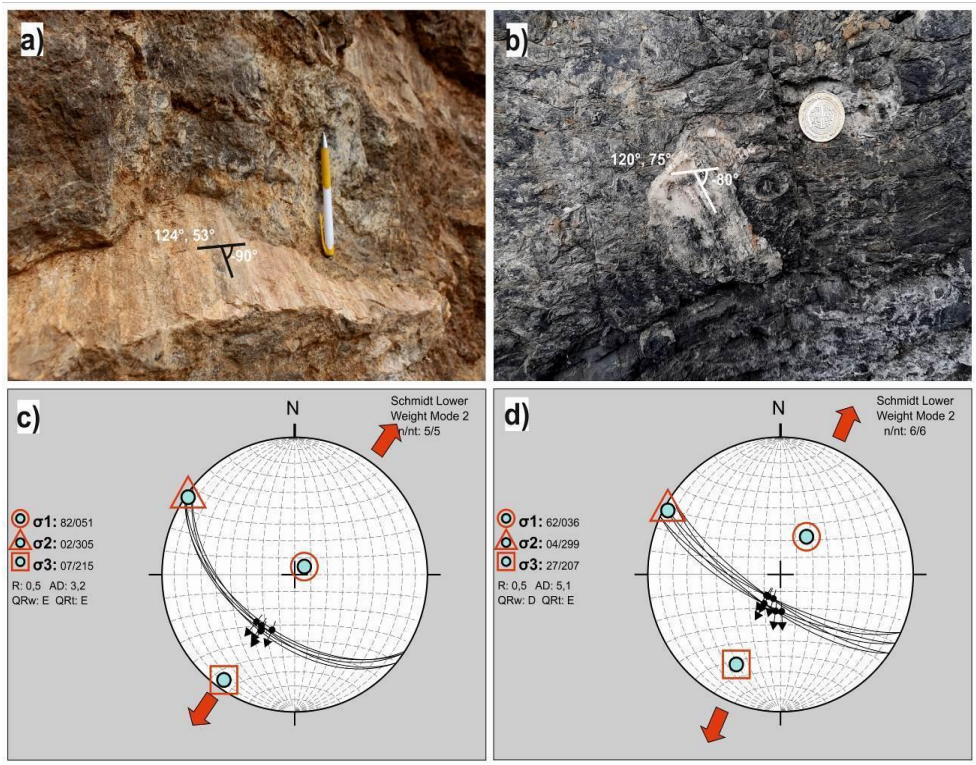

Figure 3.25: a-b). Fault planes and kinematic measurements at location 19 (a) and location 16 (b). **c-d).** The results of kinematic analysis at location 19 (c) and location 16 (d).

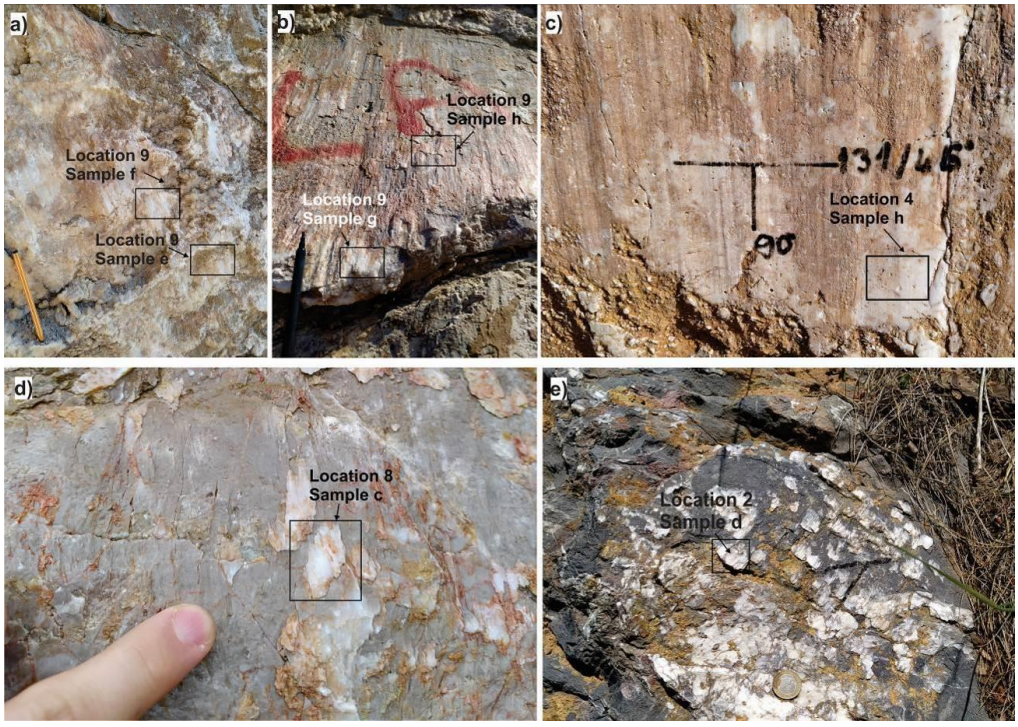

Figure 3.26: Additional syn-tectonic calcite samples on normal fault planes for U-Pb Dating. **a)-b)** Location 9, **c)** Location 4, **d)** Location 8, **e)** Location 2.

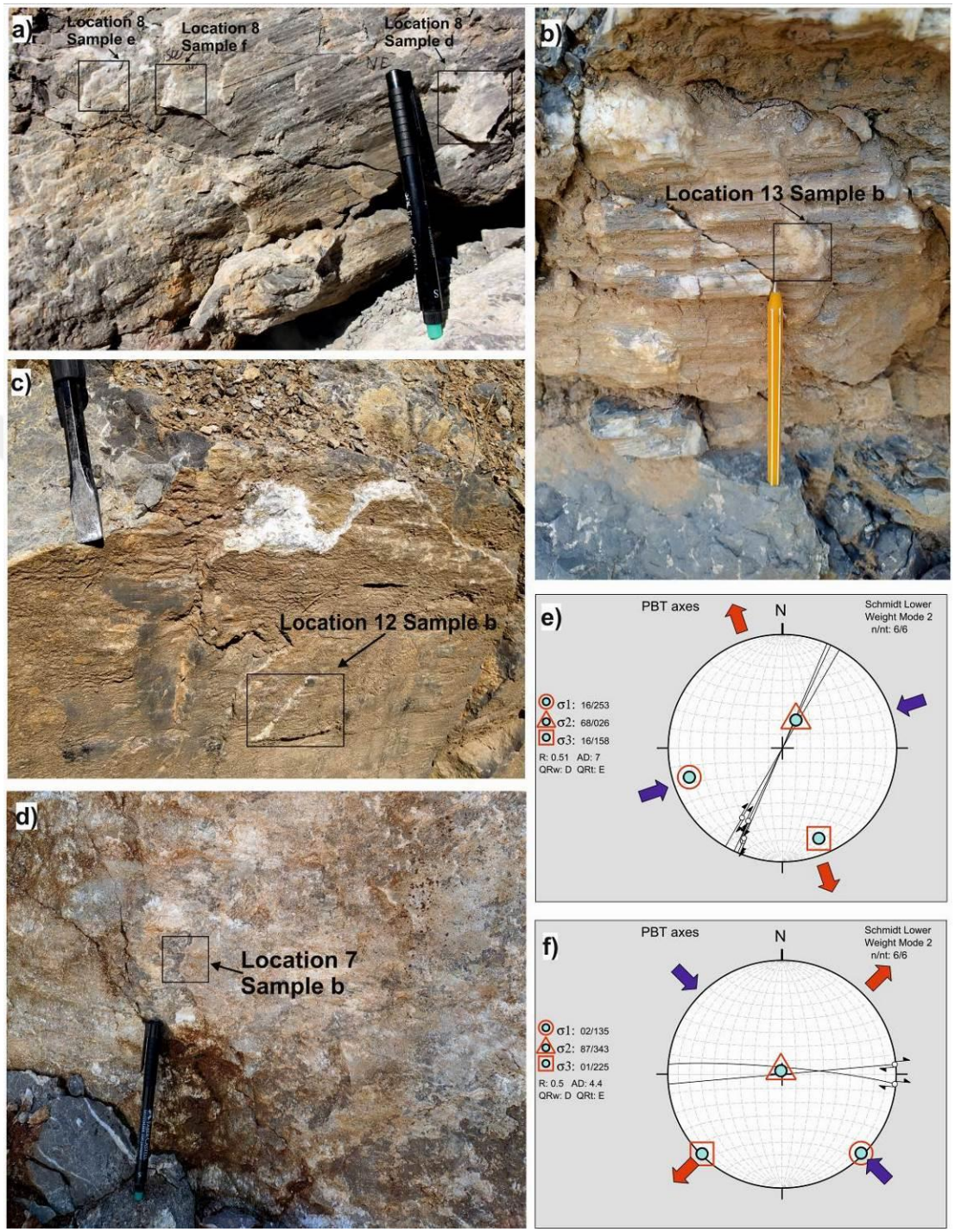

Figure 3.27: Additional syn-tectonic calcite samples on lateral fault planes for U-Pb Dating. **a)** Location 8, **b)** Location 13, **c)** Location 12, **d)** Location 7, **e)** Paleo-stress analysis results of strike-slip faulting at Location 8, **f)** Paleo-stress analysis results of strike-slip faulting at Location 7.

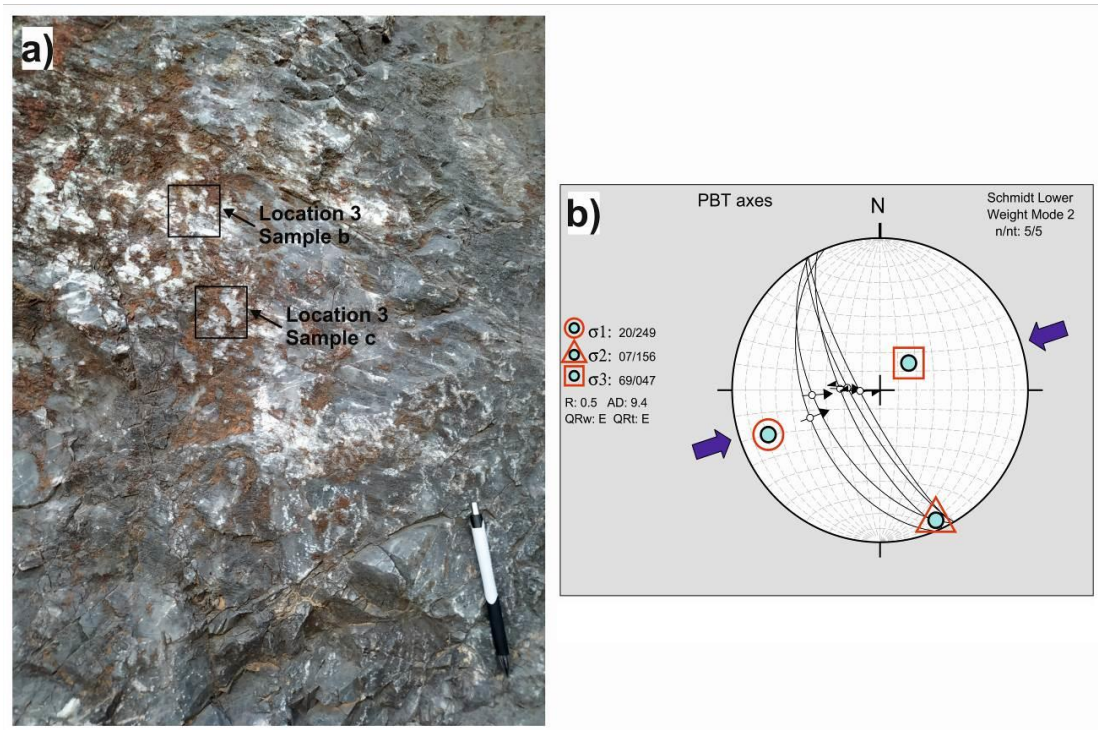

Figure 3.28: Additional syn-tectonic calcite samples on reverse fault planes for U-Pb Dating at Location 3. **a)** Syn-tectonics calcites on the fault plane **b)** Paleo-stress analysis results.

3.3 Microstructural Examinations

Thin-section microscopy and scanning electron microscope (SEM) analyses reveal that calcite micro-textures mainly have the appearance of blocky crystals. These coarse grained blocky calcites often show twinning (Figure 3.29-e,f,g,h,k) indicating significant faulting-related deformation (Burkhard, 1993; Karabacak et al., 2021). The analyzed samples contain randomly distributed calcite fragments, brecciated zones, calcite gouges, slickenlines, slickenfibres, fault grooves, microfractures and displaced dilation veins (Figure 3.29 a-o). Large and small calcite crystals in the micritic limestone matrix (fault gouge) are interpreted as brecciated zones (Figure 3.29-f,k,m,n). Partly, these gouges make sharp contacts with relatively homogenous crystalline zones (Figure 3.29 f,k,m). SEM analyses of fault-related calcites reveal marked slickensides, slickenfibers, pits and grooves (Figure 3.30). SEM images of samples from location 4-g (Figure 3.30-c) and 8-b (Figure 3.30-e) show distinct striations of calcite coatings on the fault planes, indicating syn-tectonic formation (cf., Oren et al., 2020; Karabacak et al., 2021 and references therein).

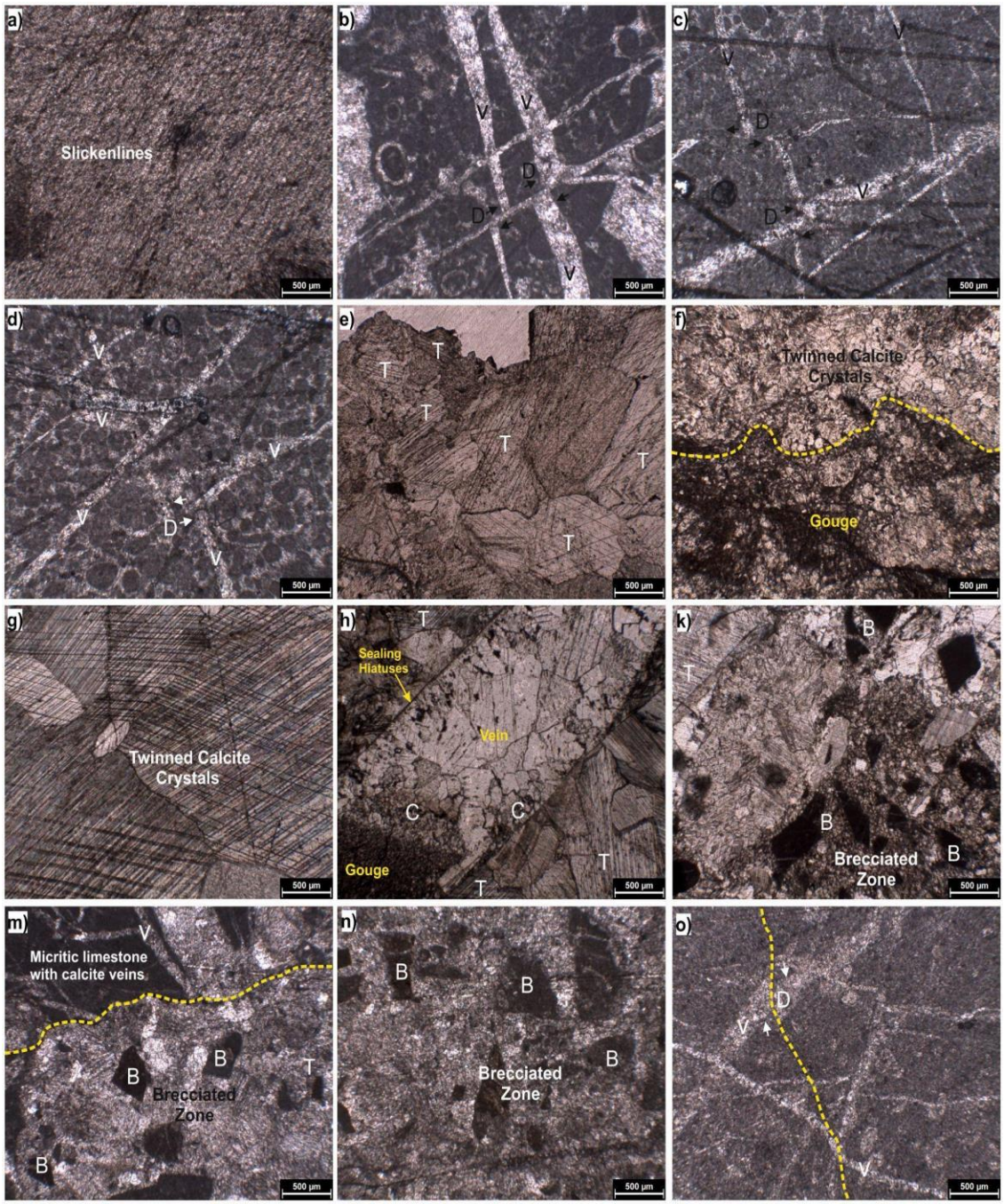

Figure 3.29: Optical microscope photomicrographs of fault-related calcite samples. **(a,b)** Location 8-sample b, **(c,d)** Location 8-sample a, **(e)** Location 9-sample d, **(f)** Location 4-sample d, **(g)** Location 12-sample a, **(h)** Location 13-sample a, **(k)** Location 12-sample a **(m, n)** Location 13-sample b **(o)** Location 7-sample a. B=Breccia, C=Cataclasis, D: Displacement, V= Vein and T= Twining.

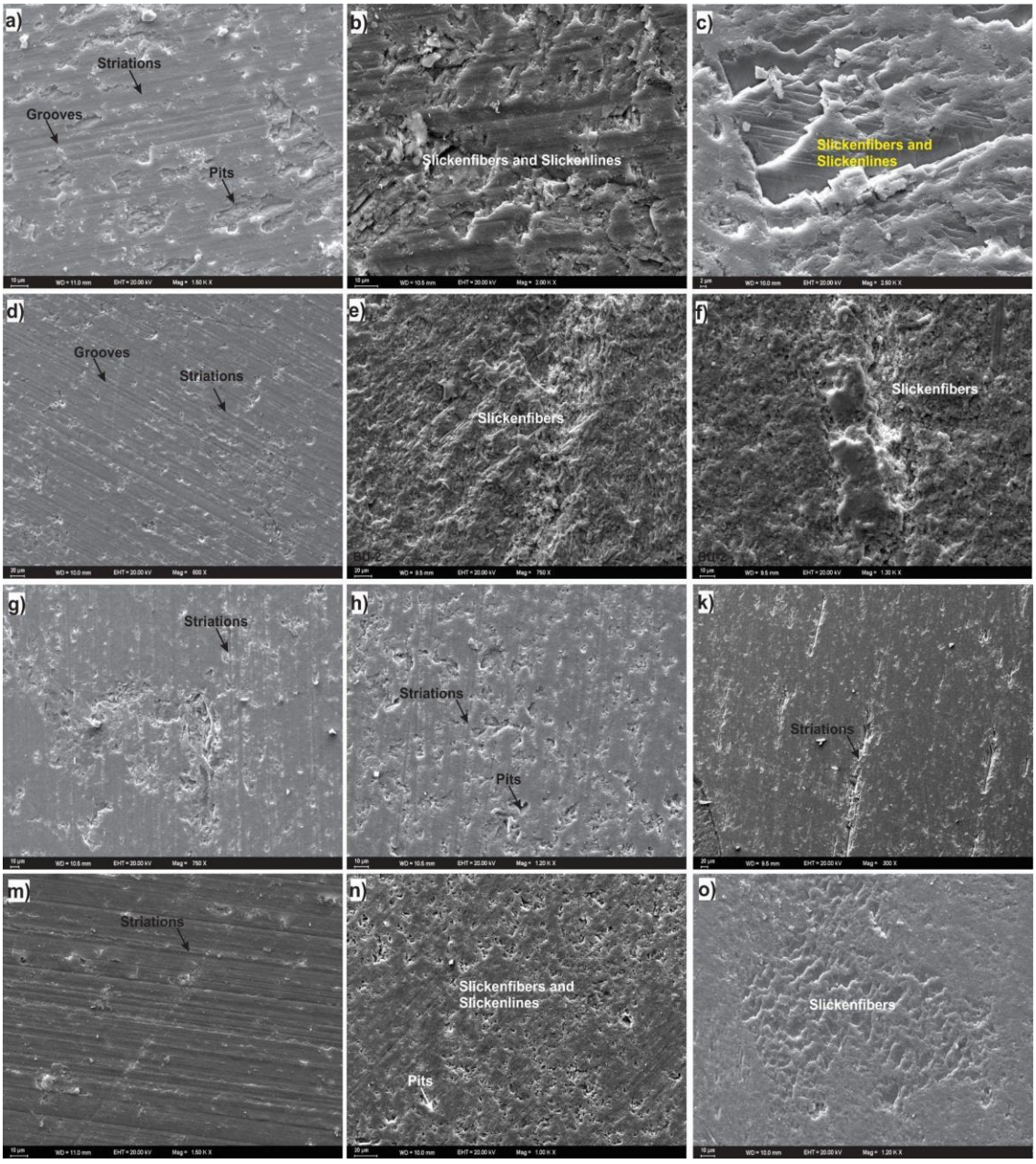

Figure 3.30: Scanning electron photomicrographs of fault-related calcite samples. **(a)** Location 4-sample c, **(b)** Location 4-sample d, **(c)** Location 4-sample g, **(d)** Location 4-sample d, **(e)** Location 8-sample b, **(f)** Location 8-sample a, **(g,h)** Location 9-sample d, **(k)** Location 12-sample a, **(m)** Location 7-sample a, **(n)** Location 8-sample e, **(o)** Location 8-sample f.

3.4 U-Th Geochronology

From Mediterranean shores to the CAP plateau interior, geochronology of the fault-related carbonates (calcite fibers, striated calcites and striated calcite coatings) yielded twenty-eight U-Th ages ranging between 714±285 ka and 18,76±0,53 ka (Table 3.3, Figure 4.1).

Syn-tectonic slickenfibres and striated calcites indicated normal faulting events at; 618±112 ka, 601±91 ka, 575±91 ka, 543±234 ka, 526±183 ka, 525±21 ka, 474±46 ka, 464±34 ka, 449±25 ka, 445±28 ka, 420±22 ka, 371±10 ka, 189±2 ka, 121±5 ka; and strike-slip movements at 714±285 ka, 690±196 ka, 423±85 ka, 246±+64 ka and 243±14 ka. Seven samples gave secular equilibrium ages (<500 ka). Striated carbonate coatings sampled on the normal fault planes gave 142±3 ka and 18,76±0,53 ka ages. Striations on carbonate coatings imply that brittle deformation might continued after 18,76±0,53 ka. The upper limits of the U-Th secular equilibrium ages are not defined but they show that both strike-slip and normal faulting also were active before the Middle Pleistocene. Our U-Th carbonate geochronology results show continuous normal faulting and strike-slip faulting events throughout the Middle-Late Pleistocene up to the Holocene. The graphical distribution of the U-Th ages present noticeable clusters at 450 ka, and 100-250 ka periods (Figure 4.1, 4.2).

Table 3.3: Summary of MC-ICP-MS U-Th age data. Please note that the sample numbers present the locations given in Figure 3.10.

Sample	U (ppm)	±2σ	^{232}Th (ppb)	±2σ	^{230}Th/^{232}Th	±2σ	^{230}Th/^{238}U	±2σ	^{234}U/^{238}U	±2σ	Uncorrected ^{230}Th Age (ka)	±2σ	Corrected ^{230}Th Age (ka)	±2σ
1a	0,0039	0,0000	0,418	0,003	29,80	0,41	1,0475	0,0151	1,0501	0,0076	426	85	423	85
2a	0,0901	0,0000	9,310	0,020	34,60	0,12	1,1782	0,0034	1,1236	0,0020	>500 secular equilibrium			
2b	2,5875	0,0067	6,850	0,102	1156,35	24,50	1,0089	0,0154	1,0113	0,0012	543	234	543	234
2c	0,5752	0,0005	4,063	0,021	437,15	2,90	1,0178	0,0044	1,0233	0,0014	464	34	464	34
3a	0,1792	0,0002	6,093	0,013	90,06	0,29	1,0089	0,0026	1,0087	0,0018	619	112	618	112
4a	0,3000	0,0002	2,546	0,006	373,79	1,28	1,0453	0,0028	1,0307	0,0018	>500 secular equilibrium			
4b	0,1801	0,0001	1,657	0,002	347,42	0,77	1,0538	0,0019	1,0258	0,0008	>500 secular equilibrium			
4c	0,2214	0,0001	1,250	0,003	558,51	2,25	1,0396	0,0035	1,0411	0,0018	449	25	449	25
4d	0,1666	0,0001	44,052	0,122	11,95	0,04	1,0410	0,0026	1,0417	0,0020	452	22	445	28
4e	0,3994	0,0002	1,216	0,004	900,86	4,16	0,9039	0,0032	1,0803	0,0014	189	2	189	2
4f	0,1743	0,0001	65,165	0,195	6,23	0,04	0,7680	0,0037	1,0815	0,0023	132	1	121	5
4g	0,1203	0,0000	4,027	0,005	14,66	0,09	0,1618	0,0009	0,9758	0,0009	19,79	0,13	18,76	0,53
5a	0,0291	0,0000	20,409	0,019	8,10	0,02	1,8702	0,0051	1,8362	0,0019	254	2	246	64
6a	14,4107	0,0233	4,29	0,044	12622,13	152,01	1,2397	0,0080	1,1740	0,0011	575	91	575	91
7a	0,5320	0,0004	92,730	0,341	17,73	0,09	1,0185	0,0034	1,0102	0,0011	>500 secular equilibrium			
8a	0,0950	0,0001	54,237	0,066	5,97	0,02	1,1244	0,0033	1,0942	0,0013	539	40	526	183
8b	0,0841	0,0001	19,935	0,055	13,98	0,06	1,0929	0,0041	1,4036	0,0025	147	1	142	3

9a	0,0518	0,0001	4,595	0,005	35,41	0,09	1,0350	0,0026	1,0276	0,0019	603	90	601	91
9b	0,1903	0,0001	13,268	0,012	46,32	0,07	1,0643	0,0014	1,0518	0,0006	527	19	525	21
9c	0,5956	0,0005	29,217	0,157	65,09	0,51	1,0523	0,0060	1,0474	0,0015	475	46	474	46
9d	0,1116	0,0001	19,010	0,048	18,92	0,07	1,0622	0,0032	1,0614	0,0021	424	19	420	22
9e	0,0655	0,0000	9,169	0,013	22,86	0,06	1,0540	0,0026	1,0657	0,0013	375	9	371	10
10a	0,1174	0,0002	194,021	0,604	2,17	0,01	1,1831	0,0038	1,0965	0,0024	>500 secular equilibrium			
10b	0,1031	0,0000	96,064	0,260	3,09	0,01	0,9472	0,0034	1,0241	0,0016	273	5	243	14
11a	0,0205	0,0001	48,219	0,105	1,42	0,01	1,0953	0,0101	1,0643	0,0027	>500 secular equilibrium			
12a	0,1547	0,0001	3,913	0,012	120,67	0,53	1,0057	0,0033	1,0050	0,0015	714	284	714	285
13	0,2072	0,0002	3,911	0,011	162,21	0,61	1,0092	0,0028	1,0077	0,0013	691	196	690	196
14	0,2487	0,0001	58,625	0,186	14,02	0,07	1,0896	0,0045	1,0565	0,0020	>500 secular equilibrium			

3.5 U-Pb Geochronology

For U-Pb carbonate geochronology, we analyzed a total of twenty-one syn-tectonic calcite samples. Priority was given to the six samples that yielded secular equilibrium U-Th ages (>500 ka) (Location 4 sample a, location 4 sample b, location 14 sample a, location 7 sample a, location 11 sample a and location 2 sample a) (Table 3.3). Additionally, we collected fifteen more calcite samples from fault planes exhibiting different kinematic features (reverse, strike-slip, and normal faulting) that we believe are older than 500 ka, aiming to constrain the long-term evolution of brittle deformation. According to the results; a total of 11 ages represent normal faulting events at 0.07±0.54 Ma, 0.20±1.5 Ma, 4±5.7 Ma, 5.75±0.22 Ma, 7.98±0.27 Ma, 8±11 Ma, 9.66±0.56 Ma, 16±2.3 Ma, 17±19 Ma, 25±20 Ma and 33.7±9.8 Ma (Figure 3.31). A total of 8 ages represent strike-slip faulting events at 22.74±0.90 Ma, 24.88±0.76 Ma, 27.7±6.6 Ma, 27.9±1.7 Ma, 30.7±3.0 Ma, 34.91±0.78 Ma, 37.5±1.7 Ma and 38.6±1.9 Ma (Figure 3.32). A total of 2 U-Pb ages represent reverse-thrust faulting events at 72.1±3.2 Ma and 74.6±3.9 Ma (Figure 3.32).

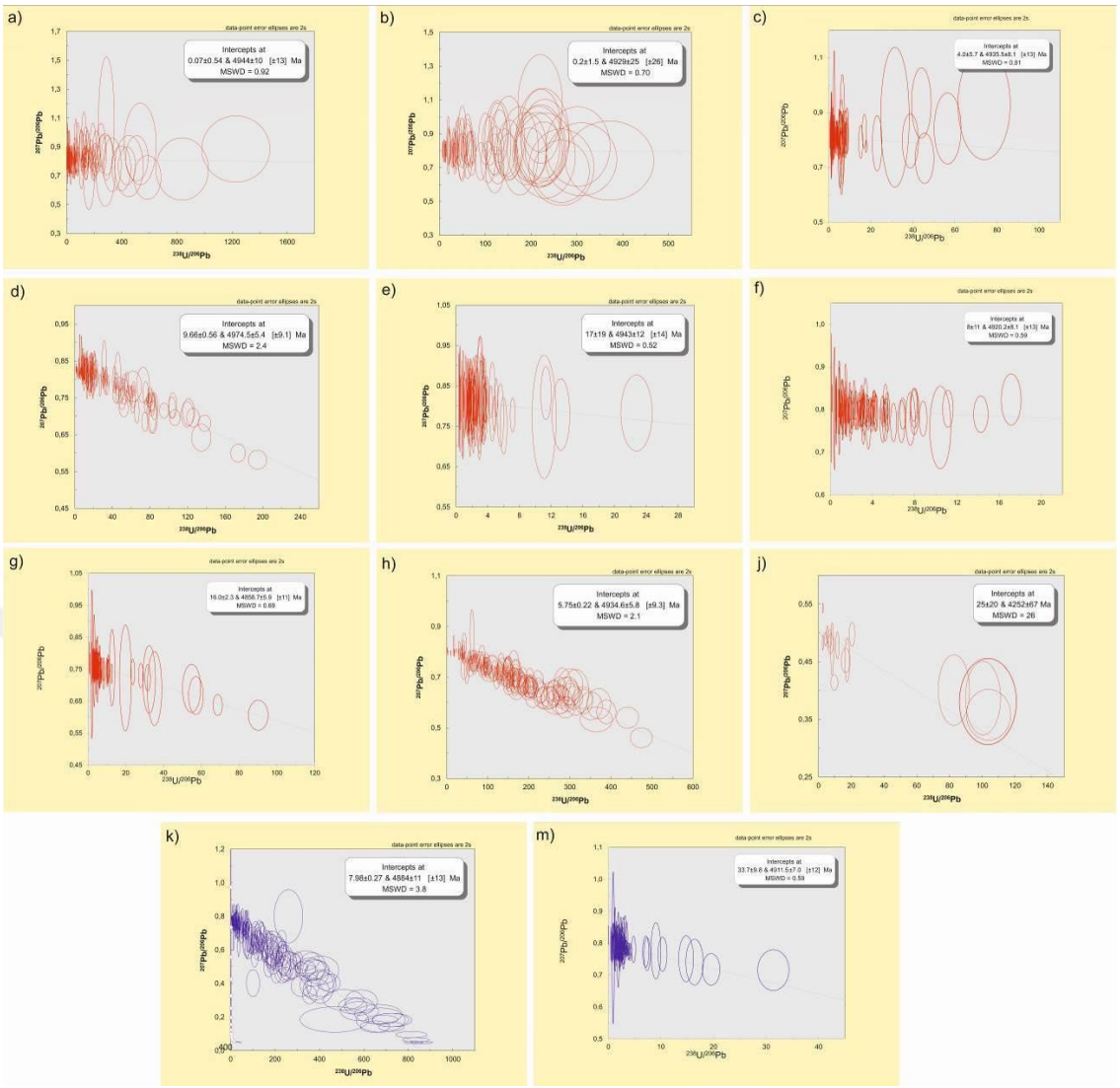

Figure 3.31: Tera-Wasserburg concordia plots showing $^{238}U/^{206}Pb$ versus $^{207}Pb/^{206}Pb$ data of syn-tectonic calcites sampled along normal faults. MSWD: mean squared weighted deviates. **a)** Location 4 Sample a, **b)** Location 4 Sample b, **c)** Location 4 Sample h, **d)** Location 7 Sample a, **e)** Location 8 Sample c, **f)** Location 9 Sample h, **g)** Location 9 Sample f, **h)** Location 2 Sample a, **j)** Location 9 Sample e, **k)** Location 2 Sample d, **m)** Location 9 Sample g.

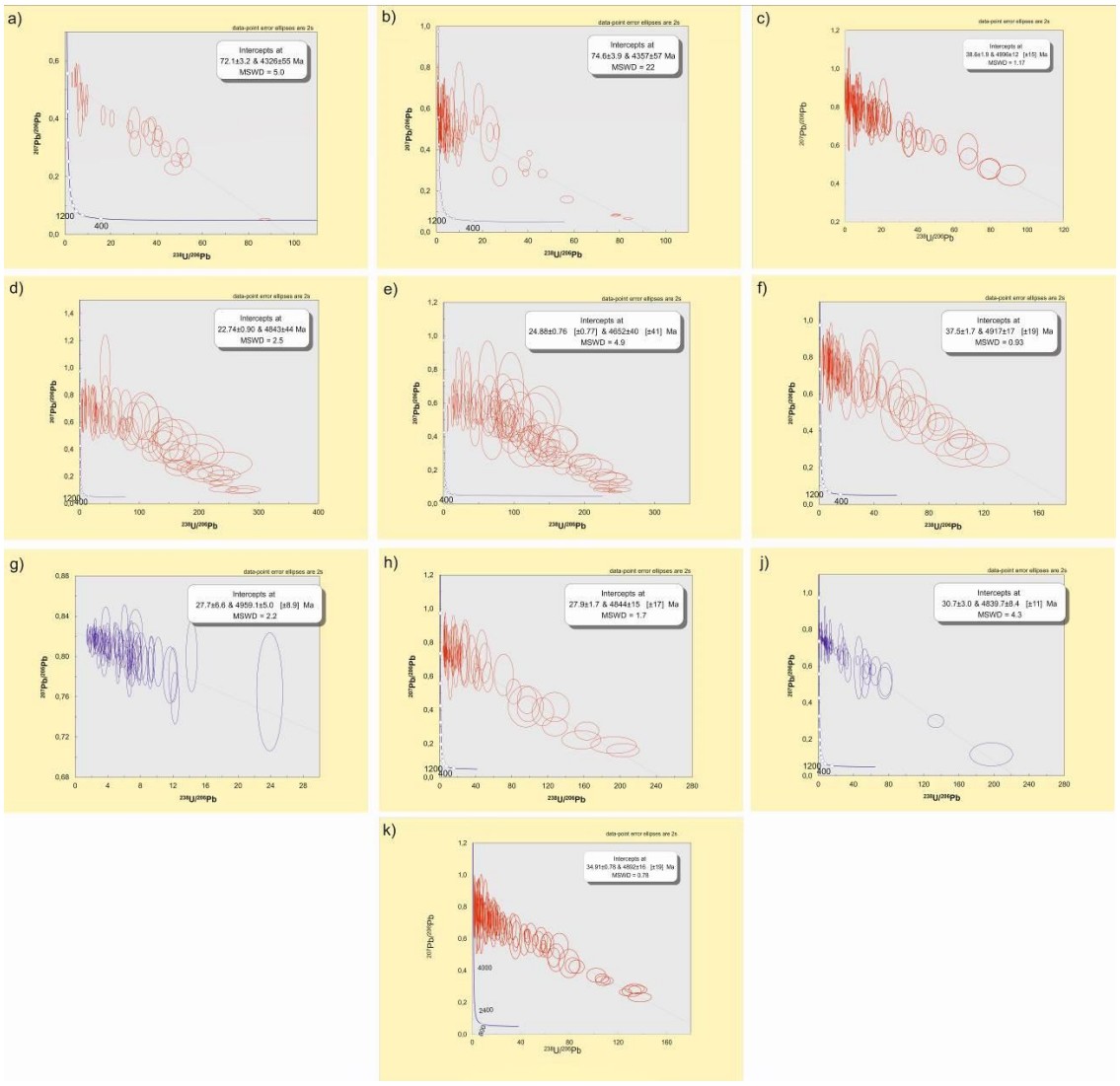

Figure 3.32: Tera-Wasserburg concordia plots showing $^{238}U/^{206}Pb$ versus $^{207}Pb/^{206}Pb$ data of syn-tectonic calcites sampled along reverse and strike-slip faults. MSWD: mean squared weighted deviates. **a)** Location 3 Sample c, **b)** Location 3 Sample b, **c)** Location 8 Sample f, **d)** Location 14 Sample a, **e)** Location 13 Sample b, **f)** Location 8 Sample e, **g)** Location 7 Sample b, **h)** Location 12 Sample b, **j)** Location 11 Sample a, **k)** Location 8 Sample d.

4. DISCUSSION

4.1. Coeval Upper Crustal Extension and Surface Uplift in the Last 500 ka

The studies show that the stress states and spatial distribution of the crustal deformation are diverse across the undergoing African Plate, subduction interface and overriding Anatolian Plate across the Eastern Mediterranean. The undergoing African Plate and subduction interface mostly deforming by aseismic processes, and the deep-rooted reverse and strike-slip earthquake focal mechanisms indicate that the infrequent brittle deformation is mostly contractional (Robertson, 1998; Wdowinski et al., 2006; Howell et al., 2017).

Contrary to ongoing contraction along the Cyprus Trench, our results show that the extensional tectonic deformation prevails on the overriding Anatolian Plate. Our combined kinematic and U-Th age results, earthquake focal mechanism solutions (Figure 4.1) and GPS-derived strain-rate fields (Howell et al., 2017) indicate active NE-SW directed horizontal extension accommodated by NW-SE striking normal fault zones between Seydişehir and Gazipaşa. Continuous U-Th ages from multiple generations of fault-related calcites range from >500 ka to 18.76±0.53 ka, providing evidence of normal faulting from the Middle/Late Pleistocene to the present. The brittle deformation ages clustering at 450 ka may indicate that an important geodynamic event caused an acceleration of extensional surface deformation in the Middle Pleistocene. This cluster (Figure 4.2) coincides with the starting point of a rapid (3.21-3.42 mm/yr) surface uplift phase that caused an uplift of 1.5 km in the last 450 ka (Öğretmen et al., 2018). The bedrock river inversions reported by Racano et al. (2021) also show peak values for rock uplift at 150-250 ka and 400-450 ka, reaching rates of 5.1 mm/yr. Studies on the modelling of marine terraces (Racano et al., 2020) revealed uplift rates ranging between 1.1 and 3.8 mm/yr with decreasing rate patterns from the Late Quaternary (500 ka) to the present. The second significant U-Th age cluster at 100-250 ka (Figure 4.2) also overlaps with high uplift rates derived from marine terrace elevations and bedrock river inversions. Thus, the data from

geomorphic markers, biostratigraphic indicators and our U-Th geochronology results show that extensional deformation was coeval with vertical deformation (surface uplift) over the last 450 ka (Figures 4.2, 4.3, 4.4).

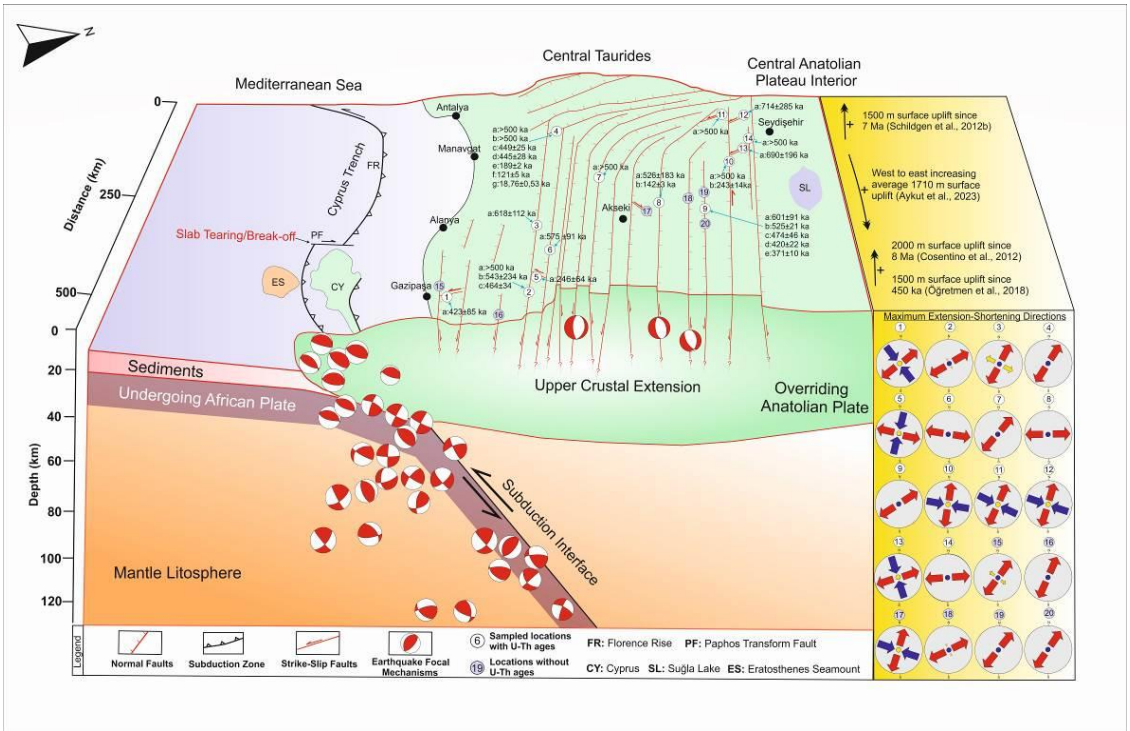

Figure 4.1: Illustrative representation of Cyprus Subduction Zone and Central Taurides. Sampled locations and U-Th ages are given in the figure. Maximum Extension (red arrows) and shortening (blue arrows) directions are given in the lower right corner. Earthquake focal mechanisms are from Boğaziçi University Kandilli Observatory and Earthquake Research Institute (http://www.koeri.boun.edu.tr/sismo/2/moment-tensor-solutions/), Disaster Emergency Management of Türkiye (AFAD) and (https://deprem.afad.gov.tr/faycozumleri?lang=en), Wdowinski et al., (2006); Imprescia et al., (2012); Howell et al., (2017) and Güvercin et al., (2021). Crustal thicknesses are derived from Tezel et al., (2013). Please note that the fault network is generalized.

Previously, various geodynamic concepts have been invoked to explain the active deformation at the southern margin, such as lower crustal flow (Fernandez-Blanco et al., 2020), slab roll-back (Koç et al., 2016, 2017) and slab deformation and asthenospheric upwelling (Schildgen et al., 2012a, 2012b, 2014; Cosentino et al., 2012; Öğretmen et al., 2018; Racano et al., 2020, 2021). Some studies have also proposed lithospheric delamination to explain the uplift of the Central and Eastern Anatolian Plateaus, partly including the Central Taurides (Bartol and Govers, 2014; Meijers et al., 2018). Our kinematic observations in the upper crust show a lack of active thrust/reverse faulting (i.e. shortening), which is remarkable despite the rapid surface uplift (Öğretmen et al., 2018), Quaternary rock uplift (Kelletat and Kayan, 1983; Racano et al., 2020, 2021; Liberatore et al., 2022) and dynamic-transient

topography (Monod et al., 2006; Schildgen et al., 2012a; Aykut et al., 2023). Our quantification of the timing of extensional surface deformation which provides evidence for contemporaneous surface uplift and normal faulting in the last 450 ka, favors mantle-driven control over upper crustal deformation. Considering the observations from P wave tomography data showing a distinct slab gap and slow velocity anomalies detected beneath southern Türkiye (Faccenna et al., 2006; Biryol et al., 2011; Mutlu & Karabulut, 2011; Portner et al., 2018), alongside evidence of various extension directions in Southern Türkiye (N-S, E-W, NE-SW, NW-SE) (Glover and Robertson 1998a, 1998b; Schildgen et al., 2012b, Howell et al., 2017, Aykut et al., 2023); it is becoming increasingly plausible that slab deformation and subsequent asthenospheric upwelling are key processes contributing to the ongoing deformation observed in the Central Taurides (Figure 4.4). Other mechanisms, such as slab roll-back, thermal or viscous crust deformation, or continental underthrusting, do not appear to explain the rapid surface uplift and concurrent extension witnessed over a relatively brief time (<500 ka) in the upper crust.

The majority of the presented U-Th ages are younger than the formation of the Paphos Transform Fault, which is proposed to have formed as a result of the underthrusting of the Eratosthenes Seamount ~2 Ma ago (Robertson, 1998; Schattner, 2010; Kinnaird and Robertson, 2013). We envisage that the underthrusting of the isolated seamount slowed down the subduction beneath the central part of the Cyprus Subduction Zone, leading to differential underthrusting that was accommodated by the formation of the Paphos Transform Fault. The Paphos Fault subsequently caused a tear in the slab (Mutlu and Karabulut, 2011; Biryol et al., 2011; Portner et al., 2018) (Figure 4.4). Mantle flow through the tear might have controlled the surface uplift after 1.6 Ma in the Central Taurides (Schildgen et al., 2012a, 2014). Ages of ≤450 ka for upper crustal extension, together with accelerating surface uplift rates (Öğretmen et al., 2018) and rock uplift rates (Racano et al., 2021) (Figure 4.1, 4.4) may indicate that the most pronounced phase of surface uplift and the widespread upper-crustal extension lagged behind initial slab deformation by ~1 Ma. Peaking surface deformation in the Middle Pleistocene may also indicate that the slab broke off at circa 450 ka (or shortly before), after the initial tearing event in the Early Pleistocene (Figure 4.4). This conclusion is consistent with observations from laboratory experiments and numerical models, which predict that mantle upwelling through slab gaps after slab break-off can lead to

rapid uplift in time windows as short as 100 ka and to extension in the overriding plates (van Hunen and Allen, 2011; Duretz and Gerya, 2013; Kiraly et al., 2020). However, to substantiate this interpretation, additional geophysical data and further geochronological constraints are essential to improve our understanding of the magnitude of the impact of geodynamic drivers on the contemporaneous Late Quaternary surface uplift and normal faulting above the Cyprus Trench.

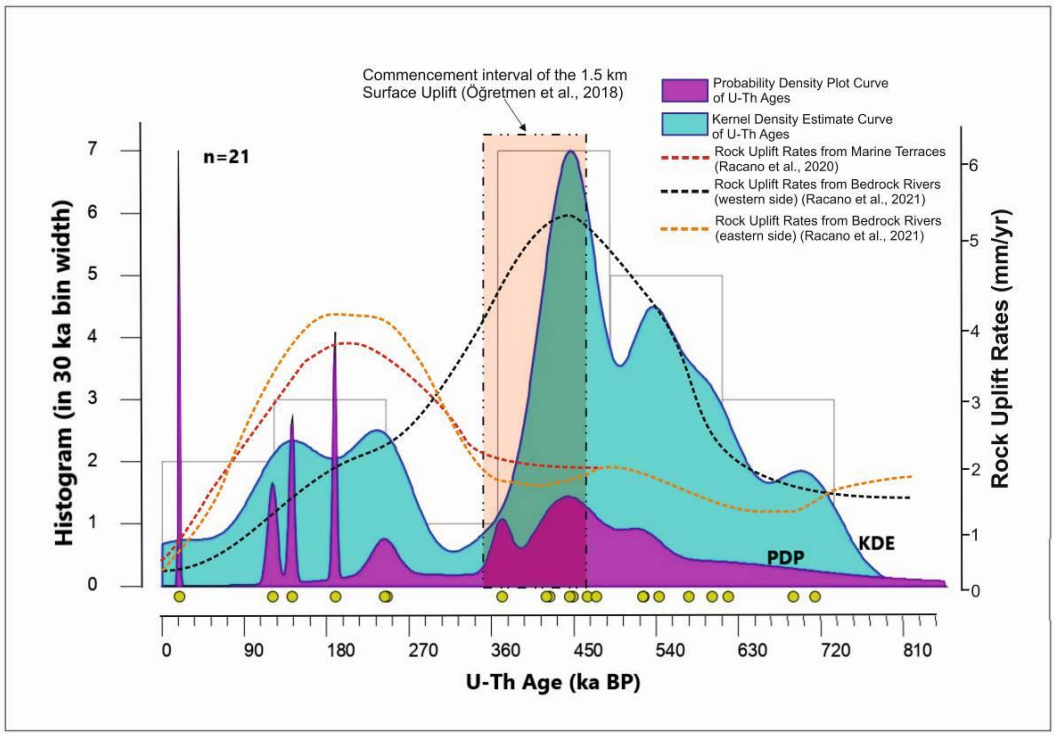

Figure 4.2: Graphical distribution of U-Th ages (DensityPlotter 8.5; Vermeesch, 2012), together with the temporal variations in surface and rock uplift values. PDP: Probability Density Plot Curve; KDE: Kernel Density Estimate Curve. Rectangles are sample histograms. Yellow circles present the U-Th ages of the samples. Secular equilibrium U-Th ages (>500 ka) are excluded.

The Central Taurides represents a distinct geological and physiographical province within Anatolia, characterized by unique geomorphological features (e.g. tectono-karstic depressions) in a high-relief topography. The neotectonic provinces of Anatolia traditionally include regions such as the East Anatolian Contractional Province, Central Anatolian Ova Province, West Anatolian Extensional Province, and North Turkish Province (Şengör et al., 1985). These provinces are defined based on their tectonic settings, deformation modes, and geological characteristics. However, the Taurides, the biggest mountain range in Türkiye, has not been included (except for the eastern Taurides) in this tectonic zonation because of lack of sufficient data to quantify the neotectonic activity of the faults within the mountain range. Our data do not cover

all of the Taurides. Still, they reveal that the Central Taurides region stands out due to its specific neotectonic features, including upper crustal extension concurrent with rapid regional Quaternary uplift. Uplift and extension suggests a different geodynamic mechanism, possibly involving slab deformation and mantle upwelling, distinguishing it from other neotectonic provinces in Anatolia. Given the distinctiveness of the Central Taurides' neotectonic features and deformation mode, “The Central Taurides Neotectonic Extensional Province" can be suggested as a new neotectonic province of Anatolia. This suggestion acknowledges the region's unique geological processes and aims to provide a more accurate classification that reflects Anatolia's specific tectonic characteristics and evolution.

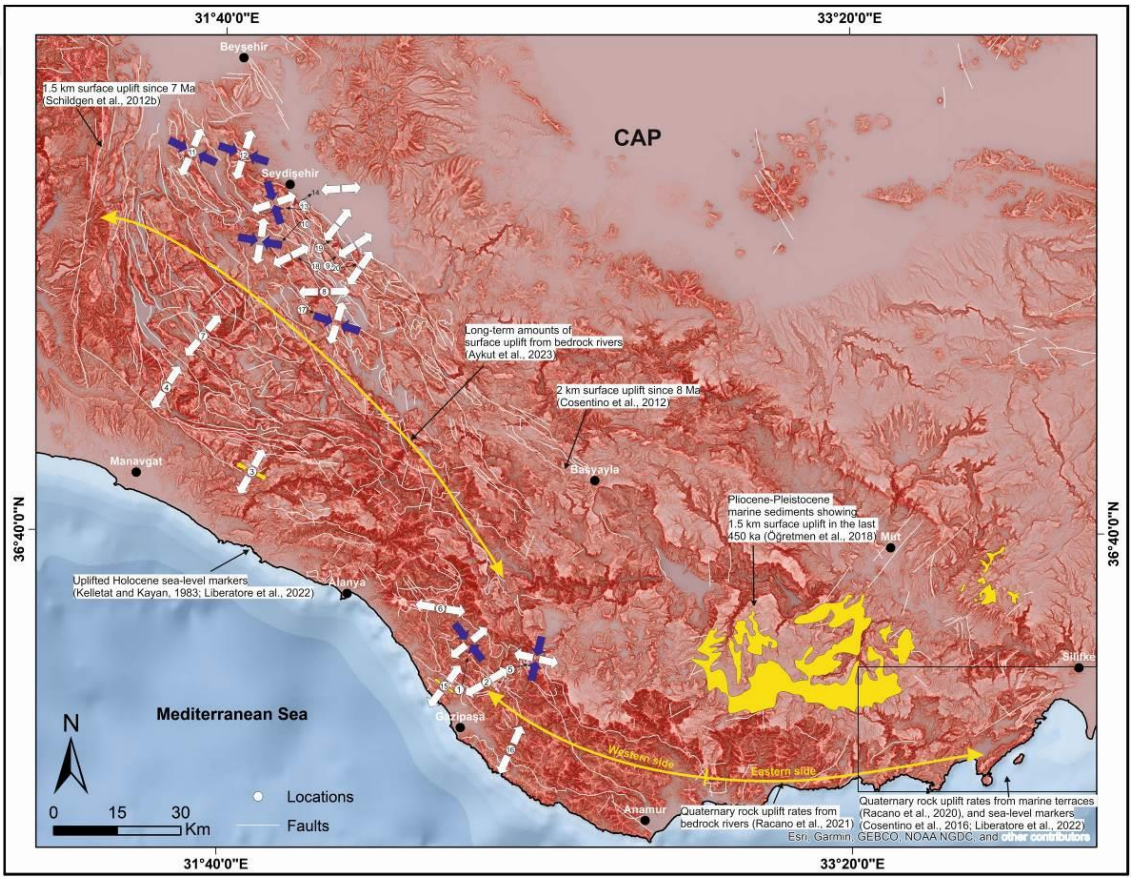

Figure 4.3: Red-relief image map (Chiba et al., 2008) illustrating the topography across the Central Taurides. Spatial distribution of uplift constraints from previous studies is depicted in the figure. Yellow polygons represent Pliocene-Pleistocene marine sediments from Öğretmen et al. (2018). White and blue arrows are maximum extension/shortening directions respectively, based on our kinematic analysis. CAP: Central Anatolian Plateau.

Mantle-driven surface uplift and upper crustal extension have been proposed as a viable process above several convergent plate boundaries worldwide (e.g. Apennines (Italy), Tibetan Plateau, Western Alps, SE China, and Central Andes) (D’Agostino et al., 2001; Blisniuk et al., 2001; Faure Walker et al., 2012; Li et al., 2014; Kar et al.,

2016; Nocquet et al., 2016). These studies have emphasised the influence of mantle-rooted processes such as slab deformation, mantle upwelling, and various mantle flows on long-wavelength topographic growth and extensional surface deformation. For example, one of the similar places which have a close geographical location and similar climatic, lithological and tectonic setting to Central Taurides, the Apennines above the Calabria Subduction Zone, has been shown to undergo rapid uplift and upper crustal extension as a result of mantle upwelling through slap gaps (D'Agostino et al., 2001; Faure Walker et al., 2012). Compared to the Central Taurides, the upper crustal extension was better constrained in the Apennines due to the higher seismic activity and the surface-breaking earthquakes (such as the earthquakes of April 6, 2009 Mw 6.3 in L'Aquila, of August 24, 2016 Mw 6.2 in Amatrice and of October 30, 2016 Mw 6.6 in Norcia) (Cowie et al., 2017). In contrast, the Central Taurides today are characterized by shallow earthquakes usually not higher than Mw 4.5 (Güvercin et al., 2021; Aykut et al., 2023), and there is no historical and paleoseismological data on the faults. Therefore, the application of U-Th geochronology to syn-tectonic calcites, combined with kinematic and microstructural observations above the Cyprus Subduction Zone, significantly advances our understanding of upper plate evolution where mantle-rooted processes control the surface deformation. This opens up a new window to constrain the timing and mechanism of upper crustal modification and to evaluate seismological hazard potential in such complex tectonic settings.

In conclusion, our results, together with previous geomorphic, geophysical, biostratigraphic and geodynamic evidence, suggest that rapid surface uplift and extensional brittle deformation may occur concurrently, creating major relief-bounding normal fault zones and high-relief dynamic landscapes on a short timescale in the overriding plates (Figure 4.4). Furthermore, our data highlight the importance of the U-Th geochronology of syn-tectonic carbonates, especially in erosional landscapes, for understanding the geodynamic evolution of convergent continental plates.

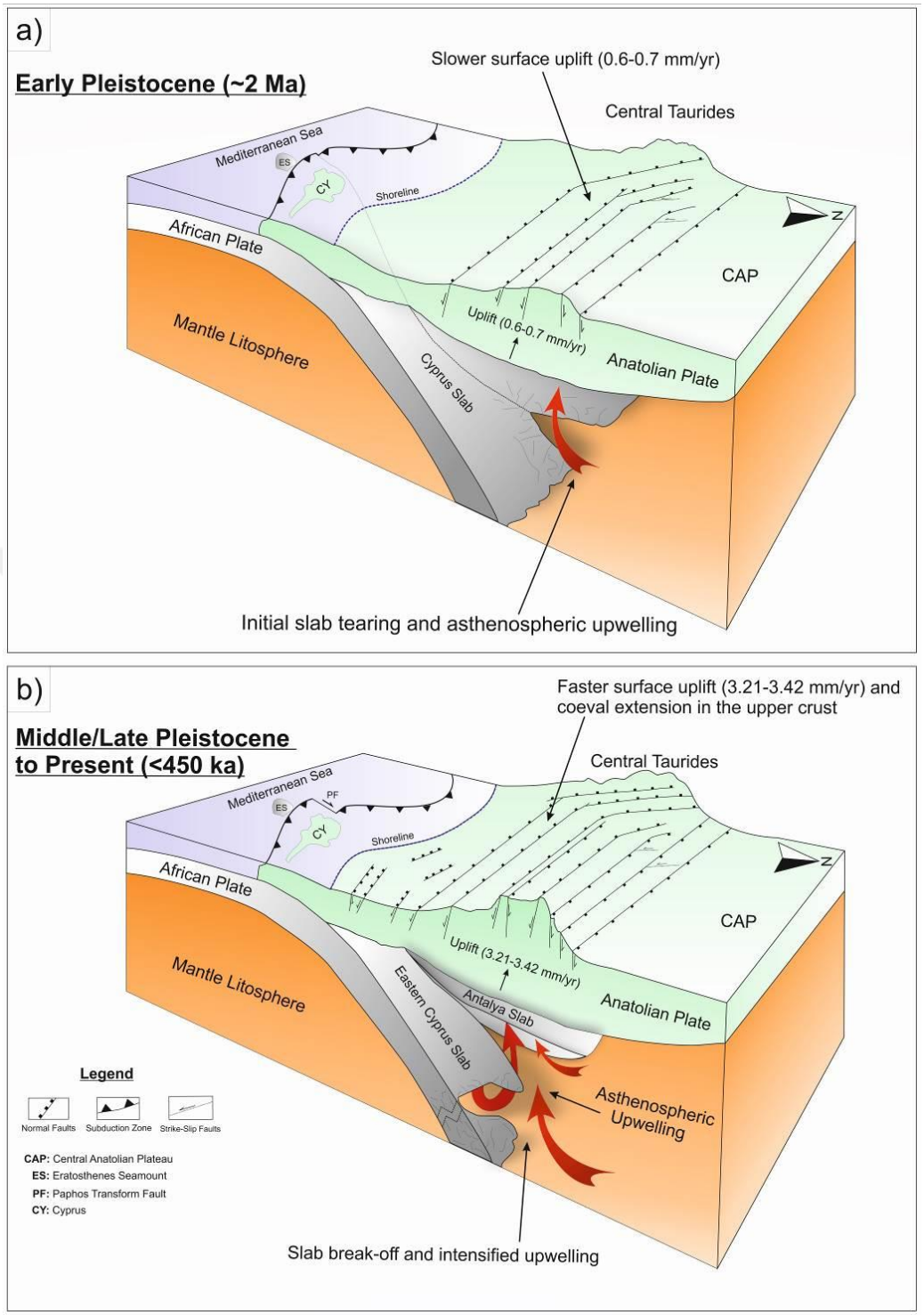

Figure 4.4: Conceptual diagram and interpretation of the relationships between deep-rooted processes and surface deformation in the Cyprus Subduction Zone from Early Pleistocene to Present. Please note that fault network and slab geometries are modified and simplified. Slab geometries are from Biryol et al., (2011) and Portner et al., (2018). Surface uplift rates are from Schildgen et al., (2012a) and Öğretmen et al., (2018).

4.2. Implications for Regional Active Deformation Pattern

Our geomorphic outputs point out to an actively deforming transient landscape and changing deformation patterns across western CT. Downstream increases in the

channel steepness values and major slope-break tectonic knickzones demonstrate different uplift pulses or periods of intensifying deformation. The ksn values demonstrate a bell-shaped trend in the north-south direction, and the best-fit ksn reaches peak values along the mountainous zone of the CT. The cumulative surface uplift slightly increases from west to east, from 1,600 ± 50 to 1,800 ± 50 m. The increasing trend of the ksn values, more rugged topography and more evident slope-break knickzones in the longitudinal profiles provide further morphometric evidence of the intensifying deformation toward the eastern parts of western CT. Results of the previous studies also mentioned a trend of increasing cumulative uplift from the western to the eastern flank of the CT for the last 8 Ma (Cosentino et al., 2012; Schildgen et al., 2012a, 2014) and an increasing Quaternary rock uplift rate from the eastern flank toward the western flank of the CT (Racano et al., 2021) (Figure 4.5). Integration of our results with findings of previous studies suggests a differential uplift pattern in the west-east direction across the southern margin that reaches up to maximum values in the region of Alanya-Başyayla-Ermenek-Gazipaşa, with a gradually decreasing pattern from this region toward the eastern and western parts of the CT (Figure 4.5).

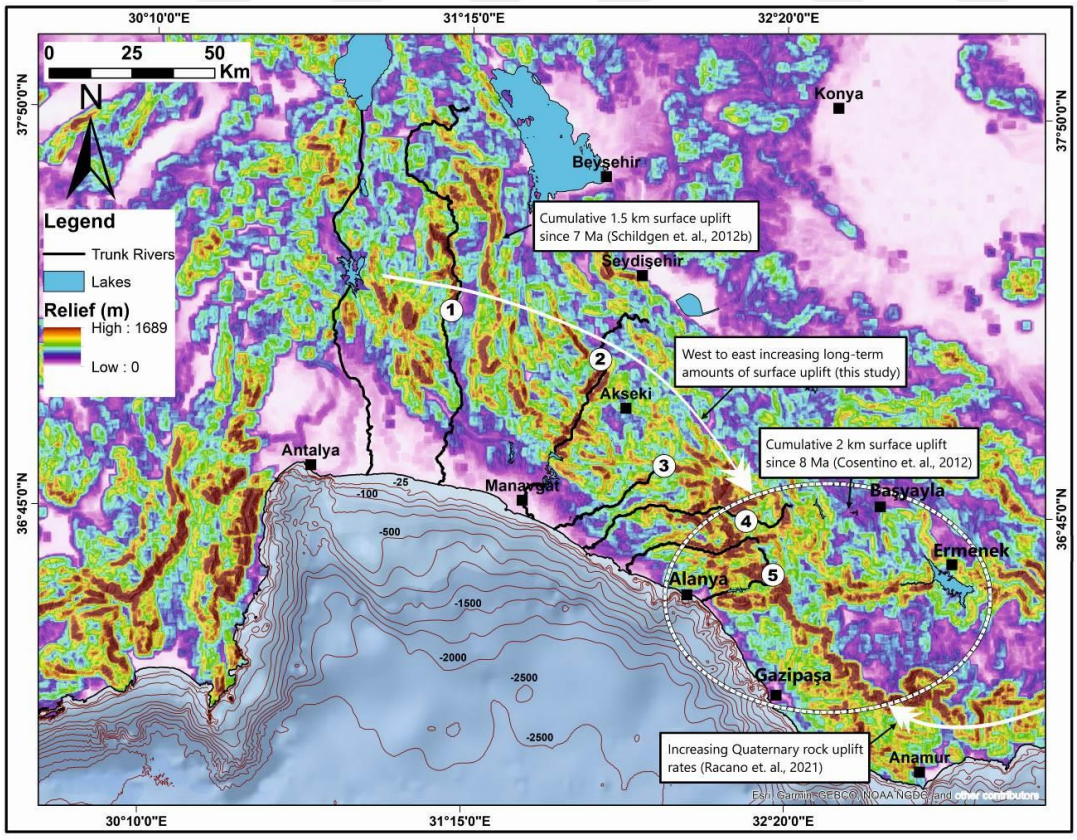

Figure 4.5: The general topographic relief across the western flank of the CT. The white arrows show the cumulative uplift trend of our results and the Quaternary rock uplift trend

from Racano et. al., (2021). The numbers within the white boxes depict the trunk rivers that have been used in paleo-longitudinal profile projection analysis: 1-Köprüçay River, 2-Manavgat River, 3- Karpuzçay River, 4- Ulugüney River, 5- Dim River. Data from the previous studies have been briefly given within the white boxes for interpreting the spatial distribution of the uplift. The white circle represents our proposed maximum uplift zone across the Central Taurides. Please note that the uplift trend is compatible with the relief character.

Tectono-karst footprints and morphotectonic expressions of the active tectonic deformation are highly prominent across western CT. The long-term cumulative mean 1,710 ± 50 m surface uplift (Figure 4.5) that has accelerated in the Pleistocene (Schildgen et al., 2014; Öğretmen et al., 2018) possibly triggered the intense karstification and gradual lowering of the karst base level; hence the formation of the polycyclic and polygenetic karst landforms. For example, abandoned three levels of Tınaztepe Cave can be found southeast of Seydişehir. Effects of the recent extensional tectonics can be seen as well, as an undefined normal fault cuts the cave entrance and compensates the uplift of the Tınaztepe Ridge block and the formation of two inactive cave levels at the 1,500 and 1,533 m elevations (Figure 4.6). Reactivation of the thrust zones as normal faults with clear geomorphic expressions is also widespread across the flank. For example, an inherited thrust zone (Akay & Uysal, 1988; McPhee et al., 2018) that reactivated as a normal fault bound the deeply incised Üzümdere Gorge of the Manavgat River near İbradı (Figure 4.6). These normal fault bounded-deeply incised valleys are widespread in the upper reaches of all bedrock streams, implying the young uplift of the western CT and high incision of the river system. The effects of the active deformation are evident on geomorphological orientations as well; NW-SE striking tectono-karst depressions (such as Eynif and Kembos Poljes) and horst-graben structures is compatible with the orientations of the youngest fault generations and active NE-SW extension. Our results show that the surface uplift and the active extensional deformation significantly controlled the morpho-tectonic development in western CT (Figure 4.7).

Although the westernmost CT (Aksu Basin) has been under the influence of active extensional deformation since the Late Pliocene (Glover & Robertson, 1998b; Üner et al., 2015), our results suggest that the earlier contractional Aksu Phase had effects on the evolution of the topography and the patterns of deformation. Higher ksn values and tectonic knickpoints across the hanging walls of the thrust faults underline the effects of the “Aksu Phase” on the topography. The contractional deformation also controlled the orientation of the main tectonic lineaments and prepared the groundwork for the

development of N-S striking extensional morphotectonic features (like Kovada Graben). Thus, although the last extensional deformation phase mainly controlled the geomorphological development in the westernmost CT, our findings suggest that the Aksu Phases' contractional deformation also had significant effects on the shaping of the topography (Figure 4.7).

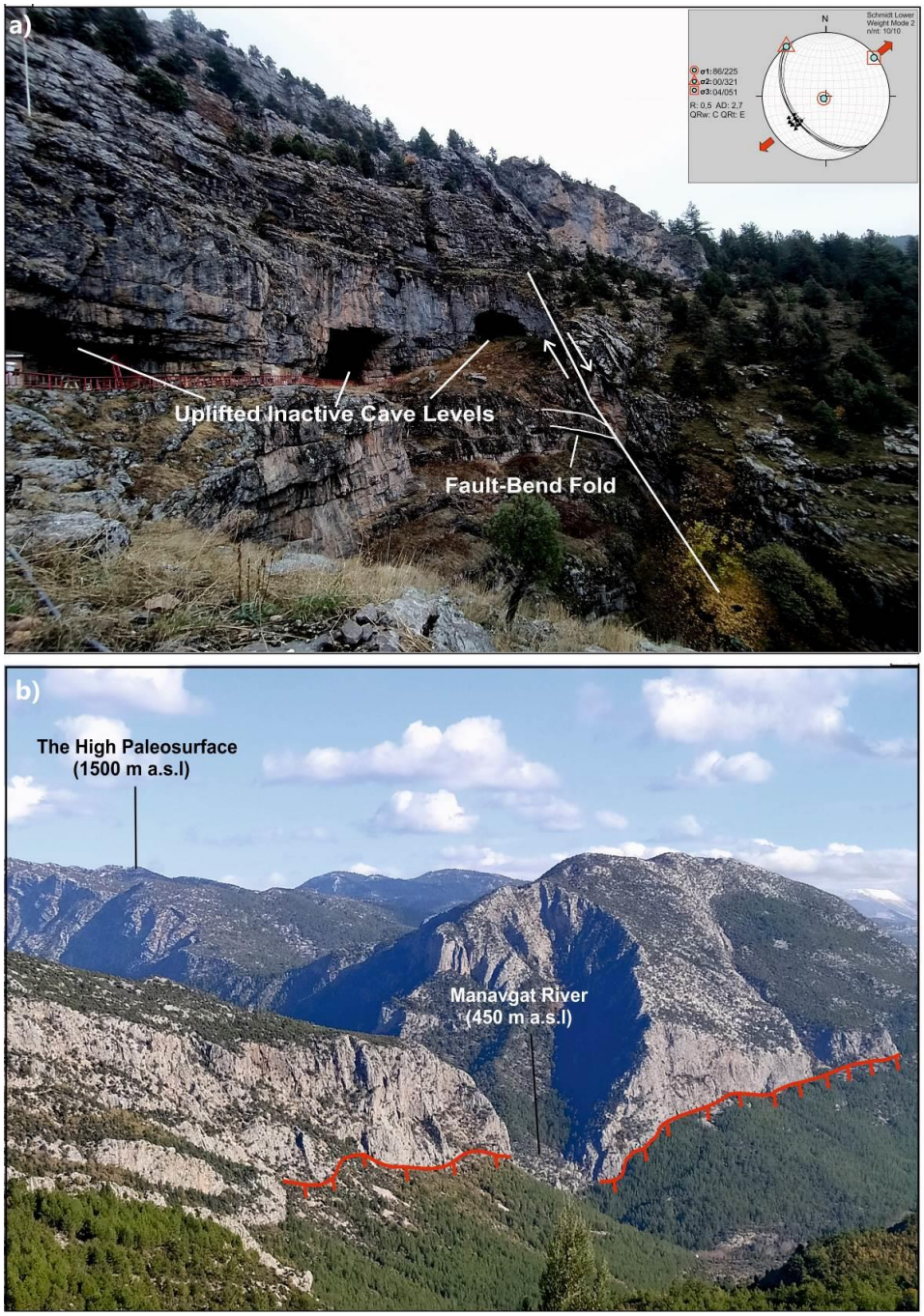

Figure 4.6: a) Normal fault cutting the entrance of the Tınaztepe Caves in the southeast of the Seydişehir. The inlet graph is the result of the paleo-stress analysis given in Figure 3.18 measurements made in the 1 km southeast of the cave entrance which corresponds to the kinematically continuous part of the fault. The location of the Tınaztepe Cave is given in Figure 3.7. **b)** Relief bounding undefined normal fault with very characteristic triangular

facets near İbradı. The high paleosurface located at 1500 m elevation (Monod et. al., 2006) demonstrates an approximately 1050 m bedrock incision of Manavgat River.

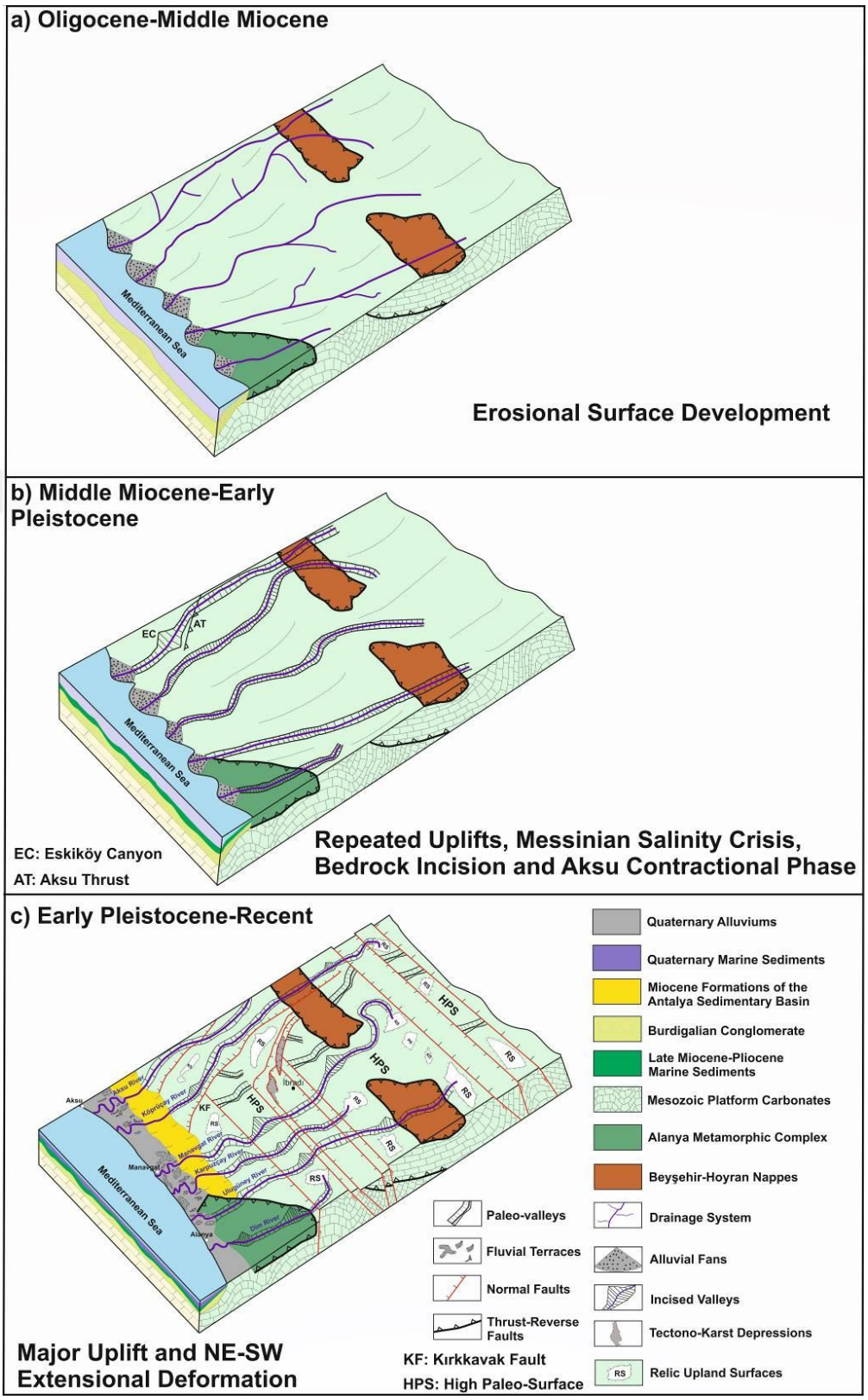

Figure 4.7: A conceptual model for the western flank of the CT, which depicts the pattern of deformation between Oligocene-Recent.

4.3. Implications for Long-term (Late Cretaceous-Quaternary) Faulting History

Precise U-Pb ages of syn-tectonic calcite precipitates and kinematic field data provide evidence for the contractional brittle deformation of the Central Taurides in the Late Cretaceous period (Figure 4.8). U-Pb ages of syn-tectonic calcite fibers from thrust/reverse faults align well with the Tethyan evolution of southern Türkiye and the large-scale internal deformation of the Anatolide-Tauride Block, which was governed by subduction, obduction, and continental collision. Previously, it has been suggested that large-scale geodynamic events occurred at the end of the Mesozoic, such as the closure of the İzmir-Ankara Ocean and collision along the İzmir-Ankara-Erzincan Suture Zone (Mueller et al., 2019; Kandemir et al., 2019; Okay et al., 2020), and the Kırşehir Block-Eurasia collision (Ballato et al., 2018). These events also drove the obduction of the Beyşehir-Hoyran-Hadim Nappes onto the Central Taurides, causing contraction, crustal thickening, and thrusting (Şengör and Yılmaz, 1981; Okay and Tüysüz, 1999; Okay et al., 2001; Andrew and Robertson, 2002; Robertson et al., 2012; Ballato et al., 2018) (Figure 4.8). Our results confirm that during the Late Cretaceous, the Central Tauride Block experienced internal brittle deformation due to NE-SW directed compression, which was compensated by thrust/reverse faulting events. These events were most probably driven by the collision between different tectonic blocks in Anatolia, as outlined above (Figure 4.8). Compression-related deformation in the Central Taurides most probably continued until the end of the Eocene. Younger thrusting events have also been reported on a local scale, such as NW-SE shortening in the westernmost CT during the Late Miocene-Pliocene (i.e., Aksu Phase), driven by younger and different geodynamic events such as the emplacement of Lycian Nappes onto the Western Taurides (Flecker et al., 1998, 2005; Üner et al., 2015) and/or the counterclockwise rotation of Anatolia in the neotectonic period (Glover and Robertson, 1998b; Çiner et al., 2008).

Although strike-slip faulting events have been reported in the westernmost part (e.g., Aksu Basin) and the easternmost part (e.g., Ecemiş Fault Zone) of the Central Taurides from the Eocene to the Quaternary (Glover and Robertson, 1998a, 1998b; Jaffey and Robertson, 2001, 2005; Sarıkaya et al., 2015; Yıldırım et al., 2016; Umhoefer et al., 2020), the extent of strike-slip faulting across the interior part of the Central Taurides remains unclear. Our U-Pb ages from lateral faults reveal the existence of strike-slip faulting events between the Early Eocene and Early Miocene, with a clear clustering

during the Oligocene (Figure 4.8). This strike-slip faulting phase coincides with the Arabia-Anatolia collision, which began with soft collision in the Middle Eocene (Darin et al., 2018) and continued until approximately 20 Ma (Ballato et al., 2018). Therefore, the Oligocene culmination in strike-slip brittle deformation events in the Central Taurides may represent internal shearing driven by general N-S shortening in Eastern Anatolia. Convergence and collision of tectonic plates in Eastern Anatolia may have governed the crustal block rotations observed in southern Türkiye, causing Oligocene shearing across the Central Taurides. Paleomagnetic studies in the Central Taurides showed a clockwise block rotation of 48.5° between the Middle Eocene and Middle Miocene (Çinku et al., 2016). In the western part of the Central Taurides, a clockwise rotation of 40.2° ± 8.7° was obtained during Middle Eocene and Oligocene (Kissel et al., 2003; Çinku et al., 2016). It has also been suggested that the major clockwise rotation occurred in the Middle Eocene, gradually fading out until the Middle Miocene, with no significant block rotations occurring after the Middle Miocene (Kissel et al., 2003; Çinku et al., 2016). Paleomagnetic results from the Ulukışla-Sivas Basins and Bolkar Mountains also provided 17° and 32.5° ± 2.2° counterclockwise block rotations for the area encompassing easternmost Central Taurides, Kırşehir Block, and Eastern Taurides in the Eocene and Oligo-Miocene periods, respectively (Gürer et al., 2018). These rotations in different directions may be the cause of Oligocene-peaking shearing across the Central Taurides, possibly driven by the collision between Arabia and Anatolia between 45-20 Ma (Darin et al., 2018; Ballato et al., 2018). Block rotations in different directions across the easternmost and westernmost parts of the orogenic belt are compatible with the variable paleo-stress directions in our kinematic analysis (NE-SW tension-NW-SE compression and NE-SW compression-NW-SE tension) and different lateral displacement directions (left-lateral and right-lateral) along the shearing zones.

Previously, Oligocene shearing in Anatolia was also identified in the Uludağ Massif (Okay et al., 2008). Our U-Pb ages from strike-slip faults align with those of Okay et al. (2008). Their findings suggested that crustal-scale strike-slip faults facilitated the westward movement of Anatolia towards the Aegean, likely due to Hellenic slab suction. Our results may support that the onset of the westward movement of Anatolia predates the Late Miocene Arabia-Eurasia collision. If Anatolia was indeed already translating westwards during Oligo-Miocene, this movement may have triggered the

block rotations seen in southern Anatolia, resulting in Oligocene strike-slip faulting in the Central Taurides (Figure 4.8).

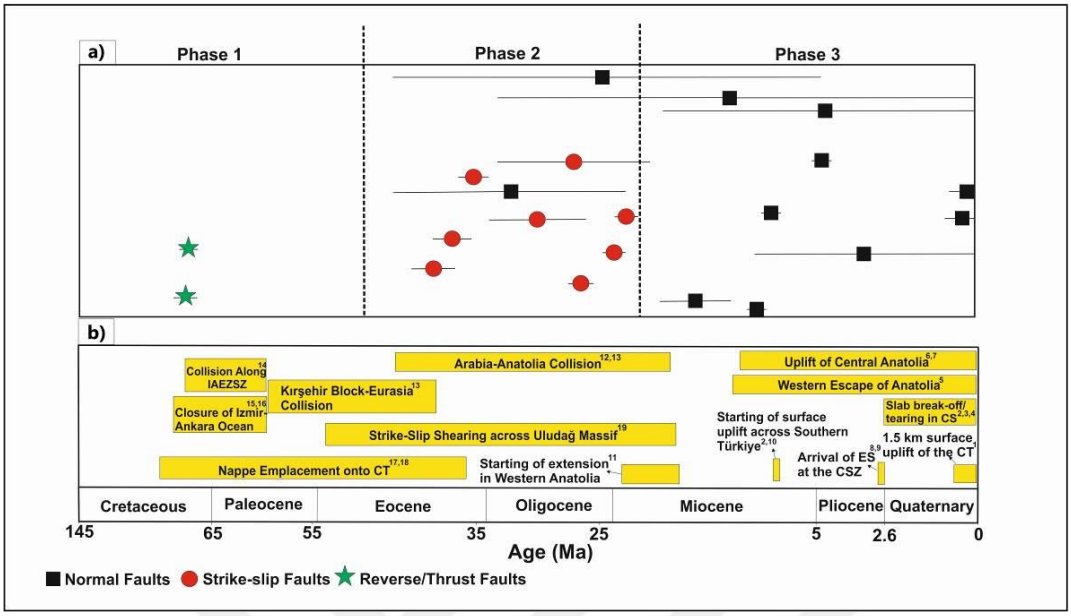

Figure 4.8 Long-term faulting history of the Central Taurides between the Late Cretaceous and Quaternary. **a)** Distribution of U-Pb calcite ages with error bars (2σ). Different symbols represent various faulting types (normal, strike-slip, thrust-reverse). The noted phases indicate proposed faulting phases between the Cretaceous and Quaternary. **b)** Timing of major geodynamic events in Anatolia and the Eastern Mediterranean. **CT:** Central Taurides, **ES:** Eratosthenes Seamount, **CS:** Cyprus Slab, **CSZ:** Cyprus Subduction Zone, **IAEZSZ:** Izmir-Ankara-Erzincan Suture Zone. Please note that references for major events are presented as superscripts: 1. Öğretmen et al., (2018); 2. Schildgen et al., (2014); 3. Biryol et al., (2011); 4. Racano et al., (2021); 5. Şengör et al., (1985); 6. Göğüş et al., (2017); 7. Çiner et al., (2015); 8. Robertson, (1998); 9. Schattner, (2010); 10. Cosentino et al., (2012); 11. Ring et al., (2010); 12. Darin et al., (2018); 13. Ballato et al., (2018); 14. Mueller et al., (2019); 15. Kandemir et al., (2019); 16. Okay et al., (2020); 17. Andrew and Robertson, (2002); 18. Okay and Tüysüz, (1999); 19. Okay et al., (2008).

Previously, the Post-Oligocene tectonic regime was linked to extensional deformation in the Central Taurides, as normal faulting was identified in the Central Tauride intramontane basins such as Aksu Basin, Akşehir Graben, Altınapa Basin, Yalvaç Basin and Manavgat Basin (Koçyiğit and Özacar, 2003; Çiner et al., 2008; Koç et al., 2012; 2016; Schildgen et al., 2012b; Üner et al., 2015). Some of these studies argued that the onset of the extension in Central Taurides is at least Middle Miocene (Koç et al., 2012; 2016). According to our U-Pb age data, extension has started earlier than previously thought, as there is a clear culmination of U-Pb ages around Early Miocene, and a gradual change in tectonic regime from strike-slip faulting to normal faulting during Oligocene-Miocene transition (Figure 4.8). The U-Pb age data from normal faults is continuous from the Late Oligocene/Early Miocene to the Quaternary, underlining that normal faulting and NE-SW extension represent the last brittle

deformation phase across the Central Taurides on a regional scale (Figure 4.8), despite some contractional deformation also being identified on a local scale (e.g., the Aksu Phase). This extensional regime seems to be still active today according to our U-Th ages, earthquake focal mechanism solutions (Schildgen et al., 2012b; Güvercin et al. 2021), geomorphic markers (Monod et al., 2006; Doğan et al., 2017) and GPS-derived strain-rate fields (Howell et al., 2017).

The tectonic history of Southern Türkiye between the Early Miocene and recent times encompasses significant geological events that have shaped the region's landscape and structural framework. During this period, the interaction between the African and Anatolian plates played a pivotal role in driving tectonic processes. The ongoing convergence between the African and Anatolian Plates along the Cyprus Subduction Zone was probably the general driving mechanism of the Miocene extension in the Central Taurides. As the African Plate subducted beneath the Anatolian Plate, the slab may have rolled back into the mantle, leading to NE-SW extension in the overriding plate during the Miocene, as previously proposed by several researchers (Glover and Robertson, 1998b; Kelling, 2005; Koç et al., 2012, 2016; Güvercin et al., 2021). Towards the end of the Miocene, surface deformation in the Central Taurides may have begun to be influenced by coupled geodynamic drivers because this period marks the onset of 2 km surface uplift in the last 8 Ma (Schildgen et al., 2012a, 2012b, 2014; Cosentino et al., 2012; Aykut et al., 2023). During this multi-phased uplift period, it was proposed that uplift accelerated around 1.6 Ma (Schildgen et al., 2012a, 2014) and 450 ka (Öğretmen et al., 2018; Racano et al., 2020, 2021). Our young U-Pb ages from normal faults, positioned at the lower limit of U-Pb dating (Figure 5, S15-a,b,k), also confirms that normal faulting most probably have persisted into the Late Quaternary, also supporting our young U-Th age results. Considering these implications, numerous slab deformation events (break-off, tearing etc.) could have occurred from the Late Miocene to the Quaternary, accelerating the rates of uplift and normal faulting in the Central Taurides. Nonetheless, without additional data and insights into the timing of slab deformation beneath Southern Anatolia, comprehending the complete extent of the driving mechanisms behind the observed Miocene to present day uplift and normal faulting in the Central Taurides remains challenging.

5. CONCLUSIONS

This study presents morpho-tectonic analysis, kinematic field observations, microstructural examinations and U-Th/U-Pb geochronology on syn-tectonic calcites to decipher the pattern, timing and mechanism of active deformation across the western flank of the Central Taurides, at the southern margin of the Central Anatolian Plateau. New geomorphic data revealed the existence of the major tectonic slope-break knickzones and steep channel segments along the river longitudinal profiles, strong relief contrasts that reflects the signals of the crustal deformation recorded within the post-orogenic transient actively deforming topography. The spatial distribution of the low relief upland surfaces constrained the long-term surface uplift pattern; the mean cumulative surface uplift is 1,710 ± 50 m, and shows an increasing trend from west to the east, from 1,600 ± 50 to 1,800 ± 50 m. Distributions of the best-fit ksn values, relief ruggedness, and slope-break tectonic knickzone elevations point out an increasing deformation intensity toward the eastern CT. Integration of our results with findings of the previous studies suggests a dome-like uplift pattern that reaches up to maximum values in the region of Alanya-Başyayla-Ermenek-Gazipaşa, with a gradually decreasing pattern from this region toward the eastern and western flanks of the CT. The kinematic measurements reveal the presence of normal, strike-slip, and thrust/reverse fault sets, indicating a complex history of brittle deformation in the region. Paleo-stress analyses illuminate the stress regimes associated with these faulting events, with NE-SW tension dominating on normal faults and a combination of NE-SW tension/NW-SE compression and NW-SE tension/NE-SW compression on strike-slip faults. Thrust/reverse faults exhibit NE-SW compression. Microscopy and scanning electron microscope analyses on syn-tectonic calcite samples show twinning, brecciated zones, calcite gouges, slickenlines, slickenfibres, fault grooves, microfractures and displaced dilation veins; underlining microstructural footprints of faulting-related deformation. U-Th dating results indicate active NE-SW directed horizontal extension accommodated by NW-SE striking normal fault zones from the Middle/Late Pleistocene to the present. The peaking brittle deformation ages at 450 ka

provide evidence for contemporaneous surface uplift and normal faulting in the last 500 ka. Rapid surface uplift and the coeval upper crustal extension favors mantle-driven control of upper crustal deformation, possibly controlled by the slab fragmentation and hot asthenosphere upwelling. The U-Pb carbonate geochronology of syn-tectonic calcite samples indicates three distinct phases of faulting from the Late Cretaceous to the Quaternary. Thrust/reverse faulting events, which represents the first faulting phase, were observed in the Late Cretaceous. The second faulting phase, strike-slip faulting, occurred from the Early Eocene to the Early Miocene with a clear cluster in the Oligocene. Normal faulting was the last faulting phase and is prevalent from the Early Miocene to the Quaternary. The Late Cretaceous thrust/reverse faulting could be associated with the collision of different tectonic blocks in Anatolia. The Oligocene peaking strike-slip shearing in the region was probably driven by the convergence and collision of tectonic plates in Eastern Anatolia and the resulting block rotations in Southern Türkiye. The onset of normal faulting in the Early Miocene indicates a shift towards extensional tectonics during the Oligocene-Miocene transition, which continuous until the present day. The last faulting phase has been possibly driven by the coupling geodynamic processes such as slab retreat, slab deformation and mantle upwelling associated with convergence along the Cyprus Subduction Zone.

The results of this study constrain the temporal relationships between surface uplift, upper crustal brittle deformation and mantle-rooted processes above the Cyprus Subduction Zone, in the western flank of the Central Taurides. Implications of this study provides valuable insights into the complex tectonic history of the Central Taurides, shedding light on the long-term faulting history and the possible mechanisms driving crustal deformation from the Late Cretaceous to the present day. Results of this study highlights the importance of U-Th and U-Pb carbonate geochronology, especially in erosional landscapes, in understanding the geodynamic evolution of convergent continental plates and the morphotectonic development and post-orogenic deformation in the plateau margins. Methods and results of this study can be utilized for further studies addressing mantle-driven crustal deformation and the seismic hazard potential above the active plate boundaries.

REFERENCES

Akay, E., & Uysal, S. (1988). *Post-Eocene tectonics of the Central Taurus Mountains*. Mineral Resources Exploration Bulletin, *108*, 23–34.

Allmendinger, R. W., Jordan, T. E., Kay, S. M., & Isacks, B. L. (1997). *The evolution of the Altiplano-Puna plateau of the Central Andes*. Annual Review of Earth and Planetary Sciences, *25(1)*, 139–174. https://doi.org/10.1146/annurev.earth.25.1.139.

Andrew, T., Robertson, A.H.F., (2002). *The Beysehir - Hoyran - Hadim Nappes: genesis and emplacement of Mesozoic marginal and oceanic units of ther northern Neotethys in southern Turkey*. J. Geol. Soc. Lond. *159*, 529–543. https://doi.org/10.1144/0016- 764901-157.

Aykut, T., Yıldırım, C, & Uysal, I. T. (2023). *Active Deformation Pattern in the Western Flank of the Central Taurides, Southern Margin of the Central Anatolian Plateau: Inferences from Geomorphic Markers and Kinematic Indicators*. Tectonics. *42* (6), e2022TC007550. https://doi.org/10.1029/2022TC007550.

Ballato, P., Parra, M., Schildgen, T. F., Dunkl, I., Yıldırım, C., Özsayın, E., et al. (2018). *Multiple exhumation phases in the Central Pontides (N Turkey): New temporal constraints on major geodynamic changes associated With the Closure of the Neo-Tethys Ocean*. Tectonics, *37*(6), 1831–1857. https://doi.org/10.1029/2017TC004808.

Bartol, J., & Govers, R., (2014). *A single cause for uplift of the Central and Eastern Anatolian plateau?* Tectonophysics, *637*, 116–136. https://doi.org/10.1016/j. tecto.2014.10.002.

Biryol, B.C., Beck, S. L., Zandt, G., & Özacar, A. A. (2011). *Segmented African lithosphere beneath the Anatolian region inferred from teleseismic P-wave tomography*. Geophysical Journal International, *184* (3), 1037–1057. https://doi.org/10.1111/j.1365-246X.2010.04910.x.

Blisniuk P M, Hacker B R, Glodny J, Ratschbacher L, Bi S W, Wu Z H, McWilliams M O, Calvert A. (2001). *Normal faulting in central Tibet since at least 13.5 Myr ago*. Nature, *412*: 628–632.

Boulton, S. J. (2020). *Geomorphic response to differential uplift: River long profiles and knickpoints from Guadalcanal and Makira (Solomon Islands).* Frontiers of Earth Science, *8*. https://doi.org/10.3389/feart.2020.00010

Bozkurt, E. (2001). *Neotectonics of Turkey – a synthesis*. Geodinamica Acta, *14*, 3–30. https://doi.org/10.1016/S0985-3111(01)01066-X.

Burkhard, M., (1993). *Calcite twins, their geometry, appearance and significance as stress strain markers and indicators of tectonic regime: a review*. J. Struct. Geol. *15* (3–5), 351–368.

Chen, Y. W., Shyu, J. B. H., & Chang, C. P. (2015). *Neotectonic characteristics along the eastern flank of the Central Range in the active Taiwan orogen inferred from fluvial channel morphology*. Tectonics, *34*(10), 2249–2270. https://doi.org/10.1002/2014TC003795.

Cheng, H., Edwards, R., Hoff, J., Gallup, C., Richards, D., and Asmerom, Y., (2000). *The half-lives of uranium-234 and thorium-230:* Chemical Geology, *v. 169*, no. 1-2, p. 17-33.

Chiba, T., Kaneta, S., & Suzuki, Y. (2008). *Red relief image map: New visualization method for three dimensional data.* In The International Archives of the Photogrammetry, Remote Sensing and Spatial Information Sciences, (*Vol. 37*, pp. 1071–1076).

Clark, M. K., Royden, L. H., Whipple, K. X., Burchfiel, B. C., Zhang, X., & Tang, W. (2006). *Use of a regional, relict landscape to measure vertical deformation of the eastern Tibetan Plateau*. Journal of Geophysical Research, *111*(F3), F03002. https://doi.org/10.1029/2005JF000294.

Clark, T. R., Zhao, J.-x., Feng, Y.-x., Done, T. J., Jupiter, S., Lough, J., and Pandolfi, J. M., (2012*). Spatial variability of initial 230Th/232Th in modern Porites from the inshore region of the Great Barrier Reef:* Geochimica et Cosmochimica Acta, *v. 78*, p. 99-118.

Clark, T. R., Zhao, J.-x., Roff, G., Feng, Y.-x., Done, T. J., Nothdurft, L. D., and Pandolfi, J. M., (2014.) *Discerning the timing and cause of historical mortality events in modern Porites from the Great Barrier Reef*: Geochimica et Cosmochimica Acta, *v. 138*, p. 57-80.

Cosentino, D., Ögretmen, N., Cipollari, P., Gliozzi, E., Radeff, G., & Yildirim, C. (2016). *Evidence for Latest Pleistocene to Holocene Uplift at the Southern Margin of the Central Anatolian Plateau (CAP), Southern Turkey*. EGU General Assembly 2016, EPSC2016-8873, *18*, 17–22.

Cosentino, D., Schildgen, T. F., Cipollari, P., Faranda, C., Gliozzi, E., Hudáčková, N. Lucifora, S., & Strecker, M. R. (2012). *Late Miocene surface uplift of the southern margin of the Central Anatolian plateau, Central Taurides, Turkey*. Bulletin of the Geological Society of America, *124* (1–2).

Cowie, P., Phillips, R., Roberts, G., McCaffrey, K., Zijerveld, L., Gregory, L., et al. (2017). *Orogen-scale uplift in the central Italian Apennines drives episodic behaviour of earthquake faults*. Scientific Reports, *7*(1), 44858. https://doi.org/10.1038/srep44858.

Çiner, A., Karabiyikoğlu, M., Monod, O., Deynoux, M., & Tuzcu, S. (2008). *Late Cenozoic sedimentary evolution of the Antalya Basin, southern Turkey*. Turkish Journal of Earth Sciences, *17*(1), 1–41.

Çiner, A., Doğan, U., Yıldırım, C., Akçar, N., Ivy-Ochs, S., Alfimov, V., et al. (2015). *Quaternary uplift rates of the Central Anatolia Plateau, Turkey: Insights from cosmogenic isochron-burial nuclide dating of the Kizilirmak River terraces*. Quaternary Science Reviews, *107*, 81–97. https://doi.org/10.1016/j.quascirev.2014.10.007

Çinku, M. C., Hisarli, Z. M., Yılmaz, Y., Ülker, B., Kaya, N., Öksüm, E., Orbay, N., and Özbey, Z. Ü. (2016). *The tectonic history of the Nigde–Kırsehir Massif and the Taurides since the Late Mesozoic: paleomagnetic evidence for two-phase orogenic curvature in central Anatolia*, Tectonics, *35*, 772–811.

Darin, M., H., Umhoefer, P., J., Thomson, S., N. (2018). *Rapid Late Eocene exhumation of the Sivas Basin (Central Anatolia) driven by Initial Arabia-Eurasia collision*. Tectonics, *37*, 3805–3833. https://doi.org/10.1029/2017TC004954

D'Agostino, N., Jackson, J. A., Dramis, F., & Funiciello, R. (2001). *Interactions between mantle upwelling, drainage evolution and active normal faulting: An example from the Central Appennines (Italy)*. Geophysical Journal International, *147*(2), 475–497. https://doi.org/10.1046/j.1365-246X.2001.00539.x.

Delvaux, D., & Sperner, B. (2003). *New aspects of tectonic stress inversion with reference to the TENSOR program*. Geological Society London Special Publications, *212*(1), 75–100. https://doi.org/10.1144/GSL.SP.2003.212.01.06.

Demoulin, A., Beckers, A., Rixhon, G., Braucher, R., Bourles, D., Siame, L., & Becker, A. (2012). *Valley downcutting in the Ardennes (W Europe): Interplay between tectonically triggered regressive erosion and climatic cyclicity*. Netherlands Journal of Geosciences, *91*(1–2), 79–90. https://doi.org/10.1017/S0016774600001517.

Demoulin, A., Mather, A., & Whittaker, A. (2017). *Fluvial archives, a valuable record of vertical crustal deformation*. Quaternary Science Reviews, *166*, 10–37. https://doi.org/10.1016/j.quascirev.2016.11.011.

Dickin, A.P. (2005). *Radiogenic Isotope Geology*, 2nd ed.; Cambridge University Press: New York, NY, USA. ISBN 9780521823166.

Doğan, U., Koçyiğit, A., & Gökkaya, E. (2017). *Development of the Kembos and Eynif structural poljes: Morphotectonic evolution of the upper Manavgat River basin, Central Taurides, Turkey*. Geomorphology, *278*, 105–120. https://doi.org/10.1016/j.geomorph.2016.10.030.

Duretz, T., & Gerya, T. V. (2013*). Slab detachment during continental collision: Influence of crustal rheology and interaction with lithospheric delamination*. Tectonophysics, *602*, 124–140. https://doi.org/10.1016/j.tecto.2012.12.024.

Edwards, R. L., Chen, J. H., and Wasserburg, G. J. (1987). *238U-234U-230Th-232Th Systematics and the precise measurement of time over the Past 500,000 years*. Earth and Planetary Science Letters, *81*(2–3), 175–192.

England, P., Houseman, G., & Nocquet, J. M. (2016). *Constraints from GPS measurements on the dynamics of deformation in Anatolia and the Aegean*. Journal of Geophysical Research: Solid Earth, *121*(12), 8888–8916. https://doi.org/10.1002/2016JB013382.

Faccenna, C., Bellier, O., Martinod, J., Piromallo, C., Regard, V., (2006). *Slab detachment beneath eastern Anatolia: a possible cause for the formation of the North Anatolian Fault*. Earth and Planetary Science Letters. *242*, 85–97. https://doi.org/10.1016/j. epsl.2005.11.046.

Faure Walker, J. P., Roberts, G. P., Cowie, P. A., Papanikolaou, I., Michetti, A. M., Sammonds, P., Wilkinson, M., McCaffrey, K. J. W., and Phillips, R. J., (2012). *Relationship between topography, rates of extension and mantle dynamics in the actively extending Italian Apennines,* Earth Planet. Sci. Lett., *325–326,* 76–84, https://doi.org/10.1016/j.epsl.2012.01.028.

Fernández-Blanco, D., Mannu, U., Bertotti, G., & Willett, S. D. (2020). *Forearc high uplift by lower crustal flow during growth of the Cyprus-Anatolian margin*. Earth and Planetary Science Letters, *544*, 116314. https://doi.org/10.1016/j.epsl.2020.116314.

Flecker, R., Ellam, R. M., Müller, C., Poisson, A., Robertson, A. H. F., & Turner, J. (1998). *Application of Sr isotope stratigraphy and sedimentary analysis to the origin and evolution of the Neogene basins in the Isparta Angle, southern Turkey*. Tectonophysics, *298*(1–3), 83–101. https:// doi.org/10.1016/S0040-1951(98)00179-6.

Flint, J. J. (1974). *Stream gradient as a function of order, magnitude, and discharge*. Water Resources Research, *10*(5), 969–973. https://doi. org/10.1029/wr010i005p00969.

Forte, A. M., & Whipple, K. X. (2019). *Short communication: The Topographic Analysis Kit (TAK) for TopoToolbox*. Earth Surface Dynamics, *7*(1), 87–95. https://doi.org/10.5194/esurf7-87-2019.

Gailleton, B., Mudd, S. M., Clubb, F. J., Peifer, D., & Hurst, M. D. (2019). *A segmentation approach for reproducible extraction and quantification of knickpoints from river long profiles*. Earth Surface Dynamics, *7*(1), 211–230. https://doi.org/10.5194/esurf-7-211-2019.

Gallen, S. F. (2018). *Lithologic controls on landscape dynamics and aquatic species evolution in postorogenic mountains*. Earth and Planetary Science Letters, *493*, 150–160. https://doi.org/10.1016/j.epsl.2018.04.029.

Gallen, S. F., & Wegmann, K. W. (2017). *River profile response to normal fault growth and linkage: An example from the Hellenic forearc of south-central Crete, Greece*. Earth Surface Dynamics, *5*(1), 161–186. https://doi.org/10.5194/esurf-5-161-2017.

Glover, C. P., & Robertson, A. H. F. (1998a). *Neotectonic intersection of the Aegean and Cyprus tectonic arcs: Extensional and strike-slip faulting in the Isparta Angle, SW Turkey*. Tectonophysics, *298*(1–3), 103–132. https://doi.org/10.1016/S0040-1951(98)00180-2.

Glover, C. P., & Robertson, A. H. F. (1998b). *Role of regional extension and uplift in the Plio-Pleistocene evolution of the Aksu Basin, SW Turkey*. Journal of the Geological Society, *155*(2), 365–387. https://doi.org/10.1144/gsjgs.155.2.0365.

Goodfellow, B. W., Viola, G., Bingen, B., Nuriel, P., & Kylander-Clark, A. R. C. (2017). *Palaeocene faulting in SE Sweden from U–Pb dating of slickenfibre calcite*. Terra Nova, *29*(5), 321–328. https://doi.org/10.1111/ter.12280.

Göğüş, O.H., Pysklywec, R.N., Şengör, A.M.C. et al. (2017). *Drip tectonics and the enigmatic uplift of the Central Anatolian Plateau*. Nat Commun *8*, 1538. https://doi.org/10.1038/s41467-017-01611-3.

Güvercin, S. E., Konca, A. Ö., Özbakır, A. D., Ergintav, S. & Karabulut, H. (2021). *New focal mechanisms reveal fragmentation and active subduction of the Antalya slab in the Eastern Mediterranean*. Tectonophysics. *805*. 228792. https.//doi.org/10.1016/j.tecto.2021.228792.

Gürer, D., van Hinsbergen, D.J.J., Özkaptan, M., Creton, I., Koymans, M.R., Cascella, A., and Langereis, C.G. (2018). *Paleomagnetic constraints on the timing and distribution of Cenozoic rotations in Central and Eastern Anatolia*, Solid Earth, *v. 9*, no. 2, p. 295–322, https:// doi .org /10 .5194 /se -9 -295.

Hack, J. T. (1973). *Stream-profile analysis and stream-gradient index*. Journal of Research of the U. S. Geological Survey, *1*, 421–429.

Hall, J., Aksu, A. E., Calon, T. J., & Yaşar, D. (2005). *Varying tectonic control on basin development at an active microplate margin: Latakia Basin, Eastern Mediterranean*. Marine Geology, *221*(1–4), 15–60. https://doi.org/10.1016/j.margeo.2004.05.034.

Hansman, R. J., Albert, R., Gerdes, A., & Ring, U. (2018). *Absolute ages of multiple generations of brittle structures by U-Pb dating of calcite*. Geology, *46*(3), 207–210. https://doi.org/10.1130/G39822.1.

Haviv, I., Enzel, Y., Whipple, K. X., Zilberman, E., Matmon, A., Stone, J., & Fifield, K. L. (2010). *Evolution of vertical knickpoints (waterfalls) with resistant caprock: Insights from numerical modeling*. Journal of Geophysical Research, *115*(F3), F03028. https://doi. org/10.1029/2008JF001187.

Howard, A. D., Seidl, M. A., & Dietrich, W. E. (1994*). Modeling fluvial erosion on regional to continental scales*. Journal of Geophysical Research, *99*(B7), 13971–13986. https://doi.org/10.1029/94JB00744.

Howell, A., Jackson, J., Copley, A., McKenzie, D., & Nissen, E. (2017). *Subduction and vertical coastal motions in the eastern Mediterranean*. Geophysical Journal International, *211*(1), 593–620. https://doi.org/10.1093/gji/ggx307.

Huguen, C., Mascle, J., Chaumillon, E., Woodside, J. M., Benkhelil, J., Kopf, A., & Volkonskaïa, A. (2001). *Deformational styles of the Eastern Mediterranean ridge and surroundings from combined swath mapping and seismic reflection profiling*. Tectonophysics, *343*(1–2), 21–47. https://doi.org/10.1016/S0040-1951(01)00185-8

Imprescia, P., Pondrelli, S., Vannucci, G., & Gresta, S. (2012). *Regional centroid moment tensor solutions in Cyprus from 1977 to the present and seismotectonic implications*. Journal of Seismology, *16*(2), 147–167. https://doi.org/10.1007/s10950-011-9254-7.

Jaffey, A. H., Flynn, K. F., Glendenin, L. E., Bentley, W. C., & Essling, A. M. (1971). *Precision measurement of half-lives and specific activities of U235 and U238*. Physical Review C, *4*(5), 1889–1906. https://doi.org/10.1103/PhysRevC.4.1889.

Jaffey, N., Robertson, A.H.F., (2001). *New sedimentological and structural data from the Ecemiş Fault Zone, southern Turkey: implications for its timing and offset and the Cenozoic tectonic escape of Anatolia*. J. Geol. Soc. (Lond.) *158*, 367–378.

Jaffey, N., Robertson, A.H.F., (2005). *Non-marine sedimentation associated with oligocene-recent exhumation and uplift of the central Taurus mountains, S Turkey*. Sediment. Geol. *173*, 53e89.

Jaiswara, N. K., Pandey, P., & Pandey, A. K. (2019). *Mio-Pliocene piracy, relict landscape and drainage reorganization in the Namcha Barwa syntaxis zone of eastern Himalaya*. Scientific Reports, *9*(1), 1–11. https://doi.org/10.1038/s41598-019-54052-x.

Jolivet, L., & Faccenna, C. (2000). *Mediterranean extension and the Africa-Eurasia collision*. Tectonics. *19*(6), 1095–1106.https://doi.org/10.1029/2000TC900018.

Kandemir, Ö., Akbayram, K., Çobankaya, M., Kanar, F., Pehlivan, Ş., Tok, T., Hakyemez, A., Ekmekçi, E., Danacı, F., Temiz, U. (2019). *From arc evolution to arc-continent collision: Late Cretaceous middle Eocene geology of the Eastern Pontides, northeastern Turkey*. The Geological Society of America, *131*, 1889-1906.

Kar, N., Garzione, C. N., Jaramillo, C., Shanahan, T., Carlotto, V., Pullen, A., et al. (2016). *Rapid regional surface uplift of the northern Altiplano plateau revealed by multiproxy paleoclimate reconstruction*. Earth and Planetary Science Letters, *447*, 33–47. https://doi.org/ 10.1016/j.epsl.2016.04.025.

Karabacak V., Ring U., Uysal, I.T. (2020) *The off-fault deformation on the North Anatolian Fault zone and assessment of slip rate from carbonate veins*. Tectonophysics *795*:228633. https://doi.org/10.1016/j.tecto.2020.228633.

Karabacak, V., Sançar, T., Yildirim, G., & Uysal, I. T. (2021). *When did the North Anatolian fault reach southern Marmara, Turkey?* Geology, *50*(4). 432-436. https://doi.org/10.1130/g49726.1.

Karabıyıkoğlu, M., Çiner, A., Monod, O., Deynoux, M., Tuzcu, S., & Orcen, S. (2000). *Tectonosedimentary evolution of the Miocene Manavgat Basin, Western Taurids, Turkey*. In E. Bozkurt, J. A. Winchester, & J. D. A. Piper (Eds.), Tectonics and magmatism in Turkey and the surrounding area (*Vol. 173*, pp. 475–498). Geological Society.

Keller, E. A., & Pinter, N. (2002). *Active tectonics, earthquakes, uplift and landscape* (2nd ed.). Prentice Hall.

Kelletat, D., & Kayan, İ. (1983). *Alanya batısındaki kıyılarda ilk C14 tarihlendirmelerinin ışığında Geç Holosen tektonik hareketleri*. TJK Bülteni, *26*, 83–87.

Keskin, M. (2003). *Magma generation by slab steepening and breakoff beneath a subduction-accretion complex: An alternative model for collision-related volcanism in Eastern Anatolia*, Turkey. Geophysical Research Letters, *30*(24), 7–10. https://doi.org/10.1029/2003GL018019.

Kelling, G., Robertson, A. H. F., & Buchem, F. V. (2005). *Cenozoic sedimentary basins of southern Turkey: An introduction*. Sedimentary Geology, *173*, 1–13.

Kinnaird, T., & Robertson, A. (2013). *Tectonic and sedimentary response to subduction and incipient continental collision in southern cyprus, easternmost mediterranean region*. Geological Society Special Publication, *372*(1), 585–614. https://doi.org/10.1144/SP372.10.

Kiraly, A., Portner, D.E., Haynie, K.L., Chilson-Parks, B.H., Ghosh, T., Jadamec, M., Makushkina, A., Manga, M., Moresi, L., O'Farrel, K.A., (2020). *The effect of slab gaps on subduction dynamics and mantle upwelling*. Tectonophysics. *785*, 228458. https://doi.org/10.1016/j.tecto.2020.228458.

Kirby, E., & Whipple, K. (2001). *Quantifying differential rock-uplift rates via stream profile analysis*. Geology, *29*(5), 415–418. https://doi.org/10.1130/0091-7613(2001)0292.0.CO;2.

Kirby, E., & Whipple, K. X. (2012). *Expression of active tectonics in erosional landscapes*. Journal of Structural Geology, *44*, 54–75. https://doi.org/10.1016/j.jsg.2012.07.009.

Kirby, E., Whipple, K. X., Tang, W., & Chen, Z. (2003). *Distribution of active rock uplift along the eastern margin of the Tibetan plateau: Inferences from bedrock channel longitudinal profiles*. Journal of Geophysical Research, *108*(B4), 2217. https://doi.org/10.1029/2001jb000861.

Kissel, C., Lai, C., Poisson, A., and Görür, N. (2003). *Paleomagnetic reconstruction of the Cenozoic evolution of the eastern Mediterranean*, Tectonophysics, *362*, 199–217, https://doi.org/10.1016/S0040-1951(02)00638-8.

Koç, A., Kaymakci, N., van Hinsbergen, D.J.J., Kuiper, K.F., Vissers, R.L.M., (2012). *Tectono-Sedimentary evolution and geochronology of the Middle Miocene Altınapa Basin, and implications for the late Cenozoic uplift history of the Taurides, southern Turkey*. Tectonophysics *532–535*, 134–155. https://doi.org/10.1016/j. tecto.2012.01.028.

Koç, A., Kaymakci, N., van Hinsbergen, D.J.J., Vissers, R.L.M., (2016). *A Miocene onset of the modern extensional regime in the Isparta Angle: constraints from the Yalvaç Basin (Southwest Turkey)*. Int. J. Earth Sci. *105* (1), 369–398. https://doi.org/ 10.1007/s00531-014-1100-z.

Koç, A., Kaymakci, N., Van Hinsbergen, D.J.J., Kuiper, K.F., (2017). *Miocene tectonic history of the Central Tauride intramontane basins, and the paleogeographic evolution of the Central Anatolian Plateau*. Glob. Planet. Chang. https://doi.org/ 10.1016/j.gloplacha.2017.09.001.

Koçyigit, A., & Özacar, A. A. (2003). *Extensional neotectonic regime through the NE edge of outer Isparta Angle, SW Turkey: New field and seismic data*. Turkish Journal of Earth Sciences, *12*, 67–90.

Lague, D. (2014). *The stream power river incision model: Evidence, theory and beyond*. Earth Surface Processes and Landforms, *39*(1), 38–61. https://doi.org/10.1002/esp.3462.

Larue, J. P. (2008). *Effects of tectonics and lithology on long profiles of 16 rivers of the southern Central Massif border between the Aude and the Orb (France)*. Geomorphology, *93*(3–4), 343–367. https://doi.org/10.1016/j.geomorph.2007.03.003.

Larue, J. P. (2011). *Longitudinal profiles and knickzones: The example of the rivers of the Cher Basin in the northern French Massif Central*. Proceedings of the Geologists' Association, *122*(1), 125–142. https://doi.org/10.1016/j.pgeola.2010.08.006.

Li, Z., Qiu, J.S., Yang, X.M., (2014). *A review of the geochronology and geochemistry of late Yanshanian (Cretaceous) plutons along the Fujian coastal area of southeastern China: implications for magma evolution related to slab break-off and rollback in the cretaceous*. Earth-Sci. Rev. *128*, 232–248.

Liberatore, M., Gliozzi, E., Cipollari, P., Öğretmen, N., Spada, G., & Cosentino, D. (2022). *Vertical velocity fields along the Eastern Mediterranean coast as revealed by late Holocene sea-level markers*. Earth-Science Reviews, *234*, 104199. https://doi.org/10.1016/j.earscirev.2022.104199.

Ludwig., K., R. (2012). *User's Manual for Isoplot/Ex version 3.75: a Geochronological Toolkit for Microsoft Excel*: Berkeley Geochronology Center Special Publication, No. 5, 75pp.

McClusky, S., Balassanian, S., Barka, A., Demir, C., Ergintav, S., Georgiev, I., Gurkan, O., Hamburger, M., Hurst, K., Kahle, H., et al. (2000). *Global Positioning System constraints on plate kinematics and dynamics in the eastern Mediterranean and Caucasus*. J. Geophys. Res. x, *105*, 5695.

McKenzie, D. (1972). *Active Tectonics of the Mediterranean Region*. Geophysical Journal of the Royal Astronomical Society, *30*(2), 109–185. https://doi.org/10.1111/j.1365-246X.1972.tb02351.xq.

McPhee, P. J., Altıner, D., & van Hinsbergen, D. J. J. (2018). *First balanced cross section across the Taurides fold-thrust belt: Geological constraints on the subduction history of the Antalya slab in southern Anatolia*. Tectonics, *37*(10), 3738–3759. https://doi.org/10.1029/2017TC004893.

Meijers, M. J. M., Brocard, G. Y., Cosca, M. A., Ludecke, T., Teyssier, C., Whitney, D. L., & Mulch, A. (2018). *Rapid late Miocene surface uplift of the Central Anatolian Plateau margin*. Earth and Planetary Science Letters, *497*, 29–41. https://doi.org/10.1016/j.epsl.2018.05.040.

Moix. P., Beccaletto. L., Kozur. H.W., Hochard. C, Rosselet. F., Stampfi. G. M., (2008). *A new classifcation of the Turkish terranes and sutures and its implication for the paleotectonic history of the region*. Tectonophysics *451*:7–39. https://doi.org/10.1016/j.tecto.2007.11.044.

Monod, O., Kuzucuoğlu, C., & Okay, A. I. (2006). *A Miocene Palaeovalley Network in the Western Taurus (Turkey)*. Turkish Journal of Earth Sciences, *15*(1), 1–23.

Mueller, M. A., Licht, A., Campbell, C., Ocakoğlu, F., Taylor, M. H., Burch, L., et al., (2019). *Collision chronology along the İzmir-Ankara-Erzincan suture zone: Insights from the Sarıcakaya Basin, western Anatolia*. Tectonics, *38*. https://doi.org/10.1029/2019TC005683

Mutlu A., K., & Karabulut., H., (2011). *Anisotropic Pn tomography of Turkey and adjacent regions*. Geophysical Journal International *187* (3): 1743-1758. https://doi.org/10.1111/ j.1365-246X.2011.05235.x.

Nocquet, J. M., Sue, C., Walpersdorf, A., Tran, T., Lenôtre, N., Vernant, P., Cushing, M., Jouanne, F., Masson, F., Baize, S., Chery, J., and van der Beek, P. A., (2016). *Present-day uplift of the western Alps*, Scientific Reports, *6*, 28404, https://doi.org/10.1038/srep28404.

Nuriel, P., Craddock, J., Kylander-Clark, A. R. C., Uysal, I. T., Karabacak, V., Dirik, R. K., Hacker, B. R., & Weinberger, R. (2019). *Reactivation history of the North Anatolian fault zone based on calcite age-strain analyses*. Geology, *47*(5), 465–469. https://doi.org/10.1130/G45727.1.

Nuriel, P., Rosenbaum, G., Uysal, T. I., Zhao, J., Golding, S. D., Weinberger, R., Karabacak, V., & Avni, Y. (2011). *Formation of fault-related calcite precipitates and their implications for dating fault activity in the east Anatolian and dead sea fault zones*. Geological Society Special Publication, *359*(1), 229–248. https://doi.org/10.1144/SP359.13.

Nuriel, P., Rosenbaum, G., Zhao, J. X., Feng, Y., Golding, S. D., Villemant, B., & Weinberger, R. (2012). *U-Th dating of striated fault planes*. Geology, *40*(7), 647–650. https://doi.org/10.1130/g32970.1.

Okay, A.I., and Tüysüz, O., (1999). *Tethyan Sutures of Northern Turkey*. Geol. Soc. Lond. Spec. Publ., *vol. 156*, pp:475–515.

Okay, A. I., Tansel, İ., & Tüysüz, O. (2001*). Obduction, subduction and collision as reflected in the Upper Cretaceous–Lower Eocene sedimentary record of western Turkey*. Geological Magazine, *138*(2), 117–142. doi:10.1017/S0016756801005088.

Okay, A.I., Satir, M., Zattin, M., Cavazza, W., and Topuz, G. (2008). *An Oligocene ductile strike-slip shear zone: The Uludağ Massif, northwest Turkey—Implications for the westward translation of Anatolia*. GSA Bulletin, *120*, 893–911.

Okay, A. I., Zattin, M., & Cavazza, W. (2010). *Apatite fission-track data for the Miocene Arabia-Eurasia collision*. Geology, *38*(1), 35–38. https:// doi.org/10.1130/g30234.1.

Okay, A. I., Sunal, G., Sherlock, S., Kylander-Clark, A. R. C., Özcan, E. (2020). *İzmir-Ankara Suture as a Triassic to Cretaceous Plate Boundary-Data from Central Anatolia*. Tectonics. https://doi.org/10.1029/2019TC005849.

Oren, O., Nuriel, P., Kylander-Clark, A. R. C., & Haviv, I. (2020). *Evolution and Propagation of an Active Plate Boundary: U-Pb Ages of Fault-Related Calcite From the Dead Sea Transform*. Tectonics, *39*(8), 1–14. https://doi.org/10.1029/2019TC005888.

Öğretmen, N., Cipollari, P., Frezza, V., Faranda, C., Karanika, K., Gliozzi, E., Radeff, G., & Cosentino, D. (2018). *Evidence for 1.5 km of Uplift of the Central Anatolian Plateau's Southern Margin in the Last 450 kyr and Implications for Its Multiphased Uplift History*. Tectonics, *37*(1), 359–390. https://doi.org/10.1002/2017TC004805.

Özgül, N. (1976). *Toroslar'ın bazı temel jeolojik özellikleri*. Turkiye Jeoloji Kurumu Bulteni, *19*, 5–78.

Paton, C., Hellstrom, J., Paul, B., Woodhead, J. and Hergt, J., (2011). *Iolite: Freeware for the visualisation and processing of mass spectrometric data*. Journal of Analytical Atomic Spectrometry, *26*(12): 2508-2518.

Pavano, F., Pazzaglia, F. J., & Catalano, S. (2016). *Knickpoints as geomorphic markers of active tectonics: A case study from northeastern Sicily (southern Italy)*. Lithosphere, *8*(6), 633–648. https://doi.org/10.1130/L577.1

Perron, J. T., & Royden, L. (2013). *An integral approach to bedrock river profile analysis*. Earth Surface Processes and Landforms, *38*(6), 570–576. https://doi.org/10.1002/esp.3302

Petit, J., (1987). *Criteria for the sense of movement on fault surfaces in brittle rocks*. Journal of Structural Geology. *9*. 597–608.

Poisson, A., Orszag-Sperber, F., Kosun, E., Bassetti, M. A., Muller, C., Wernli, R., & Rouchy, J. M. (2011). *The late Cenozoic evolution of the Aksu basin (Isparta Angle; SW Turkey).* New insights. Bulletin de la Societe Geologique de France, *182*(2), 133–148. https://doi.org/10.2113/gssgfbull.182.2.1

Poisson, A., Yağmurlu, F., Bozcu, M., & Şentürk, M. (2003). *New insights on the tectonic setting and evolution around the apex of the Isparta Angle (SW Turkey)*. Geological Journal, *38*(3–4), 257–282. https://doi.org/10.1002/gj.955.

Portner, D. E., Delph, J. R., Biryol, C. B., Beck, S. L., Zandt, G., Özacar, A. A., Sandvol, E., and Türkelli, N., (2018). *Subduction termination through progressive slab deformation across Eastern Mediterranean subduction zones from updated P-wave tomography beneath Anatolia*. Geosphere. *14*, 3. 907-925.

Prince, P. S., & Spotila, J. A. (2013). *Evidence of transient topographic disequilibrium in a landward passive margin river system: Knickpoints and paleo-landscapes of the New River basin, southern Appalachians*. Earth Surface Processes and Landforms, *38*(14), 1685–1699. https://doi.org/10.1002/esp.3406.

Racano, S., Jara-Muñoz, J., Cosentino, D., & Melnick, D. (2020). *Variable Quaternary Uplift Along the Southern Margin of the Central Anatolian Plateau Inferred from Modeling Marine Terrace Sequences*. Tectonics, *39*(12). bhttps://doi.org/10.1029/2019TC005921.

Racano, S., Schildgen, T. F., Cosentino, D., & Miller, S. R. (2021). *Temporal and Spatial Variations in Rock Uplift from River-Profile Inversions at the Central Anatolian Plateau Southern Margin*. Journal of Geophysical Research: Earth Surface, *126*(8), 1–23. https://doi.org/10.1029/2020JF006027.

Reilinger, R., McClusky, S., Vernant, P., Lawrence, S., Ergintav, S., Cakmak, R., ... and Nadariya, M., (2006). *GPS constraints on continental deformation in the Africa-Arabia-Eurasia continental collision zone and implications for the dynamics of plate interactions*. Journal of Geophysical Research: Solid Earth, *111*(B5). https://doi.org/10.1029/2005JB004051.

Ring, U., Glodny, J., Will, T., & Thomson, S. (2010). *The hellenic subduction system: High-pressure metamorphism, exhumation, normal faulting, and large-scale extension*. Annual Review of Earth and Planetary Sciences, *38* (May 2014), 45–76. https://doi.org/10.1146/annurev.earth.050708.170910.

Ring, U., & Gerdes, A. (2016). *Kinematics of the Alpenrhein-Bodensee graben system in the Central Alps: Oligocene/Miocene transtension due to formation of the Western Alps arc*. Tectonics, *35*(6), 1367–1391. https://doi.org/10.1002/2015TC004085.

Ring, U., & Pantazides, H. (2019). *The Uplift of the Troodos Massif, Cyprus*. Tectonics, *38*(8), 3124–3139. https://doi.org/10.1029/2019TC005514.

Roberts, N. M. W., & Walker, R. J. (2016). U-*Pb geochronology of calcite-mineralized faults: Absolute timing of rift-related fault events on the northeast Atlantic margin*. Geology, *44*(7), 531–534. https://doi.org/10.1130/G37868.1.

Roberts, N. M. W., Drost, K., Horstwood, M. S. A., Condon, D. J., Chew, D., Drake, H., Milodowski, A. E., McLean, N. M., Smye, A. J., Walker, R. J., Haslam, R., Hodson, K., Imber, J., Beaudoin, N., & Lee, J. K. (2020). *Laser ablation inductively coupled plasma mass spectrometry (LA-ICP-MS) U-Pb carbonate geochronology: Strategies, progress, and limitations*. Geochronology, *2*(1), 33–61. https://doi.org/10.5194/gchron-2-33-2020.

Roberts, N.M.W., Rasbury, E.T., Parrish, R.R., Smith, C.J., Horstwood, M.S.A. and Condon, D.J., (2017). *A calcite reference material for LA-ICP-MS U-Pb geochronology*. Geochemistry, Geophysics, Geosystems, *18*(7): 2807-2814.

Robertson, A.H.F., (1998). *Tectonic significance of the Eratosthenes Seamount: A continental fragment in the process of collision with a subduction zone in the Eastern Mediterranean (Ocean Drilling Program Leg 160):* Tectonophysics, *298*, 63–82, https:// doi .org /10 .1016 /S0040-1951 (98)00178 -4.

Robertson, A.H., Parlak, O. and Ustaömer, T., (2012*). Overview of the Palaeozoic–Neogene evolution of neotethys in the Eastern Mediterranean region (southern turkey, cyprus, Syria).* Petroleum Geoscience, *18*(4), 381-404.

Sarıkaya, M. A., Yıldırım, C., and Çiner, A. (2015), *No surface breaking on Ecemiş Fault, central Turkey, since Late Pleistocene (~64.5 ka); new geomorphic and geochronologic data from cosmogenic dating of offset alluvial fans*, Tectonophysics, *649*, 33–46.

Schattner, U. (2010). *What triggered the early-to-mid Pleistocene tectonic transition across the entire eastern Mediterranean?* Earth and Planetary Science Letters, *289*(3–4), 539–548. https://doi.org/10.1016/j.epsl.2009.11.048.

Schildgen, T. F., Cosentino, D., Bookhagen, B., Niedermann, S., Yildirim, C., Echtler, H., Wittmann, H., & Strecker, M. R. (2012a). *Multi-phased uplift of the southern margin of the Central Anatolian plateau, Turkey: A record of tectonic and upper mantle processes*. Earth and Planetary Science Letters, *317–318*, 85–95. https://doi.org/10.1016/j.epsl.2011.12.003.

Schildgen, T. F., Cosentino, D., Caruso, A., Buchwaldt, R., Yildirim, C., Bowring, S. A., Rojay, B., Echtler, H., & Strecker, M. R. (2012b). *Surface expression of eastern Mediterranean slab dynamics: Neogene topographic and structural evolution of the southwest margin of the Central Anatolian Plateau, Turkey*. Tectonics, *31*(2). https://doi.org/10.1029/2011TC003021.

Schildgen, T. F., Yildirim, C., Cosentino, D., & Strecker, M. R. (2014). *Linking slab breakoff, Hellenic trench retreat, and uplift of the Central and Eastern Anatolian plateaus*. Earth-Science Reviews, *128*, 147–168. https://doi.org/10.1016/j.earscirev.2013.11.006.

Schmid, S. M., Fügenschuh, B., Kounov, A., Maţenco, L., Nievergelt, P., Oberhänsli, R., et al. (2020). *Tectonic units of the Alpine collision zone between Eastern Alps and western Turkey*. Gondwana Research, *78*, 308–374. https://doi.org/10.1016/j.gr.2019.07.005.

Schwanghart, W., & Scherler, D. (2014). *Short communication: TopoToolbox 2 - MATLAB-based software for topographic analysis and modeling in Earth surface sciences*. Earth Surface Dynamics, *2(1)*, 1–7. https://doi.org/10.5194/esurf-2-1-2014.

Şengör, A. M. C., & Yilmaz, Y. (1981). *Tethyan evolution of Turkey: A plate tectonics approach*. Tectonophysics, *75*(3–4), 181–241. https://doi.org/10.1016/0040-1951(81)90275-4

Şengör, A. M. C., Görür, N., & Şaroğlu, F. (1985). *Strike slip faulting and related basin formation in zones of tectonic escape: Turkey as a case study*. In K. D. Biddle & N. Christie-Blick (Eds.), Strike- slip deformation, basin formation and sedimentation (*Vol. 17*, pp. 227–264). Society of Economic Paleontologists and Mineralogists Special Publication.

Şengör, A. M. C., Özeren, S., Genç, T., & Zor, E. (2003). *East Anatolian High Plateau as a mantle-supported, north-south shortened domal structure*. Geophysical Research Letters, *30*(24). https://doi.org/10.1029/2003GL017858.

Snyder, N. P., Whipple, K. X., Tucker, G. E., & Merritts, D. J. (2000). Landscape response to tectonic forcing: Digital elevation model analysis of stream profiles in the Mendocino triple junction region, northern California. Geological Society of America Bulletin, 112(8), 1250–1263. https://doi.org/10.1130/00167606(2000)112<1250:LRTTFD>2.0.CO;2.

Stearns, R. G. (1967). *Warping on the Western Highland Rim Peneplain in Tennesse by groundwater sapping*. Geological Society of America Bulletin, *78*(9), 1111–1124. https://doi.org/10.1130/0016-7606(1967)78[1111:WOTWHR]2.0.CO;2

Tezel, T., Shibutani, T., Kaypak, B., (2013). *Crustal thickness of Turkey determined by receiver function*. J. Asian Earth Sci. *75*, 36–45.

Tucker, G. E., & Whipple, K. X. (2002). *Topographic outcomes predicted by stream erosion models: Sensitivity analysis and intermodel comparison*. Journal of Geophysical Research, *107*(B9), ETG1-1–ETG1-16. https://doi.org/10.1029/2001JB000162

Umhoefer, P.J., Lefebvre, C., Thomson, S.N., Cosca, M.A., Teyssier, C., and Whitney, D.L., (2020). *Cenozoic tectonic evolution of a reactivated suture zone during the transition from Arabia-Eurasia collision to escape tectonics: The Ecemiş fault and adjacent basins, central Anatolia, Turkey:* Geosphere, *v. 16*, p. 1358–1384, https://doi.org/10.1130/GES02255.1

Uysal, I. T., Feng, Y. xing, Zhao, J. xin, Isik, V., Nuriel, P., & Golding, S. D. (2009). *Hydrothermal CO2 degassing in seismically active zones during the late Quaternary*. Chemical Geology, *265*(3–4), 442–454. https://doi.org/10.1016/j.chemgeo.2009.05.011.

Uysal, I. T., Feng, Y., Zhao, J. xin, Altunel, E., Weatherley, D., Karabacak, V., Cengiz, O., Golding, S. D., Lawrence, M. G., & Collerson, K. D. (2007). *U-series dating and geochemical tracing of late Quaternary travertine in co-seismic fissures*. Earth and Planetary Science Letters, *257*(3–4), 450–462. https://doi.org/10.1016/j.epsl.2007.03.004.

Uysal, I. T., Ünal-İmer, E., Shulmeister, J., Zhao, J. X., Karabacak, V., Feng, Y. X., & Bolhar, R. (2019). *Linking CO2 degassing in active fault zones to long-term changes in water balance and surface water circulation, an example from SW Turkey*. Quaternary Science Reviews, *214*, 164–177. https://doi.org/10.1016/j.quascirev.2019.04.029.

Üner, S., Özsayin, E., Kutluay, A., & Dirik, K. (2015). *Polyphase tectonic evolution of the Aksu Basin, Isparta Angle (Southern Turkey).* Geologica Carpathica, *66*(2), 157–169. https://doi.org/10.1515/geoca-2015-0017.

van Hunen, J.,& Allen, M.B., (2011). *Continental collision and slab break-off: A comparison of 3-D numerical models with observations*. Earth Planet. Sci. Lett. *302*, 27–37.

Vidal, N., Alvarez-Marrón, J., & Klaeschen, D. (2000). *The structure of the Africa-Anatolia plate boundary in the Eastern Mediterranean*. Tectonics, *19*(4), 723–739. https://doi.org/10.1029/2000TC900011.

Wang, J., Hu, Z., Pan, B., Li, M., Dong, Z., Li, X., et al. (2019). *Spatial distribution pattern of channel steepness index as evidence for differential rock uplift along the eastern Altun Shan on the northern Tibetan Plateau*. Global and Planetary Change, *181*, 102979. https://doi. org/10.1016/j.gloplacha.2019.102979

Wdowinski, S., Ben-Avraham, Z., Arvidsson, R. & Ekström, G. (2006). *Seismotectonics of the Cyprian Arc*. Geophysical Journal International. *164*(1). 176–181.

Weinberger, R., Nuriel, P., Kylander-Clark, A. R. C., & Craddock, J. P. (2020). *Temporal and spatial relations between large-scale fault systems: Evidence from the Sinai-Negev shear zone and the Dead Sea Fault.* Earth-Science Reviews, *211*(July), 103377. https://doi.org/10.1016/j.earscirev.2020.103377.

Whipple, K. X., DiBiase, R. A., Ouimet, W. B., & Forte, A. M. (2017). *Preservation or piracy: Diagnosing low-relief, high-elevation surface formation mechanisms*. Geology, *45*(1), 91–94. https://doi.org/10.1130/g38490.1.

Wobus, C., Whipple, K. X., Kirby, E., Snyder, N., Johnson, J., Spyropolou, K., et al. (2006). *Tectonics from topography: Procedures, promise, and pitfalls*. In S. D. Willett, N. Hovius, M. T. Brandon, & D. M. Fisher (Eds.), Tectonics, climate, and landscape evolution, Geological Society of America Special Paper, Penrose Conference Series, (*Vol. 398*, pp. 55–74). https://doi.org/10.1130/2006.2398(04).

Yıldırım, C., Schildgen, T. F., Echtler, H., Melnick, D., & Strecker, M. R. (2011). *Late Neogene and active orogenic uplift in the Central Pontides associated with the North Anatolian Fault: Implications for the northern margin of the Central Anatolian Plateau, Turkey*. Tectonics, *30*(5). https://doi.org/10.1029/2010TC002756.

Yıldırım, C., Sarıkaya, M. A., & Çiner, A. (2016). *Late Pleistocene intraplate extension of the Central Anatolian Plateau, Turkey: Inferences from cosmogenic exposure dating of alluvial fan, landslide, and moraine surfaces along the Ecemiş Fault Zone*. Tectonics, *35*(6), 1446–1464. https:// doi.org/10.1002/2015TC004038.

Yıldırım, C., & Tüysüz, O. (2017). *Estimation of the long-term slip, surface uplift and block rotation along the northern strand of the North Anatolian Fault Zone: Inferences from geomorphology of the Almacık Block*. Geomorphology, *297*, 55–68. https://doi.org/10.1016/j.geomorph.2017.08.038.

Zhao, J. X., Yu, K. F., and Feng, Y. X., (2009). *High-precision 238U-234U-230Th disequilibrium dating of the recent past – a review*. Quaternary Geochronology, *4*, 423–433.

Zhao, J.X. & Collins L. (2011). *Uranium Series Dating. In Encyclopedia of Modern Coral Reefs-Structure, Form and Process*, ed. David Hopley. *1128-1132*. Dordrecht, The Netherlands, Springer.

Zhou, H., Zhao, J., Qing, W., Feng, Y., and Tang, J., (2011). *Speleothem-derived Asian summer monsoon variations in Central China, 54-46 ka:* Journal of Quaternary Science, *v. 26*, no. 8, p. 781-790.

APPENDICES

APPENDIX A: Detailed LA-ICP-MS U-Pb dating data.

APPENDIX A: Detailed LA-ICP-MS U-Pb dating data.

Table A.1: Details of LA-ICP-MS U-Pb age data.

Laser spot ID	238U/206Pb	2SE	207Pb/206Pb	2SE	U_PPM	Pb_PPM	Location 12 Sample b
1	19,046	0,911	0,757	0,051	12,291	2,180	
2	0,883	0,047	0,777	0,058	0,469	1,675	
3	4,475	0,129	0,749	0,030	1,239	0,926	
4	4,766	0,169	0,738	0,037	1,217	0,831	
5	6,707	0,231	0,730	0,035	1,374	0,659	
6	6,190	0,184	0,763	0,031	1,105	0,598	
7	3,784	0,072	0,758	0,017	0,685	0,606	
8	5,620	0,517	0,770	0,097	0,809	0,444	
9	6,484	0,234	0,752	0,036	0,716	0,368	
10	7,864	0,189	0,737	0,023	0,878	0,372	
11	7,797	0,206	0,742	0,024	0,827	0,355	
12	8,467	0,235	0,727	0,025	0,773	0,301	
13	10,740	0,277	0,716	0,024	0,977	0,293	
14	10,653	0,310	0,714	0,027	0,944	0,289	
15	11,567	0,263	0,732	0,021	0,855	0,243	
16	11,380	0,269	0,714	0,023	0,803	0,227	
17	14,029	0,322	0,680	0,018	0,948	0,210	
18	9,694	0,616	0,760	0,068	0,533	0,187	
19	13,532	0,380	0,691	0,026	0,710	0,167	
20	14,611	1,468	0,748	0,119	0,628	0,147	

Table A.1 (continued): Details of LA-ICP-MS U-Pb age data.

21	21,158	1,270	0,707	0,060	0,814	0,127
22	18,359	1,030	0,718	0,058	0,604	0,107
23	9,254	1,122	0,718	0,119	0,305	0,116
24	21,969	1,422	0,708	0,068	0,619	0,091
25	40,358	1,778	0,676	0,040	0,494	0,038
26	5,453	0,422	0,834	0,098	0,045	0,029
27	22,676	1,235	0,724	0,050	0,175	0,025
28	11,745	1,958	0,633	0,141	0,079	0,023
29	16,243	0,893	0,710	0,053	0,104	0,021
30	96,944	8,925	0,458	0,065	0,964	0,025
31	23,611	1,765	0,735	0,066	0,129	0,018
32	50,061	5,471	0,678	0,095	0,419	0,019
33	39,659	3,949	0,666	0,085	0,195	0,016
34	17,858	2,576	0,721	0,153	0,083	0,015
35	27,511	2,231	0,808	0,085	0,098	0,012
36	114,230	9,828	0,388	0,068	0,815	0,016
37	8,194	0,682	0,801	0,086	0,030	0,012
38	12,264	1,149	0,763	0,091	0,039	0,010
39	26,325	3,026	0,669	0,100	0,089	0,011
40	42,809	3,401	0,583	0,057	0,167	0,012
41	40,181	2,820	0,601	0,061	0,135	0,010
42	35,509	4,267	0,700	0,117	0,091	0,009
43	6,362	0,751	0,816	0,132	0,015	0,008
44	6,232	0,678	0,750	0,107	0,015	0,008
45	53,263	4,645	0,595	0,072	0,147	0,008

Table A.1 (continued): Details of LA-ICP-MS U-Pb age data.

46	6,497	0,829	0,751	0,123	0,015	0,007
47	46,741	4,769	0,755	0,097	0,101	0,007
48	5,235	0,598	0,788	0,112	0,011	0,007
49	28,275	4,451	0,735	0,163	0,055	0,006
50	163,301	10,770	0,275	0,044	0,821	0,010
51	82,016	6,682	0,509	0,060	0,216	0,007
52	16,965	1,916	0,773	0,111	0,028	0,006
53	71,017	8,808	0,607	0,101	0,130	0,005
54	15,193	2,192	0,782	0,144	0,021	0,005
55	97,981	9,850	0,407	0,062	0,185	0,005
56	27,511	4,213	0,732	0,142	0,028	0,003
57	127,771	11,227	0,302	0,045	0,318	0,005
58	127,416	13,468	0,417	0,071	0,217	0,004
59	203,131	14,863	0,161	0,033	0,685	0,006
60	95,429	15,905	0,421	0,100	0,093	0,002
61	157,139	17,789	0,223	0,044	0,250	0,003
62	192,868	20,708	0,191	0,040	0,341	0,003

Laser spot ID	**238U/206Pb**	**2SE**	**207Pb/206Pb**	**2SE**	**U_PPM**	**Pb_PPM**
1	0,054	0,002	0,775	0,007	0,021	1,263
2	0,545	0,024	0,771	0,011	0,079	0,476
3	0,613	0,049	0,793	0,036	0,021	0,111
4	0,635	0,070	0,835	0,082	0,005	0,020
5	1,030	0,081	0,816	0,047	0,008	0,025
6	2,018	0,089	0,785	0,023	0,055	0,089

Location 11 Sample a

Table A.1 (continued): Details of LA-ICP-MS U-Pb age data.

7	2,300	0,863	0,750	0,021	0,381	0,460
8	2,698	0,135	0,751	0,013	0,292	0,344
9	3,446	0,361	0,729	0,055	0,027	0,020
10	3,883	0,197	0,811	0,050	0,037	0,033
11	4,164	0,089	0,723	0,006	1,958	1,516
12	4,183	0,247	0,724	0,007	1,900	1,460
13	4,445	0,204	0,772	0,033	0,075	0,056
14	4,580	0,176	0,767	0,024	0,140	0,101
15	4,714	0,167	0,748	0,007	1,362	0,970
16	4,768	0,346	0,735	0,006	1,881	1,283
17	4,918	0,263	0,740	0,010	0,649	0,437
18	5,429	0,218	0,740	0,007	1,476	0,887
19	5,442	0,283	0,737	0,009	1,521	0,917
20	6,176	0,245	0,727	0,009	1,522	0,778
21	6,377	0,318	0,738	0,017	0,333	0,177
22	6,444	0,320	0,727	0,011	1,144	0,564
23	6,867	0,717	0,719	0,015	0,573	0,230
24	7,379	0,266	0,723	0,012	1,103	0,482
25	7,463	0,309	0,727	0,009	1,125	0,489
26	7,542	0,680	0,960	0,110	0,029	0,013
27	7,611	0,466	0,734	0,017	0,387	0,158
28	7,733	0,650	0,761	0,064	0,034	0,013
29	7,865	1,008	0,742	0,041	0,098	0,043
30	8,136	0,460	0,721	0,016	0,449	0,175
31	8,179	0,618	0,729	0,027	0,184	0,074

Table A.1 (continued): Details of LA-ICP-MS U-Pb age data.

32	8,434	0,387	0,720	0,021	0,207	0,079
33	8,600	0,330	0,707	0,008	1,578	0,587
34	9,102	0,477	0,726	0,019	0,302	0,106
35	9,276	0,421	0,710	0,012	1,266	0,447
36	9,389	1,054	0,705	0,025	0,292	0,099
37	9,605	0,451	0,808	0,051	0,083	0,029
38	9,635	0,666	0,703	0,012	1,520	0,418
39	10,456	0,701	0,750	0,044	0,084	0,024
40	10,994	0,736	0,730	0,051	0,071	0,020
41	11,662	0,843	0,694	0,039	0,142	0,036
42	13,472	0,809	0,828	0,056	0,082	0,021
43	13,837	0,853	0,751	0,039	0,129	0,030
44	13,879	0,921	0,720	0,031	0,247	0,060
45	13,900	0,903	0,704	0,027	0,306	0,068
46	14,288	1,021	0,696	0,015	0,930	0,209
47	14,491	0,548	0,726	0,017	0,795	0,177
48	15,947	0,719	0,702	0,017	0,665	0,141
49	16,115	0,847	0,727	0,031	0,224	0,046
50	19,917	1,078	0,675	0,018	0,768	0,118
51	23,004	1,380	0,665	0,027	0,394	0,052
52	24,343	1,288	0,684	0,033	0,351	0,046
53	25,703	2,513	0,820	0,110	0,073	0,009
54	26,827	2,503	0,655	0,032	0,367	0,051
55	28,577	1,509	0,671	0,034	0,377	0,044
56	30,469	2,018	0,697	0,050	0,169	0,017
57	32,174	1,912	0,675	0,047	0,213	0,020

Table A.1 (continued): Details of LA-ICP-MS U-Pb age data.

58	33,583	3,187	0,680	0,066	0,159	0,014
59	44,864	1,619	0,639	0,021	0,820	0,056
60	46,240	4,182	0,720	0,140	0,092	0,006
61	52,883	4,559	0,730	0,110	0,149	0,008
62	53,189	3,689	0,570	0,034	0,558	0,032
63	55,768	4,056	0,645	0,066	0,146	0,008
64	56,245	2,750	0,596	0,026	0,938	0,048
65	62,174	2,815	0,589	0,026	1,055	0,046
66	65,260	5,091	0,624	0,064	0,242	0,011
67	75,424	6,801	0,557	0,072	0,304	0,011
68	76,299	6,263	0,551	0,075	0,513	0,018
69	133,746	7,582	0,319	0,029	0,853	0,013
70	197,038	19,830	0,190	0,052	0,344	0,003

Laser spot ID	**238U/206Pb**	**2SE**	**207Pb/206Pb**	**2SE**	**U_PPM**	**Pb_PPM**
1	95,377	15,220	0,463	0,131	0,100	0,003
2	114,941	19,157	0,332	0,092	0,054	0,001
3	99,616	19,923	0,556	0,153	0,052	0,002
4	129,934	22,597	0,494	0,135	0,062	0,001
5	84,579	14,363	0,582	0,158	0,056	0,002
6	95,377	15,220	0,679	0,182	0,090	0,002
7	68,965	12,201	0,391	0,104	0,106	0,003
8	62,695	10,522	0,751	0,179	0,066	0,003
9	89,654	13,448	0,551	0,131	0,036	0,001
10	32,840	5,534	0,702	0,166	0,083	0,008
11	65,441	10,031	0,593	0,140	0,305	0,015

Location 13 Sample b

Table A.1 (continued): Details of LA-ICP-MS U-Pb age data.

12	205,158	15,492	0,232	0,051	0,474	0,004
13	110,684	15,031	0,448	0,098	0,067	0,002
14	151,956	19,574	0,304	0,066	0,110	0,001
15	139,648	21,535	0,555	0,119	0,065	0,001
16	142,761	18,641	0,382	0,082	0,106	0,002
17	21,500	3,403	0,738	0,156	0,049	0,008
18	209,963	25,078	0,216	0,045	0,174	0,001
19	87,896	10,341	0,491	0,103	0,391	0,012
20	161,831	22,493	0,371	0,077	0,095	0,001
21	233,474	21,280	0,151	0,032	0,326	0,002
22	228,128	16,834	0,111	0,022	0,427	0,003
23	140,524	16,079	0,334	0,064	0,098	0,002
24	63,585	8,117	0,525	0,098	0,063	0,003
25	109,334	14,667	0,545	0,099	0,148	0,004
26	222,467	18,769	0,169	0,031	0,498	0,004
27	117,348	10,445	0,357	0,063	0,236	0,005
28	12,937	1,605	0,588	0,104	0,102	0,021
29	72,890	8,889	0,507	0,090	0,054	0,002
30	154,576	15,458	0,281	0,049	0,204	0,003
31	46,695	5,837	0,608	0,105	0,093	0,006
32	27,930	2,871	0,545	0,090	0,069	0,006
33	72,302	8,163	0,562	0,090	0,064	0,002
34	52,429	5,825	0,594	0,095	0,063	0,004
35	96,402	11,402	0,493	0,079	0,077	0,002
36	121,978	10,953	0,386	0,062	0,207	0,004
37	238,442	18,390	0,154	0,024	0,512	0,003

Table A.1 (continued): Details of LA-ICP-MS U-Pb age data.

38	200,121	14,741	0,165	0,026	0,374	0,003
39	44,827	5,155	0,424	0,065	0,044	0,002
40	131,651	12,566	0,274	0,042	0,257	0,004
41	110,548	11,723	0,455	0,069	0,124	0,003
42	169,800	17,366	0,375	0,057	0,179	0,002
43	22,470	2,422	0,624	0,094	0,047	0,007
44	168,207	9,468	0,215	0,032	1,387	0,014
45	42,692	3,863	0,539	0,079	0,670	0,042
46	33,832	3,575	0,720	0,104	0,056	0,006
47	196,610	15,522	0,253	0,036	0,446	0,004
48	141,634	12,978	0,336	0,048	0,207	0,003
49	251,132	13,366	0,126	0,018	0,915	0,005
50	126,096	9,400	0,432	0,060	0,308	0,006
51	19,791	1,922	0,562	0,077	0,419	0,058
52	57,105	6,183	0,601	0,083	0,068	0,003
53	98,197	8,389	0,447	0,060	0,201	0,005
54	250,431	12,591	0,084	0,011	1,229	0,007
55	169,479	11,534	0,252	0,033	0,459	0,005
56	92,618	7,750	0,498	0,065	0,306	0,009
57	131,073	9,007	0,406	0,051	2,497	0,043
58	33,083	2,564	0,624	0,078	0,204	0,019
59	5,784	0,522	0,508	0,064	0,063	0,026
60	124,347	10,520	0,406	0,050	0,192	0,003
61	18,562	1,768	0,590	0,071	0,114	0,017
62	225,829	10,239	0,085	0,010	1,185	0,007
63	91,019	6,284	0,474	0,056	0,290	0,008

Table A.1 (continued): Details of LA-ICP-MS U-Pb age data.

64	136,668	9,375	0,348	0,041	0,265	0,004
65	87,553	6,755	0,538	0,063	0,192	0,006
66	135,225	8,974	0,484	0,056	0,796	0,014
67	156,465	8,738	0,296	0,033	0,511	0,006
68	83,013	6,610	0,548	0,061	0,166	0,005
69	185,619	9,223	0,197	0,022	2,611	0,024
70	155,920	8,406	0,333	0,036	1,105	0,014
71	34,616	2,539	0,513	0,055	0,428	0,030
72	77,825	5,202	0,450	0,046	0,400	0,013
73	48,991	3,480	0,539	0,055	0,168	0,009
74	73,008	5,707	0,570	0,058	0,127	0,005
75	73,911	5,484	0,610	0,062	0,132	0,005
76	194,057	13,441	0,258	0,026	0,549	0,005
77	38,151	2,922	0,550	0,054	0,083	0,006
78	150,174	8,553	0,281	0,027	0,798	0,010
79	235,436	6,801	0,078	0,007	2,944	0,017
80	93,487	5,654	0,515	0,043	0,427	0,012
81	84,025	4,174	0,441	0,037	0,950	0,028
82	225,262	8,490	0,101	0,008	3,062	0,019
83	104,370	5,832	0,378	0,031	0,522	0,011
84	243,625	7,944	0,070	0,005	3,060	0,017
85	14,507	0,775	0,552	0,041	0,369	0,069
86	43,458	2,043	0,609	0,037	0,252	0,017
87	13,667	0,563	0,603	0,032	1,904	0,401
88	15,247	0,596	0,702	0,033	0,133	0,027
89	34,589	1,081	0,637	0,027	1,783	0,153

Table A.1 (continued): Details of LA-ICP-MS U-Pb age data.

90	69,607	2,324	0,543	0,023	1,048	0,041
91	54,336	1,251	0,488	0,016	20,830	0,964
92	7,716	0,193	0,615	0,017	1,662	0,619
Laser spot ID	**238U/206Pb**	**2SE**	**207Pb/206Pb**	**2SE**	**U_PPM**	**Pb_PPM**
1	106,731	21,600	0,613	0,167	0,030	0,001
2	195,751	37,184	0,382	0,105	0,072	0,001
3	161,248	28,712	0,467	0,124	0,056	0,001
4	152,993	25,586	0,435	0,108	0,077	0,001
5	110,684	17,764	0,636	0,136	0,059	0,002
6	22,929	3,636	0,655	0,155	0,016	0,002
7	42,897	6,773	0,996	0,201	0,022	0,002
8	44,827	6,948	0,689	0,143	0,039	0,004
9	21,195	3,157	0,679	0,144	0,060	0,009
10	88,766	13,183	0,589	0,128	0,101	0,003
11	140,524	20,704	0,419	0,096	0,072	0,001
12	171,096	24,815	0,341	0,080	0,083	0,001
13	132,233	19,113	0,569	0,118	0,072	0,002
14	4,170	0,601	0,692	0,133	0,003	0,002
15	60,577	8,595	0,677	0,144	0,049	0,003
16	246,303	34,509	0,293	0,071	0,139	0,001
17	6,183	0,853	0,681	0,130	0,061	0,031
18	147,700	20,196	0,513	0,096	0,098	0,002
19	85,385	11,385	0,511	0,097	0,079	0,003
20	31,130	4,107	0,615	0,106	0,026	0,002
21	101,880	12,735	0,610	0,112	0,082	0,002

Location 14 Sample a

Table A.1 (continued): Details of LA-ICP-MS U-Pb age data.

22	210,456	25,689	0,228	0,055	0,168	0,001
23	57,105	6,911	0,615	0,115	0,071	0,004
24	22,929	2,756	0,739	0,111	0,024	0,003
25	163,008	19,561	0,327	0,060	0,200	0,003
26	202,837	23,863	0,361	0,064	0,171	0,002
27	121,154	13,589	0,386	0,061	0,135	0,003
28	77,288	8,662	0,688	0,121	0,090	0,004
29	196,180	21,893	0,245	0,054	0,168	0,002
30	43,103	4,766	0,778	0,135	0,077	0,005
31	228,128	24,961	0,222	0,044	0,245	0,002
32	25,542	2,765	0,631	0,092	0,038	0,004
33	10,894	1,178	0,674	0,103	0,074	0,020
34	155,920	16,812	0,387	0,059	0,149	0,002
35	165,109	17,636	0,265	0,047	0,202	0,002
36	10,006	1,061	0,717	0,108	0,064	0,021
37	36,895	3,796	0,615	0,083	0,056	0,004
38	4,094	0,411	0,659	0,089	0,025	0,020
39	42,692	4,269	0,643	0,089	0,050	0,004
40	136,668	13,333	0,518	0,066	0,183	0,003
41	117,502	11,242	0,455	0,064	0,225	0,005
42	25,326	2,361	0,754	0,084	0,037	0,005
43	75,340	6,964	0,548	0,066	0,117	0,004
44	242,309	22,266	0,210	0,030	0,339	0,002
45	232,265	19,857	0,173	0,029	0,472	0,003
46	241,655	20,192	0,106	0,019	0,465	0,003
47	72,127	5,803	0,548	0,061	0,213	0,009

Table A.1 (continued): Details of LA-ICP-MS U-Pb age data.

48	275,859	22,069	0,104	0,021	0,480	0,003
49	9,630	0,745	0,818	0,084	0,037	0,014
50	269,232	20,213	0,092	0,017	0,502	0,003
51	28,017	1,751	0,664	0,054	0,146	0,016
52	176,485	10,770	0,269	0,030	0,473	0,005
53	72,477	4,277	0,580	0,051	0,421	0,016
54	83,090	4,851	0,584	0,046	0,320	0,011
55	56,636	3,148	0,587	0,047	0,464	0,022
56	30,085	1,615	0,653	0,049	0,396	0,039
57	191,569	9,824	0,293	0,022	0,832	0,008
58	15,144	0,742	0,695	0,044	0,235	0,047
59	14,942	0,672	0,813	0,047	0,191	0,045
60	45,812	2,013	0,607	0,037	3,590	0,220
61	27,086	1,146	0,688	0,041	0,676	0,078
62	229,295	9,383	0,149	0,014	1,842	0,013

Laser spot ID	**238U/206Pb**	**2SE**	**207Pb/206Pb**	**2SE**	**U_PPM**	**Pb_PPM**
1	3,012	0,076	0,763	0,025	0,558	0,626
2	31,590	1,198	0,723	0,034	0,494	0,052
3	12,724	1,149	0,755	0,098	0,474	0,128
4	4,681	0,158	0,760	0,035	0,759	0,536
5	3,093	0,072	0,741	0,021	0,502	0,538
6	5,241	0,129	0,761	0,022	0,597	0,384
7	35,235	3,117	0,689	0,095	0,712	0,059
8	57,186	3,177	0,667	0,048	0,443	0,024
9	90,169	4,260	0,606	0,039	0,879	0,028

Location 9 Sample f

Table A.1 (continued): Details of LA-ICP-MS U-Pb age data.

10	3,335	0,075	0,768	0,020	0,514	0,516
11	4,608	0,202	0,765	0,046	1,599	1,186
12	3,203	0,347	0,776	0,119	0,732	0,806
13	2,454	0,046	0,758	0,017	0,731	1,002
14	54,858	3,942	0,690	0,062	0,246	0,014
15	3,377	0,093	0,753	0,028	0,253	0,244
16	1,782	0,090	0,769	0,054	0,133	0,243
17	3,662	0,066	0,764	0,015	0,768	0,711
18	5,127	0,158	0,768	0,030	0,196	0,131
19	1,022	0,029	0,765	0,028	1,048	3,490
20	23,734	0,861	0,741	0,032	0,806	0,112
21	8,382	0,230	0,744	0,026	0,433	0,171
22	8,253	0,335	0,737	0,040	0,438	0,168
23	2,918	0,121	0,763	0,042	0,290	0,341
24	5,552	0,168	0,763	0,031	0,487	0,297
25	19,829	2,575	0,722	0,135	6,040	0,389
26	2,013	0,354	0,765	0,191	0,407	0,960
27	6,615	0,162	0,760	0,024	0,270	0,137
28	12,464	0,356	0,735	0,025	0,835	0,219
29	4,968	0,105	0,739	0,019	0,256	0,172
30	6,003	0,240	0,752	0,041	0,471	0,269
31	5,012	0,104	0,757	0,018	0,778	0,525
32	32,372	2,745	0,718	0,087	1,025	0,103
33	2,373	0,098	0,763	0,044	0,935	1,343
34	10,363	0,352	0,743	0,032	0,696	0,223
35	5,953	0,135	0,749	0,020	0,466	0,262

Table A.1 (continued): Details of LA-ICP-MS U-Pb age data.

36	2,545	0,092	0,766	0,038	0,352	0,474
37	4,174	0,074	0,756	0,014	0,721	0,578
38	6,186	0,322	0,758	0,055	0,896	0,486
39	3,298	0,096	0,761	0,030	0,381	0,383
40	5,662	0,126	0,757	0,021	0,795	0,470
41	3,153	0,069	0,771	0,020	0,436	0,471
42	11,091	0,282	0,754	0,023	0,471	0,141
43	4,581	0,112	0,748	0,022	0,445	0,322
44	2,411	0,076	0,764	0,030	0,359	0,507
45	4,979	0,406	0,749	0,085	0,759	0,504
46	5,182	0,132	0,750	0,025	0,425	0,274
47	4,092	0,091	0,764	0,020	0,921	0,765
48	3,214	0,135	0,761	0,046	0,410	0,428
49	7,140	0,217	0,751	0,029	0,726	0,334
50	4,245	0,096	0,765	0,020	0,480	0,380
51	3,638	0,127	0,760	0,036	0,339	0,319
52	4,473	0,111	0,740	0,024	0,314	0,233
53	6,003	0,283	0,746	0,047	0,342	0,188
54	3,637	0,141	0,758	0,041	0,693	0,623
55	4,202	0,118	0,763	0,028	0,547	0,440
56	6,318	0,157	0,749	0,023	0,358	0,187
57	3,201	0,105	0,771	0,033	0,767	0,821
58	4,043	0,141	0,759	0,036	0,481	0,388
59	10,665	0,410	0,751	0,037	0,550	0,171
60	3,096	0,076	0,772	0,022	0,468	0,508
61	4,362	0,291	0,757	0,070	0,187	0,140

Table A.1 (continued): Details of LA-ICP-MS U-Pb age data.

62	3,431	0,084	0,774	0,023	0,320	0,318
63	2,617	0,090	0,761	0,033	0,710	0,907
64	4,325	0,088	0,781	0,019	3,252	2,585
65	4,307	0,077	0,767	0,015	0,653	0,511
66	0,488	0,019	0,786	0,041	0,899	6,190
67	3,211	0,060	0,777	0,016	0,580	0,620
68	3,739	0,085	0,770	0,021	0,519	0,471
69	4,016	0,100	0,784	0,024	0,233	0,198
70	5,376	0,158	0,752	0,029	0,805	0,486
71	4,142	0,079	0,762	0,017	0,707	0,578
72	3,211	0,068	0,766	0,020	0,667	0,706
73	4,881	0,094	0,747	0,016	0,607	0,416
74	6,951	0,142	0,728	0,018	0,900	0,422
75	4,212	0,083	0,760	0,017	0,722	0,575
76	4,669	0,102	0,746	0,018	0,537	0,382
77	10,179	0,373	0,741	0,037	0,315	0,102
78	2,933	0,062	0,759	0,019	0,404	0,464
79	28,016	1,028	0,730	0,032	0,984	0,113
80	68,726	2,011	0,637	0,027	4,164	0,182
Laser spot ID	**238U/206Pb**	**2SE**	**207Pb/206Pb**	**2SE**	**U_PPM**	**Pb_PPM**
1	**3,127**	0,149	0,783	0,053	0,221	0,234
2	0,905	0,020	0,788	0,019	0,166	0,634
3	2,170	0,035	0,791	0,013	0,504	0,806
4	3,331	0,145	0,818	0,046	0,137	0,140
5	5,208	0,204	0,772	0,037	0,146	0,094

Location 9 Sample h

Table A.1 (continued): Details of LA-ICP-MS U-Pb age data.

6	6,867	0,221	0,790	0,030	0,218	0,110
7	11,159	0,408	0,802	0,036	0,266	0,082
8	3,586	0,094	0,782	0,025	0,230	0,220
9	8,800	0,296	0,779	0,034	0,190	0,074
10	17,156	0,771	0,823	0,049	0,248	0,050
11	2,965	0,115	0,808	0,040	0,172	0,203
12	5,402	0,185	0,794	0,038	0,180	0,112
13	7,973	0,347	0,796	0,045	0,214	0,093
14	3,765	0,110	0,794	0,028	0,183	0,166
15	14,270	0,556	0,789	0,035	0,237	0,057
16	1,349	0,046	0,810	0,037	0,185	0,459
17	3,547	0,076	0,807	0,022	0,243	0,239
18	5,329	0,140	0,795	0,026	0,243	0,158
19	3,113	0,080	0,809	0,025	0,201	0,226
20	3,014	0,083	0,793	0,029	0,134	0,154
21	4,177	0,141	0,805	0,033	0,172	0,143
22	5,235	0,176	0,815	0,037	0,217	0,143
23	1,036	0,027	0,813	0,028	0,136	0,460
24	5,205	0,136	0,796	0,024	0,305	0,203
25	3,418	0,102	0,797	0,031	0,248	0,248
26	4,251	0,146	0,794	0,038	0,167	0,132
27	2,405	0,076	0,792	0,033	0,095	0,137
28	2,827	0,075	0,792	0,027	0,134	0,163
29	1,782	0,038	0,791	0,021	0,352	0,682
30	3,913	0,119	0,785	0,031	0,388	0,335
31	1,420	0,048	0,784	0,036	0,176	0,412

Table A.1 (continued): Details of LA-ICP-MS U-Pb age data.

32	4,114	0,100	0,814	0,025	0,178	0,152
33	2,059	0,056	0,788	0,026	0,109	0,182
34	6,741	0,273	0,772	0,041	0,176	0,088
35	2,677	0,077	0,792	0,029	0,299	0,381
36	4,990	0,109	0,782	0,019	0,434	0,300
37	0,975	0,022	0,790	0,022	0,163	0,577
38	3,188	0,098	0,775	0,029	0,194	0,206
39	1,369	0,039	0,807	0,031	0,108	0,278
40	4,334	0,152	0,792	0,034	0,147	0,116
41	2,734	0,082	0,805	0,029	0,116	0,149
42	3,014	0,109	0,797	0,039	0,362	0,403
43	1,147	0,022	0,806	0,018	0,203	0,620
44	3,971	0,110	0,796	0,025	0,211	0,184
45	3,160	0,090	0,802	0,029	0,122	0,133
46	1,160	0,056	0,806	0,053	0,101	0,290
47	1,847	0,082	0,805	0,049	0,109	0,203
48	1,158	0,061	0,800	0,059	0,279	0,741
49	1,678	0,046	0,799	0,025	0,162	0,332
50	1,452	0,041	0,800	0,029	0,129	0,306
51	2,441	0,065	0,810	0,028	0,152	0,219
52	2,036	0,081	0,793	0,042	0,095	0,163
53	1,889	0,093	0,787	0,050	0,141	0,245
54	1,138	0,037	0,792	0,033	0,095	0,284
55	2,240	0,060	0,795	0,028	0,890	1,358
56	1,732	0,036	0,793	0,021	0,162	0,322
57	0,179	0,005	0,826	0,027	0,317	6,280

Table A.1 (continued): Details of LA-ICP-MS U-Pb age data.

58	0,450	0,015	0,817	0,037	0,145	1,091
59	0,103	0,011	0,827	0,125	0,307	8,120
60	0,820	0,021	0,815	0,028	0,261	1,115
61	0,388	0,041	0,802	0,119	0,023	0,203
62	1,069	0,044	0,814	0,046	0,171	0,544
63	1,517	0,073	0,801	0,054	0,202	0,462
64	0,887	0,021	0,807	0,023	0,181	0,713
65	0,836	0,068	0,804	0,091	0,215	0,852
66	0,536	0,034	0,798	0,067	0,016	0,099
67	2,262	0,073	0,822	0,038	0,144	0,226
68	4,048	0,122	0,796	0,030	0,189	0,161
69	7,925	0,247	0,810	0,031	0,199	0,088
70	4,936	0,133	0,799	0,025	0,192	0,136
71	7,973	0,291	0,803	0,038	0,160	0,069
72	1,450	0,092	0,824	0,068	0,033	0,075
73	0,820	0,047	0,821	0,065	0,042	0,176
74	0,582	0,028	0,808	0,053	0,029	0,175
75	2,584	0,073	0,786	0,027	0,202	0,269
76	5,996	0,232	0,770	0,037	0,156	0,088
77	3,607	0,170	0,766	0,048	0,137	0,121
78	7,590	0,365	0,778	0,051	0,181	0,078

Table A.1 (continued): Details of LA-ICP-MS U-Pb age data.

79	4,971	0,210	0,777	0,045	0,089	0,060	
80	10,434	0,820	0,758	0,079	0,066	0,021	
Laser spot ID	**238U/206Pb**	**2SE**	**207Pb/206Pb**	**2SE**	**U_PPM**	**Pb_PPM**	**Location 9 Sample e**
1	103,87	11,08	0,36	0,04	0,34	0,01	
2	100,47	8,78	0,39	0,05	0,27	0,01	
3	82,70	7,85	0,40	0,05	0,27	0,01	
4	2,64	0,17	0,54	0,01	0,64	0,66	
5	9,63	1,79	0,41	0,01	1,12	0,37	
6	16,59	2,29	0,45	0,02	1,74	0,22	
7	6,84	0,90	0,49	0,01	0,87	0,30	
8	5,27	0,47	0,50	0,01	0,50	0,23	
9	4,29	0,53	0,49	0,01	0,76	0,34	
10	7,33	1,43	0,48	0,01	1,66	0,47	
11	20,49	1,42	0,50	0,02	0,67	0,09	
12	17,50	1,15	0,45	0,03	0,12	0,02	
13	2,59	0,30	0,48	0,01	0,29	0,28	
14	11,48	0,89	0,48	0,02	0,35	0,07	
15	8,27	0,74	0,47	0,04	0,07	0,02	
Laser spot ID	**238U/206Pb**	**2SE**	**207Pb/206Pb**	**2SE**	**U_PPM**	**Pb_PPM**	**Location 9 Sample g**
1	31,381	2,431	0,757	0,047	0,267	0,027	
2	19,545	1,372	0,748	0,037	0,242	0,039	
3	16,383	1,355	0,872	0,085	0,091	0,018	
4	14,780	1,152	0,782	0,036	0,182	0,039	
5	10,303	0,703	0,799	0,040	0,204	0,067	

Table A.1 (continued): Details of LA-ICP-MS U-Pb age data.

6	9,048	0,772	0,789	0,028	0,256	0,097
7	7,372	0,500	0,786	0,033	0,118	0,052
8	7,124	0,473	0,787	0,034	0,114	0,054
9	3,160	0,224	0,835	0,035	0,058	0,062
10	2,345	0,167	0,828	0,033	0,039	0,056
11	3,413	0,222	0,834	0,036	0,057	0,056
12	4,797	0,310	0,785	0,020	0,197	0,134
13	4,167	0,234	0,774	0,009	1,039	0,821
14	4,136	0,230	0,774	0,008	1,120	0,897
15	4,088	0,244	0,773	0,009	1,019	0,802
16	3,828	0,214	0,772	0,011	0,705	0,599
17	3,792	0,210	0,782	0,010	0,999	0,871
18	3,666	0,196	0,778	0,009	1,010	0,918
19	3,510	0,194	0,777	0,008	1,001	0,940
20	3,466	0,189	0,782	0,009	0,930	0,889
21	3,372	0,191	0,781	0,009	0,956	0,942
22	3,242	0,177	0,780	0,008	0,931	0,951
23	3,189	0,183	0,782	0,012	0,531	0,550
24	3,157	0,179	0,790	0,010	0,803	0,842
25	3,077	0,170	0,785	0,008	0,933	1,022
26	3,021	0,195	0,782	0,021	0,119	0,128
27	2,946	0,166	0,781	0,009	0,762	0,859
28	2,943	0,165	0,782	0,007	0,959	1,082
29	2,855	0,165	0,787	0,010	0,493	0,575
30	2,848	0,173	0,797	0,010	0,640	0,741
31	2,829	0,225	0,791	0,008	1,057	1,199

Table A.1 (continued): Details of LA-ICP-MS U-Pb age data.

32	2,819	0,160	0,794	0,008	0,931	1,128
33	2,742	0,186	0,788	0,009	0,960	1,094
34	2,629	0,155	0,786	0,018	0,157	0,201
35	2,561	0,169	0,789	0,008	0,903	1,119
36	2,532	0,165	0,804	0,010	0,600	0,744
37	2,527	0,143	0,798	0,009	0,677	0,891
38	2,515	0,149	0,790	0,009	0,614	0,809
39	2,489	0,153	0,788	0,020	0,091	0,122
40	2,334	0,128	0,792	0,009	0,596	0,850
41	2,321	0,163	0,787	0,028	0,041	0,058
42	2,309	0,138	0,802	0,019	0,125	0,184
43	2,234	0,146	0,793	0,009	0,685	1,009
44	2,127	0,132	0,798	0,021	0,130	0,198
45	2,122	0,141	0,780	0,028	0,050	0,077
46	2,092	0,133	0,783	0,010	0,450	0,675
47	2,073	0,149	0,787	0,033	0,035	0,056
48	2,047	0,113	0,801	0,008	0,651	1,078
49	1,998	0,112	0,793	0,008	0,814	1,376
50	1,921	0,132	0,802	0,017	0,165	0,278
51	1,868	0,196	0,796	0,015	0,257	0,349
52	1,804	0,121	0,810	0,025	0,069	0,123
53	1,737	0,102	0,794	0,014	0,186	0,356
54	1,727	0,100	0,797	0,012	0,179	0,347
55	1,720	0,096	0,792	0,007	0,681	1,313
56	1,711	0,112	0,803	0,023	0,073	0,146
57	1,650	0,098	0,790	0,015	0,117	0,237

Table A.1 (continued): Details of LA-ICP-MS U-Pb age data.

58	1,606	0,098	0,810	0,009	0,413	0,877	
59	1,493	0,093	0,809	0,017	0,108	0,245	
60	1,480	0,096	0,812	0,026	0,047	0,105	
61	1,426	0,105	0,794	0,009	0,434	0,953	
62	1,419	0,088	0,798	0,007	0,683	1,543	
63	1,375	0,091	0,794	0,012	0,212	0,507	
64	1,357	0,085	0,797	0,014	0,141	0,342	
65	1,264	0,115	0,817	0,019	0,066	0,156	
66	1,151	0,071	0,792	0,010	0,244	0,688	
67	1,141	0,088	0,813	0,032	0,022	0,060	
68	1,134	0,081	0,795	0,013	0,129	0,359	
69	1,020	0,063	0,799	0,013	0,111	0,358	
70	0,998	0,064	0,813	0,021	0,035	0,118	
71	0,799	0,052	0,814	0,007	0,379	1,578	
72	0,772	0,047	0,783	0,011	0,112	0,478	
73	0,647	0,042	0,791	0,006	0,435	2,227	
74	0,444	0,029	0,798	0,009	0,133	0,950	
75	0,050	0,003	0,825	0,004	0,123	8,390	
76	0,909	0,167	0,784	0,008	0,660	1,058	
Laser spot ID	**238U/206Pb**	**2SE**	**207Pb/206Pb**	**2SE**	**U_PPM**	**Pb_PPM**	**Location 8 Sample c**
1	22,755	1,617	0,783	0,077	0,121	0,018	
2	13,223	0,917	0,779	0,072	0,138	0,037	
3	11,334	0,530	0,832	0,054	0,148	0,047	
4	11,110	1,239	0,773	0,125	0,181	0,054	
5	7,144	0,256	0,778	0,034	0,122	0,057	

Table A.1 (continued): Details of LA-ICP-MS U-Pb age data.

6	6,001	0,357	0,751	0,057	0,021	0,012
7	5,617	0,331	0,777	0,063	0,119	0,072
8	5,059	0,186	0,821	0,039	0,299	0,200
9	4,857	0,184	0,781	0,035	0,103	0,069
10	4,574	0,327	0,811	0,080	0,597	0,442
11	4,397	0,155	0,810	0,033	0,076	0,060
12	3,864	0,183	0,816	0,047	0,092	0,084
13	3,709	0,169	0,809	0,042	0,057	0,053
14	3,644	0,207	0,785	0,059	0,115	0,106
15	3,612	0,146	0,798	0,045	0,162	0,148
16	3,601	0,202	0,839	0,064	0,059	0,056
17	3,586	0,172	0,816	0,048	0,036	0,035
18	3,462	0,241	0,796	0,075	0,069	0,064
19	3,383	0,230	0,838	0,070	0,013	0,013
20	3,358	0,226	0,823	0,080	0,093	0,092
21	3,237	0,234	0,804	0,076	0,061	0,063
22	3,191	0,227	0,837	0,078	0,045	0,047
23	3,124	0,218	0,812	0,081	0,075	0,089
24	3,124	0,207	0,824	0,072	0,074	0,077
25	3,044	0,103	0,816	0,034	0,131	0,152
26	2,979	0,297	0,827	0,118	0,553	0,664
27	2,939	0,202	0,747	0,065	0,063	0,070
28	2,724	0,070	0,800	0,023	0,255	0,318
29	2,714	0,090	0,817	0,032	0,107	0,138
30	2,599	0,128	0,829	0,054	0,048	0,064
31	2,591	0,157	0,841	0,070	0,079	0,099

Table A.1 (continued): Details of LA-ICP-MS U-Pb age data.

32	2,562	0,088	0,790	0,034	0,145	0,186
33	2,483	0,076	0,818	0,029	0,091	0,129
34	2,450	0,147	0,839	0,071	0,078	0,108
35	2,417	0,111	0,808	0,048	0,040	0,055
36	2,410	0,162	0,786	0,070	0,037	0,049
37	2,281	0,139	0,798	0,064	0,080	0,118
38	2,261	0,063	0,812	0,025	0,142	0,217
39	2,171	0,189	0,801	0,096	0,874	1,306
40	2,105	0,153	0,804	0,079	0,138	0,209
41	2,100	0,084	0,797	0,044	0,054	0,088
42	2,095	0,142	0,805	0,072	0,060	0,095
43	2,090	0,073	0,807	0,037	0,145	0,232
44	2,061	0,095	0,826	0,050	0,439	0,738
45	2,052	0,108	0,802	0,054	0,029	0,046
46	2,042	0,093	0,788	0,049	0,090	0,143
47	1,988	0,119	0,809	0,065	0,097	0,166
48	1,837	0,124	0,828	0,073	0,015	0,028
49	1,815	0,066	0,815	0,036	0,050	0,095
50	1,793	0,129	0,797	0,080	0,097	0,171
51	1,786	0,057	0,828	0,035	0,054	0,106
52	1,751	0,157	0,795	0,099	0,526	0,987
53	1,744	0,081	0,807	0,045	0,055	0,106
54	1,692	0,105	0,819	0,067	0,042	0,084
55	1,688	0,086	0,803	0,056	0,018	0,037
56	1,679	0,069	0,842	0,042	0,062	0,127
57	1,601	0,109	0,793	0,071	0,038	0,079

Table A.1 (continued): Details of LA-ICP-MS U-Pb age data.

58	1,595	0,082	0,816	0,061	0,035	0,080	
59	1,592	0,059	0,808	0,038	0,103	0,220	
60	1,573	0,088	0,808	0,062	0,046	0,101	
61	1,556	0,073	0,766	0,042	0,029	0,062	
62	1,482	0,081	0,849	0,056	0,014	0,033	
63	1,444	0,077	0,840	0,057	0,012	0,029	
64	1,396	0,063	0,783	0,047	0,037	0,086	
65	1,371	0,044	0,800	0,031	0,059	0,145	
66	1,352	0,041	0,808	0,028	0,048	0,125	
67	1,292	0,060	0,808	0,050	0,118	0,327	
68	1,207	0,086	0,828	0,080	0,024	0,065	
69	1,148	0,056	0,804	0,052	0,211	0,621	
70	1,044	0,064	0,803	0,067	0,112	0,331	
71	0,976	0,027	0,815	0,025	0,125	0,438	
72	0,968	0,030	0,821	0,030	0,036	0,129	
73	0,937	0,037	0,822	0,041	0,043	0,151	
74	0,870	0,085	0,803	0,110	0,024	0,091	
75	0,773	0,067	0,794	0,097	0,050	0,223	
76	0,591	0,026	0,819	0,048	0,019	0,108	
77	0,493	0,035	0,841	0,082	0,042	0,283	
78	0,477	0,046	0,818	0,107	0,041	0,315	
79	0,475	0,024	0,808	0,053	0,098	0,720	
80	0,353	0,029	0,814	0,096	0,040	0,442	
Laser spot ID	**238U/206Pb**	**2SE**	**207Pb/206Pb**	**2SE**	**U_PPM**	**Pb_PPM**	**Location 8 Sample e**
1	0,709	0,020	0,801	0,030	0,275	1,352	

Table A.1 (continued): Details of LA-ICP-MS U-Pb age data.

2	3,473	0,097	0,848	0,032	0,199	0,207
3	20,313	0,766	0,693	0,035	0,312	0,049
4	9,445	0,380	0,779	0,042	0,337	0,120
5	17,893	0,769	0,665	0,037	0,209	0,036
6	10,317	0,441	0,730	0,042	0,682	0,214
7	3,770	0,171	0,757	0,045	0,088	0,079
8	6,741	0,308	0,777	0,048	0,604	0,297
9	7,364	0,332	0,763	0,047	0,095	0,044
10	7,214	0,358	0,789	0,051	0,131	0,061
11	14,848	0,770	0,719	0,047	0,174	0,038
12	4,383	0,231	0,802	0,054	0,127	0,099
13	14,138	0,742	0,731	0,050	0,154	0,038
14	11,991	0,675	0,741	0,052	0,141	0,037
15	7,837	0,429	0,773	0,059	0,153	0,066
16	20,223	1,161	0,724	0,055	0,171	0,029
17	18,213	1,159	0,754	0,058	0,108	0,020
18	14,427	0,818	0,726	0,057	0,216	0,049
19	45,353	2,919	0,626	0,054	0,386	0,025
20	9,767	0,604	0,765	0,066	0,544	0,183
21	9,107	0,597	0,796	0,069	0,060	0,023
22	6,663	0,422	0,741	0,065	0,126	0,062
23	85,459	5,261	0,446	0,039	0,379	0,011
24	67,214	4,487	0,509	0,045	0,277	0,011
25	8,999	0,619	0,798	0,075	0,203	0,085
26	0,907	0,064	0,797	0,076	0,016	0,059
27	59,877	4,305	0,522	0,050	0,270	0,012

Table A.1 (continued): Details of LA-ICP-MS U-Pb age data.

28	103,517	7,018	0,344	0,033	0,528	0,011
29	26,100	1,933	0,622	0,061	0,085	0,010
30	15,218	1,087	0,693	0,068	0,095	0,020
31	7,047	0,542	0,776	0,082	0,170	0,077
32	33,193	2,526	0,647	0,068	0,322	0,029
33	45,578	3,175	0,614	0,069	0,398	0,025
34	13,923	1,121	0,749	0,085	0,151	0,034
35	21,109	1,751	0,685	0,078	0,110	0,017
36	19,787	1,624	0,669	0,077	0,097	0,015
37	12,347	0,915	0,723	0,084	0,160	0,040
38	87,084	6,540	0,437	0,051	0,275	0,008
39	103,987	8,380	0,354	0,041	0,329	0,007
40	3,148	0,260	0,805	0,095	0,030	0,033
41	21,556	1,927	0,691	0,084	0,088	0,013
42	55,861	4,769	0,566	0,069	0,160	0,008
43	19,916	1,775	0,732	0,090	0,124	0,022
44	9,348	0,830	0,800	0,099	0,034	0,012
45	21,305	2,031	0,714	0,092	0,073	0,012
46	34,441	3,496	0,676	0,088	0,080	0,007
47	5,798	0,440	0,776	0,105	0,096	0,057
48	28,900	2,735	0,634	0,086	0,127	0,014
49	36,068	3,124	0,726	0,100	0,325	0,028
50	37,241	4,239	0,605	0,087	0,095	0,007
51	13,902	1,540	0,753	0,109	0,055	0,012
52	6,993	0,747	0,792	0,119	0,029	0,012
53	12,940	1,407	0,754	0,113	0,024	0,006

Table A.1 (continued): Details of LA-ICP-MS U-Pb age data.

54	8,405	0,925	0,706	0,107	0,027	0,010
55	37,856	4,693	0,729	0,119	0,057	0,005
56	5,949	0,695	0,792	0,132	0,022	0,012
57	11,730	1,382	0,761	0,128	0,095	0,022
58	84,826	10,211	0,446	0,079	0,125	0,004
59	51,758	6,726	0,639	0,114	0,053	0,003
60	106,526	12,387	0,315	0,056	0,165	0,003
61	69,933	9,075	0,487	0,088	0,087	0,003
62	60,670	7,634	0,548	0,103	0,125	0,005
63	30,537	4,173	0,617	0,119	0,169	0,019
64	122,804	13,169	0,267	0,052	0,204	0,003
65	36,792	5,319	0,699	0,140	0,066	0,007
66	2,727	0,406	0,723	0,145	0,036	0,044
67	36,940	5,660	0,761	0,153	0,046	0,004
68	8,725	1,330	0,788	0,163	0,023	0,008
69	8,253	1,115	0,680	0,144	0,015	0,006
70	16,359	2,395	0,736	0,157	0,145	0,027
71	20,046	3,246	0,633	0,142	0,200	0,032
72	64,516	11,358	0,577	0,130	0,062	0,002
73	104,105	15,379	0,284	0,064	0,095	0,002
74	72,136	10,792	0,457	0,105	0,061	0,002
75	91,612	13,742	0,368	0,085	0,077	0,002

Table A.1 (continued): Details of LA-ICP-MS U-Pb age data.

76	7,214	1,193	0,726	0,174	0,039	0,017	
77	56,902	9,543	0,491	0,119	0,055	0,002	
Laser spot ID	**238U/206Pb**	**2SE**	**207Pb/206Pb**	**2SE**	**U_PPM**	**Pb_PPM**	**Location 8 Sample d**
1	106,667	4,552	0,351	0,023	1,220	0,025	
2	5,505	0,721	0,794	0,153	0,920	0,547	
3	58,680	2,197	0,550	0,032	1,406	0,066	
4	62,067	4,166	0,560	0,065	1,440	0,068	
5	19,470	1,599	0,722	0,087	0,747	0,126	
6	7,519	1,406	0,755	0,204	0,272	0,140	
7	85,948	5,112	0,424	0,035	0,456	0,013	
8	107,535	4,877	0,336	0,025	1,118	0,023	
9	7,340	0,816	0,737	0,115	0,818	0,370	
10	133,642	6,566	0,286	0,024	1,099	0,016	
11	24,146	1,765	0,668	0,075	0,428	0,057	
12	69,015	5,665	0,482	0,071	1,239	0,048	
13	24,661	1,776	0,638	0,070	0,216	0,025	
14	60,484	3,402	0,568	0,047	0,783	0,037	
15	17,888	1,799	0,714	0,104	0,436	0,071	
16	20,415	0,901	0,717	0,047	0,561	0,091	
17	45,024	1,907	0,618	0,035	0,517	0,034	
18	71,690	6,113	0,554	0,066	0,209	0,008	
19	26,499	1,898	0,653	0,075	0,601	0,073	
20	17,548	2,198	0,702	0,126	0,250	0,048	
21	58,495	2,627	0,526	0,033	0,701	0,032	

Table A.1 (continued): Details of LA-ICP-MS U-Pb age data.

22	44,228	1,396	0,627	0,024	1,225	0,083
23	4,842	0,355	0,725	0,075	0,077	0,053
24	19,511	1,358	0,707	0,071	0,212	0,034
25	36,267	2,560	0,629	0,068	0,511	0,036
26	30,026	1,852	0,664	0,056	0,507	0,054
27	15,311	0,786	0,718	0,047	0,177	0,039
28	12,898	0,558	0,716	0,041	0,214	0,056
29	4,301	0,200	0,765	0,047	0,111	0,084
30	3,670	0,684	0,731	0,186	0,018	0,016
31	7,070	0,373	0,772	0,055	0,142	0,068
32	138,030	7,829	0,233	0,024	0,840	0,012
33	126,167	4,303	0,264	0,017	1,644	0,026
34	26,348	0,901	0,698	0,036	1,159	0,144
35	56,736	4,177	0,596	0,062	0,226	0,012
36	25,477	1,544	0,697	0,057	0,185	0,022
37	10,140	0,745	0,740	0,075	0,491	0,166
38	79,724	6,873	0,444	0,073	0,669	0,021
39	35,569	1,778	0,567	0,039	0,292	0,023
40	6,855	0,432	0,773	0,066	0,111	0,054
41	21,163	1,792	0,700	0,090	0,585	0,090
42	131,178	6,512	0,272	0,028	1,138	0,017
43	7,993	0,566	0,777	0,079	0,790	0,328
44	15,675	1,355	0,712	0,094	0,128	0,022
45	13,422	0,331	0,746	0,023	0,671	0,168
46	1,752	0,249	0,802	0,159	0,445	0,890
47	10,391	0,514	0,759	0,055	0,973	0,313

Table A.1 (continued): Details of LA-ICP-MS U-Pb age data.

48	10,754	1,626	0,767	0,166	1,474	0,470
49	7,851	0,520	0,771	0,075	0,377	0,166
50	67,112	4,042	0,483	0,049	1,155	0,046
51	4,999	0,865	0,749	0,183	0,884	0,569
52	2,002	0,256	0,777	0,142	0,098	0,175
53	13,782	1,294	0,731	0,097	0,322	0,077
54	7,952	0,506	0,746	0,065	0,144	0,058
55	35,569	4,241	0,611	0,113	1,251	0,116
56	11,319	0,707	0,740	0,067	0,539	0,160
57	4,056	0,356	0,783	0,098	0,765	0,664
58	33,507	2,307	0,675	0,068	0,556	0,051
59	111,021	4,132	0,336	0,019	1,563	0,031
60	51,868	2,094	0,590	0,030	0,648	0,036
61	4,842	0,279	0,782	0,061	0,079	0,056
62	101,963	6,408	0,371	0,036	0,567	0,013
63	42,815	3,370	0,594	0,079	0,945	0,064
64	45,987	1,898	0,610	0,041	0,893	0,057
65	2,964	0,238	0,788	0,089	1,097	1,290
66	82,645	5,096	0,431	0,040	0,450	0,014
67	21,260	1,222	0,690	0,060	0,932	0,140
68	18,169	1,107	0,734	0,066	0,833	0,148
69	12,514	1,338	0,750	0,116	0,424	0,115
70	11,589	1,205	0,677	0,091	0,053	0,015
71	8,056	0,442	0,761	0,050	0,085	0,035
72	48,167	4,265	0,604	0,075	0,364	0,025
73	136,201	6,218	0,280	0,021	1,038	0,015

Table A.1 (continued): Details of LA-ICP-MS U-Pb age data.

74	5,780	0,397	0,798	0,081	0,582	0,351	
75	1,657	0,151	0,780	0,101	0,230	0,448	
76	12,137	1,083	0,751	0,094	0,090	0,025	
77	6,445	0,193	0,766	0,032	1,001	0,535	
78	54,722	4,209	0,566	0,064	0,283	0,015	
79	16,633	1,047	0,702	0,061	0,161	0,032	
80	30,827	2,055	0,633	0,059	0,313	0,030	
Laser spot ID	**238U/206Pb**	**2SE**	**207Pb/206Pb**	**2SE**	**U_PPM**	**Pb_PPM**	**Location 8 Sample f**
1	4,489	0,262	0,834	0,069	0,379	0,301	
2	1,468	0,072	0,854	0,057	0,074	0,191	
3	16,969	0,716	0,752	0,041	0,201	0,040	
4	16,723	1,240	0,750	0,081	0,374	0,067	
5	35,164	3,209	0,632	0,073	0,097	0,008	
6	20,148	1,756	0,721	0,081	0,060	0,010	
7	16,282	1,003	0,760	0,069	0,267	0,056	
8	29,929	1,453	0,671	0,043	0,271	0,028	
9	4,927	0,249	0,815	0,056	0,172	0,123	
10	13,155	0,973	0,732	0,069	0,063	0,015	
11	40,704	1,487	0,646	0,032	0,537	0,041	
12	6,835	0,333	0,807	0,055	0,157	0,080	
13	2,218	0,410	0,842	0,222	0,250	0,333	
14	52,997	2,187	0,591	0,032	0,676	0,037	
15	0,689	0,017	0,857	0,029	0,168	0,891	
16	2,820	0,258	0,840	0,108	0,596	0,726	
17	3,961	0,137	0,863	0,043	0,231	0,198	

Table A.1 (continued): Details of LA-ICP-MS U-Pb age data.

18	14,055	0,918	0,750	0,065	0,076	0,018
19	6,513	0,688	0,797	0,117	0,160	0,083
20	67,455	4,428	0,582	0,065	0,620	0,025
21	13,762	0,410	0,775	0,031	0,439	0,110
22	3,289	0,083	0,849	0,026	0,218	0,244
23	8,369	0,538	0,824	0,077	0,579	0,252
24	2,042	0,086	0,865	0,051	0,139	0,245
25	1,251	0,046	0,864	0,045	0,246	0,718
26	4,381	0,125	0,831	0,030	0,255	0,209
27	67,950	4,094	0,530	0,045	0,313	0,013
28	2,483	0,053	0,851	0,023	0,192	0,281
29	9,880	0,348	0,822	0,039	0,269	0,095
30	16,084	0,951	0,787	0,067	0,183	0,040
31	8,184	0,869	0,828	0,126	0,426	0,183
32	1,557	0,071	0,864	0,056	0,587	1,388
33	0,506	0,017	0,861	0,039	0,051	0,366
34	0,418	0,030	0,870	0,089	0,041	0,352
35	0,213	0,012	0,864	0,067	0,162	2,750
36	3,947	0,140	0,846	0,041	0,435	0,403
37	6,422	0,580	0,841	0,107	0,499	0,297
38	21,114	2,025	0,808	0,115	0,291	0,046
39	2,657	0,084	0,861	0,037	0,365	0,512
40	0,537	0,022	0,874	0,050	0,055	0,371
41	1,319	0,113	0,871	0,108	0,046	0,107
42	5,138	0,400	0,758	0,082	0,056	0,031
43	1,672	0,085	0,788	0,051	0,029	0,057

Table A.1 (continued): Details of LA-ICP-MS U-Pb age data.

44	7,114	0,711	0,809	0,116	0,581	0,300
45	1,258	0,065	0,858	0,057	0,033	0,096
46	1,283	0,066	0,895	0,069	0,401	1,141
47	13,461	1,078	0,774	0,092	0,141	0,033
48	14,656	0,790	0,767	0,060	0,293	0,069
49	14,679	1,118	0,679	0,064	0,311	0,069
50	1,279	0,064	0,798	0,049	0,074	0,212
51	1,077	0,055	0,781	0,049	0,023	0,073
52	1,955	0,112	0,869	0,071	0,210	0,417
53	6,249	0,317	0,752	0,053	0,060	0,032
54	16,514	0,737	0,776	0,044	0,335	0,069
55	41,658	2,064	0,634	0,048	0,432	0,033
56	8,619	0,450	0,799	0,058	0,642	0,252
57	10,414	0,364	0,787	0,037	0,374	0,126
58	34,000	2,250	0,661	0,061	0,237	0,021
59	6,800	0,210	0,826	0,034	0,445	0,234
60	5,469	0,152	0,815	0,031	0,736	0,481
61	8,339	0,331	0,806	0,040	0,451	0,190
62	13,025	0,899	0,738	0,065	0,109	0,027
63	5,112	0,266	0,838	0,062	0,405	0,276
64	44,893	2,397	0,624	0,047	0,532	0,035
65	23,005	1,545	0,742	0,071	0,292	0,040
66	35,030	2,256	0,607	0,055	0,187	0,016
67	35,030	1,858	0,709	0,052	0,393	0,035
68	2,341	0,154	0,791	0,067	0,021	0,030
69	23,413	1,423	0,725	0,060	0,153	0,021

Table A.1 (continued): Details of LA-ICP-MS U-Pb age data.

70	78,975	5,058	0,476	0,041	0,430	0,014	
71	19,068	1,494	0,745	0,077	0,089	0,016	
72	11,604	0,844	0,763	0,078	0,209	0,062	
73	5,538	0,531	0,708	0,094	0,015	0,009	
74	14,940	1,665	0,785	0,120	0,057	0,012	
75	79,587	4,589	0,477	0,044	0,662	0,021	
76	24,273	1,147	0,723	0,045	0,278	0,038	
77	91,114	6,463	0,444	0,044	0,404	0,011	
78	20,829	0,751	0,735	0,035	0,278	0,044	
79	51,694	2,485	0,610	0,037	0,510	0,029	
80	10,185	0,550	0,760	0,058	0,361	0,123	
Laser spot ID	**238U/206Pb**	**2SE**	**207Pb/206Pb**	**2SE**	**U_PPM**	**Pb_PPM**	**Location 7 Sample b**
1	2,383859	0,080285	0,807300	0,006300	1,032	1,554	
2	1,797206	0,091264	0,806000	0,006500	0,837	1,637	
3	2,222632	0,085899	0,815500	0,006600	0,921	1,464	
4	1,498647	0,048816	0,814400	0,006700	0,845	2,002	
5	1,933129	0,077163	0,808100	0,006700	1,036	1,870	
6	1,921022	0,080210	0,813600	0,006800	1,013	1,882	
7	2,460347	0,105255	0,806900	0,006800	1,016	1,450	
8	2,521012	0,075976	0,811100	0,007100	1,010	1,411	
9	2,300424	0,103519	0,811800	0,007200	1,086	1,700	
10	3,309962	0,142876	0,799800	0,007300	0,992	1,064	
11	1,581047	0,089647	0,816700	0,007600	0,760	1,720	
12	3,240034	0,125494	0,808500	0,007700	0,898	0,964	
13	2,335456	0,094841	0,817300	0,007800	0,893	1,348	

Table A.1 (continued): Details of LA-ICP-MS U-Pb age data.

14	2,614118	0,111397	0,811000	0,007800	0,914	1,232
15	3,983418	0,189687	0,810800	0,008200	0,984	0,861
16	1,822118	0,165975	0,806100	0,008200	0,814	1,610
17	2,930476	0,130658	0,812100	0,008300	0,879	1,105
18	2,599349	0,176227	0,806900	0,008400	0,814	1,081
19	2,460347	0,098677	0,813200	0,008500	0,670	0,968
20	2,473574	0,152936	0,809000	0,008500	0,795	1,146
21	3,598629	0,068961	0,807500	0,008600	0,827	0,810
22	3,408036	0,201958	0,805000	0,008600	0,786	0,804
23	2,893615	0,073705	0,804400	0,008800	0,635	0,775
24	2,875530	0,170735	0,803200	0,008900	0,664	0,807
25	3,151266	0,194256	0,810100	0,009000	0,719	0,807
26	4,211302	0,088659	0,808800	0,009300	0,821	0,686
27	2,115333	0,165336	0,802200	0,009300	0,663	1,109
28	3,404253	0,105793	0,806900	0,009600	0,584	0,609
29	4,152389	0,127420	0,801000	0,010000	0,799	0,674
30	3,566549	0,276477	0,799000	0,010000	0,670	0,664
31	4,141177	0,117414	0,798000	0,010000	0,713	0,600
32	4,881536	0,119125	0,814000	0,011000	0,627	0,451
33	3,740527	0,212876	0,813000	0,011000	0,511	0,475
34	3,026874	0,179223	0,812000	0,011000	0,644	0,756
35	4,000737	0,208734	0,808000	0,011000	0,663	0,583
36	5,979010	0,384615	0,802000	0,011000	0,866	0,500
37	4,126321	0,277555	0,801000	0,011000	0,740	0,623
38	5,570034	0,252877	0,800000	0,011000	0,744	0,468
39	6,902997	0,222677	0,815000	0,012000	0,655	0,327

Table A.1 (continued): Details of LA-ICP-MS U-Pb age data.

40	3,498743	0,172942	0,813000	0,012000	0,615	0,670
41	5,160794	0,234450	0,812000	0,012000	0,669	0,453
42	4,018207	0,333388	0,807000	0,012000	0,703	0,607
43	4,673283	0,156646	0,804000	0,012000	0,645	0,492
44	6,457330	0,217510	0,796000	0,012000	0,544	0,296
45	5,252110	0,191858	0,789000	0,012000	0,601	0,396
46	5,634841	0,165629	0,808000	0,013000	0,628	0,395
47	5,634841	0,203586	0,801000	0,013000	0,674	0,414
48	6,721472	0,265127	0,799000	0,013000	0,512	0,260
49	5,412762	0,413917	0,792000	0,013000	0,558	0,350
50	6,619925	0,152401	0,791000	0,013000	0,589	0,305
51	6,398954	0,298143	0,787000	0,013000	0,517	0,277
52	5,055876	0,305575	0,804000	0,014000	0,568	0,386
53	7,396861	0,368654	0,795000	0,014000	0,545	0,266
54	6,846499	0,147730	0,794000	0,014000	0,661	0,332
55	6,653431	0,182813	0,788000	0,014000	0,505	0,259
56	6,658246	0,240892	0,786000	0,014000	0,581	0,296
57	6,897823	0,160294	0,802000	0,015000	0,408	0,208
58	5,356051	0,190174	0,796000	0,015000	0,414	0,268
59	7,420722	0,227409	0,795000	0,015000	0,613	0,293
60	3,755794	0,429234	0,802000	0,016000	0,451	0,421
61	7,898451	0,203394	0,802000	0,016000	0,534	0,234
62	7,573412	0,392695	0,798000	0,016000	0,536	0,241
63	8,607760	0,297930	0,788000	0,016000	0,525	0,219
64	6,976266	0,375523	0,803000	0,017000	0,506	0,246
65	7,133097	0,774135	0,800000	0,017000	0,488	0,244

Table A.1 (continued): Details of LA-ICP-MS U-Pb age data.

66	9,220136	0,277158	0,797000	0,017000	0,532	0,202
67	6,073726	0,332752	0,797000	0,017000	0,487	0,283
68	6,448279	0,447358	0,792000	0,017000	0,406	0,218
69	7,804661	0,297888	0,805000	0,018000	0,425	0,191
70	9,399072	0,316823	0,795000	0,018000	0,539	0,198
71	9,332350	0,255551	0,796000	0,019000	0,434	0,163
72	8,043440	0,604664	0,795000	0,019000	0,354	0,152
73	10,190142	0,462675	0,790000	0,020000	0,448	0,151
74	7,420722	0,718134	0,788000	0,020000	0,391	0,188
75	12,268924	0,408964	0,770000	0,021000	0,413	0,112
76	12,028364	0,440254	0,781000	0,022000	0,410	0,116
77	11,662477	0,694723	0,794000	0,023000	0,417	0,121
78	14,310569	0,556398	0,815000	0,029000	0,370	0,090
79	23,900511	1,303664	0,802000	0,048000	0,171	0,025

Laser spot ID	**238U/206Pb**	**2SE**	**207Pb/206Pb**	**2SE**	**U_PPM**	**Pb_PPM**	**Location 7 Sample a**
1	61,830	7,676	0,786	0,147	0,760	0,044	
2	20,705	2,295	0,828	0,128	1,376	0,231	
3	11,797	1,118	0,831	0,112	0,659	0,139	
4	22,414	1,849	0,773	0,085	0,279	0,040	
5	6,017	0,485	0,828	0,095	0,868	0,451	
6	72,653	5,593	0,764	0,081	0,667	0,030	
7	15,812	1,199	0,814	0,085	0,214	0,043	
8	15,431	1,169	0,807	0,085	1,204	0,238	
9	52,125	3,940	0,730	0,081	1,339	0,080	
10	47,943	3,589	0,780	0,082	2,659	0,183	

Table A.1 (continued): Details of LA-ICP-MS U-Pb age data.

11	17,579	1,275	0,828	0,082	0,176	0,034
12	43,948	3,016	0,736	0,066	1,258	0,092
13	14,531	0,966	0,831	0,076	1,275	0,280
14	52,738	3,412	0,785	0,078	1,040	0,062
15	134,616	8,489	0,625	0,053	1,621	0,035
16	6,865	0,431	0,818	0,070	1,216	0,597
17	15,511	0,966	0,802	0,071	0,160	0,036
18	9,724	0,601	0,795	0,064	0,106	0,035
19	50,368	3,113	0,742	0,064	0,877	0,051
20	21,095	1,291	0,835	0,071	0,200	0,032
21	14,893	0,866	0,799	0,064	2,087	0,461
22	4,229	0,239	0,842	0,067	0,152	0,122
23	45,742	2,567	0,781	0,048	0,291	0,022
24	19,322	1,083	0,788	0,054	0,099	0,018
25	31,238	1,742	0,814	0,059	0,251	0,028
26	2,490	0,138	0,814	0,061	0,453	0,618
27	5,222	0,289	0,819	0,054	0,027	0,018
28	7,065	0,373	0,844	0,055	0,044	0,022
29	81,801	4,180	0,668	0,045	0,579	0,021
30	16,852	0,824	0,837	0,050	0,140	0,028
31	13,088	0,631	0,769	0,046	0,115	0,029
32	11,613	0,557	0,821	0,051	0,197	0,058
33	12,808	0,604	0,815	0,050	0,243	0,065
34	119,698	5,434	0,705	0,041	3,532	0,095
35	17,545	0,790	0,785	0,047	0,468	0,089
36	53,144	2,363	0,787	0,046	1,285	0,077

Table A.1 (continued): Details of LA-ICP-MS U-Pb age data.

37	12,214	0,533	0,811	0,044	0,302	0,085
38	125,919	5,482	0,682	0,039	3,380	0,083
39	17,683	0,767	0,846	0,040	0,253	0,050
40	83,477	3,575	0,672	0,035	0,578	0,021
41	6,192	0,265	0,816	0,045	1,520	0,827
42	106,351	4,542	0,695	0,042	5,849	0,173
43	94,973	4,024	0,716	0,043	3,300	0,105
44	12,993	0,546	0,822	0,044	0,152	0,039
45	34,180	1,433	0,777	0,040	1,205	0,116
46	8,173	0,343	0,808	0,041	0,086	0,037
47	120,991	5,062	0,704	0,038	1,734	0,045
48	10,365	0,431	0,842	0,045	0,176	0,060
49	13,243	0,548	0,796	0,041	0,250	0,064
50	194,478	8,015	0,576	0,030	2,982	0,042
51	23,047	0,948	0,791	0,043	0,651	0,094
52	138,142	5,534	0,686	0,040	3,680	0,085
53	32,483	1,295	0,783	0,041	1,063	0,114
54	7,892	0,313	0,825	0,040	0,183	0,084
55	51,348	2,029	0,762	0,038	3,440	0,215
56	57,841	2,276	0,775	0,043	2,162	0,124
57	10,341	0,406	0,809	0,038	0,107	0,036
58	8,355	0,327	0,831	0,038	0,137	0,058
59	60,050	2,333	0,761	0,040	4,481	0,249
60	42,190	1,628	0,773	0,034	0,701	0,055
61	44,143	1,695	0,781	0,039	1,193	0,092
62	1,808	0,069	0,831	0,042	0,469	0,906

Table A.1 (continued): Details of LA-ICP-MS U-Pb age data.

63	81,727	3,129	0,728	0,034	1,515	0,060
64	18,039	0,690	0,803	0,035	0,210	0,040
65	77,555	2,952	0,726	0,034	2,054	0,083
66	13,543	0,511	0,808	0,036	0,131	0,033
67	74,712	2,802	0,675	0,030	1,623	0,066
68	49,152	1,832	0,762	0,037	0,693	0,046
69	173,748	6,398	0,599	0,031	2,826	0,046
70	9,065	0,330	0,849	0,046	0,172	0,069
71	18,875	0,676	0,782	0,033	0,237	0,042
72	61,660	2,205	0,738	0,033	0,636	0,034
73	81,801	2,911	0,743	0,031	1,287	0,051
74	18,409	0,643	0,818	0,033	0,274	0,052
75	84,579	2,952	0,724	0,031	1,817	0,069
76	20,753	0,721	0,820	0,034	0,285	0,048
77	13,401	0,461	0,824	0,032	0,227	0,059
78	16,154	0,553	0,826	0,036	1,123	0,243
79	17,012	0,581	0,786	0,034	0,267	0,053
80	104,249	3,515	0,712	0,031	1,594	0,048
81	79,410	2,673	0,747	0,035	9,688	0,400
82	26,923	0,889	0,788	0,029	0,440	0,056
83	9,852	0,325	0,824	0,033	0,175	0,062
84	45,120	1,453	0,752	0,027	1,076	0,079
85	4,704	0,151	0,833	0,033	0,362	0,268
86	30,567	0,959	0,793	0,029	3,020	0,332
87	6,802	0,212	0,833	0,032	0,126	0,065
88	75,340	2,342	0,741	0,027	1,579	0,067

Table A.1 (continued): Details of LA-ICP-MS U-Pb age data.

89	66,117	2,048	0,719	0,026	1,102	0,053
90	33,366	1,018	0,812	0,029	0,739	0,077
91	79,200	2,379	0,753	0,029	8,970	0,363
92	1,489	0,045	0,817	0,029	0,312	0,707
93	62,087	1,849	0,748	0,025	1,967	0,108
94	55,479	1,648	0,794	0,025	0,914	0,056
95	81,876	2,393	0,724	0,026	2,186	0,085
96	21,761	0,634	0,822	0,029	4,074	0,644
97	32,889	0,953	0,813	0,028	2,072	0,217
98	103,288	2,975	0,716	0,023	2,411	0,074
99	1,419	0,040	0,831	0,028	0,427	1,077
100	5,470	0,154	0,807	0,027	0,773	0,491
101	9,589	0,267	0,833	0,025	0,249	0,090
102	29,222	0,800	0,801	0,025	1,233	0,144
103	30,360	0,822	0,793	0,025	2,065	0,231
104	59,969	1,605	0,741	0,020	1,699	0,092
105	30,474	0,787	0,801	0,021	0,863	0,096
106	43,041	1,095	0,786	0,021	2,052	0,162
107	35,563	0,875	0,792	0,021	3,760	0,353
108	62,520	1,526	0,781	0,021	2,971	0,160
109	80,192	1,937	0,755	0,021	2,257	0,093
110	3,056	0,073	0,833	0,023	0,485	0,549

Table A.1 (continued): Details of LA-ICP-MS U-Pb age data.

111	1,210	0,028	0,817	0,021	0,292	0,852	
112	12,067	0,276	0,829	0,018	0,634	0,182	
113	2,744	0,052	0,825	0,014	0,435	0,548	
Laser spot ID	**238U/206Pb**	**2SE**	**207Pb/206Pb**	**2SE**	**U_PPM**	**Pb_PPM**	**Location 4 Sample a**
1	1228,139	201,886	0,885	0,188	0,452	0,001	
2	837,889	156,615	0,746	0,177	0,324	0,002	
3	585,975	80,428	0,688	0,124	0,355	0,002	
4	533,656	95,296	0,920	0,232	0,347	0,002	
5	509,399	66,569	0,820	0,128	0,462	0,003	
6	452,799	84,614	0,766	0,174	0,173	0,001	
7	437,337	51,200	0,768	0,108	0,446	0,003	
8	396,700	56,170	0,751	0,128	0,243	0,002	
9	330,827	53,714	0,776	0,152	0,163	0,002	
10	292,987	33,512	0,842	0,112	0,300	0,004	
11	288,277	46,347	1,097	0,349	0,173	0,003	
12	281,047	57,267	0,739	0,206	0,083	0,001	
13	257,627	25,170	0,853	0,108	0,467	0,007	
14	249,733	25,738	0,912	0,123	0,436	0,006	
15	224,135	17,370	0,818	0,079	0,503	0,008	
16	214,998	22,170	0,880	0,106	0,294	0,005	
17	206,102	18,478	0,812	0,093	0,493	0,008	
18	204,690	15,889	0,752	0,072	0,360	0,006	
19	193,220	17,073	0,774	0,086	0,327	0,006	
20	192,805	12,024	0,772	0,060	0,591	0,010	
21	189,945	16,097	0,939	0,102	0,416	0,008	

Table A.1 (continued): Details of LA-ICP-MS U-Pb age data.

22	186,391	13,563	0,819	0,072	0,391	0,007
23	180,028	12,291	0,857	0,076	0,465	0,009
24	172,081	10,239	0,823	0,056	0,489	0,010
25	160,097	31,448	0,672	0,169	0,243	0,005
26	151,187	13,003	0,897	0,095	0,216	0,005
27	147,215	8,219	0,836	0,058	0,536	0,013
28	143,217	10,066	0,808	0,069	0,375	0,009
29	141,410	12,267	0,781	0,090	0,485	0,011
30	138,999	12,499	0,831	0,098	0,199	0,005
31	137,718	18,828	0,857	0,151	0,114	0,003
32	133,812	7,789	0,828	0,063	0,431	0,011
33	133,613	7,766	0,836	0,059	0,445	0,012
34	129,558	11,982	0,868	0,100	0,207	0,006
35	126,630	7,691	0,826	0,058	0,413	0,011
36	124,867	14,261	0,960	0,149	0,141	0,005
37	118,747	8,021	0,803	0,070	0,552	0,015
38	116,132	7,070	0,777	0,060	0,301	0,009
39	112,773	5,249	0,815	0,045	0,599	0,019
40	107,628	4,264	0,779	0,037	0,589	0,019
41	106,731	15,247	0,812	0,168	0,300	0,009
42	104,249	8,728	0,907	0,092	0,211	0,007
43	84,739	5,286	0,813	0,067	0,291	0,012
44	80,770	10,187	0,882	0,153	0,174	0,006
45	78,369	3,151	0,849	0,043	0,700	0,032
46	72,890	7,111	0,832	0,104	0,518	0,026
47	67,612	4,334	0,798	0,060	0,299	0,015

Table A.1 (continued): Details of LA-ICP-MS U-Pb age data.

48	67,308	4,194	0,782	0,058	0,269	0,013
49	66,657	3,816	0,793	0,057	0,387	0,019
50	64,967	7,062	0,941	0,126	0,374	0,025
51	60,171	4,846	0,857	0,087	0,116	0,007
52	59,295	2,863	0,764	0,043	0,719	0,041
53	56,743	4,669	0,790	0,091	0,440	0,025
54	56,209	2,502	0,809	0,042	0,323	0,020
55	53,144	2,552	0,772	0,045	0,344	0,022
56	52,125	4,546	0,793	0,088	0,186	0,012
57	51,823	3,295	0,846	0,066	0,161	0,011
58	43,103	2,901	0,760	0,062	0,167	0,013
59	41,507	2,114	0,835	0,048	0,272	0,023
60	37,356	2,179	0,840	0,058	0,210	0,019
61	37,356	2,023	0,783	0,058	0,221	0,020
62	35,577	1,835	0,822	0,051	0,191	0,019
63	34,337	1,197	0,815	0,034	0,524	0,053
64	33,193	1,217	0,808	0,037	0,420	0,044
65	32,331	1,283	0,803	0,037	0,247	0,027
66	31,792	1,240	0,823	0,039	0,575	0,062
67	29,203	3,234	0,773	0,111	0,264	0,030
68	29,108	1,796	0,792	0,063	0,338	0,040
69	25,689	0,957	0,803	0,036	0,378	0,051
70	24,973	1,600	0,804	0,071	0,479	0,066
71	22,583	0,910	0,826	0,042	0,328	0,050
72	20,753	2,258	0,853	0,133	0,263	0,044
73	20,102	1,577	0,802	0,084	0,428	0,069

Table A.1 (continued): Details of LA-ICP-MS U-Pb age data.

74	19,704	0,953	0,797	0,046	0,107	0,019
75	19,618	0,816	0,846	0,043	0,378	0,068
76	17,045	0,972	0,789	0,061	0,308	0,063
77	16,980	0,450	0,800	0,023	0,509	0,101
78	16,125	1,102	0,853	0,089	0,265	0,055
79	15,068	0,532	0,802	0,032	0,207	0,047
80	14,578	0,687	0,821	0,049	0,164	0,039
81	14,391	1,086	0,897	0,095	0,306	0,075
82	12,937	0,765	0,797	0,064	0,567	0,149
83	12,717	0,469	0,812	0,035	0,227	0,062
84	12,452	0,432	0,800	0,037	0,302	0,084
85	10,246	0,410	0,829	0,040	0,258	0,088
86	9,951	0,663	0,832	0,074	0,437	0,153
87	9,300	0,714	0,799	0,082	0,424	0,155
88	8,646	0,367	0,826	0,047	0,265	0,107
89	7,598	1,095	0,855	0,174	0,288	0,126
90	7,471	0,623	0,810	0,095	0,169	0,085
91	7,428	0,277	0,799	0,037	0,218	0,101
92	7,259	0,500	0,805	0,075	0,289	0,136
93	7,213	0,267	0,820	0,037	0,376	0,179
94	5,031	0,138	0,822	0,027	0,130	0,088
95	4,696	0,180	0,823	0,039	0,125	0,094
96	4,556	0,164	0,798	0,036	0,319	0,240
97	3,383	0,192	0,824	0,064	0,330	0,346
98	3,154	0,111	0,819	0,037	0,447	0,492
99	2,837	0,144	0,806	0,055	0,233	0,285

Table A.1 (continued): Details of LA-ICP-MS U-Pb age data.

100	2,776	0,120	0,811	0,045	0,148	0,187
101	2,171	0,089	0,819	0,042	0,239	0,388
102	1,936	0,075	0,818	0,041	0,381	0,685
103	1,916	0,094	0,811	0,054	0,408	0,726
104	1,914	0,045	0,817	0,019	0,178	0,321
105	1,804	0,062	0,804	0,034	0,134	0,253
106	1,615	0,076	0,804	0,049	0,208	0,442
107	1,200	0,072	0,824	0,067	0,296	0,862
Laser spot ID	**238U/206Pb**	**2SE**	**207Pb/206Pb**	**2SE**	**U_PPM**	**Pb_PPM**
1	7,170	0,467	0,827	0,032	0,189	0,089
2	14,445	0,936	0,843	0,040	0,241	0,058
3	11,979	0,805	0,826	0,031	0,196	0,055
4	24,620	1,700	0,836	0,041	0,304	0,042
5	12,378	0,860	0,838	0,046	0,130	0,036
6	13,106	0,983	0,869	0,059	0,115	0,030
7	9,103	0,697	0,850	0,051	0,064	0,024
8	31,271	2,524	0,843	0,058	0,278	0,029
9	52,425	4,317	0,903	0,075	0,238	0,015
10	54,014	4,583	0,925	0,082	0,266	0,017
11	27,938	2,365	0,827	0,059	0,187	0,023
12	36,377	3,118	0,960	0,093	0,129	0,012
13	33,631	2,919	0,766	0,035	0,387	0,036
14	71,931	6,386	1,000	0,140	0,253	0,012
15	33,379	3,250	0,905	0,077	0,160	0,016
16	66,017	6,357	1,020	0,110	0,212	0,011

Location 4 Sample b

Table A.1 (continued): Details of LA-ICP-MS U-Pb age data.

17	21,898	2,044	0,881	0,063	0,161	0,026
18	70,176	7,736	1,000	0,220	0,168	0,008
19	68,033	6,751	1,050	0,160	0,185	0,009
20	90,023	10,003	1,020	0,150	0,250	0,009
21	31,716	3,273	1,030	0,130	0,103	0,011
22	36,229	3,829	0,915	0,070	0,177	0,018
23	19,849	1,945	0,880	0,059	0,145	0,026
24	119,789	13,364	1,000	0,240	0,218	0,006
25	106,225	12,661	1,020	0,160	0,296	0,008
26	150,039	17,429	0,950	0,290	0,256	0,006
27	38,250	4,104	1,070	0,130	0,160	0,014
28	61,464	7,206	1,160	0,190	0,164	0,009
29	61,464	7,630	1,260	0,190	0,142	0,008
30	47,659	6,117	1,050	0,180	0,161	0,011
31	120,599	16,319	0,440	0,520	0,199	0,005
32	142,142	18,363	0,180	0,830	0,217	0,005
33	42,039	4,561	1,040	0,160	0,168	0,014
34	110,437	13,411	0,870	0,380	0,190	0,006
35	122,086	15,888	0,550	0,530	0,222	0,006
36	49,239	5,985	1,000	0,110	0,130	0,010
37	100,138	12,377	1,020	0,290	0,154	0,006
38	127,137	15,597	0,500	0,670	0,208	0,006
39	130,679	15,712	1,230	0,290	0,257	0,007
40	196,739	29,967	0,570	0,760	0,218	0,004
41	227,354	33,059	0,020	0,620	0,248	0,004
42	19,166	2,555	0,885	0,049	0,264	0,045

Table A.1 (continued): Details of LA-ICP-MS U-Pb age data.

43	152,870	21,764	0,400	0,760	0,168	0,004	
44	266,039	50,031	2,100	0,890	0,169	0,002	
45	61,464	9,326	1,090	0,170	0,194	0,009	
46	214,238	39,140	1,830	0,880	0,163	0,003	
47	190,434	35,401	1,750	0,790	0,133	0,002	
48	309,455	63,395	1,180	0,810	0,244	0,002	
49	221,699	34,744	0,590	0,850	0,204	0,004	
50	49,513	8,527	0,330	0,770	0,057	0,004	
51	266,039	57,973	2,020	0,740	0,132	0,002	
52	371,346	78,911	1,220	0,640	0,182	0,002	
53	302,112	57,350	2,000	1,000	0,253	0,003	
54	217,373	44,005	1,790	0,890	0,146	0,002	
55	221,149	43,900	1,880	0,850	0,143	0,002	
56	230,292	42,845	0,680	0,640	0,176	0,003	
57	127,318	23,645	1,700	0,870	0,083	0,002	
58	151,056	28,163	2,380	0,970	0,087	0,002	
59	230,889	53,834	3,200	1,300	0,194	0,003	
60	175,094	33,368	0,840	0,630	0,154	0,003	
61	225,628	47,410	1,900	1,000	0,147	0,002	
62	220,057	39,665	1,110	0,770	0,117	0,002	
Laser spot ID	**238U/206Pb**	**2SE**	**207Pb/206Pb**	**2SE**	**U_PPM**	**Pb_PPM**	**Location 4 Sample h**
1	6,497	0,922	0,839	0,164	0,103	0,064	
2	3,968	0,115	0,814	0,028	0,184	0,164	
3	1,209	0,030	0,814	0,026	0,311	0,902	
4	2,610	0,097	0,819	0,043	0,165	0,225	

Table A.1 (continued): Details of LA-ICP-MS U-Pb age data.

5	1,403	0,041	0,808	0,029	0,216	0,538
6	1,185	0,032	0,810	0,029	0,237	0,695
7	0,965	0,059	0,818	0,069	0,315	1,182
8	0,797	0,023	0,804	0,030	0,408	1,813
9	5,798	0,404	0,808	0,079	0,160	0,100
10	0,834	0,020	0,808	0,024	0,571	2,412
11	1,355	0,046	0,821	0,037	0,173	0,453
12	73,881	10,129	0,930	0,165	0,074	0,004
13	3,635	0,144	0,819	0,042	0,110	0,107
14	3,134	0,077	0,818	0,025	0,281	0,324
15	1,582	0,033	0,789	0,019	0,336	0,733
16	1,866	0,084	0,789	0,047	0,093	0,173
17	7,358	0,319	0,812	0,046	0,176	0,084
18	1,361	0,150	0,818	0,127	0,192	0,556
19	5,590	0,153	0,796	0,027	0,303	0,188
20	1,532	0,038	0,803	0,025	0,561	1,317
21	15,269	0,789	0,793	0,050	0,197	0,045
22	1,097	0,043	0,802	0,044	0,317	1,017
23	2,595	0,154	0,810	0,067	0,172	0,239
24	6,465	0,228	0,821	0,037	0,160	0,087
25	3,865	0,179	0,805	0,050	0,156	0,145
26	23,076	1,860	0,788	0,082	0,089	0,013
27	31,482	5,517	0,883	0,208	0,153	0,018
28	1,490	0,046	0,811	0,031	0,149	0,345
29	4,222	0,121	0,814	0,030	0,208	0,174
30	1,131	0,087	0,811	0,087	0,254	0,845

Table A.1 (continued): Details of LA-ICP-MS U-Pb age data.

31	8,172	0,292	0,823	0,036	0,128	0,056
32	6,852	0,241	0,834	0,039	0,116	0,060
33	17,792	0,380	0,776	0,018	1,659	0,318
34	4,064	0,103	0,826	0,027	0,262	0,228
35	56,551	5,236	0,842	0,106	0,161	0,010
36	6,039	0,235	0,783	0,041	0,140	0,078
37	7,980	0,528	0,821	0,071	0,170	0,076
38	38,819	3,125	0,796	0,081	0,170	0,015
39	1,970	0,119	0,808	0,069	0,190	0,344
40	4,181	0,145	0,808	0,033	0,159	0,132
41	4,567	0,164	0,809	0,033	0,178	0,140
42	8,659	0,450	0,820	0,050	0,121	0,049
43	2,625	0,338	0,931	0,160	0,006	0,008
44	1,178	0,032	0,810	0,027	0,471	1,411
45	1,752	0,054	0,819	0,034	0,242	0,489
46	1,599	0,039	0,803	0,024	0,275	0,598
47	6,977	0,489	0,822	0,069	0,074	0,036
48	4,899	0,288	0,800	0,057	0,040	0,028
49	16,997	0,851	0,832	0,051	0,157	0,033
50	1,996	0,074	0,808	0,040	0,110	0,193
51	1,818	0,043	0,811	0,023	0,245	0,470
52	1,311	0,034	0,816	0,026	0,243	0,661
53	0,568	0,021	0,820	0,042	0,460	2,910
54	1,499	0,042	0,812	0,028	0,170	0,401
55	5,583	0,187	0,788	0,035	0,182	0,113
56	44,044	3,812	0,935	0,105	0,118	0,010

Table A.1 (continued): Details of LA-ICP-MS U-Pb age data.

57	8,834	0,528	0,833	0,069	0,123	0,049
58	2,498	0,061	0,798	0,025	0,340	0,478
59	1,759	0,034	0,812	0,019	0,201	0,405
60	2,126	0,099	0,788	0,048	0,198	0,320
61	0,884	0,046	0,814	0,059	0,396	1,541
62	1,889	0,148	0,814	0,087	0,132	0,258
63	4,273	0,143	0,831	0,034	0,182	0,151
64	45,578	3,628	0,733	0,075	0,136	0,010
65	2,092	0,062	0,815	0,031	0,131	0,222
66	3,147	0,093	0,786	0,029	0,149	0,163
67	4,688	0,175	0,785	0,040	0,704	0,481
68	1,604	0,056	0,811	0,037	0,227	0,495
69	5,586	0,177	0,807	0,032	0,241	0,153
70	7,553	0,174	0,778	0,022	0,964	0,434
71	2,769	0,083	0,799	0,031	0,339	0,415
72	3,091	0,095	0,800	0,032	0,307	0,349
73	1,218	0,057	0,816	0,052	0,389	1,125
74	1,218	0,139	0,816	0,131	0,750	2,120
75	6,107	0,855	0,774	0,142	0,102	0,056
76	5,042	0,255	0,845	0,055	0,148	0,103
77	6,653	0,372	0,815	0,062	0,111	0,059

Table A.1 (continued): Details of LA-ICP-MS U-Pb age data.

78	7,994	0,356	0,805	0,045	0,109	0,048	
79	6,572	0,372	0,822	0,060	0,156	0,084	
80	5,421	0,770	0,766	0,116	0,146	0,102	
Laser spot ID	**238U/206Pb**	**2SE**	**207Pb/206Pb**	**2SE**	**U_PPM**	**Pb_PPM**	**Location 3 Sample b**
1	4,170	0,272	0,608	0,049	0,024	0,016	
2	4,551	0,323	0,538	0,053	0,036	0,021	
3	2,767	0,128	0,587	0,037	0,036	0,037	
4	2,969	0,187	0,591	0,047	0,025	0,024	
5	8,612	0,811	0,526	0,058	0,062	0,020	
6	3,475	0,216	0,681	0,056	0,024	0,021	
7	26,292	1,079	0,487	0,030	0,461	0,046	
8	6,459	0,442	0,520	0,047	0,092	0,037	
9	1,060	0,125	0,520	0,085	0,025	0,059	
10	4,769	0,685	0,455	0,098	0,072	0,035	
11	5,569	0,415	0,468	0,045	0,057	0,024	
12	2,742	0,109	0,638	0,033	0,066	0,070	
13	3,979	0,162	0,514	0,028	0,358	0,228	
14	3,530	0,208	0,674	0,057	0,040	0,035	
15	6,691	0,799	0,569	0,110	0,084	0,020	
16	1,666	0,102	0,564	0,048	0,172	0,288	
17	2,920	0,075	0,579	0,018	0,414	0,395	
18	1,876	0,259	0,568	0,112	0,018	0,019	
19	3,225	0,151	0,508	0,034	0,033	0,027	
20	5,065	0,429	0,578	0,069	0,075	0,032	
21	46,261	1,623	0,284	0,017	2,364	0,095	

Table A.1 (continued): Details of LA-ICP-MS U-Pb age data.

22	3,141	0,105	0,435	0,020	0,132	0,101
23	10,270	1,000	0,444	0,062	0,265	0,057
24	17,545	0,481	0,542	0,020	1,630	0,251
25	4,665	0,243	0,549	0,037	0,034	0,019
26	2,504	0,182	0,638	0,067	0,035	0,041
27	38,946	1,134	0,288	0,014	1,147	0,057
28	12,067	0,650	0,532	0,038	0,430	0,094
29	5,153	0,592	0,480	0,074	0,032	0,014
30	4,310	0,414	0,450	0,063	0,046	0,023
31	1,565	0,055	0,475	0,021	0,155	0,246
32	3,014	0,073	0,693	0,019	0,191	0,198
33	1,849	0,057	0,410	0,017	0,084	0,103
34	3,168	0,179	0,423	0,034	0,079	0,054
35	3,409	0,259	0,571	0,060	0,141	0,105
36	15,701	0,660	0,508	0,028	0,127	0,021
37	1,399	0,124	0,526	0,065	0,033	0,052
38	7,920	0,637	0,435	0,051	0,051	0,014
39	1,618	0,126	0,436	0,046	0,082	0,106
40	56,959	2,388	0,158	0,014	0,733	0,021
41	1,826	0,100	0,575	0,041	0,084	0,112
42	83,555	1,635	0,066	0,003	4,784	0,075
43	2,258	0,154	0,501	0,048	0,039	0,041
44	1,916	0,156	0,538	0,061	0,105	0,142
45	23,287	1,270	0,484	0,038	0,996	0,106
46	1,081	0,039	0,541	0,029	0,050	0,126
47	78,028	1,630	0,080	0,004	3,186	0,056

Table A.1 (continued): Details of LA-ICP-MS U-Pb age data.

48	8,877	0,826	0,466	0,062	1,047	0,275
49	3,448	0,225	0,466	0,042	0,025	0,017
50	78,644	1,518	0,085	0,003	4,366	0,076
51	40,549	0,917	0,383	0,011	2,883	0,157
52	11,781	1,269	0,536	0,079	0,026	0,006
53	2,010	0,117	0,486	0,039	0,095	0,102
54	4,769	0,431	0,563	0,080	0,112	0,055
55	3,630	0,235	0,433	0,037	0,082	0,052
56	1,072	0,041	0,522	0,026	0,086	0,222
57	3,831	0,262	0,395	0,038	0,184	0,104
58	6,691	0,549	0,446	0,048	0,054	0,018
59	1,936	0,075	0,484	0,026	0,063	0,083
60	2,056	0,184	0,486	0,063	0,132	0,125
61	9,620	0,929	0,388	0,056	0,218	0,043
62	1,392	0,058	0,503	0,026	0,074	0,135
63	7,149	0,274	0,441	0,023	0,370	0,125
64	27,586	2,462	0,270	0,038	0,287	0,019
65	1,642	0,066	0,587	0,030	0,086	0,149
66	10,270	0,459	0,462	0,029	0,941	0,221
67	38,314	2,129	0,330	0,029	0,730	0,041

Laser spot ID	**238U/206Pb**	**2SE**	**207Pb/206Pb**	**2SE**	**U_PPM**	**Pb_PPM**	**Location 3 Sample c**
1	87,297	1,870	0,052	0,003	3,874	0,057	
2	52,645	1,978	0,257	0,021	2,975	0,108	
3	51,202	2,135	0,296	0,029	2,720	0,101	
4	48,619	1,846	0,259	0,018	2,820	0,107	

Table A.1 (continued): Details of LA-ICP-MS U-Pb age data.

5	47,436	3,263	0,230	0,019	2,229	0,082	
6	43,884	1,740	0,295	0,022	1,858	0,084	
7	40,567	1,358	0,349	0,022	1,760	0,092	
8	40,367	1,781	0,335	0,025	1,159	0,057	
9	39,652	1,473	0,297	0,024	1,620	0,079	
10	37,973	1,399	0,379	0,022	1,508	0,088	
11	36,895	1,974	0,355	0,038	2,140	0,094	
12	34,912	1,346	0,365	0,022	2,151	0,135	
13	30,599	1,984	0,315	0,035	1,830	0,093	
14	30,187	2,033	0,386	0,044	3,340	0,172	
15	28,327	0,985	0,372	0,019	0,438	0,033	
16	20,469	0,794	0,401	0,023	1,488	0,166	
17	16,603	0,738	0,411	0,028	1,850	0,242	
18	9,497	0,402	0,483	0,028	0,214	0,055	
19	9,252	0,439	0,444	0,030	0,689	0,180	
20	8,055	0,405	0,429	0,030	0,405	0,114	
21	7,428	0,363	0,485	0,033	0,233	0,077	
22	6,592	0,824	0,432	0,076	0,810	0,209	
23	5,977	0,638	0,507	0,066	0,119	0,050	
24	4,931	0,203	0,552	0,033	0,115	0,063	
25	3,103	0,107	0,535	0,021	0,120	0,102	
26	4,321	0,160	0,543	0,028	0,939	0,548	
Laser spot ID	**238U/206Pb**	**2SE**	**207Pb/206Pb**	**2SE**	**U_PPM**	**Pb_PPM**	**Location 2 Sample a**
1	273,211	12,928	0,654	0,039	2,185	0,022	
2	162,187	10,630	0,744	0,050	1,399	0,026	

Table A.1 (continued): Details of LA-ICP-MS U-Pb age data.

3	233,444	12,585	0,619	0,035	2,400	0,028
4	128,689	7,266	0,720	0,030	2,490	0,059
5	278,482	14,327	0,620	0,035	3,410	0,034
6	167,520	11,341	0,717	0,044	1,515	0,026
7	368,544	23,524	0,595	0,049	2,047	0,017
8	307,120	18,514	0,619	0,037	3,180	0,027
9	198,187	10,884	0,659	0,033	2,858	0,042
10	105,619	24,473	0,733	0,041	1,527	0,039
11	187,870	9,373	0,669	0,030	3,030	0,046
12	260,084	14,059	0,647	0,034	3,220	0,034
13	169,156	18,171	0,662	0,041	2,293	0,041
14	208,694	9,555	0,650	0,029	2,650	0,035
15	36,087	2,255	0,797	0,021	1,670	0,140
16	200,018	8,777	0,674	0,029	3,083	0,045
17	249,590	17,263	0,619	0,035	2,604	0,028
18	204,747	13,553	0,658	0,031	3,170	0,044
19	222,642	10,302	0,659	0,031	3,309	0,043
20	171,501	8,830	0,679	0,026	3,355	0,056
21	362,376	31,841	0,533	0,040	3,280	0,019
22	331,831	17,799	0,604	0,040	2,516	0,020
23	204,747	11,617	0,671	0,031	3,170	0,042
24	258,531	12,348	0,615	0,027	3,580	0,037
25	165,916	9,853	0,725	0,033	2,620	0,044
26	164,967	6,913	0,656	0,025	2,864	0,050
27	271,498	12,766	0,632	0,033	3,232	0,033
28	150,361	10,703	0,667	0,030	3,390	0,057

Table A.1 (continued): Details of LA-ICP-MS U-Pb age data.

29	181,949	9,556	0,665	0,030	2,490	0,038
30	99,207	7,387	0,743	0,028	2,470	0,064
31	301,770	18,926	0,632	0,035	3,776	0,034
32	131,823	6,019	0,758	0,030	2,730	0,062
33	167,197	7,424	0,706	0,025	3,900	0,067
34	69,901	2,708	0,781	0,020	2,663	0,120
35	173,911	17,810	0,676	0,034	2,780	0,042
36	146,050	6,896	0,738	0,030	2,300	0,046
37	196,836	15,210	0,648	0,031	3,650	0,047
38	154,934	5,820	0,698	0,024	4,660	0,089
39	226,130	12,989	0,642	0,036	2,238	0,027
40	63,682	7,960	0,757	0,025	3,290	0,118
41	67,242	4,229	0,754	0,024	2,360	0,105
42	85,244	6,712	0,780	0,037	2,000	0,050
43	76,985	3,558	0,756	0,029	1,860	0,076
44	146,793	6,966	0,747	0,026	3,270	0,066
45	136,821	5,188	0,718	0,026	2,680	0,060
46	163,411	8,633	0,673	0,029	3,520	0,060
47	184,272	9,802	0,662	0,028	3,569	0,053
48	66,621	7,687	0,755	0,028	4,020	0,103
49	133,861	8,896	0,741	0,028	2,790	0,059
50	41,638	6,206	0,735	0,036	2,130	0,073
51	208,694	15,086	0,621	0,033	3,200	0,040
52	166,554	9,289	0,705	0,038	2,570	0,043
53	145,805	6,382	0,686	0,028	2,711	0,054
54	54,164	1,965	0,745	0,018	2,510	0,144

Table A.1 (continued): Details of LA-ICP-MS U-Pb age data.

55	174,261	12,973	0,685	0,037	2,567	0,041
56	23,663	1,099	0,805	0,006	24,690	3,410
57	131,224	7,158	0,732	0,025	3,727	0,088
58	153,560	8,168	0,707	0,037	1,772	0,034
59	202,829	11,400	0,667	0,027	3,612	0,052
60	229,729	10,968	0,638	0,033	3,188	0,041
61	120,792	6,233	0,688	0,027	2,440	0,055
62	89,379	6,088	0,729	0,025	2,520	0,079
63	97,973	5,874	0,733	0,025	2,490	0,072
64	193,754	7,369	0,666	0,023	3,826	0,057
65	157,756	10,345	0,708	0,024	2,945	0,053
66	96,445	5,585	0,766	0,023	3,050	0,094
67	150,100	6,764	0,744	0,033	2,607	0,054
68	192,035	13,626	0,672	0,031	2,746	0,040
69	113,213	8,287	0,714	0,025	3,630	0,093
70	94,447	4,429	0,746	0,024	2,392	0,078
71	62,443	2,701	0,779	0,023	2,435	0,123
72	181,949	8,409	0,686	0,027	3,700	0,059
73	164,341	9,355	0,700	0,031	2,637	0,048
74	55,129	2,035	0,785	0,018	2,914	0,170
75	18,233	0,768	0,798	0,011	3,550	0,610
76	126,067	8,992	0,716	0,021	3,680	0,077
77	95,383	4,727	0,735	0,022	2,654	0,085
78	151,944	6,931	0,679	0,029	2,568	0,049
79	37,574	1,255	0,797	0,016	2,817	0,240
80	109,353	5,523	0,714	0,018	4,670	0,125

Table A.1 (continued): Details of LA-ICP-MS U-Pb age data.

81	93,027	5,795	0,733	0,020	3,070	0,095
82	155,211	6,954	0,699	0,026	3,810	0,076
83	471,464	21,815	0,461	0,032	5,260	0,025
84	115,786	4,953	0,734	0,026	2,633	0,070
85	129,847	5,451	0,701	0,026	2,649	0,061
86	330,564	18,925	0,619	0,036	3,490	0,028
87	41,618	1,680	0,771	0,017	1,944	0,147
88	29,885	1,134	0,789	0,018	1,479	0,163
89	9,031	0,245	0,795	0,009	1,810	0,652
90	266,486	31,158	0,610	0,046	3,180	0,028
91	1,831	0,077	0,799	0,008	0,750	1,283
92	17,391	1,257	0,831	0,028	0,479	0,086
93	30,177	1,998	0,807	0,029	0,743	0,070
94	78,734	7,873	0,768	0,027	2,370	0,077
95	173,563	12,174	0,696	0,031	2,509	0,044
96	147,292	12,274	0,701	0,032	2,574	0,051
97	60,906	3,855	0,867	0,081	0,264	0,014
98	100,009	7,160	0,725	0,024	2,560	0,069
99	312,664	25,961	0,640	0,074	1,081	0,009
100	279,380	12,617	0,627	0,034	3,750	0,037
101	66,621	5,637	0,747	0,028	1,360	0,052
102	102,132	5,540	0,738	0,023	2,730	0,079
103	34,923	1,690	0,790	0,016	2,598	0,242
104	140,369	7,508	0,696	0,027	2,470	0,050
105	130,630	5,320	0,717	0,028	3,304	0,076

Table A.1 (continued): Details of LA-ICP-MS U-Pb age data.

106	184,665	8,662	0,699	0,032	2,705	0,042
107	92,927	3,091	0,739	0,023	2,822	0,094
108	287,734	18,163	0,580	0,034	4,110	0,033
109	17,532	0,852	0,795	0,011	3,510	0,578
110	299,681	24,887	0,669	0,052	2,154	0,023
111	48,384	4,325	0,725	0,041	0,436	0,023
112	110,048	11,746	0,743	0,037	1,760	0,043
113	274,946	16,584	0,590	0,028	3,234	0,032
114	248,160	10,666	0,641	0,032	3,145	0,035
115	169,156	7,268	0,689	0,028	3,290	0,057
116	200,946	12,588	0,660	0,035	2,361	0,032
117	96,985	4,453	0,755	0,018	4,720	0,157
118	206,209	8,838	0,658	0,032	3,122	0,043
119	155,490	7,816	0,716	0,025	3,472	0,068
120	201,414	7,963	0,698	0,030	3,720	0,056
121	89,471	5,361	0,728	0,018	3,902	0,134
122	39,242	1,191	0,783	0,014	3,350	0,271
123	56,606	7,770	0,736	0,027	2,260	0,076
124	126,805	4,827	0,698	0,020	3,772	0,089
125	85,921	3,580	0,771	0,025	2,356	0,087
126	55,305	2,225	0,776	0,019	2,905	0,170
127	116,096	4,358	0,713	0,022	3,440	0,088
128	0,565	0,018	0,807	0,007	0,314	1,842
129	71,518	2,953	0,760	0,024	1,991	0,088

Table A.1 (continued): Details of LA-ICP-MS U-Pb age data.

130	55,164	3,865	0,766	0,014	4,650	0,256	
131	42,043	4,286	0,832	0,035	0,638	0,043	
Laser spot ID	**238U/206Pb**	**2SE**	**207Pb/206Pb**	**2SE**	**U_PPM**	**Pb_PPM**	**Location 2 Sample d**
1	30,477	0,892	0,754	0,012	3,581	0,365	
2	136,161	10,293	0,674	0,024	5,510	0,113	
3	357,283	54,626	0,483	0,056	5,290	0,006	
4	67,920	2,348	0,702	0,025	1,835	0,076	
5	229,953	17,736	0,664	0,043	1,850	0,018	
6	317,877	23,373	0,493	0,029	4,650	0,028	
7	124,406	14,141	0,660	0,059	0,674	0,014	
8	262,007	27,789	0,538	0,047	0,668	0,010	
9	72,354	4,783	0,766	0,050	1,240	0,060	
10	208,343	23,093	0,536	0,048	1,125	0,012	
11	33,001	1,889	0,737	0,038	0,315	0,038	
12	236,236	28,400	0,533	0,062	0,503	0,004	
13	183,963	15,656	0,525	0,040	0,650	0,008	
14	153,575	12,002	0,593	0,044	0,832	0,012	
15	375,924	53,937	0,462	0,065	0,620	0,004	
16	116,057	10,282	0,611	0,057	0,492	0,012	
17	220,567	23,632	0,598	0,064	0,556	0,008	
18	172,925	13,142	0,565	0,045	0,668	0,008	
19	404,030	49,088	0,381	0,081	0,473	0,002	

Table A.1 (continued): Details of LA-ICP-MS U-Pb age data.

20	119,423	11,052	0,685	0,058	0,423	0,010
21	80,806	10,573	0,687	0,083	0,142	0,006
22	317,877	37,397	0,384	0,050	1,036	0,006
23	260,429	52,556	0,800	0,130	0,283	0,006
24	33,383	4,125	0,770	0,086	0,153	0,014
25	121,950	12,900	0,664	0,044	0,579	0,016
26	340,403	48,246	0,538	0,047	0,489	0,004
27	188,371	23,803	0,595	0,080	0,298	0,004
28	249,891	18,056	0,460	0,031	1,425	0,010
29	244,244	33,808	0,520	0,090	0,268	0,004
30	53,372	4,283	0,776	0,059	0,287	0,016
31	49,806	2,668	0,744	0,041	0,654	0,037
32	67,707	4,772	0,765	0,058	0,540	0,026
33	96,498	5,277	0,612	0,034	0,788	0,023
34	146,299	14,605	0,667	0,062	0,661	0,012
35	24,917	1,795	0,759	0,027	0,336	0,047
36	24,917	2,154	0,774	0,047	0,176	0,024
37	47,247	8,004	0,692	0,045	0,484	0,032
38	39,301	1,965	0,746	0,033	0,625	0,058
39	118,118	6,132	0,623	0,029	1,401	0,031
40	17,901	1,001	0,777	0,035	0,317	0,053
41	2,566	0,160	0,799	0,021	0,187	0,208
42	20,392	1,106	0,788	0,034	0,260	0,041
43	105,058	8,680	0,652	0,045	0,589	0,018
44	88,227	10,803	0,655	0,063	0,313	0,010

Table A.1 (continued): Details of LA-ICP-MS U-Pb age data.

45	177,906	25,990	0,594	0,083	0,327	0,006
46	28,917	1,451	0,706	0,030	0,505	0,053
47	153,031	14,626	0,600	0,056	0,460	0,006
48	103,672	10,690	0,633	0,050	0,373	0,008
49	233,052	28,896	0,474	0,059	0,542	0,008
50	726,575	73,268	0,182	0,033	3,300	0,002
51	22,874	2,663	0,785	0,050	0,286	0,043
52	139,456	7,872	0,636	0,050	0,758	0,015
53	181,644	18,699	0,587	0,067	0,379	0,006
54	238,847	25,072	0,541	0,078	0,410	0,006
55	163,755	22,640	0,613	0,052	0,483	0,006
56	720,520	66,048	0,182	0,033	1,256	0,002
57	100,538	24,550	0,402	0,066	0,095	0,002
58	47,093	2,206	0,790	0,035	0,951	0,065
59	171,213	17,969	0,501	0,052	0,518	0,006
60	25,505	1,730	0,814	0,045	0,308	0,040
61	367,925	48,535	0,501	0,068	0,677	0,006
62	550,716	52,616	0,266	0,038	1,567	0,002
63	13,221	0,687	0,771	0,026	0,551	0,131
64	63,669	4,688	0,727	0,036	0,873	0,062
65	130,806	16,425	0,702	0,060	0,504	0,011
66	205,374	21,952	0,480	0,064	0,425	0,004
67	75,381	3,352	0,665	0,065	0,662	0,024
68	834,580	49,140	0,064	0,010	8,060	0,002
69	405,927	57,173	0,396	0,060	0,636	0,002
70	74,090	4,952	0,726	0,038	0,525	0,035

Table A.1 (continued): Details of LA-ICP-MS U-Pb age data.

71	94,186	6,464	0,638	0,050	0,447	0,013
72	108,078	9,592	0,670	0,057	0,330	0,009
73	138,562	15,100	0,678	0,074	0,617	0,013
74	861,180	39,456	0,048	0,005	12,880	0,000
75	192,139	24,338	0,518	0,052	0,460	0,005
76	70,871	13,361	0,634	0,062	0,227	0,015
77	112,289	17,500	0,676	0,076	0,410	0,011
78	61,321	8,698	0,706	0,038	0,423	0,022
79	363,288	22,896	0,466	0,033	2,628	0,013
80	675,488	89,713	0,182	0,059	0,583	0,002
81	131,203	10,950	0,608	0,060	0,342	0,007
82	36,026	4,954	0,679	0,100	0,082	0,005
83	12,009	2,001	0,680	0,069	0,070	0,013
84	276,238	33,537	0,506	0,063	0,582	0,003
85	650,094	53,767	0,143	0,028	1,645	0,002
86	428,032	33,904	0,421	0,051	0,903	0,003
87	12,110	0,543	0,809	0,022	0,560	0,176
88	233,682	15,789	0,608	0,042	1,948	0,023
89	245,632	23,726	0,503	0,048	0,816	0,007
90	165,637	13,962	0,644	0,060	0,718	0,011
91	32,875	2,125	0,762	0,034	0,572	0,056
92	217,242	17,467	0,547	0,038	1,601	0,016
93	355,813	26,356	0,331	0,043	0,790	0,003
94	110,566	10,887	0,635	0,049	0,465	0,013
95	39,123	2,655	0,724	0,043	0,278	0,024
96	21,402	1,218	0,715	0,031	0,255	0,039

Table A.1 (continued): Details of LA-ICP-MS U-Pb age data.

97	74,537	7,068	0,611	0,055	0,367	0,014
98	291,119	20,584	0,532	0,039	3,900	0,020
99	129,241	11,012	0,649	0,055	0,740	0,018
100	176,095	14,346	0,658	0,044	1,030	0,022
101	6,279	0,242	0,769	0,022	0,189	0,099
102	35,435	2,905	0,719	0,059	0,213	0,020
103	11,748	0,527	0,767	0,026	0,250	0,060
104	14,197	0,466	0,771	0,021	0,622	0,143
105	5,250	0,156	0,778	0,018	0,483	0,299
106	59,140	2,710	0,724	0,038	0,636	0,034
107	233,052	21,986	0,565	0,050	0,773	0,009
108	88,953	5,582	0,698	0,050	0,533	0,016
109	15,923	0,674	0,747	0,029	0,264	0,046
110	25,208	1,911	0,772	0,038	0,283	0,040
111	9,870	0,473	0,755	0,027	0,260	0,086
112	13,041	0,728	0,777	0,024	0,227	0,057
113	13,856	0,910	0,833	0,033	0,550	0,143
114	25,281	1,552	0,797	0,055	0,566	0,059
115	12,678	0,520	0,771	0,018	0,667	0,163
116	41,568	2,598	0,767	0,046	0,981	0,073
117	7,290	0,289	0,775	0,019	0,827	0,344
118	33,907	1,729	0,772	0,042	0,760	0,068
119	81,568	20,007	0,658	0,093	0,278	0,011
120	76,111	5,025	0,763	0,061	0,391	0,016
121	35,147	1,715	0,761	0,039	0,374	0,036
122	10,821	0,474	0,750	0,031	0,242	0,071

Table A.1 (continued): Details of LA-ICP-MS U-Pb age data.

123	5,890	0,209	0,782	0,020	0,340	0,198
124	8,751	0,283	0,747	0,020	0,382	0,139
125	23,495	1,468	0,758	0,038	0,579	0,079
126	8,362	0,534	0,770	0,029	0,456	0,199
127	15,385	0,931	0,756	0,027	0,336	0,069
128	51,774	4,030	0,730	0,055	0,283	0,022
129	16,375	0,713	0,761	0,030	0,389	0,073
130	9,501	0,365	0,783	0,021	0,460	0,166
131	18,126	0,798	0,743	0,030	0,394	0,075
132	29,112	2,254	0,784	0,045	0,291	0,036
133	9,792	0,410	0,728	0,026	0,242	0,078
134	20,635	1,133	0,771	0,029	0,394	0,062
135	22,227	1,028	0,791	0,031	0,467	0,071
136	75,185	6,538	0,727	0,051	0,378	0,016
137	38,089	2,685	0,745	0,043	0,581	0,034
138	23,624	1,097	0,744	0,025	0,516	0,065
139	41,231	1,966	0,755	0,039	0,634	0,045
140	60,043	4,587	0,703	0,047	0,438	0,025
141	108,078	14,861	0,588	0,075	0,271	0,009
142	22,995	1,529	0,713	0,040	0,420	0,051
143	73,900	4,421	0,711	0,044	0,685	0,029
144	337,744	36,941	0,490	0,037	0,866	0,005
145	14,221	0,538	0,791	0,021	1,132	0,244
146	5,511	0,274	0,770	0,024	0,215	0,126
147	6,307	0,225	0,845	0,021	0,365	0,199
148	231,803	16,158	0,603	0,039	1,379	0,014

Table A.1 (continued): Details of LA-ICP-MS U-Pb age data.

149	190,866	23,595	0,570	0,069	0,450	0,007
150	5,882	0,224	0,780	0,024	0,636	0,354
151	4,306	0,152	0,774	0,019	0,392	0,276
152	55,639	1,898	0,726	0,032	1,058	0,059
153	77,894	5,684	0,730	0,028	1,840	0,064
154	69,392	3,342	0,786	0,040	0,751	0,036
155	9,628	0,311	0,780	0,021	0,649	0,202
156	114,672	3,954	0,689	0,015	6,110	0,146
157	29,887	0,992	0,761	0,017	3,997	0,448
158	56,144	3,062	0,717	0,024	5,300	0,272
159	391,233	42,487	0,481	0,046	2,463	0,005
160	301,263	19,944	0,543	0,036	5,090	0,028
161	580,285	54,523	0,263	0,043	5,720	0,005
162	823,452	35,291	0,048	0,006	11,890	0,000
163	680,807	58,968	0,184	0,022	1,920	0,003
164	588,180	60,018	0,293	0,056	1,020	0,002
165	200,609	15,825	0,560	0,038	1,280	0,014
166	723,535	46,621	0,142	0,022	2,900	0,003
167	189,196	40,158	0,609	0,084	0,120	0,003
168	508,603	74,795	0,302	0,050	0,890	0,003
169	153,031	10,834	0,591	0,054	0,669	0,009
170	384,278	47,821	0,366	0,051	0,571	0,003
171	355,813	35,142	0,390	0,057	0,594	0,003
172	275,358	22,800	0,482	0,048	0,976	0,008
173	258,870	34,103	0,503	0,071	0,355	0,003
174	405,927	66,702	0,479	0,069	0,622	0,008

Table A.1 (continued): Details of LA-ICP-MS U-Pb age data.

175	167,888	13,692	0,621	0,035	0,949	0,021
176	467,365	126,315	0,185	0,062	0,240	0,000
177	173,619	10,808	0,655	0,042	1,300	0,019
178	665,096	86,974	0,217	0,047	1,010	0,002
179	580,285	70,102	0,235	0,046	0,874	0,002
180	814,147	56,730	0,095	0,016	3,754	0,002
181	64,912	2,339	0,727	0,021	2,282	0,101
182	447,992	37,139	0,403	0,044	2,200	0,007
183	230,567	12,297	0,553	0,028	2,286	0,021
184	62,428	2,479	0,698	0,023	1,184	0,057
185	141,048	6,673	0,724	0,033	3,410	0,058
186	210,371	15,867	0,572	0,041	1,120	0,014
187	60,846	3,768	0,722	0,034	0,748	0,038
188	203,921	23,566	0,609	0,058	0,739	0,009

CURRICULUM VITAE

Name Surname : Tunahan AYKUT

EDUCATION :

- **B.Sc.** : 2017, Istanbul University, Faculty of Letters, Department of Geography**.**
- **M.Sc.** : 2019, Istanbul University, Institute of Social Sciences, Department of Geography**.**

PROFESSIONAL EXPERIENCE AND REWARDS:

- Scientific and Technological Research Council of Türkiye (TUBITAK), 2214-A International Research Fellowship Programme for PhD Students award, July 2022.
- Researcher at the Scientific and Technological Research Council of Türkiye (TUBITAK) under the "2232 International Fellowship for Outstanding Researchers Program" (Grant No: 118C275) from 2020 to 2023.

PUBLICATIONS, PRESENTATIONS AND PATENTS ON THE THESIS:

- **Aykut, T., Yıldırım, C., Uysal, I. T., Ring, U., and Zhao, J.,** (2024). Constraining the <500 Ka faulting history of the Central Taurides above the Cyprus Subduction Zone: Insights from U-Th carbonate geochronology, EGU General Assembly 2024, Vienna, Austria, 14–19 Apr 2024, EGU24-378, https://doi.org/10.5194/egusphere-egu24-378, 2024.
- **Aykut, T., Yıldırım, C, & Uysal, I. T.** (2023). Active Deformation Pattern in the Western Flank of the Central Taurides, Southern Margin of the Central Anatolian Plateau: Inferences from Geomorphic Markers and Kinematic Indicators. Tectonics. 42, e2022TC007550. https://doi.org/10.1029/2022TC007550.

OTHER PUBLICATIONS, PRESENTATIONS AND PATENTS:

- **Aykut. T. & Turoğlu. H.** (2024). Effects of Climate Change on Streamflow in NE Edirne (NW Türkiye): Implications for Sustainable Hydrological Development. Sustainable Water Resources Management, 10 (2). https://doi.org/10.1007/s40899-023-00985-1.
- **Diercks, M., Mildon, Z., Boulton, S., Hussain, E., Alçiçek, C., Aykut, T., and Yıldırım, C.,** (2024). Fault interactions and Coulomb stress-triggering in complex

fault networks, EGU General Assembly 2024, Vienna, Austria, 14–19 Apr 2024, EGU24-10216, https://doi.org/10.5194/egusphere-egu24-10216, 2024.

- **Diercks, M.-L., Mildon, Z. K., Boulton, S. J., Hussain, E., Alçiçek, C., Yıldırım, C., & Aykut, T.** (2023). Constraining historical earthquake sequences with Coulomb stress models: An example from western Türkiye. Journal of Geophysical Research: Solid Earth, 128, e2023JB026627. https://doi.org/10.1029/2023JB026627.
- **Aykut, T.** (2021). Determination of Groundwater Potential Zones Using Geographical Information Systems (GIS) and Analytic Hierarchy Process (AHP) Between Edirne-Kalkansogut (Northwestern Turkey). Groundwater for Sustainable Development, 12, 100545. https://doi.org/10.1016/j.gsd.2021.100545.
- **Turoğlu, H., Uludağ, M., & Aykut, T.** (2020). Geomorphic Assesment of in-Channel Sand Excavation on The River Meriç, Turkey. Journal of Geography,(40), 295-305. DOI: 10.26650/JGEOG2020-0023.
- **Aykut, T. & Turoğlu, H**. (2020). The Effects of Structural Geomorphology Features on Drainage System Around Sinanköy (Lalapaşa-Edirne-Turkey) and Its Surroundings. Journal of Geography, (40), 25-37. https://doi.org/10.26650/jgeog2019-0022.
- **Aykut, T & Turoğlu, H.** (2019). The Effects of Structrual Features on Applied Geomorphology in Between Edirne-Lalapaşa (Turkey), Journal of Geomorphological Researches, (3), 28-48.
- **Turoğlu, H. & Aykut, T.** (2019). Flood Susceptibilty Assessment through Hydromorphometric Analysis for Ergene River Basin, Journal of Geomorphological Researches, (2), 1-15.
- **Aykut T.** (2019). An Evaluation about Consistency of Using Expert Dependent Multivariable De cision Making Method in Flood Risk Analysis: A Case Study in Pehlivanköy (Kırklareli) District. International Symposium on Geomorphology (UJES 2019), Ankara University, Ankara, Türkiye.
- **Aykut T.** (2018). The Effects of Structural Features on River Development at the Kaynarca River Basin [Abstract]. International Geography Symposium on the 30th Anniversary of TUCAUM, Ankara University, Ankara, Türkiye. http://kitaplar.ankara.edu.tr/detail.php?id =920.